TRANSIENT RESPONSE OF A PARTICIPATING MEDIUM SUBJECTED TO SHORT-PULSE RADIATION SOURCES

A THESIS

submitted by

R. MUTHUKUMARAN

for the award of the degree

of

DOCTOR OF PHILOSOPHY

DEPARTMENT OF MECHANICAL ENGINEERING

INDIAN INSTITUTE OF TECHNOLOGY GUWAHATI

APRIL 2008


भारतीय प्रौद्योगिकी संस्थान गुवाहाटी
Indian Institute of Technology Guwahati

CERTIFICATE

It is certified that the work contained in the thesis entitled **Transient Response of a Participating Medium Subjected to Short-Pulse Radiation Sources** by Mr. R. Muthukumaran, a student in the Department of Mechanical Engineering, Indian Institute of Technology Guwahati for the award of the degree of the Doctor of Philosophy (PhD) has been carried out under my supervision and that this work has not been submitted elsewhere for a degree.

Dr. Subhash C. Mishra
Professor
Department of Mechanical Engineering
I.I.T. Guwahati-781039
Assam, India

Acknowledgements

I am deeply indebted to my Thesis Supervisor, Prof. Subhash C. Mishra, for his invaluable guidance and steady encouragement throughout my PhD program. The vigor and attention bestowed by him in taking my research ahead in difficult times will never be forgotten. Starting from formulating the problems to the final numerical results and their physical interpretations, he remained deeply involved in my thesis work. He provided me with the most innovative ideas, helpful books and journals that were very helpful in successfully completing the present thesis. I have immensely benefited from each and every moment of my association with him. I am highly inspired by his intellectual prowess, punctuality and exemplary professionalism.

I am thankful to my doctoral committee members: Dr. U.K. Saha, Dr. M. Pandey, Dr. M. K. Das (currently at IIT Kharagpur) for providing insightful comments and valuable suggestions during my PhD work. Their suggestions helped me work in a focused manner and improve my communication skill. I am grateful to all of them. I would like to express my sincere thanks to Prof. U.S Dixit and other faculty members of the Department of Mechanical Engineering for their encouragement and support.

I am thankful to the other faculty members and staff of IIT Guwahati who directly or indirectly motivated me to complete my thesis work. I specially thank Mr. Amal Kalita for providing me a good computing environment in the CAD lab. He always helped me in resolving network or related problems. Bittu needs a special mention for being my partner in primary to advanced discussions on radiation and other CFD - related stuff. Without him, it would have been difficult to sustain interest in seven-dimensional radiation problems. A special gratitude is necessary for all the Siang research folks and the Tamil gang who always kept me rejuvenated. And how can I forget my parents and wife, Kala? I venerate their patience and the enormous trust they repose in my abilities. Without their moral support and wishes it would have been difficult for me to stay 3000 km away from my home for so long.

R. Muthukumaran

List of Publications from this thesis work

Journals

1. R. Muthukumaran and S.C. Mishra, Interaction of a short-pulse laser of a Gaussian temporal profile with an inhomogeneous medium, Numerical Heat Transfer, Part A, 53, 625-640, 2008.
2. R. Muthukumaran and S. C. Mishra, Thermal signatures of a localized inhomogeneity in a 2D participating medium subjected to an ultra-fast step-pulse laser wave, Journal of Quantitative Spectroscopy and Radiative Transfer, 109, 705-726, 2008.
3. R. Muthukumaran and S.C. Mishra, Transient response of a planar participating medium subjected to a train of short-pulse radiation, International Journal of Heat and Mass Transfer 51, 2418 – 2432, May 2008.
4. R. Muthukumaran and S.C. Mishra, Transport of a train of short-pulse radiation of step temporal profile through a 2-D participating medium, International Journal of Heat and Mass Transfer, 51, 2482 – 2298, May 2008.
5. R. Muthukumaran and S.C. Mishra, Effect of a step short-pulse laser train on an inhomogeneous planar participating medium, International Communications in Heat and Mass Transfer, (in press) 2008.
6. S.C. Mishra and R. Muthukumaran, Radiative transfer of a short-pulse laser wave of Gaussian temporal profile through a 2-D participating medium containing inhomogeneities of different shapes at various locations communicated to Numerical Heat Transfer Part A (accepted) 2008.
7. R. Muthukumaran and S.C. Mishra, Effects of the incidence of a Gaussian-temporal short-pulse laser of different spatial profiles on a 2D rectangular inhomogeneous participating medium communicated to Numerical Heat Transfer Part A (accepted) 2008.
8. R. Muthukumaran and S.C. Mishra, Analysis of the transport of a train of short-pulse radiation of Gaussian temporal profile through a 2-D participating medium, Heat Transfer Engineering (submitted) 2008.
9. S.C. Mishra and R. Muthukumaran, Effects of a localized inhomogeneity in a 2-D participating medium on the propagation of a short-pulse laser of Gaussian temporal profile, International Journal of Heat and Mass Transfer (under review) 2007.
10. S. C. Mishra and R. Muthukumaran, Thermal signatures of an inhomogeneous 2-D participating medium under the influence of a short-pulse laser – effects of shapes and locations of inhomogeneities, International Journal for Numerical Methods in Engineering, (submitted) 2007.

Conferences

1. S. C. Mishra and R. Muthukumaran, Transport of a Short-Pulse Radiation Through a Participating Medium, 9th National & 8th ISHMT-ASME Heat and Mass Transfer Conference, Hyderabad 3-5 January 2008 (keynote paper).

2. R. Muthukumaran and S. C. Mishra, Short-Pulse Laser Wave Propagation through a 2D rectangular participating medium containing an Inhomogeneity of different shapes and at different locations, 9th National & 8th ISHMT-ASME Heat and Mass Transfer Conference, Hyderabad 3-5 January 2008.

3. R. Muthukumaran and S. C. Mishra, Analysis of the Interaction of a Diffuse Short-Pulse Wave of Radiation with a Radiatively-Participating Homogeneous Slab, 9th National & 8th ISHMT-ASME Heat and Mass Transfer Conference, Hyderabad 3-5 January 2008.

4. R. Muthukumaran and S. C. Mishra, Finite volume method solutions for short-pulse laser incidence in an inhomogeneous planar participating medium, 9th National & 8th ISHMT-ASME Heat and Mass Transfer Conference, Hyderabad 3-5 January 2008.

5. R. Muthukumaran and S.C. Mishra, Analysis of a short-pulse laser irradiation on a planar inhomogeneous participating medium using the finite volume method,_International Congress on Computational Mechanics and Simulation (ICCMS- 06), 8-10 December 2006, IIT Guwahati.

Abstract

Thermal radiation is important in many areas such as internal combustion engines, boilers, furnaces, solar collectors, reentry vehicles, remote sensing, bio-medical imaging and surgery. Its propagation speed in vacuum is $3\times10^{8}\ {}^{\mathrm{m}}\!/_{\mathrm{s}}$. In many heat transfer problems involving thermal radiation, in which temporal information is sought at time levels above micro-seconds, radiative transfer is essentially an instantaneous process, and thus the time dependent term in the governing radiative transfer equation is neglected.

In the recent past, in certain heat transfer problems involving thermal radiation, transience is investigated at time scale of $O\left(10^{-9}\mathrm{s}\right)$ - $O\left(10^{-18}\mathrm{s}\right)$ and thus consideration of the time-dependent term in the radiative transfer equation becomes essential. Such problems are found in the fields of bio-technology, medical diagnostics, laser tissue-welding, cosmetic surgery, remote sensing, fiber optic communication, laser machining, laser marking, laser surface finishing etc.

Recently, applications of the short-pulse radiation having pulse width of $O\left(10^{-9}\mathrm{s}\right)$ - $O\left(10^{-18}\mathrm{s}\right)$ in characterizing turbid media such as tissues and water bodies have received a great attention. Under the influence of a short-pulse radiation, the time-resolved reflected and transmitted signals provide useful information about the medium. Both diffuse and collimated (laser) radiation having step as well as Gaussian temporal profiles have been investigated by many researchers. 1-D, 2-D and 3-D homogeneous as well as inhomogeneous media have been studied. Various numerical radiative transfer methods such as the differential approximation, the P-N approximation, the discrete ordinates method, the Monte Carlo method, the radiation element method, the discrete transfer method, the finite element method and the finite volume method used for the steady-state radiative transfer analyses have also been used for transient studies.

In the past, effects of the transport of a single pulse in a participating medium have been studied in detail. However, the literature on the effects of multiple-pulses on

transmittance and reflectance signals originating from the medium is scarce. The present work, therefore, deals with the analysis of transport of single and/or multiple pulses in both 1-D and 2-D homogeneous and inhomogeneous participating media. In case of the 2-D medium, localized inhomogeneities of square, circular and elliptical shapes placed at different locations in the medium have been considered. Study has been made with both diffuse and collimated (laser) short-pulse radiation of either step or Gaussian temporal profile. The pulse-width of the incident radiation is $O\left(10^{-9}\,\mathrm{s}\right)$. In case of a step-pulse, the half period of the multiple pulses is the same as the pulse-width, while it is three times that of the pulse-width in the case of a Gaussian pulse. The loading on the boundary is either spatially uniform or Gaussian. In all the cases, analyses have been done using the finite volume method.

This thesis is organized into 9 chapters. In the Introduction chapter, the importance of analyzing transport of a short-pulse radiation through a participating medium is established and literature in this field is reviewed. Different numerical methods used in the transient analysis are briefly discussed. In Chapter 2, a general formulation of the finite volume method applicable to transient radiative transfer analysis is given and its solution procedure is presented. Chapters 3-8 deal with investigation on 40 different combinations of the incident radiation, its temporal profile, its spatial loading, the geometry of the medium and its inhomogeneities. Concluding remarks and scope for the future work are presented in Chapter 9. The problems considered in Chapters 3-8 are briefly described below.

The problem in Chapter 3 analyzes transient radiative transport through a homogeneous 1-D planar participating medium. Both diffuse and collimated radiation having a step or a Gaussian temporal profile has been considered. The north boundary of the medium is under the influence of a pulse train consisting of 1-4 pulses. Effects of the extinction coefficient and the scattering albedo on transmittance and reflectance signals have been studied. Results of the present work for a single-pulse have been compared with those available in the literature. An excellent agreement has been obtained. A train of pulses has been found to provide useful information about the nature of the signals and its temporal spans.

The case of a 1-D inhomogeneous planar participating medium subjected to a train of 1-4 collimated pulses has been considered in Chapter 4. Temporal profile of the pulse train is a step or a Gaussian function. Discrete variations in the scattering albedo and the optical depth across the layers are considered to be the cause of inhomogeneities in the medium. Transmittance and reflectance signals are studied for different situations. Characteristic signals are obtained for specific inhomogeneities in the medium. With a single pulse, results of the present work have been compared with those available in the literature and a very good comparison has been obtained. Pulse train has been found to provide a good insight about the nature of inhomogeneities in a 1-D planar medium.

In Chapter 5, the transport of a train of short-pulse radiation through a 2-D homogeneous participating medium has been studied. The south boundary of the medium is under the influence of either a diffuse or a collimated radiation whose temporal profile can be a step or a Gaussian function. Transmittance and reflectance signals are analyzed for the effects of the extinction coefficient and the scattering albedo. Heat flux distributions inside the medium are also studied. With a single-pulse, results of the present work have been benchmarked against the published results.

A 2-D inhomogeneous medium closely represents many practical situations. In Chapter 6, thus the transport of a train of short-pulse radiation through a 2-D square participating medium containing localized inhomogeneities has been investigated. The inhomogeneities differ from the main medium by their scattering properties. The extinction coefficient of the medium and its inhomogeneities are the same. The effects of a square shaped inhomogeneity placed at three different locations in the medium are studied. The analysis is done with the collimated radiation and both step and Gaussian temporal profiles are considered. Transmittance and reflectance signals are analyzed for the effects of the extinction coefficient and the scattering albedo. Heat flux distributions inside the medium are also studied. The square-shaped inhomogeneity and its location in the medium have been found to influence the results. With a centrally located inhomogeneity, for a single pulse, results have been compared with those available in the literature and a good comparison has been obtained.

The effects of circular and elliptical shape inhomogeneities in a 2-D square medium have been studied in Chapter 7. Three different positions of the localized inhomogeneity have been considered. Inhomogeneities differ from the main medium by their scattering properties. Study has been made with collimated radiation. Both step and Gaussian profiles have been considered. Transmittance and reflectance signals are analyzed for the effects of the extinction coefficient and the scattering albedo. Temporal heat flux distributions inside the medium are studied. In comparison of the square-shaped inhomogeneity considered in Chapter 6, in this case, due to the curvature in the shape of the inhomogeneity, abrupt spatial distributions in the signals are found absent.

The problems considered in Chapters 3-7 have uniform loading at the boundary. In practical situation, the spatial intensity distribution of the incident collimated radiation can be a Gaussian function. In Chapter 8, therefore, the south boundary of the 2-D medium is subjected to a Gaussian loading and the temporal profile of the pulse radiation is also considered to be a Gaussian. Study is made for both homogenous and inhomogeneous media. Transmittance and reflectance signals are analyzed for the effects of the extinction coefficient and the scattering albedo. Heat flux distributions at various time levels in the medium are also analyzed.

Contents

List of Figures

B04	5.0	1.0	5.0	0.9	0.1	0.9

Case	τ_1	τ_2	τ_3	ω_1	ω_2	ω_3
B11	1.0	9.0	1.0	0.9	0.1	0.9
B12	1.0	6.0	1.0	0.9	0.1	0.9
B13	1.0	3.0	1.0	0.9	0.1	0.9
B14	1.0	2.0	1.0	0.9	0.1	0.9
B15	1.0	1.3	1.0	0.9	0.1	0.9
B16	1.0	1.0	1.0	0.9	0.1	0.9

List of Tables

Nomenclature

A - area

a - anisotropy factor

c - speed of light

G - incident radiation

H - Heaviside function

I - intensity

I_b - blackbody intensity, $\dfrac{\sigma T^4}{\pi}$

$\hat{i}, \hat{j}, \hat{k}$ - unit vectors in x, y-, z-directions, respectively

M - number of discrete directions

N - pulse number

p - scattering phase function

$\hat{n}$ - outward normal

q - heat flux

r - position

S - source term

s - geometric distance in the direction of the intensity

T - temperature

T_P - pulse period

t - time

t_p - pulse-width

V - volume of the cell

X, Y, Z - dimensions of the 3-D rectangular enclosure

x, y, z - Cartesian coordinate directions

Greek Symbols

α - finite-difference weighing factor

β - extinction coefficient $(= \kappa_a + \sigma_s)$

δ - Dirac-delta function

κ_a - absorption coefficient

μ - direction cosine with respect to the x-axis

ε - emissivity

θ - polar angle

ξ - direction cosine with respect to the y-axis

η - direction cosine with respect to the z-axis

σ - Stefan-Boltzmann constant = $5.67 \times 10^{-8}\ \mathrm{W/m^2.K^4}$

σ_s - scattering coefficient

τ - optical depth

Ω - direction, (θ, ϕ)

$\Delta\Omega$ - solid angle, $\sin\theta d\theta d\phi$

ω - scattering albedo $\left(= \dfrac{\sigma_s}{\beta}\right)$

ϕ - azimuthal angle

Subscripts

av - average

0 - for collimated radiation

c - collimated

d - diffuse

E, W, N, S, F, B - east, west, north, south, front, back

w - wall/boundary

e - exit

i - inlet

P - cell center

ref - reflectance

s - start

x, y, z - for x-, y-, z-faces of the control volume

t - total

tr - transmittance

Superscripts

m - index for the discrete direction

$*$ - dimensionless quantity

Abbreviations

1-D/2-D/ 3-D	one/two/three- dimensional
DOM	discrete ordinate method
DTM	discrete transfer method
FEM	finite element method
FVM	finite volume method
MCM	Monte Carlo method
MDA	modified differential approximation
REM	radiation element method
RTE	radiative transfer equation
TRTE	transient radiative transfer equation

CHAPTER 1

Introduction

1.1 Radiation as a Mode of Heat Transfer

Conduction, convection and radiation are the three modes of heat transfer. Presence of a medium is a must for conduction and convection. Radiative transfer between two bodies can even be without a medium. With conduction through solids, heat is carried through the atomic lattice by free electrons or by increase of vibrational energy levels of the inter-atomic bonds. In conduction through fluids, energy is transferred between molecules by collisions. In the presence of a temperature gradient, in convection, the heat transfer takes place due to the bulk motion. There lies a common notion that convection is nothing but a special form of conduction.

Mechanism of radiation is different from conduction and convection. According to the duality principle, all matters emit or absorb electromagnetic waves or photons, by raising or lowering their molecular energy levels. Thermal radiation is essentially a part of the electromagnetic spectrum that is owing to the finite temperature of a matter. One of implications of the second law of Thermodynamics is that temperature of a body will always be greater than 0 K. Thus, thermal radiation is always associated with an object and is all-pervasive. Thermal radiation is a spectral quantity and its wavelength ranges from 0.1 μm to 1000 μm which covers part of ultraviolet and infrared regions of the electromagnetic spectrum. The visible light which ranges from 0.3 μm to 0.7 μm is part of thermal radiation.

Solar heating of earthly objects and the faster cooling of black surfaces than that of white ones are day-to-day examples of the effects of thermal radiation. Temperature of a body is the main factor influencing the wavelength and intensity of the emitted radiation. Unlike conduction and convection which are proportional to the temperature difference, emitted radiation is proportional to the fourth power of the absolute temperature. Thus, although radiation is at all temperatures, it is a dominant mode at high temperatures.

Conduction and convection are essentially short-range phenomena. In these, an energy balance is feasible in an infinitesimal control volume which is very small compared to the overall dimensions of the physical domain and very large compared with the molecular mean free path of collision. Analyses of conduction and convection may involve utmost four independent variables (three space and one time) and these are less nonlinear if the properties such as thermal conductivity k and heat transfer coefficient h are independent of temperature [1]. Thermal radiation, on the other hand, is a long-range phenomenon. The mean free path of a given photon can be in the range [10^{-10}, 10^{+10}]. The principle of conservation of energy in this case has to account for all the volumes or surfaces that can be viewed from the point under consideration. Radiation transport through a medium being a volumetric phenomenon, the transport equation becomes an integro-differential one in seven variables viz., the frequency of radiation, three space co-ordinates, two co-ordinates pertaining to the direction of travel of photons in space and time. Radiative properties are also usually more complex than that of properties associated with conduction and convection. Compared to properties pertinent to conduction and convection, like kinematic viscosity, density and thermal conductivity which are usually weak functions of temperature, radiative properties are dependent on wavelengths, surface textures and temperature. Owing to all these, solution of radiative heat transfer problems are more complicated.

Radiation can be considered as electromagnetic waves or mass-less energy packets (photons). Both the views are equally competent to explain the observed radiative phenomena. Radiative properties of gases are usually described by photon theory of quantum mechanics. The wave nature of radiation is preferred to describe radiative phenomena in liquids and solids. Velocity, frequency, wave number, wavelength and angular frequency are the basic parameters needed to describe radiation. Refractive index is a property of the medium which determines the change in the velocity of radiation during travel from one medium to another. For the conservation of energy, radiation cannot change its frequency but its wavelength and wave number can.

Based on the response of a medium to the incident radiation, a medium can be categorized as *opaque, transparent*, *semi-transparent* and *translucent* [2]. Radiation can be continuously attenuated as it passes through a medium. If the attenuation is complete enough so that no radiation comes out, the medium is said to be opaque (e.g., most metals). If radiation re-emerges without any attenuation, the medium is transparent (e.g., glass). A medium that affects the wave with partial attenuation is called semi-transparent (e.g., tainted glass). A medium that allows a fraction of light to pass through it and scatters the transmitted light into many different directions is called translucent (e.g., milky glass). An opaque surface that does not reflect any radiation is called a *black surface*. As a corollary of the *Kirchoff's law* of radiation, a black surface emits and absorbs maximum amount of radiative energy at any wavelength and in any direction than any body at the same conditions.

1.2 Surface and Volumetric Radiation

Depending on the nature of the medium through which two surfaces are exchanging thermal radiation, radiation can be categorized as surface radiation and volumetric radiation. If the intervening medium does not influence the radiative transfer between the surfaces it is called a non-participating medium, and the radiative transfer in this case is called surface radiation. In this case, radiation originates from a very thin layer of the solid surface. Radiation emitted from layers deep inside get absorbed by the adjacent layers. Radiation originating from one surface is received at the other surface without any change in the magnitude. Radiation in the outer space where there is an almost perfect vacuum, and in some practical engineering applications on earth in which the media are transparent to all wavelengths of radiation, can be classified as surface radiation [1].

If the medium takes part in the radiative transfer, it is called a participating medium and radiation from such a medium is a volumetric one. The radiative intensity emitted from a point undergoes absorption, emission and/or scattering in the medium. Thus, unlike surface radiation/radiation without a participating medium, analysis in this case is more complex. Unlike emissive power, intensity of radiation is the basis quantity. Many practical applications of volumetric radiation and associated difficulties in computations to solve the problems have produced an immense volume of literature in this area.

1.3 Transient Radiative Heat Transfer

In many practical engineering applications, thermal radiation is considered to be a steady state process and in the governing radiative transfer equation, the effect of terms containing speed of light is not significant. However, in certain situations, transience is studied at time-scales as low as a nano-second. In such cases, consideration of time-dependent term in radiative transfer equation becomes important [3-9]. Pulse radiation is an important tool in many fields like remote sensing of oceans and atmospheres [3], bio-medical applications [4] and laser material processing of microstructures [5-9]. In these, radiative transport is a transient process. This thesis deals with applications of pulse radiation transport through an optically participating medium.

1.3.1 A summary of the specific applications of pulse radiation

In the recent past, ultra-fast lasers of pulse width ranging from of a nano-second to a femto-second have been developed. Developments of cost-effective methods have also been made to detect and use them in many applications like optical readers, laser surgery, combustion diagnostics, etc. Some of the areas in which pulse radiation find applications are the following :

- Automotive engineering
- Bio-medical and bio-technology
- Combustion diagnostics
- Earth science and environmental engineering
- Electronic components
- Hydraulics and hydrodynamics
- Materials research
- Mechanical engineering
- Mixing processes
- Paper production

- Process/chemical engineering
- Sprays (atomization of liquids)
- Turbulence research
- Wind engineering

Three of the important areas in which pulse radiation finds applications are briefly described in the following sections.

1.3.1.1 Remote Sensing

The study of atmosphere by remote sensing includes probing its constituents like clouds (liquid), aerosols (suspended particles), and ozone and water vapor (gases). Laser-based systems called lidars (**li**ght detection **a**nd **r**anging) are used to study the atmosphere with high precision [3, 12, 36, 50]. A lidar can penetrate thin or broken clouds in the lower atmosphere. It enables meteorologists and researchers to study the vertical stratum of the atmosphere and hence global measurements of the vertical structure of clouds and atmospheric gases with phenomenal accuracy [72-74]. It uses a short pulse laser to detect particles or gases in the atmosphere. Propagating through the atmosphere as a dense unbroken beam, the laser disperses very little as it moves away from its origin, such as from space down to the earth's surface. The laser energy is scattered by tiny particles and even molecules in the atmosphere and the reflected light reaches back at a telescope and is collected and measured. By precisely timing the collected radiation, and by measuring the magnitude of reflected radiation received by the telescope, the location, distribution and nature of the particles can be determined accurately [27-30]. Thus, the lidar enables collection and processing of data related to atmospheric constituents ranging from cloud droplets to industrial pollutants, many of which are difficult to detect by other means.

1.3.1.2 Medicine

Medicine has greatly benefited from lasers. Lasers have found applications in almost every field of medicine. Examples include but are not limited to burn therapy, cardiology, dermatology, gynecology, neurosurgery, oncology, ophthalmology, orthopedics, plastic and reconstructive surgery, urology, vascular and general surgery [10, 11, 14-21, 33-41, 70, 71, 107, 108, 119, 120]. Laser surgery has been established to be easier for both the surgeon and the patient than traditional surgery enabling the surgeon to perform nearly bloodless surgery. For the patient, the advantages are numerous. The most important being the shorter hospital stay, the lessened need or total elimination of drugs thus reducing the cost of surgery. There are four basic types of lasers used in surgery today. The most commonly used is the carbon dioxide laser which penetrates tissues by turning its water content into steam. This laser cuts through the tissue with its intense heat, and then closes the broken blood vessels with the same heat. On initial contact, it penetrates only 0.1 to 0.2 mm [70]. The second-most used laser in medicine today is the Nd:YAG laser which is based of a neodymium-yttrium-aluminum-garnet medium. This laser beam cooks the tissue instead of cutting it and seals broken blood vessels as it penetrates. However, this laser penetrates tissue four to five millimeters on initial contact. Due to this, though it is little less accurate, it has proven to be effective for larger surgeries. The third most used laser is the argon laser which uses argon gas as a medium. Since it reacts to red color, it penetrates only until it comes into contact with blood. This laser is applied in dermatology for removing skin lesions. The fourth type of laser is called the excimer laser which is used in corneal surgery in ophthalmology [107].

1.3.1.3 Laser Machining

The devices and tools used in medicine are attaining greater functionality and are expected to last longer than earlier devices, and most importantly they are becoming smaller in size. Design, manufacturing and packaging the devices and components pose new challenges for manufacturers. Of the technologies available, the use of laser technology for such processes as welding, drilling, ablation, cutting, and marking can provide options for manufacturing small medical devices [5-8].

Lasers are used in device manufacturing for a variety of processes. Laser cutting, for example, is a common application and is often employed for manufacturing small devices such as stents. Lasers can also be used for drilling either through-cut or blind holes. This process can be adapted for drilling micro-fluidic channels in medical diagnostic equipment and for holes in micro-syringes used for drug delivery. Silicon-based micro-machines for micro-sensors and actuators are being developed for lab-on-a-chip devices using laser processing [6]. Laser welding and marking are often used for implantable and surgical tools. In addition, lasers are routinely used for surface texturing, such as surface modification of orthopedic implants to improve surface adhesion.

Laser wavelengths used in material processing extend from ultraviolet to infrared and include the visible spectra. In addition to laser type, there are many important aspects of laser selection, including laser cavity design, delivery optics and laser-material interaction. As a beam of laser light impinges on a material's surface, energy is partially reflected, partially absorbed, and partially transmitted depending on the material type and laser wavelength [23-26]. Of the light energy impinging on the surface, the portion that is absorbed is of interest in material processing [56]. Light is absorbed in the form of electronic and vibration excitation of the atoms, and energy converts into heat, which dissipates to adjacent atoms. As more and more photons are absorbed, the material temperature increases, thereby increasing the fraction of light absorbed. The process sets off a chain reaction resulting in a rapid rise in temperature in a very short time, typically within a millisecond for welding applications. The rate of temperature rise depends on a balance between energy absorbed and dissipated by the material [57-62]. For example, stainless steel has poor heat conductivity compared with nickel and, therefore, can be micro-machined by much longer pulse widths. On the other hand, silicon is quite conductive and requires shorter pulse durations, compared with nickel, to produce ablation [59].

With femto-second pulses, the interaction between the laser and materials is thought to occur in a nonlinear multi-photon process because of the high power density and short time frames. The process is so fast that one can think of the beam practically plucking atoms from the surface without disturbing adjacent atoms. Femto-second lasers are suitable for micromachining because they do not leave a disturbed layer on the exposed surfaces. Pulse energy, power density, pulse duration and repetition rate, peak power and spot diameter are some important parameters in laser machining [63-67]

Gaining knowledge of laser parameters and laser-material interaction initiates many opportunities to use lasers in medical device manufacturing. A review of the laser's wavelength, power level, and pulse duration and a parametric study to know how these qualities work with each other is essential for any specific instance of laser machining. As devices become smaller and more sophisticated, engineers are bound to more carefully consider the characteristics of laser systems and how they affect material processing.

1.4 Numerical Methods for Solutions of Pulse Radiation Transport through a Participating Medium

The governing transport equation (Eq. (1.1)) for transient radiative heat transfer (TRTE) is a complex integro-differential equation of hyperbolic nature[1]. The main objective of numerical methods to solve the TRTE (Eq. (1.1)) is to reduce the source term integral on the right hand side of the equation due to in-scattering, to a simpler term [1]. Researchers have applied the following numerical methods to obtain the solutions of various kinds of problems related to transport of pulse radiation through participating media [12, 16, 17, 21, 30, 31-32, 47, 54, 70, 71-73, 79-123]:

$$\left(\frac{1}{c}\right)\frac{\partial I}{\partial t}+\frac{dI}{ds}=-\beta I+\kappa_a I_b+\frac{\sigma_s}{4\pi}\int_{4\pi} I\ p\left(\Omega,\Omega'\right)d\Omega' \tag{1.1}$$

- The two-flux method considers the scattering intensity to be constant over the forward- and backward- facing hemispheres [31].

- The general P_N approximation models intensity by expanding it as a series of Legendre polynomials of the direction cosines. P_1 and P_3 approximations are normally used. The P_1 approximation converts the TRTE into a system of parabolic equations by omitting the heat flux transient [31]. Higher order approximations are difficult to use.

- The quasi-steady (traditional) transient method involves solving the TRTE by neglecting the time-derivative term. The time-dependence of intensity is introduced only through the source term or the boundary conditions [31].

- The Galerkin method is a finite-element based procedure in which the integral form of the TRTE is transformed into a set of algebraic equations for the calculation of

---

[1] Details of this equation are described in Chapter 2.

the coefficients in the power series expansion of either radiative intensity or source term [102].

- The REM [79] is a method in which the physical domain is discretized into arbitrary configurations called as radiation elements consisting of numerous polyhedrons such as triangles, quadrilaterals, wedges and hexahedrons. The concepts of absorption view factor and diffusely scattering view factor are introduced and their values obtained using ray-tracing method. An effective area for each radiation element including volume element is calculated and it is identical to the surface area when a surface element is considered. The analysis of radiative transfer is based on the net radiation method commonly used in surface radiation transfer. Radiative flux at the boundaries and radiative flux divergence inside the medium can be obtained directly.

- Hsu et. al. [121] have used the YIX method which is efficient in treating inhomogeneous media and the quadrature method used to generate high-order accuracy solutions which are mathematically more demanding.

- Tan and Hsu [84] have proposed an integral equation formulation of Volterra type which defines a time-dependent zone of integration called the domain of influence, representing a volume within which the radiation effect can reach a particular position in a specific time.

- Wu and Ou [95] have used the MDA suggested by Chandrasekhar to transient radiative transfer in a scattering planar medium exposed to collimated pulse irradiation. The propagation speed of the scattered component in the MDA is $\frac{c}{\sqrt{3}}$, while the remnant of the collimated irradiation propagates at a correct speed c. To correct the propagation speed of the scattered component they have followed a hybrid technique which they have referred to as the modified $P_{1/3}$ approximation

- The MCM which is a stochastic and time-consuming method to solve the TRTE has been used by many researchers [98,106,111,112].

- Rath et al. [96] and Mishra et al. [97] have applied the DTM which is a ray tracing method and it uses a mathematical interpolation between two cell faces to get the value of the source term at a cell centre.

- Mishra et al. [97], Sakami and Mitra [100], Kumar [31] have dealt with original and modified forms of the DOM [9, 12, 17, 21, 31, 46, 72, 74] which is a standard method used in atmospheric radiation problems and it discretizes the RTE on standard discrete directions.

- The finite volume method (FVM) [80, 81, 97] is another an efficient method in which the TRTE is integrated along each elemental solid angle and it is gaining more popularity in the recent times due to its successful applications to complex grid structures. All the problems in the present thesis have been solved by using this method.

The numerical methods which are used for the treatment of steady-state radiative transport problems are also used in the analysis of transient radiative transfer problems.

In previous studies, [31, 79, 80, 81, 84, 96, 97, 100, 111, 112, 121] investigations of a transport of a pulse radiation through a participating medium have been mostly done using the P_N approximation, differential approximation, DTM, DOM and MCM. Studies with the FVM, with is a robust method are scarce. Further, geometries and medium composition considered in earlier studies have been relatively simple and investigations were carried out with a single pulse.

This thesis explores the usage of the FVM for different types of problems involving transport of pulse radiation through a participating medium. Radiation pulse of collimated as well as diffuse are considered. Single and multiples pulses of radiation having step or Gaussian temporal profiles are considered. Effects of inhomogeneities of different shapes not considered in earlier studies are investigated. This thesis gives a comprehensive study of transport of a short-pulse diffuse or collimated radiation through an optically participating medium. The objective and organization of thesis are given in the next section.

1.6 Objective and Organization of Thesis

Any numerical method has to satisfy certain basic criteria to be used as a successful approach to solve a variety of problems. Ease, computational efficiency, applicability to different geometries, compatibility with commercial software packages and accuracy are some of the important criteria. A large number of problems involving pulse radiation which have been solved by a wide range of numerical methods have been reported in the literature. Problems in 1-D [11, 30-32, 36, 73, 79, 80, 84, 86, 91, 95-97, 101, 102, 104, 117], 2-D [12, 17, 45, 70, 71, 72, 82, 98, 100, 113,119-121] and 3-D Cartesian as well as cylindrical geometries [15, 81, 85, 97, 118] subjected to collimated [79-104] or diffuse pulses [79, 88-89] having continuous pulses [118,119] have been considered. Medium having non-unity refractive indices [79], graded media [115], long time span radiation-conduction [98,123], non-Fourier heat conduction due to laser pulses [54,123] etc, have also been studied.

In earlier studies, analyses have been done for a single short-pulse laser incidence. More explicit information about the medium can be obtained when it is subjected to multiple pulses. However, such studies have not been done before. Thus the need for a treatise encompassing the effects of a single and or multiple pulses with and without local inhomogeneity of certain shapes in a medium has been felt.

In the past, for some simple cases, some of the problems in this area have been solved by computationally more demanding methods like the MCM and the less accurate method like the differential approximation. The FVM is a robust method adaptable to any geometry. Unlike the DTM and DOM, it is less prone to ray effect. The application of the FVM to exhaustive combinations of pulse radiation problems of various medium geometries, inhomogeneity geometries, pulse temporal profiles, pulse periods, pulse widths and directional nature of the sources of incidence viz. collimated and diffuse has not been studied elaborately. Therefore, in the present work, we have done the analysis using FVM studying its applicability and computational efficiency to a variety of problems addressing the above features. The details of the methodologies of the FVM used in the present work can be found in [80] and [103].

This dissertation deals with the analysis of transport of single and/or multiple pulses in both 1-D and 2-D homogeneous and inhomogeneous participating media. The participating media considered are of a wide range of optical properties, which cover a variety of engineering, bio- and other matter of due importance in sciences, engineering and technology. In case of the 2-D medium, localized inhomogeneities of square, circular and elliptical shapes placed at different locations in the medium have been considered. Study has been made with both diffuse and collimated (laser) short-pulse radiation of either step or Gaussian temporal profile. The pulse-width of the incident radiation is $O\left(10^{-9}\text{s}\right)$. In case of a step-pulse, the half period of the multiple pulses is the same as the pulse-width, while it is three times that of the pulse-width in the case of a Gaussian pulse. The loading on the boundary is either spatially uniform or Gaussian. In all the cases, analyses have been done using the finite volume method.

This thesis is organized into 9 chapters. In Chapter 1, the importance of analyzing transport of a short-pulse radiation through a participating medium is established and literature in this field is reviewed. Different numerical methods used in the transient analysis are briefly discussed. In Chapter 2, a general formulation of the finite volume method applicable to transient radiative transfer analysis is given and its solution procedure is presented. Chapters 3-8 deal with investigation on 40 different combinations of the incident radiation, its temporal profile, its spatial loading, the geometry of the medium and its inhomogeneities. Concluding remarks and scope for the future work are presented in Chapter 9. The problems considered in Chapters 3-8 are briefly described below.

The problem in Chapter 3 analyzes transient radiative transport through a homogeneous 1-D planar participating medium. Both diffuse and collimated radiation having a step or a Gaussian temporal profile has been considered. The north boundary of the medium is under the influence of a pulse train consisting of 1-4 pulses. Effects of the extinction coefficient and the scattering albedo on transmittance and reflectance signals have been studied. Results of the present work for a single-pulse have been compared with those available in the literature. An excellent agreement has been obtained. A train of pulses has been found to provide useful information about the nature of the signals and its temporal spans.

The case of a 1-D inhomogeneous planar participating medium subjected to a train of 1-4 collimated pulses has been considered in Chapter 4. Temporal profile of the pulse train is a step or a Gaussian function. Discrete variations in the scattering albedo and the optical depth across the layers are considered to be the cause of inhomogeneities in the medium. Transmittance and reflectance signals are studied for different situations. Characteristic signals are obtained for specific inhomogeneities in the medium. With a single pulse, results of the present work have been compared with those available in the literature and a very good comparison has been obtained. Pulse train has been found to provide a good insight about the nature of inhomogeneities in a 1-D planar medium.

In Chapter 5, the transport of a train of short-pulse radiation through a 2-D homogeneous participating medium has been studied. The south boundary of the medium is under the influence of either a diffuse or a collimated radiation whose temporal profile can be a step or a Gaussian function. Transmittance and reflectance signals are analyzed for the effects of the extinction coefficient and the scattering albedo. Heat flux distributions inside the medium are also studied. With a single-pulse, results of the present work have been benchmarked against the published results.

A 2-D inhomogeneous medium closely represents many practical situations. In Chapter 6, thus the transport of a train of short-pulse radiation through a 2-D square participating medium containing localized inhomogeneities has been investigated. The inhomogeneities differ from the main medium by their scattering properties. The extinction coefficient of the medium and its inhomogeneities are the same. The effects of a square shaped inhomogeneity placed at three different locations in the medium are studied. The analysis is done with the collimated radiation and both step and Gaussian temporal profiles are considered. Transmittance and reflectance signals are analyzed for the effects of the extinction coefficient and the scattering albedo. Heat flux distributions inside the medium are also studied. The square-shaped inhomogeneity and its location in the medium have been found to influence the results. With a centrally located inhomogeneity, for a single pulse, results have been compared with those available in the literature and a good comparison has been obtained.

The effects of circular and elliptical shape inhomogeneities in a 2-D square medium have been studied in Chapter 7. Three different positions of the localized inhomogeneity have been considered. Inhomogeneities differ from the main medium by their scattering properties. Study has been made with collimated radiation. Both step and Gaussian profiles have been considered. Transmittance and reflectance signals are analyzed for the effects of the extinction coefficient and the scattering albedo. Temporal heat flux distributions inside the medium are studied. In comparison of the square-shaped inhomogeneity considered in Chapter 6, in this case, due to the curvature in the shape of the inhomogeneity, abrupt spatial distributions in the signals are found absent.

The problems considered in Chapters 3-7 have uniform loading at the boundary. In practical situation, the spatial intensity distribution of the incident collimated radiation can be a Gaussian function. In Chapter 8, therefore, the south boundary of the 2-D medium is subjected to a Gaussian loading and the temporal profile of the pulse radiation is also considered to be a Gaussian. Study is made for both homogenous and inhomogeneous media. Transmittance and reflectance signals are analyzed for the effects of the extinction coefficient and the scattering albedo. Heat flux distributions at various time levels in the medium are also analyzed.

1.7 Summary

Importance of thermal radiation was discussed. Complexity involved in treatment of thermal radiation was addressed briefly. Cases in which radiation transport needs to be considered a transient phenomenon were highlighted. Various applications of pulse radiation were enumerated. Three major applications, including that of the biomedical applications, were discussed. Numerical radiative transfer methods used in the analyses of pulse radiation through a participating medium were mentioned. The background for using the FVM as a numerical method for solving a variety of pulse radiation problems in present work was set up. Objectives and organization of the thesis were presented. In Chapter 2, a general formulation of the problem dealing with the transport of a pulse radiation through a participating medium will be discussed.

CHAPTER 2

The General 3D FVM Formulation for a Short-pulse Laser Transport through a Participating Medium

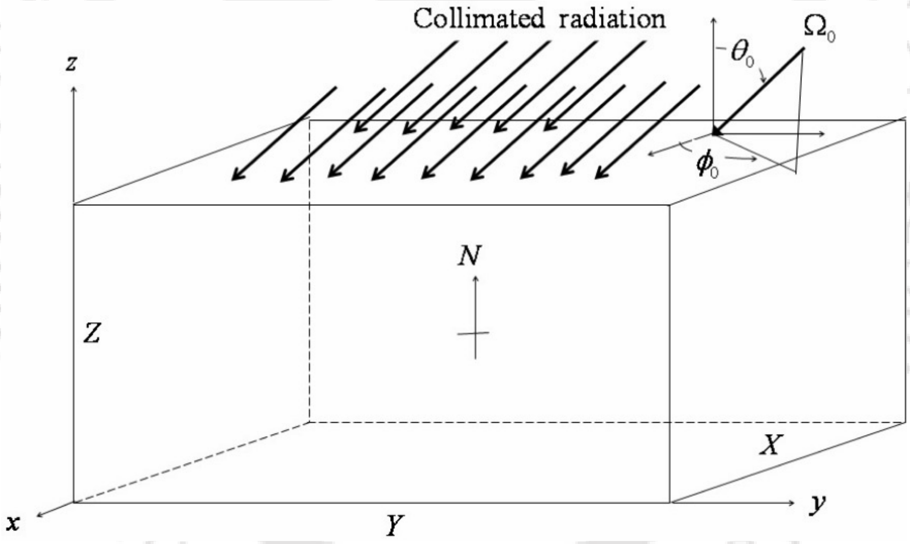

Figure: A 3-D rectangular Cartesian enclosure being subjected to collimated radiation on its top boundary

2.1 Introduction

A basic mathematical model for the transport of a short-pulse laser through a participating medium is essential for the solution of a variety of problems. This chapter presents a mathematical formulation in the finite volume method for the transport of a short-pulse laser through a three dimensional absorbing-emitting-scattering medium. The development of formulation pertaining to multiple pulses of step or Gaussian temporal profiles, collimated or diffuse pulses for 1-D and 2-D cases and different spatial profiles will be presented in subsequent chapters.

2.2 Formulation

Consider an absorbing, emitting and scattering three-dimensional medium as shown in Fig. 2.1(a). Its top boundary is subjected to a collimated radiation I_c at an angle Ω_0. At this boundary, the incident collimated radiation having intensity I_c traveling with the speed of light c is available only for duration t_p (Fig. 2.1(b)). The participating medium and the boundaries being at finite temperatures, the diffuse radiation also becomes time dependent. In this situation, the transient radiative transfer equation (TRTE) in any direction $\hat{s}$ identified by the angle Ω (Fig. 2.2) about the elemental solid angle $\Delta\Omega$ is given by [12].

Considering the effect of absorption, emission and scattering, an energy balance over the elemental control volume in any direction $\hat{s}$ about the elemental solid angle $\Delta\Omega$ (Fig. 2.2) can be given as

$$\begin{aligned} I_\eta\left(s+ds,\hat{s},t+dt\right)-I_\eta\left(s,\hat{s},t\right) &= \underbrace{\kappa_{a\eta} I_{b\eta}(s,t)ds}_{\text{gain by emission}} - \underbrace{\kappa_{a\eta} I_\eta\left(s,\hat{s},t\right)ds}_{\text{loss by absorption}} \\ & \quad - \underbrace{\sigma_{s\eta} I_\eta\left(s,\hat{s},t\right)ds}_{\text{loss by out-scattering}} + \underbrace{\frac{\sigma_{s\eta}}{4\pi}\int_{4\pi} I_\eta(\hat{s}_i)\,p_\eta(\hat{s}_i,\hat{s})\,d\Omega_i\,ds}_{\text{gain by in-scattering}} \end{aligned} \tag{2.1}$$

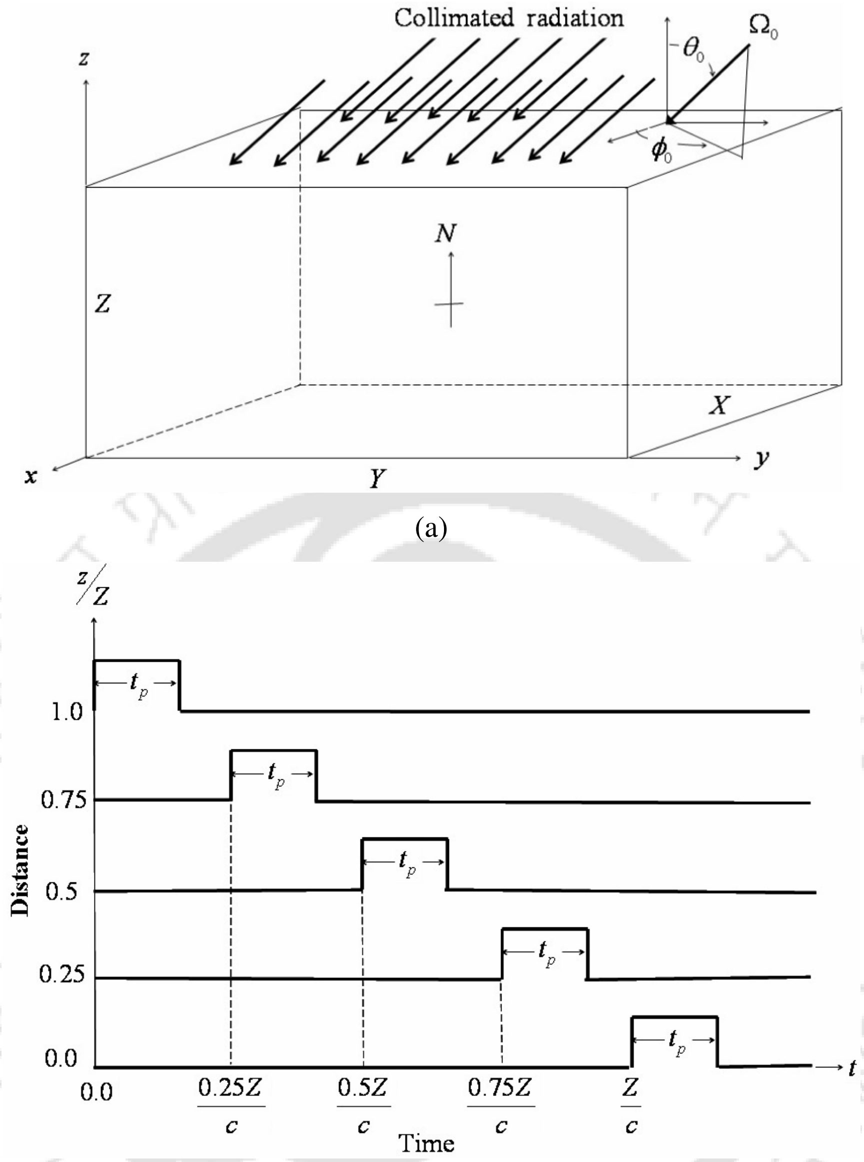

(a)

(b)

Figure 2.1: (a) A 3-D rectangular geometry and the coordinates under consideration, (b) time of arrival of the collimated square pulse at different locations for a normal angle of incidence, $\theta_0 = 0^0$.

By expanding first term on the left-hand side of Eq. (2.1) into a Taylor series and neglecting the higher order terms, we get

$$I_\eta\left(s+ds,\hat{s},t+dt\right)=I_\eta\left(s,\hat{s},t\right)+dt\frac{\partial I_\eta}{\partial t}+ds\frac{\partial I_\eta}{\partial s}=I_\eta\left(s,\hat{s},t\right)+\frac{ds}{c}\frac{\partial I_\eta}{\partial t}+ds\frac{\partial I_\eta}{\partial s} \tag{2.2}$$

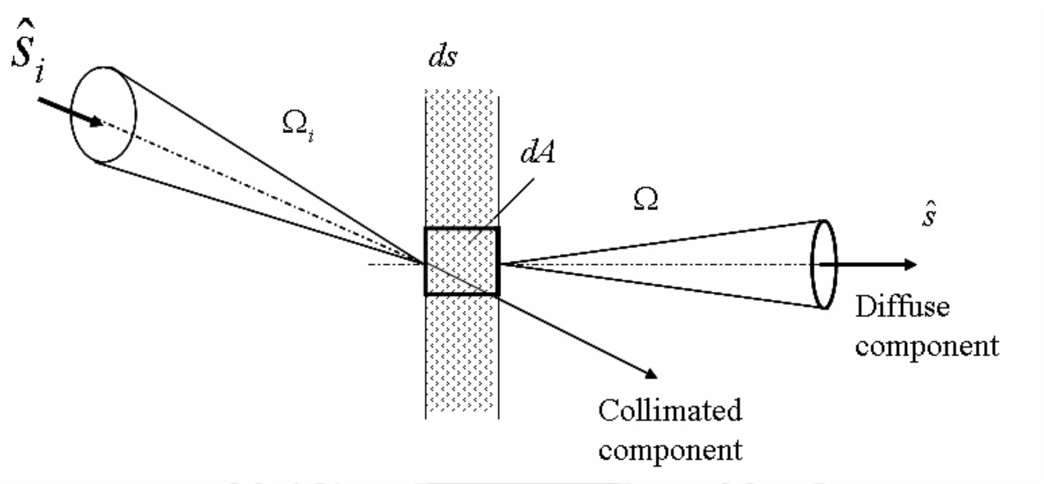

Figure 2.2: A control volume of a 1-D planar participating medium interacting with an incident ray of laser

In Eq. (2.1), where s is the geometric distance in the direction $\hat{s} = (\sin\theta\cos\phi)\hat{i} + (\sin\theta\sin\phi)\hat{j} + \cos\theta\hat{k}$, k_a is the absorption coefficient, σ_s is the scattering coefficient and p is the scattering phase function. Subscript η in the above equations shows dependence of quantities on wavelength of radiation. For the sake of simplicity, in the following pages, subscript η is dropped. In the above equation, terms containing κ_a and σ_s have the same effect and thus the these two can be clubbed together. The summation of the two terms, defined a below, is called the extinction coefficient.

$$\beta = \kappa_a + \sigma_S \tag{2.3}$$

Eq. (2.2) can be written as

$$\left(\frac{1}{c}\right)\frac{\partial I}{\partial t} + \frac{\partial I}{\partial s} = -\beta I + \kappa_a I_b + \frac{\sigma_s}{4\pi}\int_{4\pi} I\, p\,(\Omega,\Omega')\,d\Omega' \tag{2.4}$$

In Eq. (2.4), the intensity I within the medium has two components, *viz.*, the collimated intensity I_c and the diffuse intensity I_d related by

$$I = I_c + I_d \tag{2.5}$$

The variation of the collimated component I_c within the medium is given by

$$\left(\frac{1}{c}\right)\frac{\partial I}{\partial t} + \frac{\partial I}{\partial s} = -\beta I_c \tag{2.6}$$

Substituting Eqs. (2.5) and (2.6) in Eq. (2.4) yields

$$\left(\frac{1}{c}\right)\frac{\partial I_c}{\partial t}+\left(\frac{1}{c}\right)\frac{\partial I_d}{\partial t}+\frac{\partial I_d}{\partial s}=-\beta I_d+\kappa_a I_b+\frac{\sigma_s}{4\pi}\int_{4\pi} I_d\, p\left(\Omega,\Omega'\right)d\Omega' + \frac{\sigma_s}{4\pi}\int_{4\pi} I_c\, p\left(\Omega,\Omega'\right)d\Omega' \tag{2.7}$$

Equation (2.7) can be written as

$$\left(\frac{1}{c}\right)\frac{\partial I_c}{\partial t}+\left(\frac{1}{c}\right)\frac{\partial I_d}{\partial t}+\frac{\partial I_d}{\partial s}=-\beta I_d+S_c+S_d=-\beta I_d+S_t \tag{2.8}$$

where S_c and S_d are the source terms resulting from the collimated and the diffuse components of radiation, respectively. In Eq. (2.8), $S_t=S_c+S_d$ is the total source term.

At any point in the medium, the collimated radiation I_c remains available only for the pulse duration t_p. Equation (2.8) can then be written as

$$\left(\frac{1}{c}\right)\frac{\partial I_d}{\partial t}+\frac{\partial I_d}{\partial s}=-\beta I_d+S_t \tag{2.9}$$

The source term S_c resulting from the collimated radiation I_c is given by

$$S_c\left(t\right)=\frac{\sigma_s}{4\pi}\int_{\Omega'=0}^{4\pi} I_c\left(\Omega,t\right)p\left(\Omega,\Omega'\right)d\Omega' \tag{2.10}$$

For a linear anisotropic phase function $p(\Omega,\Omega')=1+a\cos\theta\cos\theta'$, the source term S_c is given by

$$S_c\left(t\right)=\left(\frac{\sigma_s}{4\pi}\right)\int_0^{2\pi}\int_0^{\pi} I_c\left(\theta,\phi,t\right)\left(1+a\cos\theta\cos\theta_0\right)\sin\theta\, d\theta\, d\phi \tag{2.11}$$

where θ and ϕ are the polar and azimuthal angles, respectively. In terms of the incident radiation G_c and heat flux q_c, Eq. (2.11) can be written as

$$S_c\left(t\right)=\frac{\sigma_s}{4\pi}\left[G_c\left(t\right)+a\cos\theta\, q_c\left(t\right)\right] \tag{2.12}$$

where G_c and q_c are given by

$$G_c=I_c(\theta_0,\phi_0) \tag{2.13}$$

$$q_c=I_c(\theta,\phi)\cos\theta_0=I_c(\theta_0,\phi_0)\cos\theta_0\,\delta(\theta-\theta_0)\delta(\phi-\phi_0) \tag{2.14}$$

In Eq. (2.14), δ is the Dirac delta function defined as

$$\delta(\theta-\theta_0)=\begin{cases}1, & \text{for } \theta=\theta_0\\ 0, & \text{for } \theta\neq\theta_0\end{cases} \tag{2.15}$$

In Eqs. (2.13) and (2.14) above, I_c is given by

$$\begin{aligned}I_c(\theta,\phi,t)&=I_c(\theta_0,\phi_0,t)\exp(-\beta ds_0)\\&\times\left[H\{\beta(ct-ds_0)\}-H\{\beta(ct-ds_0)-\beta ct_p\}\right]\times\delta(\theta-\theta_0)\delta(\phi-\phi_0)\end{aligned} \tag{2.16}$$

where $ds_0={dz}/{\cos\theta_0}$ is the geometric distance in the direction Ω_0 of the collimated radiation and $t^*=\beta ct$ is the non-dimensional time. Equation (2.16) can be written as

$$\begin{aligned}I_c(\theta,\phi,t^*)&=I_c(\theta_0,\phi_0,t^*)\exp(-\beta ds_0)\\&\times\left[H\{(t^*-\beta ds_0)\}-H\{(t^*-\beta ds_0)-t_p^*\}\right]\times\delta(\theta-\theta_0)\delta(\phi-\phi_0)\end{aligned} \tag{2.17}$$

In the Eqs.(2.16) and (2.17), H is the Heaviside function defined as

$$H(y)=\begin{cases}1, & y>0\\ 0, & y<0\end{cases} \tag{2.18}$$

Radiation travels with the speed of light c and hence takes some finite time to reach a particular point in the domain, the time of arrival of the pulse at that point will depend upon its location. Moreover, at any location in the medium, I_c remains available only for the duration t_p^* (Fig. 2.1(b)). These effects are taken care, mathematically by the introduction of the Heaviside function in the above equations.

In Eq. (2.8), the source term S_d resulting from the diffuse radiation I_d is given by

$$S_d(t^*)=\kappa_a I_b(t^*)+\frac{\sigma_s}{4\pi}\int_{\Omega'=0}^{4\pi}I_d(t^*)\,p(\Omega,\Omega')\,d\Omega' \tag{2.19}$$

In terms of G and q, for linear anisotropic phase function $p(\Omega,\Omega')=1+a\cos\theta\cos\theta'$, Eq. (2.19) is given by

$$S_d(t^*)=\kappa_a I_b(t^*)+\frac{\sigma_s}{4\pi}\left[G_d(t^*)+a\cos\theta\, q_d(t^*)\right] \tag{2.20}$$

In Eq. (2.16), G_d and q_d are given by [97]

$$
\begin{aligned}
G_d\left(t^*\right) = \int_{\Omega=0}^{4\pi} I_d\left(t^*\right) d\Omega &= \int_{\phi=0}^{2\pi}\int_{\theta=0}^{\pi} I_d(\theta,\phi,t^*)\sin\theta\, d\theta\, d\phi \\
&\approx \sum_{k=1}^{M_\phi}\sum_{l=1}^{M_\theta} I_d(\theta_l,\phi_k,t^*)\, 2\sin\theta_l \sin\left(\frac{\Delta\theta_l}{2}\right)\Delta\phi_k
\end{aligned}
\tag{2.21}
$$

where M_θ and M_ϕ are the number of discrete points considered over the complete span of the polar angle θ $\left(0 \le \theta \le \pi\right)$ and azimuthal angle ϕ $\left(0 \le \phi \le 2\pi\right)$, respectively.

$$
\begin{aligned}
q_d\left(t^*\right) = \int_{\Omega=0}^{4\pi} I_d\left(t^*\right)\cos\theta\, d\Omega &= \int_{\phi=0}^{2\pi}\int_{\theta=0}^{\pi} I_d(\theta,\phi,t^*)\cos\theta\sin\theta\, d\theta\, d\phi \\
&\approx \sum_{k=1}^{M_\phi}\sum_{l=1}^{M_\theta} I_d(\theta_{l,}\phi_k,t^*)\, 2\sin\theta_l \cos\theta_l \sin(\Delta\theta_l)\Delta\phi_k
\end{aligned}
\tag{2.22}
$$

For a boundary having temperature T_w and emissivity ε_w, the boundary intensity $I_d\left(r_w,t^*\right)$ is given by and computed from

$$
\begin{aligned}
I_d\left(r_w,t^*\right) &= \frac{\varepsilon\sigma T_w^4}{\pi} + \left(\frac{1-\varepsilon}{\pi}\right)\int_{\hat{n}_w\cdot\hat{s}<0}\left[I_{d,w}\left(t^*\right) + I_{c,w}\left(t^*\right)\right]\cos\theta d\Omega \\
&\approx \frac{\varepsilon\sigma T_w^4}{\pi} + \left(\frac{1-\varepsilon}{\pi}\right)\sum_{k=1}^{M_\phi}\sum_{l=1}^{M_\theta/2}\left[I_{d,w}\left(\theta_l,\phi_k,t^*\right) + I_{c,w}\left(\theta_l,\phi_k,t^*\right)\right]\sin\theta_l\cos\theta_l\sin\Delta\theta_l\Delta\phi_k
\end{aligned}
\tag{2.23}
$$

where in Eq. (2.23), the first and the second terms represent emitted and reflected components of the boundary intensity, respectively. The reflected term is composed of the irradiation due to diffuse and collimated radiation.

In terms of non-dimensional time t^*, the RTE given in Eq. (2.6) is now written as

$$
\beta\frac{\partial I_d}{\partial t^*} + \frac{dI_d}{ds} + \beta I_d = S_t \tag{2.24}
$$

Using backward differencing scheme in time, Eq. (2.20) can be written as

$$
\beta\frac{I_d\left(t^*\right) - I_d\left(t^* - \Delta t^*\right)}{\Delta t^*} + \frac{dI_d\left(t^*\right)}{ds} + \beta I_d\left(t^*\right) = S_t\left(t^*\right) \tag{2.25}
$$

Equation (2.25) can be written in a simplified form as

$$
B\frac{dI_d\left(t^*\right)}{ds} + \beta I_d\left(t^*\right) = BS_t\left(t^*\right) + CI_d\left(t^* - \Delta t^*\right) \tag{2.26}
$$

where $B = \dfrac{\Delta t^*}{(1+\Delta t^*)}$ and $C = \dfrac{\beta}{1+\Delta t^*}$.

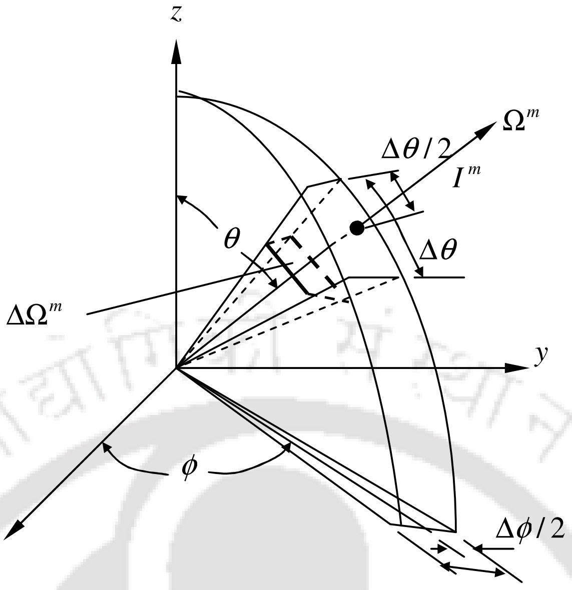

Figure 2.3: Intensity I^m in direction Ω^m in the center of the elemental sub-solid angle $\Delta\Omega^m$.

In the present work, we solve Eq. (2.26) using the FVM and the methodology to solve this equation is presented below. The discretization of the angular space according to the FVM is given by Fig. 2.3. Discretization of a 2D rectangular participating medium is given by Fig. 2.4

Writing Eq. (2.22) for a discrete direction Ω^m and integrating it over the elemental solid angle $\Delta\Omega^m$, we get

$$B\int_{\Delta\Omega^m}\frac{dI_d^m\left(t^*\right)}{ds}d\Omega+\int_{\Delta\Omega^m}\beta I_d^m\left(t^*\right)d\Omega=\int_{\Delta\Omega^m}\left[BS_t^m\left(t^*\right)+CI_d^m\left(t^*-\Delta t^*\right)\right]d\Omega \qquad (2.23)$$

In the Cartesian coordinate directions, Eq. (2.23) can be written as

$$B\left[\frac{\partial I_d^m\left(t^*\right)}{\partial x}D_x^m+\frac{\partial I_d^m\left(t^*\right)}{\partial y}D_y^m+\frac{\partial I_d^m\left(t^*\right)}{\partial z}D_z^m\right]+\beta I_d^m\left(t^*\right)$$
$$=\left[BS_t^m\left(t^*\right)+CI_d^m\left(t^*-\Delta t^*\right)\right]\Delta\Omega^m \qquad (2.24)$$

If $\hat{n}$ is the outward normal to a surface, then D^m is given by

$$D^m = \int_{\Delta\Omega^m} \left(\hat{n}\cdot\hat{s}^m\right) d\Omega \tag{2.25}$$

where $\hat{s}^m = \left(\sin\theta^m \cos\phi^m\right)\hat{i} + \left(\sin\theta^m \sin\phi^m\right)\hat{j} + \left(\cos\theta^m\right)\hat{k}$. When $\hat{n}$ is pointing towards one of the positive coordinate directions, D_x^m, D_y^m and D_z^m are given by

$$\begin{aligned} D_x^m &= \int_{\Delta\Omega^m} \sin\theta\cos\phi\, d\Omega = \int_{\phi^m-\frac{\Delta\phi^m}{2}}^{\phi^m+\frac{\Delta\phi^m}{2}} \int_{\theta^m-\frac{\Delta\theta^m}{2}}^{\theta^m+\frac{\Delta\theta^m}{2}} \cos\phi\sin^2\theta\, d\theta\, d\phi \\ &= \cos\phi^m \sin\left(\frac{\Delta\phi^m}{2}\right)\left[\Delta\theta^m - \cos 2\theta^m \sin\left(\Delta\theta^m\right)\right] \end{aligned} \tag{2.26a}$$

$$\begin{aligned} D_y^m &= \int_{\Delta\Omega^m} \sin\theta\sin\phi\, d\Omega = \int_{\phi^m-\frac{\Delta\phi^m}{2}}^{\phi^m+\frac{\Delta\phi^m}{2}} \int_{\theta^m-\frac{\Delta\theta^m}{2}}^{\theta^m+\frac{\Delta\theta^m}{2}} \sin\phi\sin^2\theta\, d\theta\, d\phi \\ &= \sin\phi^m \sin\left(\frac{\Delta\phi^m}{2}\right)\left[\Delta\theta^m - \cos 2\theta^m \sin\left(\Delta\theta^m\right)\right] \end{aligned} \tag{2.26b}$$

$$\begin{aligned} D_z^m &= \int_{\Delta\Omega^m} \cos\theta\, d\Omega = \int_{\phi^m-\frac{\Delta\phi^m}{2}}^{\phi^m+\frac{\Delta\phi^m}{2}} \int_{\theta^m-\frac{\Delta\theta^m}{2}}^{\theta^m+\frac{\Delta\theta^m}{2}} \cos\theta\sin\theta\, d\theta\, d\phi \\ &= \sin\theta^m \cos\theta^m \sin\left(\Delta\theta^m\right)\Delta\phi^m \end{aligned} \tag{2.26c}$$

For $\hat{n}$ pointing towards the negative coordinate directions, signs of D_x^m, D_y^m and D_z^m are opposite to those obtained from Eq. (2.26).In Eq. (2.24), $\Delta\Omega^m$ is given by

$$\Delta\Omega^m = \int_{\Delta\Omega^m} d\Omega = \int_{\phi^m-\frac{\Delta\phi^m}{2}}^{\phi^m+\frac{\Delta\phi^m}{2}} \int_{\theta^m-\frac{\Delta\theta^m}{2}}^{\theta^m+\frac{\Delta\theta^m}{2}} \sin\theta\, d\theta\, d\phi = 2\sin\theta^m \sin\left(\frac{\Delta\theta^m}{2}\right)\Delta\phi^m \tag{2.27}$$

Integrating Eq. (2.24) over the control volume and using the concept of the FVM for the computational fluid dynamics, we get

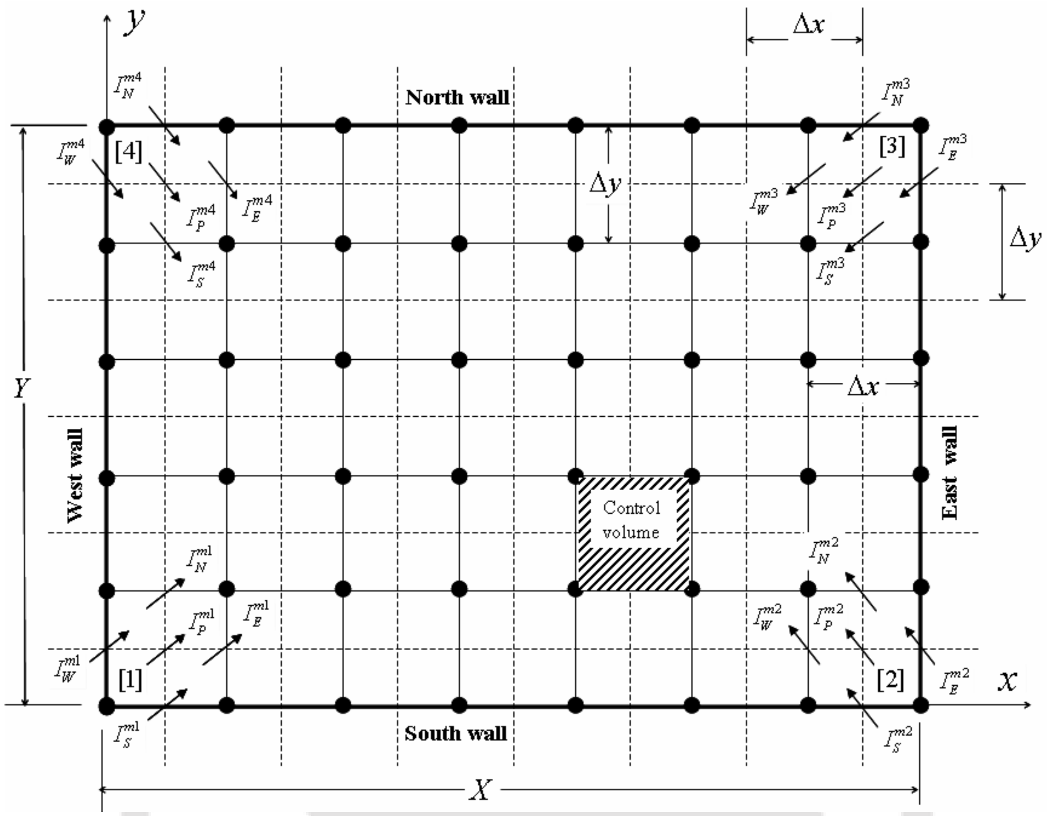

Figure 2.4: Discretisation and ray tracing procedure for of a 2D Rectangular participating medium.

$$\begin{aligned}\left[I_{d,E}^{m}\left(t^{*}\right)-I_{d,W}^{m}\left(t^{*}\right)\right]A_{EW}D_{x}^{m}+\left[I_{d,N}^{m}\left(t^{*}\right)-I_{d,S}^{m}\left(t^{*}\right)\right]A_{NS}D_{y}^{m}&\\ +\left[I_{d,F}^{m}\left(t^{*}\right)-I_{d,B}^{m}\left(t^{*}\right)\right]A_{FB}D_{z}^{m}&\\ =\left[-\frac{\beta V}{B}I_{d,P}^{m}\left(t^{*}\right)+VS_{t,P}^{m}+\frac{CV}{B}I_{d,P}^{m}\left(t^{*}-\Delta t^{*}\right)\right]\Delta\Omega^{m}&\end{aligned} \tag{2.28}$$

The general form of the cell-centre intensities $I_{d,P}^{m}\left(t^{*}\right)$ in terms of known cell-surface intensities can be written as

$$I_{d,P}^{m}(t^{*})=\frac{\left[\begin{aligned}\frac{\left|D_{x}^{m}\right|A_{x}}{\alpha_{x}}I_{d,x_{i}}^{m}(t^{*})+\frac{\left|D_{y}^{m}\right|A_{y}}{\alpha_{y}}I_{d,y_{i}}^{m}(t^{*})+\frac{\left|D_{z}^{m}\right|A_{z}}{\alpha_{z}}I_{d,z_{i}}^{m}(t^{*})\\ +\left(V\Delta\Omega^{m}\right)S_{t,P}^{m}(t^{*})+\left(\frac{CV\Delta\Omega^{m}}{B}\right)I_{d,P}^{m}(t^{*}-\Delta t^{*})\end{aligned}\right]}{\frac{\left|D_{x}^{m}\right|A_{x_{e}}}{\alpha_{x}}+\frac{\left|D_{y}^{m}\right|A_{y_{e}}}{\alpha_{y}}+\frac{\left|D_{z}^{m}\right|A_{z_{e}}}{\alpha_{z}}+\left(\frac{\beta V\Delta\Omega^{m}}{B}\right)} \tag{2.29}$$

In any discrete direction Ω^m, the cell-surface intensities are related to the cell-centre intensity $I_{d,P}^m$ as

$$I_{d,P}^m = \alpha_x I_{d,E}^m + (1-\alpha_x) I_{d,W}^m = \alpha_y I_{d,N}^m + (1-\alpha_y) I_{d,S}^m = \alpha_z I_{d,F}^m + (1-\alpha_z) I_{d,B}^m \qquad (2.30)$$

where α is the finite-difference weighting factor.

In Eq. (2.29), x_i, y_i and z_i suffixes over I_d^m are for the intensities entering the control volume through x-, y- and z-faces, respectively and A_x, A_y and A_z are given by

$$A_x = (1-\alpha_x) A_{x_e} + \alpha_x A_{x_i},\ A_y = (1-\alpha_y) A_{y_e} + \alpha_y A_{y_i},\ A_{FB} = (1-\alpha_z) A_{z_e} + \alpha_z A_{z_i} \qquad (2.31)$$

In Eq. (2.31) A with suffixes x_i, y_i and z_i represent control surface areas through which intensities enter the control volume while A with suffixes x_e, y_e and z_e represent control surface areas through which intensities leave the control volume.

Once the intensity distributions are calculated using Eqs. (2.29) and Eq. (2.30), from Eq. (2.22), heat flux at any point can be calculated. In transport of a short-pulse radiation through a participating medium, reflectance and transmittance are the two quantities whose temporal variations provide useful information about the medium. Reflectance is the thermal signal obtained from the boundary which is subjected to pulse radiation. Transmittance is the thermal signal received at the opposite boundary. Since radiation takes some final time to travel to the other boundary, unlike reflectance signal, it becomes available only after some finite time.

For the 3-D geometry shown in Fig. (2.1a), in non-dimensional form, at any time t^*, reflectance and transmittance signals are computed from

$$\text{Reflectance:} \qquad q_r^*\left(0,t^*\right) = \frac{q_d\left(x,y,0,t^*\right)}{q_{in}\left(x,y,0,t^*\right)} \qquad (2.32)$$

$$\text{Transmittance:} \qquad q_t^*\left(Z,t^*\right) = \frac{q_c\left(x,y,Z,t^*\right) + q_d\left(x,y,Z,t^*\right)}{q_{in}\left(x,y,0,t^*\right)} \qquad (2.33)$$

where in Eqs. (2.32) and (2.33), $q_{in}\left(0,t^*\right)$ is the flux input to the medium through the top boundary.

The brief solution methodology for a FVM solution for short-pulse laser transport through a participating medium is presented as a flowchart in Fig. 2.5.

2.3 Summary

The development of the FVM formulation of the transport of a single-short pulse laser through a 3-D cubical absorbing-emitting-scattering medium was presented in this chapter. FVM formulation pertaining to the transport of multiple pulses of step or Gaussian, collimated or diffuse pulses for 1-D and 2-D homogeneous and inhomogeneous participating medium and different spatial profiles will be presented in subsequent chapters. The next chapter deals with the transport of a step and Gaussian temporal 4-pulse radiation through a 1-D participating medium.

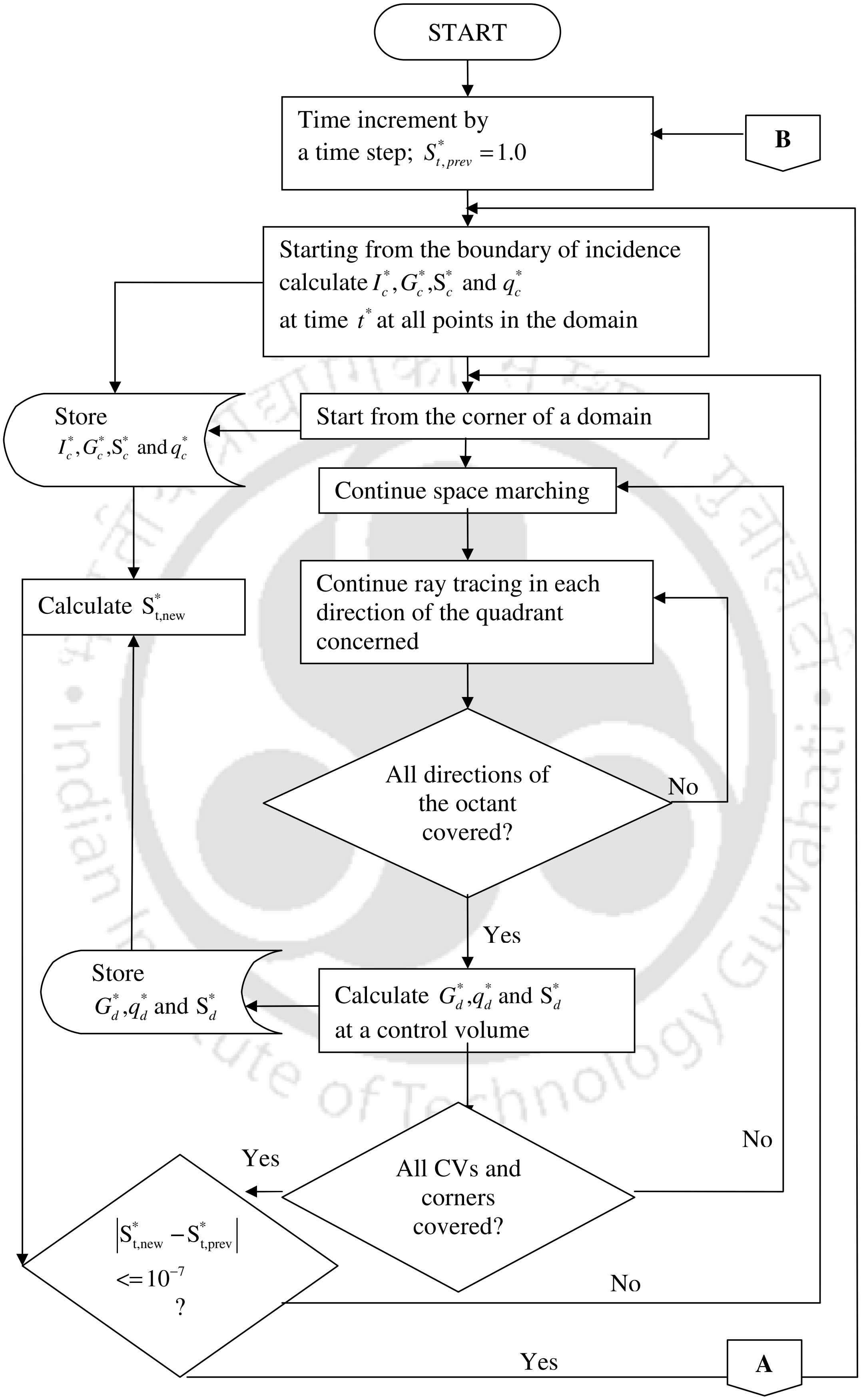

Figure 2.5: The FVM solution methodology presented as a flowchart

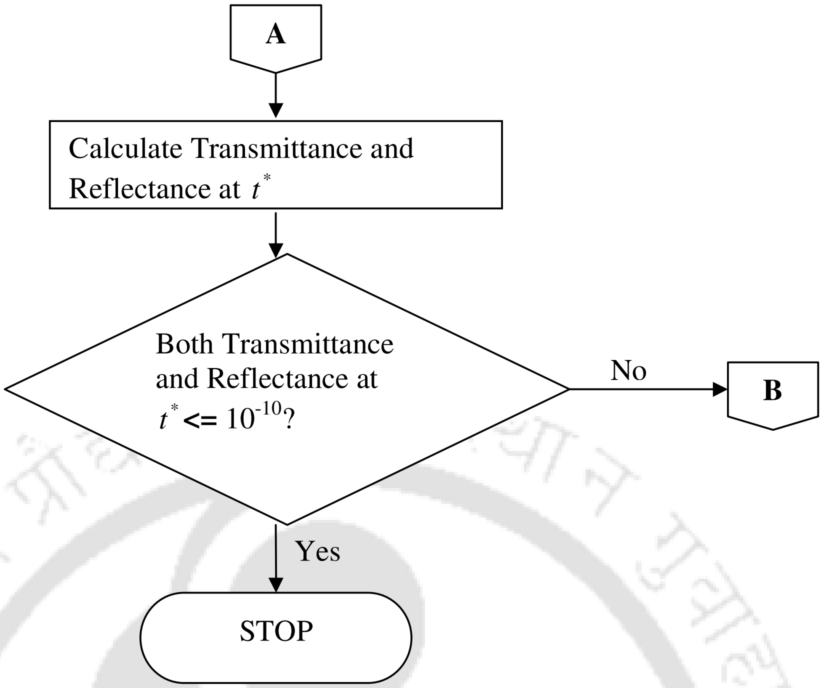

Figure 2.5(continued): The FVM solution methodology presented as a flowchart

CHAPTER 3

Transient Response of a 1-D Planar Participating Medium Subjected to a Train of Short-Pulse Radiation

---

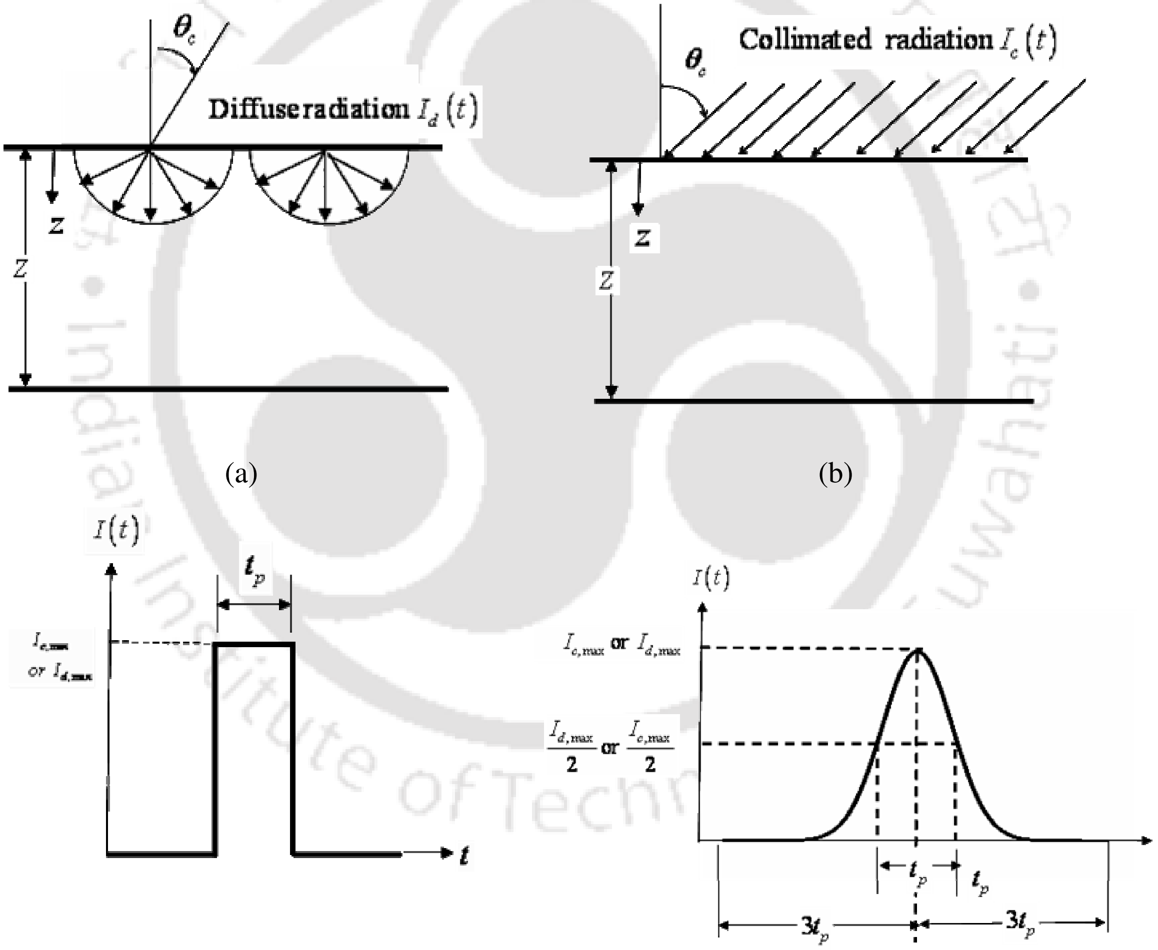

(a) (b)

(c) (d)

Figure: A planar medium with its north boundary subjected to a short-pulse (a) diffuse radiation and (b) collimated radiation; (c) step and (d) Gaussian temporal profiles of diffuse and collimated radiations incident on the north boundary.

3.1 Introduction

Owing to its wide range of applications, the problem of transport of pulse-radiation through 1-D participating media has been studied extensively in literature [11, 30-32, 36, 73, 79, 80, 84, 86, 91, 95-97, 101, 102, 104, 117]. The efficacy and suitability of some numerical methods to solve the TRTE have been studied in these works [30, 31, 73, 80, 91, 96, 104, 117]. Chai [80] has studied the effect of a collimated step pulse train on a 1-D planar medium. He limited his study to temporal variations of the incident radiation inside the medium. Transmittance and reflectance signals at the boundaries which are received by the detectors were not considered in his study. Further, his study was limited to a collimated step pulse and the effect of scattering albedo was not considered.

This chapter deals with the study of a train of diffuse as well as collimated pulses having a step or a Gaussian temporal variation. Formulation is given for a 1-D planar participating medium. Temporal transmittance and reflectance signals are studied for different number of pulses. Effects of the extinction coefficient and the scattering albedo are considered. For the four combinations of radiation (diffuse and collimated) and temporal variations (step and Gaussian), transmittance and reflectance signals are analyzed.

3.2 Problem

The north boundary of the absorbing, emitting and scattering 1-D planar medium as shown in Fig. 3.1a and 3.1b is subjected to either a diffuse (Fig. 3.1a) or a collimated (Fig. 3.1b) short-pulse radiation. Temporal variations of radiation can either be a step (Fig. 3.1c) or a Gaussian function (Fig. 3.1d). The boundary can be under the influence of either a single or a train of pulses.

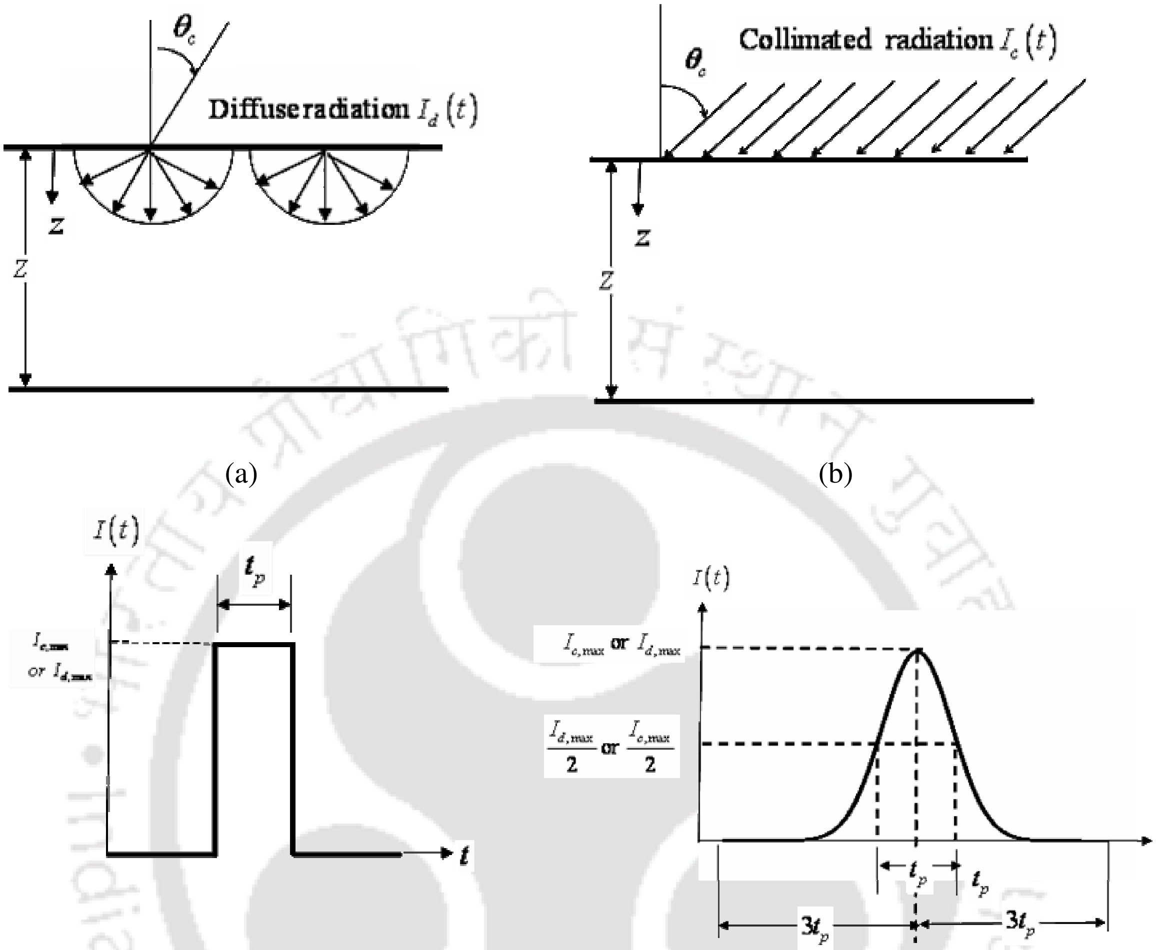

(a) (b)

(c) (d)

Figure 3.1: A planar medium with its north boundary subjected to a short-pulse (a) diffuse radiation and (b) collimated radiation; (c) step and (d) Gaussian temporal profiles of diffuse and collimated radiations incident on the north boundary.

3.3 Formulation

The pulse width t_p of the radiation is of the order of 10^{-9} s. The time interval between two consecutive pulses in the case of a pulse train is a multiple of t_p. To analyze the transmittance and the reflectance signals caused only by the short-pulse radiation, the homogeneous medium and its diffuse-gray boundaries are considered cold. The incident pulse travels with the speed of light $c\left(=3\times10^8\,\text{m/s}\right)$. In case of the step-pulse

(Fig. 3.1c), at any location in the medium, the part of the radiation source remains available only for the duration of the pulse-width t_p, whereas the Gaussian-pulse (Fig. 3.1d) remains available for the duration of $6t_p$. When the short-pulse radiation propagates through participating medium, the time-dependent diffuse radiation manifests and its life span in the medium is of the order of the pulse-width of the radiation source.

In the present case in which radiation transport is a time-dependent phenomenon, the radiative transfer equation (RTE) in any direction $\hat{s}$ is given by [1, 80, 103]

$$\left(\frac{1}{c}\right)\frac{\partial I}{\partial t}+\frac{\partial I}{\partial s}=-\beta I+\kappa_a I_b+\frac{\sigma_s}{4\pi}\int_{4\pi} I\, p\left(\Omega,\Omega'\right) d\Omega' \tag{3.1}$$

where s is the geometric distance in the direction $\hat{s}$, k_a is the absorption coefficient, β is the extinction coefficient, σ_s is the scattering coefficient and p is the scattering phase function.

Since in the present work, we are dealing with both diffuse as well as collimated radiation, in the following pages we provide a general formulation for the latter case. The changes in the formulation for the diffuse radiation will be highlighted wherever its need is felt.

When the collimated radiation encounters the medium and passes through it, its decay gives rise to the diffuse radiation. Thus within the medium, the intensity I is composed of two components, *viz.*, the collimated intensity I_c and the diffuse intensity I_d.

$$I = I_c + I_d \tag{3.2}$$

The variation of the collimated intensity I_c within the medium is given by

$$\left(\frac{1}{c}\right)\frac{\partial I_c}{\partial t}+\frac{\partial I_c}{\partial s}=-\beta I_c \tag{3.3}$$

Substituting Eq. (3.2) in Eq. (3.1), we get

$$\left(\frac{1}{c}\right)\frac{\partial I_c}{\partial t}+\frac{\partial I_c}{\partial s}+\left(\frac{1}{c}\right)\frac{\partial I_d}{\partial t}+\frac{\partial I_d}{\partial s} = -\beta I_c - \beta I_d + \kappa_a I_b + \frac{\sigma_s}{4\pi}\int_{4\pi} I_d \, p(\Omega,\Omega')\, d\Omega' + \frac{\sigma_s}{4\pi}\int_{4\pi} I_c \, p(\Omega,\Omega')\, d\Omega' \qquad (3.4)$$

From Eqs. (3.3) and (3.4), we get

$$\left(\frac{1}{c}\right)\frac{\partial I_d}{\partial t}+\frac{\partial I_d}{\partial s} = -\beta I_d + S_c + S_d = -\beta I_d + S_t \qquad (3.5)$$

where S_c and S_d are the source terms resulting from the collimated and the diffuse components of radiation, respectively. In Eq. (3.5), $S_t = S_c + S_d$ is the total source term. The source term S_c resulting from the collimated radiation I_c is given by

$$S_c(t) = \frac{\sigma_s}{4\pi}\int_{\Omega'=0}^{4\pi} I_c(\Omega,t)\, p(\Omega,\Omega')\, d\Omega' \qquad (3.6)$$

For a linear anisotropic phase function $p(\Omega,\Omega') = 1 + a\cos\theta\cos\theta'$, the source term S_c in terms of the incident radiation G_c and heat flux q_c is written as

$$S_c(t) = \frac{\sigma_s}{4\pi}\left[G_c(t) + a\cos\theta\, q_c(t)\right] \qquad (3.7)$$

Since the collimated intensity $I_c(\theta,t)$ for a step (Fig. 3.1c) and a Gaussian (Fig. 3.1d) pulse are defined by Eqs. (3.9) and (3.10), respectively, G_c and q_c in Eq. (3.7) are given by

$$G_c(t) = I_c(\theta,t) \qquad (3.8a)$$

$$q_c(t) = I_c(\theta,t)\cos\theta \qquad (3.8b)$$

$$I_c(\theta,t) = I_{c,\max}(\theta,t)\exp(-\beta s_c) \times \begin{bmatrix} H\{\beta(ct-s_c)\} \\ -H\{\beta(ct-s_c) - \beta c t_p - \beta(N-1)cT_p\} \end{bmatrix} \times \delta(\theta-\theta_c) \qquad (3.9)$$

$$I_c(\theta,t) = I_{c,\max}(\theta,t)\exp(-\beta s_c) \times \exp\left[-4\left(\frac{t - \frac{s_c}{c} - t_c - (N-1)T_p}{t_p}\right)^2 \ln 2\right] \times \delta(\theta-\theta_c), \quad 0 < t < 2t_c \qquad (3.10)$$

where in Eqs. (3.9) and (3.10), $I_{c,\max}$ is the collimated intensity at the north boundary, $s_c = z/\cos\theta_c$ is the geometric distance in the direction θ_c of the collimated radiation, δ is the Dirac-delta function and H is the Heaviside function defined as

$$H(y) = \begin{cases} 1, & y > 0 \\ 0, & y < 0 \end{cases} \tag{3.11}$$

In Eqs. (3.9) and (3.10), the Dirac-delta function δ takes care of existence of collimated radiation in θ_c direction while the Heaviside function H guarantees that the short-pulse radiation is available at any location in the medium only for the time duration t_p for a step-function. Since the Gaussian-pulse is a continuous one, it is always available for the time span of $0 \le t \le 6t_p$ and the cut-off period $t_c = 3t_p$

In case of a diffuse radiation (Fig. 3.1a), whose temporal variations could either be a step (Fig. 3.1c) or a Gaussian function (Fig. 3.1d), the diffuse intensity at the boundary is given by

$$I_d(\theta,t) = I_{d,\max}(\theta,t) \times \left[H(\beta c t) - H\left(\beta c t - \beta c t_p - \beta c (N-1) T_p\right) \right] \tag{3.12}$$

$$I_d(\theta,t) = I_{d,\max}(\theta,t) \times \exp\left[-4 \left(\frac{t - t_c - (N-1)T_p}{t_p} \right)^2 \ln 2 \right], \quad 0 < t < 2t_c \tag{3.13}$$

It is to be noted that Eqs. (3.9) and (3.10) are valid for all locations $0.0 \le z \le Z$ whereas Eq. (3.12) and (3.13) are applicable to the boundary of incidence, in the present case $z = 0.0$, the north boundary. Equations governing the variation of the diffuse intensity $I_d(\theta,t)$ are given afterwards.

If $t^* = \beta c t$, $t_p^* = \beta c t_p$ and $t_c^* = \beta c t_c$ are the dimensionless times, Eqs. (3.9) - (3.13) can be written as

$$I_c(\theta,t^*) = I_{c,\max}(\theta,t^*) \exp(-\beta s_c) \times \begin{bmatrix} H\left(t^* - \beta s_c\right) \\ -H\left(t^* - \beta s_c - t_p^* - (N-1)T_p^*\right) \end{bmatrix} \times \delta(\theta - \theta_c) \tag{3.14}$$

$$I_c\left(\theta,t^*\right)=I_{c,\max}\left(\theta,t^*\right)\exp\left(-\beta s_c\right)\times\exp\left[-4\left(\frac{t^*-\beta s_c-t_c^*-(N-1)T_p^*}{t_p^*}\right)^2\ln 2\right]$$
$$\times\delta\left(\theta-\theta_c\right),\quad 0<t^*<2t_c^* \tag{3.15}$$

$$I_d\left(\theta,t^*\right)=I_{d,\max}\left(\theta,t^*\right)\times\left[H\left(t^*\right)-H\left(t^*-t_p^*-(N-1)T_p^*\right)\right] \tag{3.16}$$

$$I_d\left(\theta,t^*\right)=I_{d,\max}\left(\theta,t^*\right)\times\exp\left[-4\left(\frac{t^*-t_c^*-(N-1)T_p^*}{t_p^*}\right)^2\ln 2\right],\quad 0<t^*<2t_c^* \tag{3.17}$$

In Eq. (5), for linear anisotropic phase function $p(\Omega,\Omega')=1+a\cos\theta\cos\theta'$, the source term S_d in terms of incident radiation G_d and heat flux q_d resulting from the diffuse radiation I_d is given by

$$S_d\left(t^*\right)=\kappa_a I_b\left(t^*\right)+\frac{\sigma_s}{4\pi}\left[G_d\left(t^*\right)+a\cos\theta\, q_d\left(t^*\right)\right] \tag{3.18}$$

In case of a planar medium in which radiation is azimuthally symmetric, G_d and q_d are given by and numerically computed from [103]

$$\begin{aligned} G_d\left(t^*\right) &= 2\pi\int_{\theta=0}^{\pi} I_d(\theta,t^*)\sin\theta\, d\theta \\ &\approx 4\pi\sum_{k=1}^{M_\theta} I_d(\theta_k,t^*)\sin\theta_k\ \sin\left(\frac{\Delta\theta_k}{2}\right) \end{aligned} \tag{3.19}$$

$$\begin{aligned} q_d\left(t^*\right) &= 2\pi\int_{\theta=0}^{\pi} I_d(\theta,t^*)\cos\theta\sin\theta\, d\theta \\ &\approx 2\pi\sum_{k=1}^{M_\theta} I_d(\theta_k,t^*)\sin\theta_k\ \cos\theta_k\sin\Delta\theta_k \end{aligned} \tag{3.20}$$

where M_θ is the number of discrete points considered over the complete span of the polar angle θ $\left(0\le\theta\le\pi\right)$.

For a boundary having temperature T_w and emissivity ε_w, the boundary intensity $I_d\left(r_w,t^*\right)$ is given by and computed from

$$I_d\left(r_w,t^*\right)\approx\frac{\varepsilon_w\sigma T_w^4}{\pi}+\left(\frac{1-\varepsilon_w}{\pi}\right)2\pi\sum_{k=1}^{M_\theta/2}\left[I_{d,w}\left(\theta_k,t^*\right)+I_{c,w}\left(\theta_k,t^*\right)\right]\sin\theta_k\cos\theta_k\sin\Delta\theta_k \tag{3.21}$$

where in Eq. (3.21), the first and the second terms represent emitted and reflected components of the boundary intensity, respectively.

It is to be noted that if the boundary is subjected to only the diffuse radiation, in Eq. (3.21) $I_{c,w} = 0.0$.

In terms of non-dimensional time t^*, the RTE given in Eq. (3.5) is now written as

$$\beta\frac{\partial I_d}{\partial t^*} + \frac{\partial I_d}{\partial s} + \beta I_d = S_t \tag{3.22}$$

Using backward differencing scheme in time, Eq. (22) becomes

$$\beta\frac{I_d\left(t^*\right) - I_d\left(t^* - \Delta t^*\right)}{\Delta t^*} + \frac{\partial I_d\left(t^*\right)}{\partial s} + \beta I_d\left(t^*\right) = S_t\left(t^*\right) \tag{3.23}$$

Equation (23) can be written in simplified form as

$$B\frac{\partial I_d\left(t^*\right)}{\partial s} + \beta I_d\left(t^*\right) = BS_t\left(t^*\right) + CI_d\left(t^* - \Delta t^*\right) \tag{3.24}$$

where $B = \dfrac{\Delta t^*}{(1+\Delta t^*)}$ and $C = \dfrac{\beta}{1+\Delta t^*}$.

With expressions for the source terms, incident radiation and heat flux given above, Eq. (3.24) is the resulting radiative transfer equation to be used in the present analysis. Below we briefly present formulation and methodology to solve Eq. (3.24) using the FVM. Details of the FVM formulation for the steady-state radiative transfer in general can be found in Mishra and Roy [103] and for the transient radiation study, the same can be found in Mishra et al. [97].

Writing Eq. (3.24) for a discrete direction Ω^m and integrating it over the elemental solid angle $\Delta\Omega^m$, we get

$$B\int_{\Delta\Omega^m}\frac{\partial I_d^m\left(t^*\right)}{\partial s}d\Omega + \int_{\Delta\Omega^m}\beta I_d^m\left(t^*\right)d\Omega = \int_{\Delta\Omega^m}\left[BS_t^m\left(t^*\right) + CI_d^m\left(t^* - \Delta t^*\right)\right]d\Omega \tag{3.25}$$

In case of a 1-D planar medium, Eq. (3.25) can be written as

$$B\frac{\partial I_d^m\left(t^*\right)}{\partial z}D_z^m+\beta I_d^m\left(t^*\right)=\left[BS_t^m\left(t^*\right)+CI_d^m\left(t^*-\Delta t^*\right)\right]\Delta\Omega^m \tag{3.26}$$

where D_z^m and $\Delta\Omega^m$ are given by

$$D_z^m=\left|\int_{\Delta\Omega^m}\cos\theta d\Omega\right|=\left|2\pi\sin\theta^m\cos\theta^m\sin\left(\Delta\theta^m\right)\right| \tag{3.27}$$

$$\Delta\Omega^m=\int_{\Delta\Omega^m}d\Omega=4\pi\sin\theta^m\sin\left(\frac{\Delta\theta^m}{2}\right) \tag{3.28}$$

Integrating Eq. (3.26) over the 1-D control volume $\left(dV=1\times1\times dz\right)$ we get

$$\left[I_{d,N}^m\left(t^*\right)-I_{d,S}^m\left(t^*\right)\right]D_z^m=\left[-\frac{\beta}{B}I_{d,P}^m\left(t^*\right)+S_{t,P}^m+\frac{C}{B}I_{d,P}^m\left(t^*-\Delta t^*\right)\right]dz\Delta\Omega^m \tag{3.29}$$

where $I_{d,N}^m$ and $I_{d,S}^m$ are north and south control surface average intensities, respectively and $I_{d,P}^m$ and $S_{t,P}^m$ are the intensities and source terms at the cell centre P, respectively. In any discrete direction Ω^m, the cell-surface intensities are related to the cell-centre intensity $I_{d,P}^m$ as

$$I_{d,P}^m=\frac{I_{d,N}^m+I_{d,S}^m}{2} \tag{3.30}$$

From Eq. (3.29) and (3.30), while marching from the north boundary for which $\theta<\frac{\pi}{2}$, we get

$$I_{d,P}^m=\frac{\left[2D_z^mI_{d,N}^m\left(t^*\right)+S_{t,P}^m\left(t^*\right)dz\Delta\Omega^m+\left(\frac{C}{B}dz\Delta\Omega^mI_{d,P}^m\left(t^*-\Delta t^*\right)\right)\right]}{2D_z^m+\left(\frac{\beta}{B}dz\Delta\Omega^m\right)} \tag{3.31a}$$

and while marching from the south boundary for which $\theta>\frac{\pi}{2}$, we get

$$I_{d,P}^{m} = \frac{\left[2D_z^m I_{d,S}^m\left(t^*\right) + S_{t,P}^m\left(t^*\right) dz\Delta\Omega^m + \left(\frac{C}{B} dz\Delta\Omega^m I_{d,P}^m\left(t^* - \Delta t^*\right) \right) \right]}{2D_z^m + \left(\frac{\beta}{B} dz\Delta\Omega^m \right)} \tag{3.31b}$$

3.4 Solution Procedure

The planar participating medium is discretized into a number of control volumes and the angular space, the polar angle θ is divided equally into a finite number of directions M_θ (Eqs. (3.19) and (3.20)). Calculation starts with a guess value of the source term $S_{t,P}^m$ and the volume average diffuse intensity $I_{d,P}^m\left(t^* - \Delta t^*\right)$ required for Eq. (3.31). For all the discrete directions for which $\theta < \frac{\pi}{2}$, marching starts from the north boundary and $I_{d,P}^m\left(t^*\right)$ is calculated from Eq. (3.31a). The marching is done from the south boundary for all the directions for which $\frac{\pi}{2} < \theta < \pi$ and $I_{d,P}^m\left(t^*\right)$ is calculated from Eq. (3.31b). For the control volume whose one boundary is the boundary of the medium, the boundary intensities required in Eq. (3.31) are calculated from Eq. (3.21). With $I_{d,P}^m\left(t^*\right)$ calculated, the unknown cell-surface intensities in the same direction are calculated from Eq. (3.30). For the next control volume, the calculated cell-surface intensity serves as the known intensity in Eq. (3.31). The source term $S_{t,P}^m = S_{c,P}^m + S_{d,P}^m$ is calculated from Eqs. (3.7) and (3.18). Collimated incident radiation G_c and heat flux q_c for $S_{c,P}^m$ are computed from Eqs. (3.8a) and (3.8b), respectively and for the diffuse component $S_{d,P}^m$, G_d and q_d are computed from Eqs. (3.19) and (3.20), respectively. All directions at a particular point are covered when marching is completed from both the boundaries. Before marching for the next time level, the maximum change in the source term $S_{t,P}^m$ of a given control volume between the consecutive iteration levels are noted. Iteration is terminated when $\left| S_{t,\text{old},P}^m - S_{t,\text{new},P}^m \right| \le 1.0 \times 10^{-7}$. For any time t^*, reflectance and transmittance signals are computed from

Reflectance: $$q_r^*\left(0,t^*\right)=\frac{q_d\left(0,t^*\right)}{q_{in}\left(0,t^*\right)} \tag{3.32}$$

Transmittance: $$q_t^*\left(Z,t^*\right)=\frac{q_c\left(Z,t^*\right)+q_d\left(Z,t^*\right)}{q_{in}\left(0,t^*\right)} \tag{3.33}$$

where in Eqs. (3.32) and (3.33), $q_{in}\left(0,t^*\right)$ is the flux input to the medium through the north boundary. It should be noted that in Eqs. (3.32) and (3.33), reflectance $q_r^*\left(0,t^*\right)$ and transmittance are the fluxes at the north and the south boundaries, respectively because of the contributions only from the medium.

3.5 Results and Discussions

In the following pages, we consider the north boundary subjected to a single or a train of 2-4 diffuse and/or collimated pulses and analyze the time-dependent reflectance and transmittance signals that are basically the net heat fluxes on the north and the south boundaries, respectively. Temporal variations of these pulses could either be a step or a Gaussian function.

To validate the results, first we compare our results for a single pulse with those available in the literature. Next we present and analyze results for a train of pulses. This analysis is done for the range of values of the extinction coefficient β and two values of the scattering albedo ω. For grid independent results, 500 equal size control volumes were used and a maximum of 40 equally spaced directions in the polar space $\left(0\le\theta\le\pi\right)$ were found enough for the ray-independent solutions. 1000 divisions of the total time t^* domain were found sufficient for marching in the time dimension.

The code was written in Turbo C++. To study the computational time, the CPU times were recorded for all the combinations. The code was executed on a Xeon 300 dual

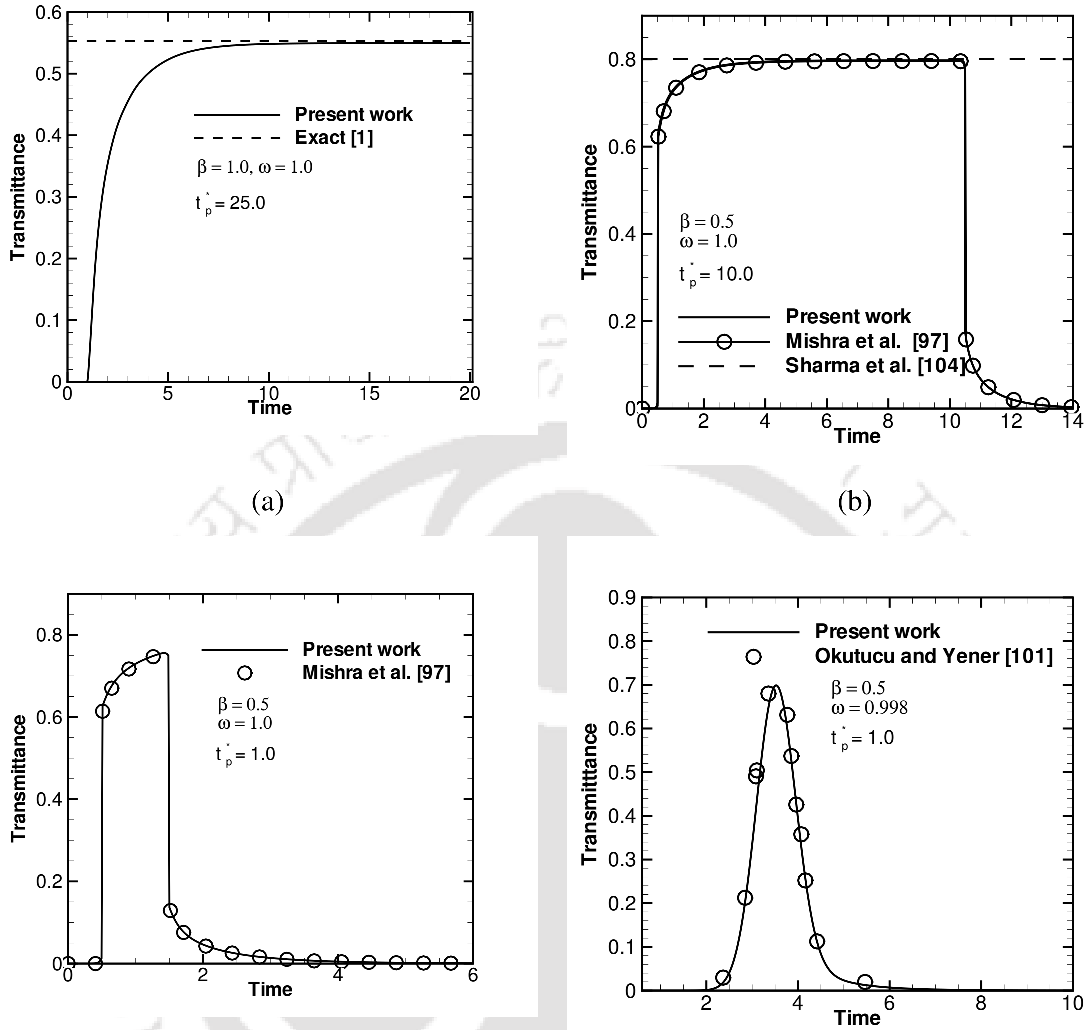

(a) (b)

(c) (d)

Figure 3.2: Comparison of results with literature[1,97,101,104]

processor 800 MHz computer. The CPU times for optically thin $(\beta = 1.0)$ to thick $(\beta = 5.0)$ cases ranged from 36 seconds to 200 seconds, respectively.

3.5.1 Validation of results for a single pulse

In this case, the north boundary of the planar medium is subjected to a single diffuse or a collimated pulse. Temporal variations of the pulse could either be a step or a

Gaussian function. In Figs. 3.2a-d, for extinction coefficient $\beta = 0.5$ with scattering albedo $\omega = 1.0$ $(\omega = 0.998)$ in Fig. 3.2d, transmittance $q_t^*(Z,t^*)$ results of the present work for a single-step diffuse, a single-step collimated and a single Gaussian pulses are compared with those from the literature [1, 97, 101, 104]. Whether radiation is diffuse or collimated, with a large step pulse, transient results approach steady state. Figs. 3.2a and 3.2b shows this for transmittance $q_t^*(Z,t^*)$ results for a large pulse width $t_p^* = 25.0$ for a single-step diffuse and $t_p^* = 10.0$ for single-step collimated pulses, respectively. Results have been compared with those from the literature [1, 101]. Since with a Gaussian pulse, energy input to the medium is always changing, steady-state condition can never be approached for any value of the pulse-width t_p^*. For a single-step collimated and a single-Gaussian collimated pulses with $t_p^* = 1.0$, Figs. 3.2c and 3.2d provide comparison of our results with those from the literature [97] and [104], respectively. Results are in good agreement.

3.5.2 Results with a train of pulses

In the following pages, transmittance $q_t^*(Z,t^*)$ and reflectance $q_r^*(0,t^*)$ results with a train of pulses are provided for different values of the extinction coefficient β and the scattering albedo ω. In Figs. 3.3-3.10, these results are presented for pulse width $t_p^* = 1.0$ and while dealing with collimated irradiation, its direction of incidence on the north boundary is considered to be normal, $\theta_c = 0.0$. In all the cases, the homogeneous medium is considered absorbing and isotropically scattering, and the diffuse-gray boundaries are black and cold. In the present work, transmittance and reflectance results have been provided for a medium whose physical depth $Z = 1$ m. However, it should be noted that the results presented are valid equally for any physical depth as long as for a given value the optical depth $\tau_Z = \beta Z$, the product of β and Z remains the same. For an example, results will be the same for $Z = 1.0$ m and $\beta = 1.0$ and $Z = 1/10$ m and $\beta = 10.0$ or any other combination of β and Z.

In all the cases of train of pulses considered in the present work, the pulses repeat after $t_p^* = 1.0$ and the north boundary is subjected to a maximum of four pulses. While considering the effect of the extinction coefficient β, (Fig. 3.3-3.6), scattering albedo $\omega = 1.0$ and when considering the effect of the scattering albedo ω (Figs. 3.7-3.10) the extinction coefficient $\beta = 1.0$.

3.5.2.1 Effect of the extinction coefficient β

(a) Diffuse step pulse train: The north boundary of the planar medium is subjected to diffuse radiation (Fig. 3.1a) whose temporal variation is a step function (Fig. 3.1c).

Figures 3.3a-f show the effect of the extinction coefficient β for $N-$pulses on transmittance $q_t^*\left(Z,t^*\right)$ and reflectance $q_r^*\left(0,t^*\right)$ signals, where $N = 1-4$. In these figures, results have been presented for extinction coefficient β =1.0, 2.0 and 5.0. It is observed from the figure that for a single pulse $(N = 1)$, the magnitude of the transmittance $q_t^*\left(Z,t^*\right)$ signal decreases with increase in β. An opposite trend is observed for the reflectance $q_r^*\left(0,t^*\right)$ signal. Both the signals last longer for a higher value of β.

It is observed from Figs. 3.3a-d that when the medium is less participating ($\beta = 1.0$ and 2.0), with boundary subjected to N pulses, the $(N-1)$ maxima of the transmittance $q_t^*\left(Z,t^*\right)$ and reflectance $q_r^*\left(0,t^*\right)$ signals occur almost at the same time as that of the $(N-1)$ pulses. The same is the case with the minima. However, when the medium is highly participating $(\beta = 5.0)$, for any number of pulses, only one maximum is present for the transmittance $q_t^*\left(Z,t^*\right)$ signals and the maximum of any pulse train is shifted slightly in time (Fig. 3.3e). Observation of Figs. 3.3a, 3.3c and 3.3e show that for $N \geq 2$, the difference in consecutive maximum and minimum decreases with increase in β.

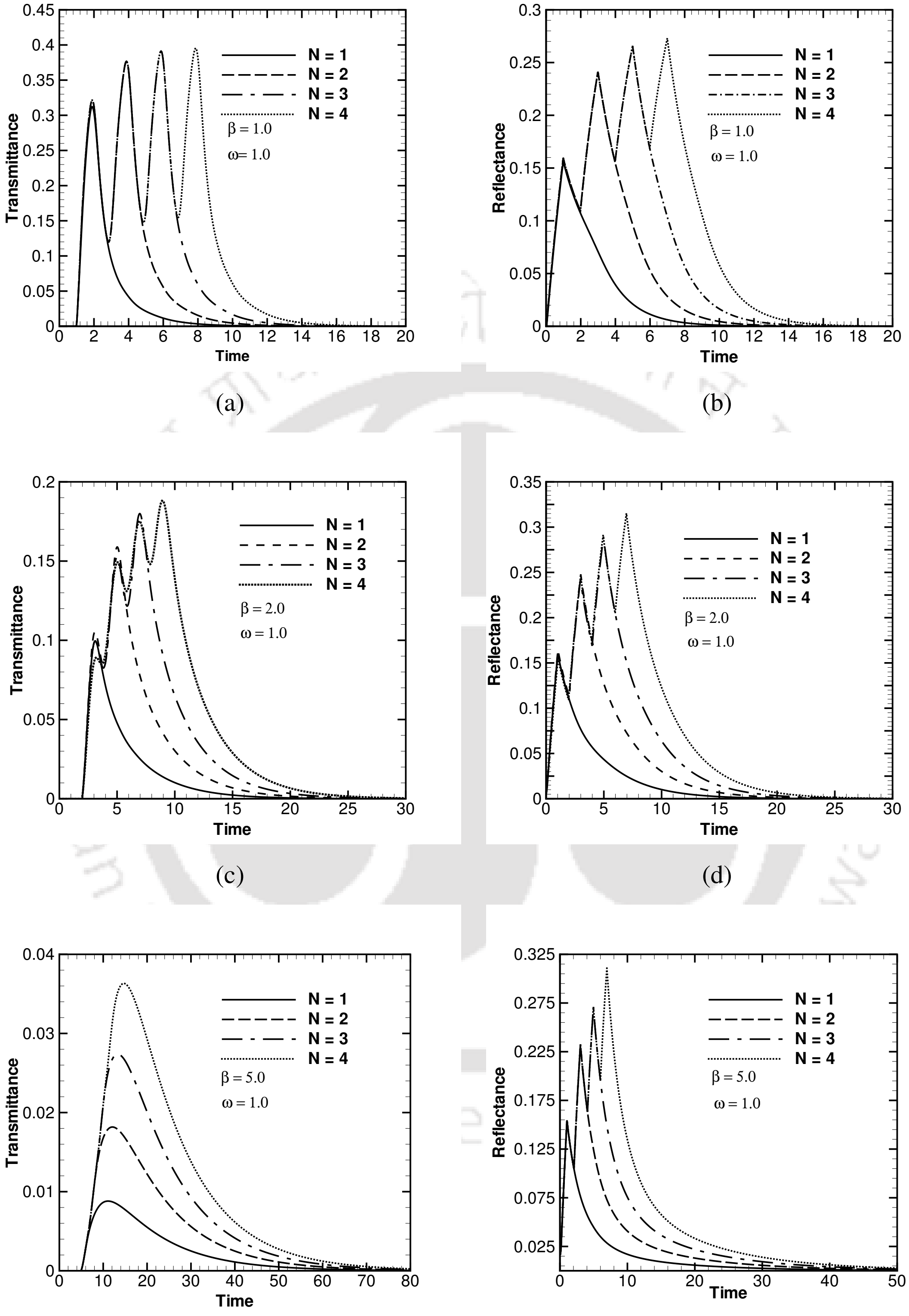

(a) (b)

(c) (d)

(e) (f)

Figure 3.3: Comparison of temporal variations of transmittance and reflectance signals for different values of the extinction coefficient β ; Radiation source: Diffuse step pulses.

For $\beta = 5.0$, difference is not noticeable. In case of reflectance signals, maxima are always distinct.

A higher value of β signifies medium to be radiatively more participating and thus less amount of radiation reaches the bottom boundary, and consequently the magnitude of the transmittance $q_t^*\left(Z, t^*\right)$ signal decreases with increase in β. With increase in β, radiation stays for a longer duration in the medium and when the next pulse comes, radiation owing to previous pulses still remain present and this causes existence of multiple maxima and minima of transmittance $q_t^*\left(Z, t^*\right)$ and reflectance $q_r^*\left(0, t^*\right)$ signals for $N \geq 2$.

(b) Diffuse Gaussian pulse train: The north boundary of the planar medium is subjected to diffuse radiation (Fig. 3.1a) whose temporal variation is a Gaussian function (Fig. 3.1d).

With $N = 1 - 4$, Figs. 3.4a-f show the effect of the extinction coefficient β =1.0, 2.0 and 5.0 on transmittance $q_t^*\left(Z, t^*\right)$ and reflectance $q_r^*\left(0, t^*\right)$ signals. It is observed that like the results of the diffuse step pulses, magnitudes of transmittance $q_t^*\left(Z, t^*\right)$ signals decrease with increase in β. Further because each pulse of the multiple Gaussian pulses remains available for time duration which is six times more than the step pulse, maxima are more widely spread over time. Further, like diffuse step pulses (Fig. 3.3e), for the same reason, for a higher value of the extinction coefficient $(\beta = 5.0)$, multiple maxima and minima are not observed.

In the case of Gaussian pulses, time span of a given pulse is six times more than that of the step pulse (Figs. 3.1c and 3.1d) and input too is very gradual. Thus, unlike step pulses (Figs. 3.3b, d, f), reflectance signals appear after some time (Figs. 3.4b, d, f). Distinct maxima and minima are observed. Because of more energy input to the medium and its existence for a longer duration at the boundary, transmittance

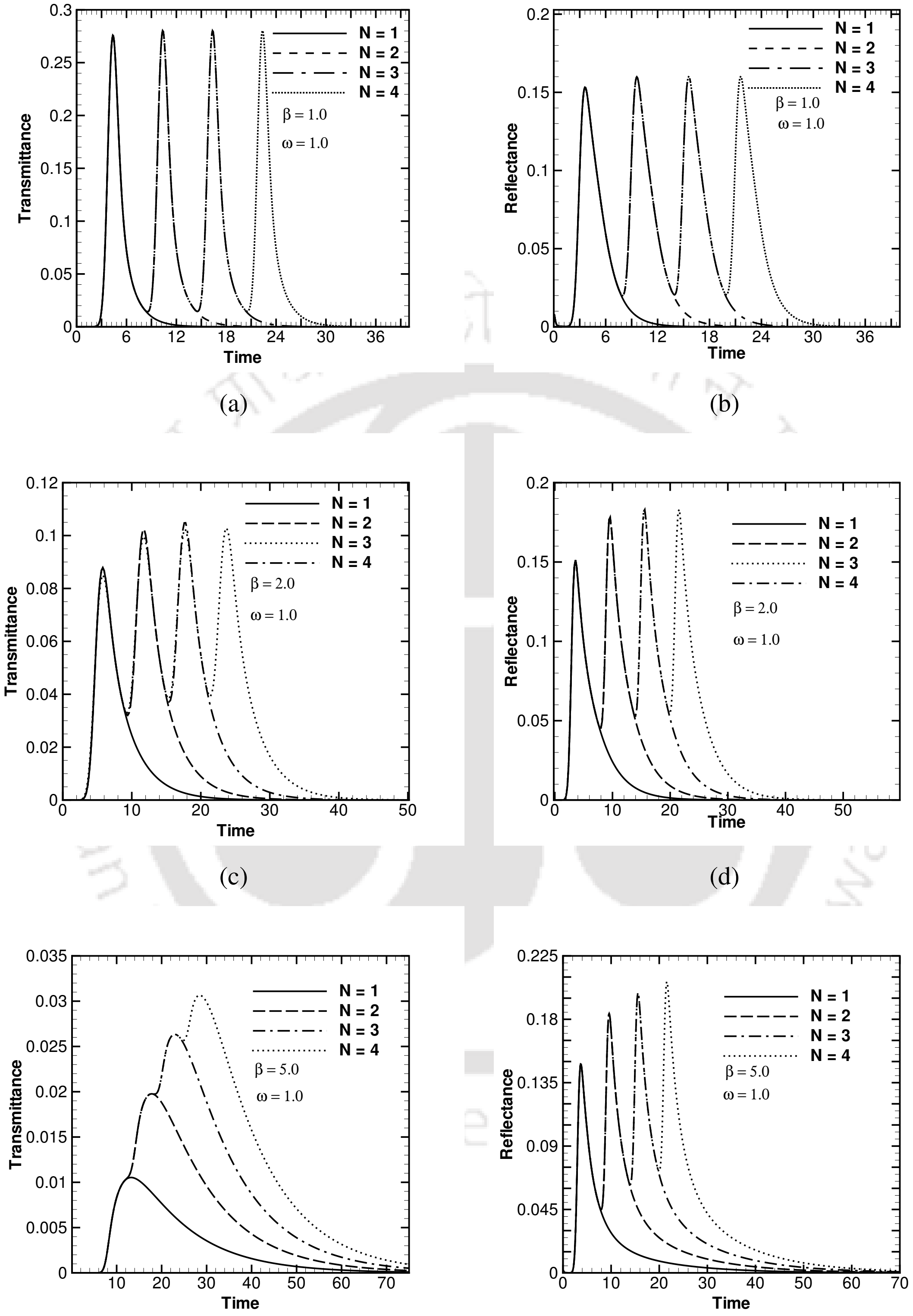

(a) (b)

(c) (d)

(e) (f)

Figure 3.4: Comparison of temporal variations of transmittance and reflectance signals for different values of the extinction coefficient β; Radiation source: Diffuse Gaussian pulses.

$q_t^*\left(Z,t^*\right)$ and reflectance $q_r^*\left(0,t^*\right)$ signals in case of Gaussian pulses last longer (Figs. 3.4a-f) than that of step pulses (Fig. 3.3a-f).

(c) Collimated step pulse train: The north boundary of the planar medium is subjected to collimated radiation (Fig. 1b) whose temporal variation is a step function (Fig. 3.1c). Angle of incidence θ_c of the collimated radiation is zero. For β =1.0, 2.0 and 5.0, Figs. 3.5a-f show the transmittance $q_t^*\left(Z,t^*\right)$ and reflectance $q_r^*\left(0,t^*\right)$ signals for $N=1-4$ pulses Like the previous two cases, it is observed that the magnitudes of transmittance $q_t^*\left(Z,t^*\right)$ signals decrease and that of the reflectance $q_r^*\left(0,t^*\right)$ signals increases with increase in β.Distinct maxima and minima are observed with transmittance $q_t^*\left(Z,t^*\right)$ signals for lower values of β. However, for $\beta=5.0$ (Fig. 3.5e), unlike diffuse step pulse trains (Fig. 3.3e), for $N\le 3$, two distinct maximum and one minimum are observed. With increase in N, it is observed that the magnitude of the first maximum decreases and that of the second maximum increases. For $N=4$, the first maximum and minimum disappear like all values of N in case of diffuse step pulses (Fig. 3.3e).

In case of a pulse train consisting of N pulses, radiation reaches the south boundary at time $t^*=\beta ct+NT_p^*$, where T_p^* is the time period. With a single collimated pulse, magnitudes of collimated and diffuse components are comparable, and thus for all values of β, distinct maximum in the transmittance $q_t^*\left(Z,t^*\right)$ signals is observed. The difference in magnitudes of single pulse and multi-pulse in Fig.3.3c is due to a relaxed source term for convergence. In the case of a slightly more attenuating medium, $\beta=2.0$, it can be observed from Fig 3.5c that transmittance signal for a single-pulse has a different trend compared with the cases of multiple pulses. The pulse width being unity, and the time of travel of the signal and the optical thickness being the same, the collimated component reinforces the transmittance considerably higher in the case of a single-pulse when compared with the multiple-pulses. When the number of pulses increase, in case of a higher value of β (Fig. 3.5e), because of the arrival of

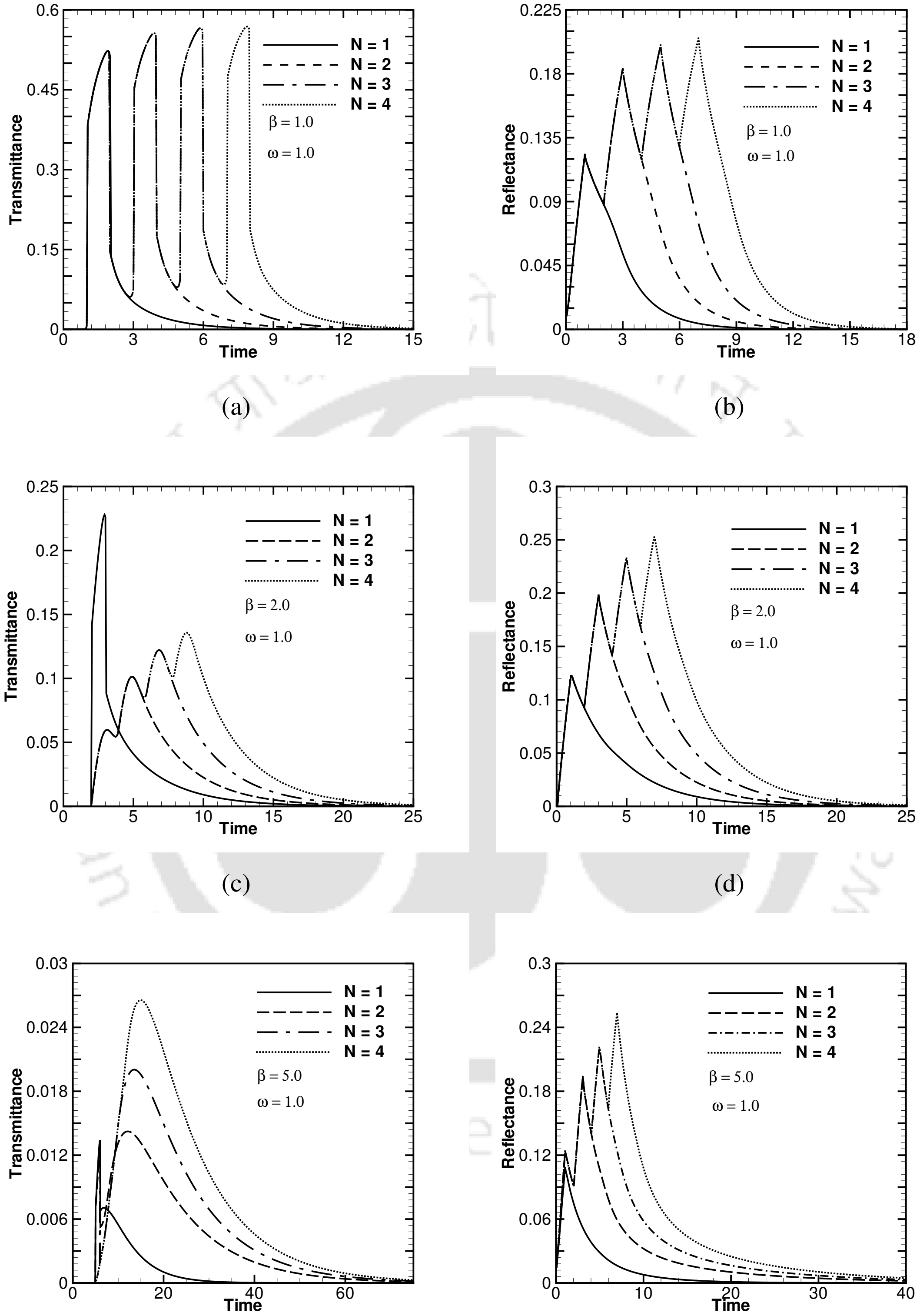

(a) (b)

(c) (d)

(e) (f)

Figure 3.5: Comparison of temporal variations of transmittance and reflectance signals for different values of the extinction coefficient β; Radiation source: Collimated step pulses.

the successive pulses, the overall contribution of the collimated component decaying exponentially is dominated more by the diffuse component. Thus many maxima that are observed for lower values of β disappear at higher values of β. Radiation enters the medium through the north boundary and thus this boundary receives radiation from the medium much earlier than the south boundary. Any change in the input signal will be more noticeable on this boundary. Thus with the reflectance $q_r^*\left(0,t^*\right)$ signals, unlike transmittance $q_r^*\left(Z,t^*\right)$ signals, distinct peaks are observed for all values of β.

(d) Collimated Gaussian pulse train: The north boundary of the planar medium is subjected to collimated radiation (Fig. 3.1b) whose temporal variation is a Gaussian function (Fig. 3.1d). Angle of incidence θ_c of the collimated radiation is zero.

For β =1.0, 2.0 and 5.0, Figs. 3.6a-f show the transmittance $q_t^*\left(Z,t^*\right)$ and reflectance $q_r^*\left(0,t^*\right)$ signals for $N = 1-4$ pulses.

In comparison to diffuse Gaussian pulses (Fig. 3.4a-f), in this case, for $\beta = 1.0$, due to a higher collimated component, the magnitude of transmittance $q_t^*\left(Z,t^*\right)$ is much higher and also reflectance $q_r^*\left(0,t^*\right)$ signal is much lower due to the lesser contribution from the diffuse radiation. But as β increases to 5.0, the magnitudes of the maxima are less than that of the diffuse Gaussian pulses due to the fact that both the radiation source and the medium are highly diffusive in the latter case. The same reasoning can be attributed to the higher values of the reflectance that are observed in diffuse Gaussian pulses.

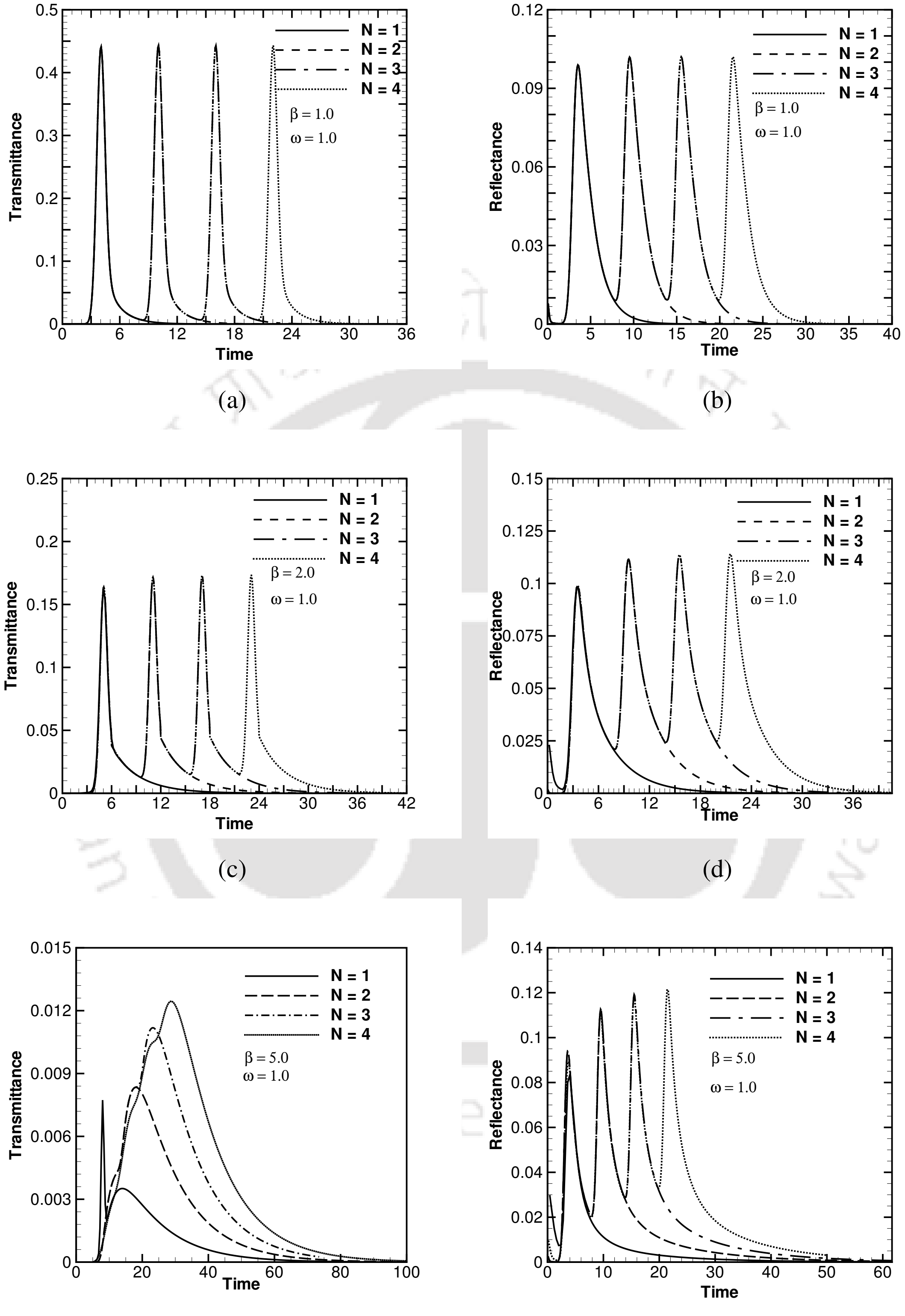

(a) (b)

(c) (d)

(e) (f)

Figure 3.6: Comparison of temporal variations of transmittance and reflectance signals for different values of the extinction coefficient β; Radiation source: Collimated Gaussian pulses.

3.5.2.2 Effect of the scattering albedo ω

For the four cases described before, in Figs. 3.7-3.10, we now present the effect of the scattering albedo ω on transmittance $q_t^*\left(Z,t^*\right)$ and reflectance $q_r^*\left(0,t^*\right)$ signals for different pulse trains, $N=1,2$ and 3. For the sake of legibility, unlike the effect of the β, here we compare the effects of ω for individual pulse trains. In all the cases, $\beta=1.0$ has been considered.

(a) Diffuse step pulse train: For diffuse-step pulses, effects of ω on transmittance $q_t^*\left(Z,t^*\right)$ and reflectance $q_r^*\left(0,t^*\right)$ signals are presented in Fig. 3.7a-f. With decrease in ω, magnitudes of $q_t^*\left(Z,t^*\right)$ decrease. For all pulses, decrease is noticeable throughout and the changes are confined more towards maxima and minima. Scattering albedo ω is seen to have the same effect on $q_r^*\left(0,t^*\right)$. Further it is observed that ω is not having any effect on the time span of the signals.

(b) Collimated step pulse train: For collimated step pulses, effects of ω on transmittance $q_t^*\left(Z,t^*\right)$ and reflectance $q_r^*\left(0,t^*\right)$ signals are given in Figs. 3.8a-f. In this case too, for all values of N, magnitudes of both signals are less for lower value of ω. Effect of ω is more pronounced on the reflectance $q_r^*\left(0,t^*\right)$ signals.

(c) Diffuse Gaussian pulse train: Effects of ω on $q_t^*\left(Z,t^*\right)$ and $q_r^*\left(0,t^*\right)$ signals for diffuse Gaussian pulses are given in Figs. 3.9a-f. Compared to diffuse step pulses (Figs. 3.7a-f), effect of ω in this case is more prominent on both types of signals.

For lower values of the scattering albedo ω, because of more absorption, a higher amount of radiation is trapped in the medium and accordingly in all the cases, both transmittance $q_t^*\left(Z,t^*\right)$ and reflectance $q_r^*\left(0,t^*\right)$ signals have lower magnitudes.

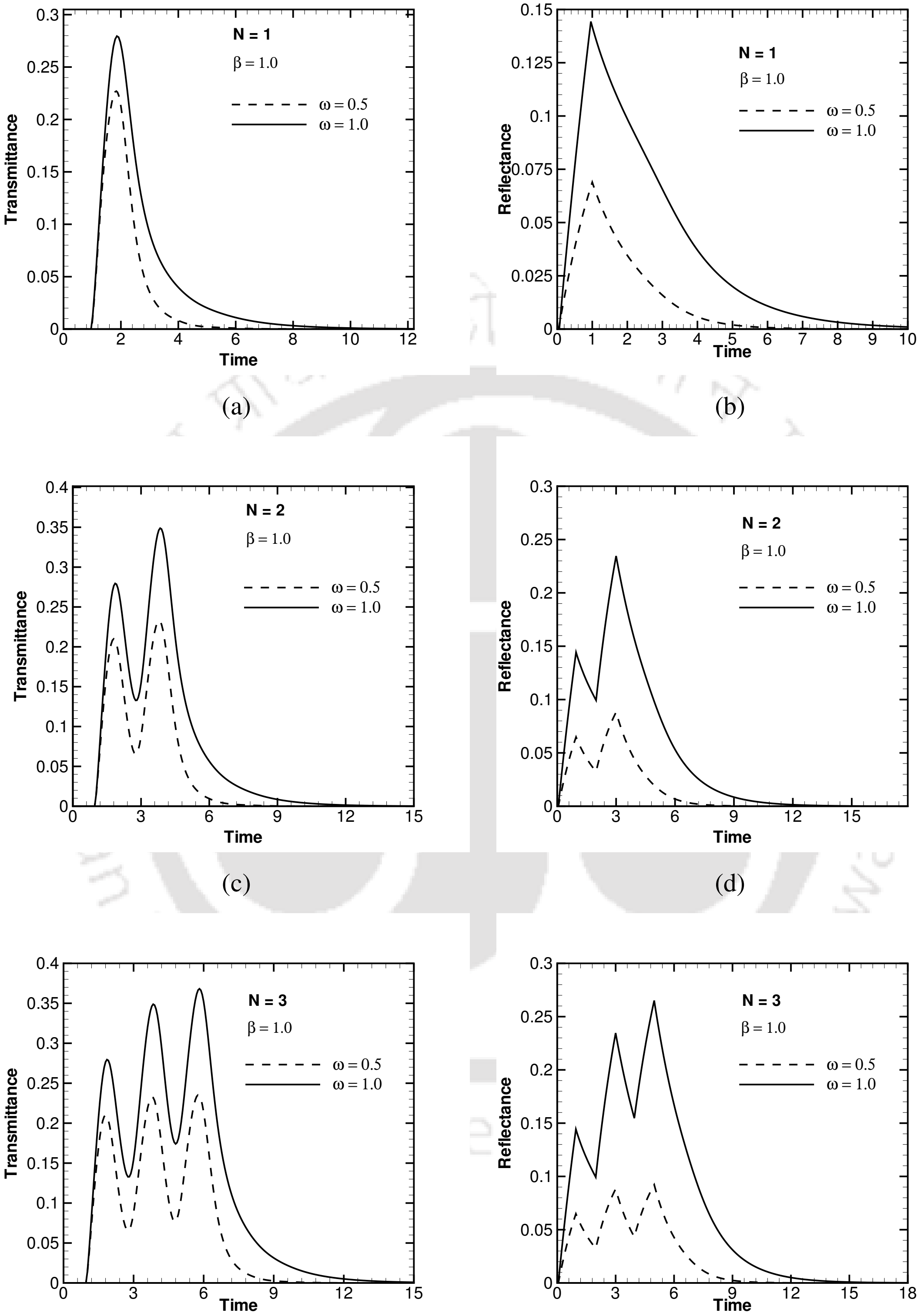

(a) (b)

(c) (d)

(e) (f)

Figure 3.7: Effect of scattering albedo ω on temporal variations of transmittance and reflectance signals; Radiation source: Diffuse step pulses.

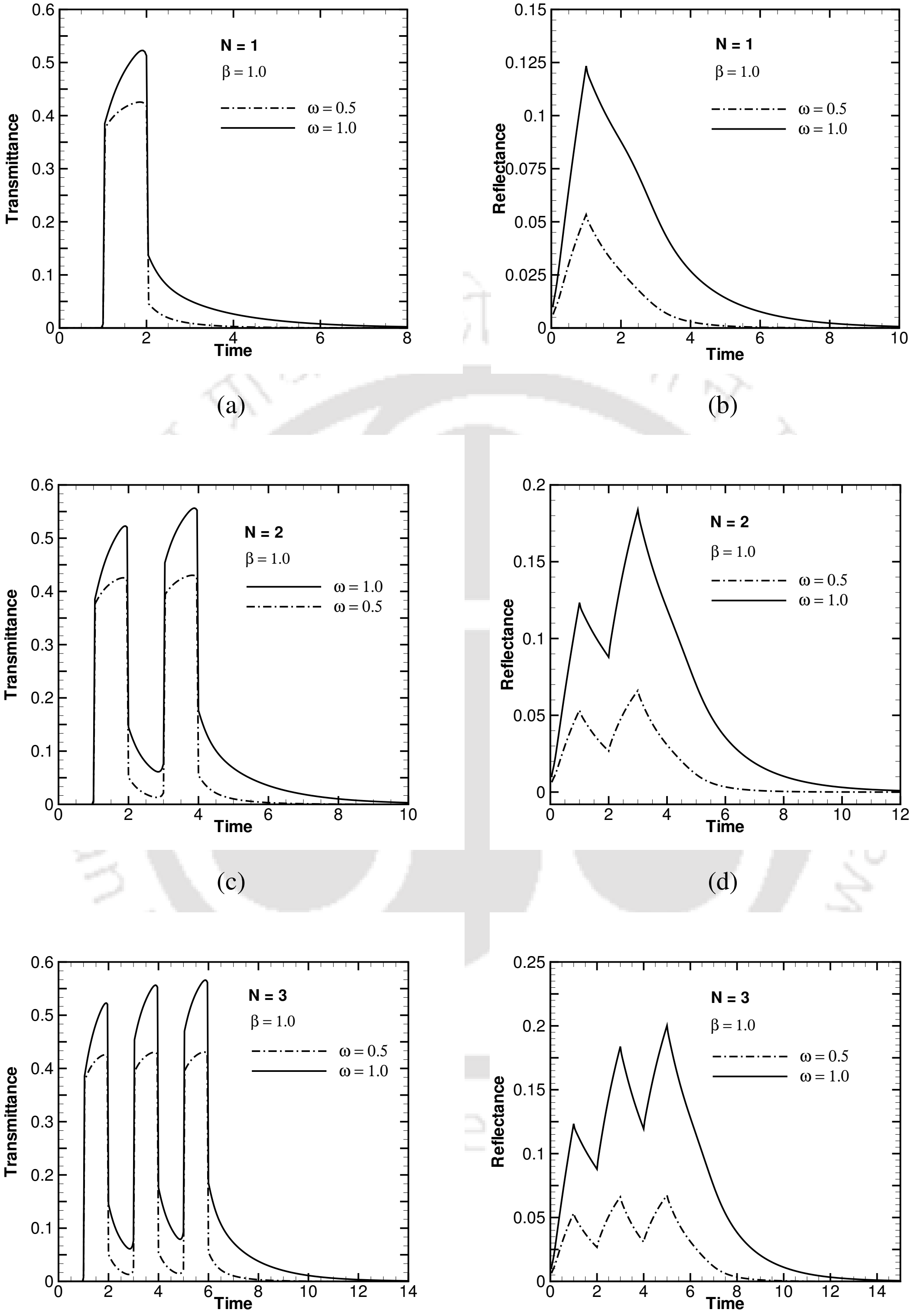

(a) (b)

(c) (d)

(e) (f)

Figure 3.8: Effect of scattering albedo ω on temporal variations of transmittance and reflectance signals; Radiation source: Collimated step pulses.

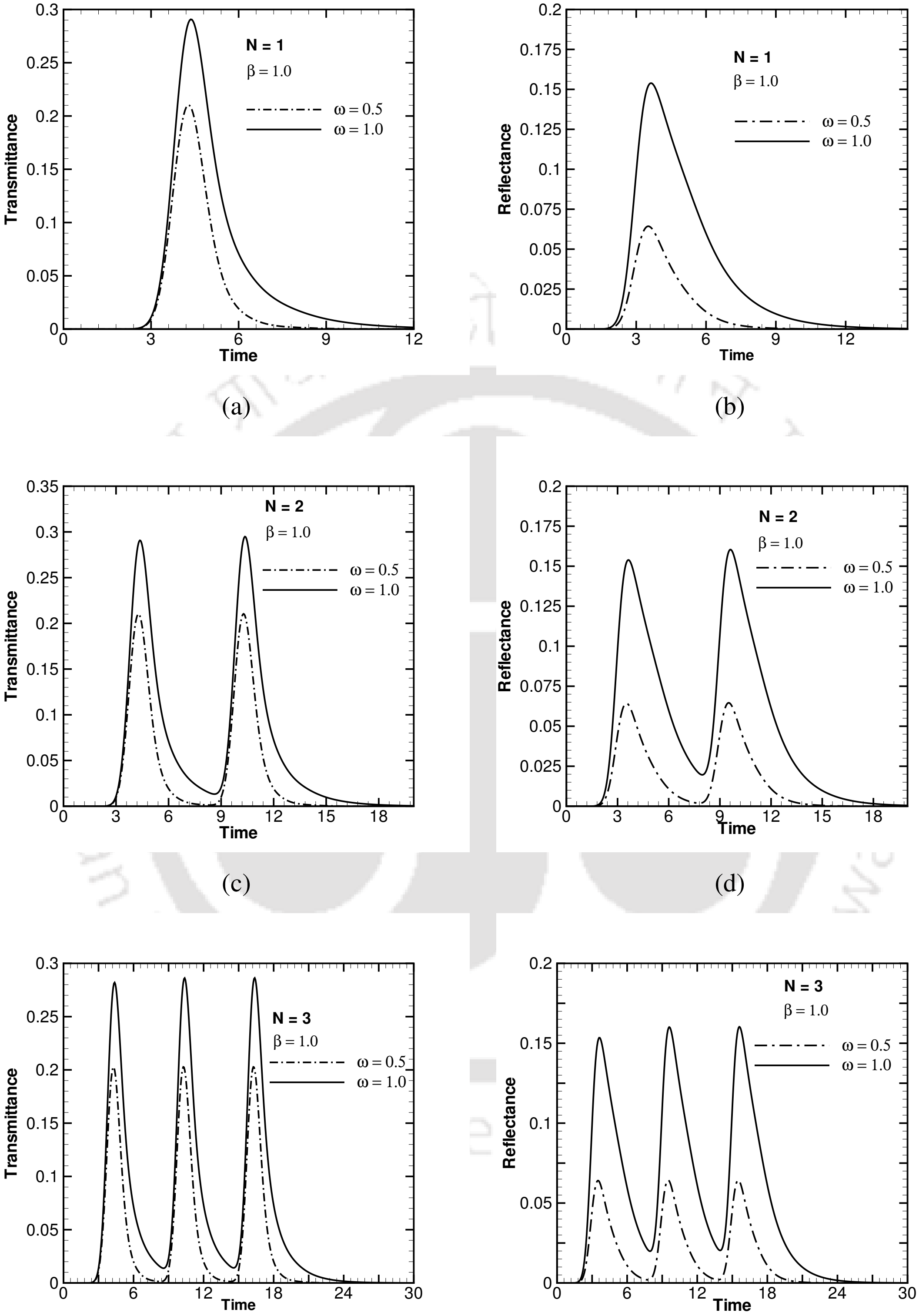

(a) (b)

(c) (d)

(e) (f)

Figure 3.9: Effect of scattering albedo ω on temporal variations of transmittance and reflectance signals; Radiation source: Diffuse Gaussian pulses.

The radiation decays as it travels towards the south boundary and ω will have less effect on $q_t^*\left(Z,t^*\right)$ in comparison to $q_r^*\left(0,t^*\right)$.

(d) Collimated Gaussian pulse train: For collimated Gaussian pulse trains, effects of ω on transmittance $q_t^*\left(Z,t^*\right)$ and reflectance $q_r^*\left(0,t^*\right)$ signals are given in Figs. 3.10a-f. It is observed here that effects of ω on transmittance $q_t^*\left(Z,t^*\right)$ signals are less pronounced in comparison to reflectance $q_r^*\left(0,t^*\right)$ signals. Since β is less, the major amount of the energy received at the south boundary is due to collimated component. Thus even as the radiation travels throughout the medium, the magnitude of ω which influences only the diffuse component is insignificant. But at the north boundary, the energy received being only due to the diffusive component, the difference due to the two values of ω=1.0 and 0.5, is felt distinctly.

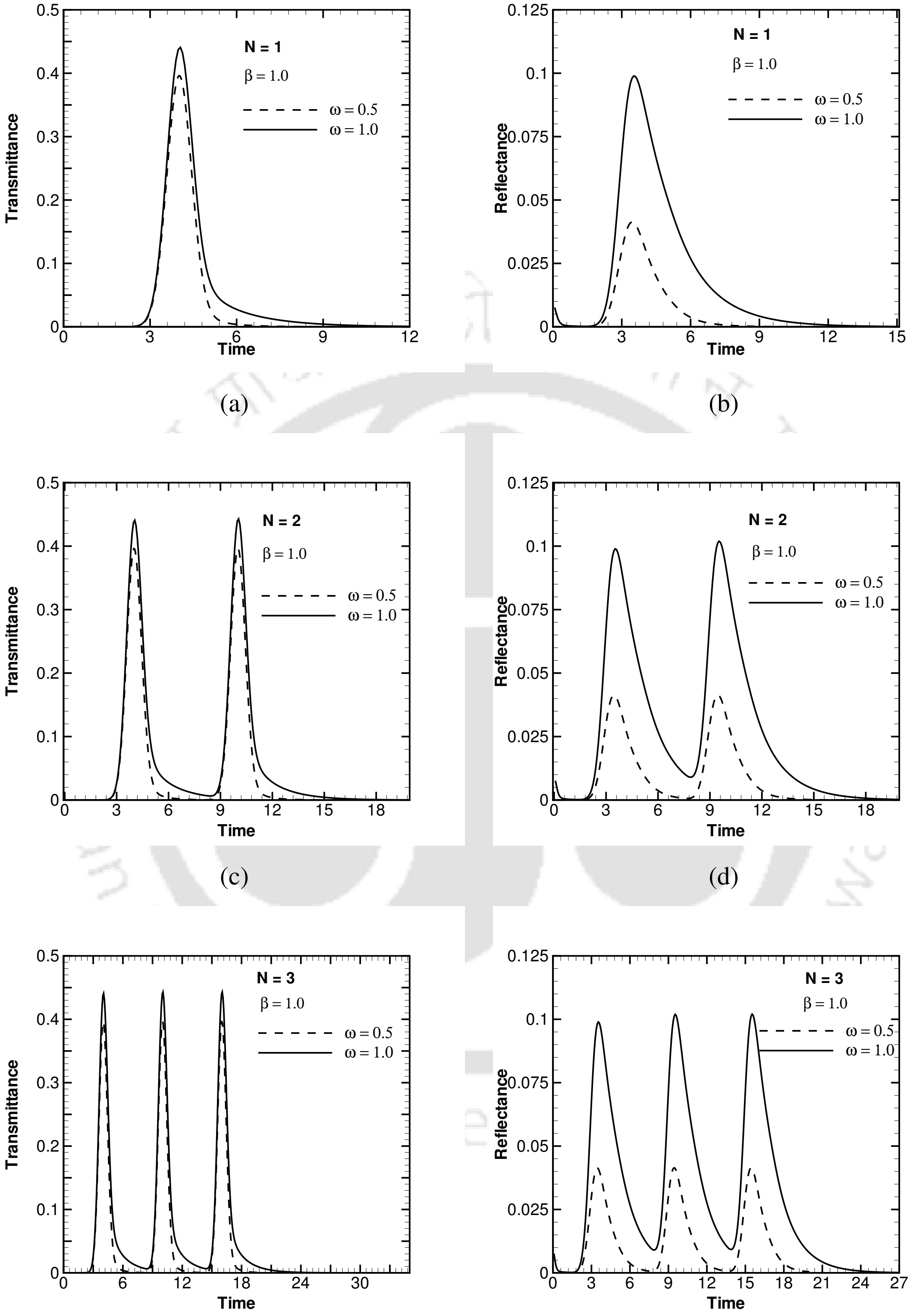

(a) (b)

(c) (d)

(e) (f)

Figure 3.10: Effect of scattering albedo ω on temporal variations of transmittance and reflectance signals; Radiation source: Collimated Gaussian pulses.

3.6 Summary

Transient response of a 1-D planar absorbing-scattering medium subjected to a train of radiation pulses was analyzed. Four different combinations of diffuse and collimated radiation with step and Gaussian temporal variations were considered. Analysis was done using the finite volume method. Results for the train of pulses were first validated for a single pulse with those available in the literature. Effects of the extinction coefficient and the scattering albedo were studied on transmittance and reflectance signals. For lower values of the extinction coefficient, distinct maxima and minima were observed in the signals of multiple pulses. With higher value of the extinction coefficient, multiple maxima in the transmittance signals were found to disappear. Scattering albedo was found to have relatively less effect on the transmittance signals. Signals were found to last for the same duration for the two values of the scattering albedo.

In the present chapter, medium was considered a homogeneous one. One of the objectives of pulse radiation transport through an optically participating medium is to predict the inhomogeneities in the medium. The next chapter deals with the transport of multiple pulses of step and Gaussian temporal profile through an inhomogeneous 1-D planar participating medium.

CHAPTER 4

Propagation of a Laser Wave through a 1-D Planar Participating Inhomogeneous Medium

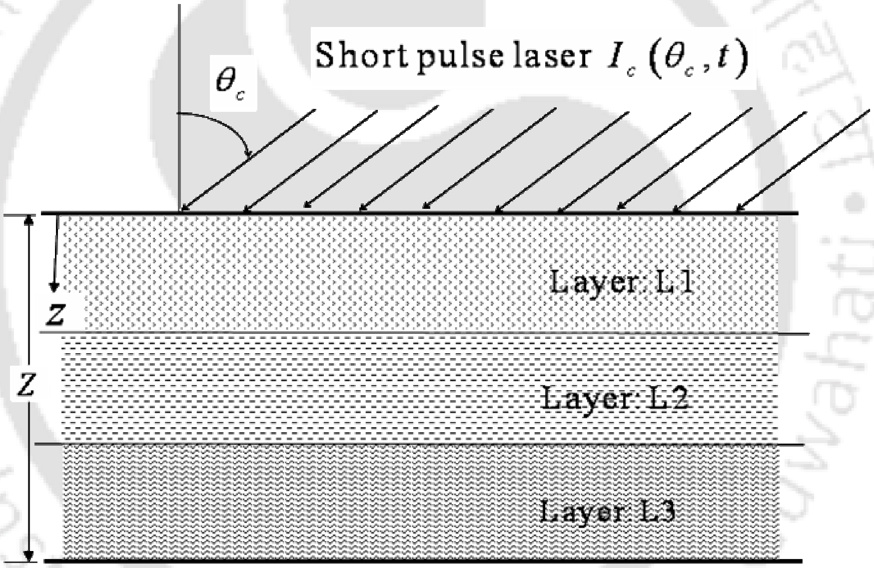

Figure: 1-D planar participating inhomogeneous medium.

4.1 Introduction

Detection of inhomogeneities of any form in a given medium has been one of the potential applications of a short-pulse laser [3, 5, 10-18, 21-22, 27, 32]. In radiation oncology [4], a malicious cancerous tumor which is morphologically different from the surrounding healthy tissues is considered an inhomogeneity in a participating medium. In non-destructive testing [76, 120], the presence of an internal flaw or inclusion of any foreign material is also an inhomogeneity. By radiative transport analysis, in all such cases, important information which characterizes the properties of the medium are obtained.

A good amount of literature has been devoted to the study of interaction of a short-pulse laser with a homogeneous participating medium [30, 31, 32, 79, 86, 91, 93, 95, 96-102, 112, 115, 117, 118]. Some works have also been reported on the effect of inhomogeneities on transport of a short-pulse laser in a participating medium [14, 16, 20-29, 34, 35, 37, 39-47, 70-76, 107-111, 114, 119-120]. In these studies, experimental as well as various numerical radiative transfer methods such as the spherical harmonics method (P_N approximation), the discrete ordinates method, the discrete transfer method, the Monte Carlo method, the radiation element method and the finite volume method (FVM) have been employed. In all the above cases, the analyses were carried out for a single pulse or a many-pulse laser.

A laser pulse train finds potential applications in the emerging areas such as laser tissue welding and soldering, laser metal surface finishing, laser metal marking and engraving, nano-photonics and fiber optic communications [1-99]. Unlike numerical studies in with a single pulse laser in which the transmittance and the reflectance signals have mainly been analyzed, studies with pulse trains are scarce. In the present chapter, the study with a single and a train of four laser pulses is presented. The pulse train has a 1- or 4-pulse step or Gaussian temporal profile. The planar participating medium consists of 2-3 layer having different optical properties. Temporal transmittance and reflectance signals are studied for different arrangements of layers. The FVM formulation given in Chapter 3 is used for this study.

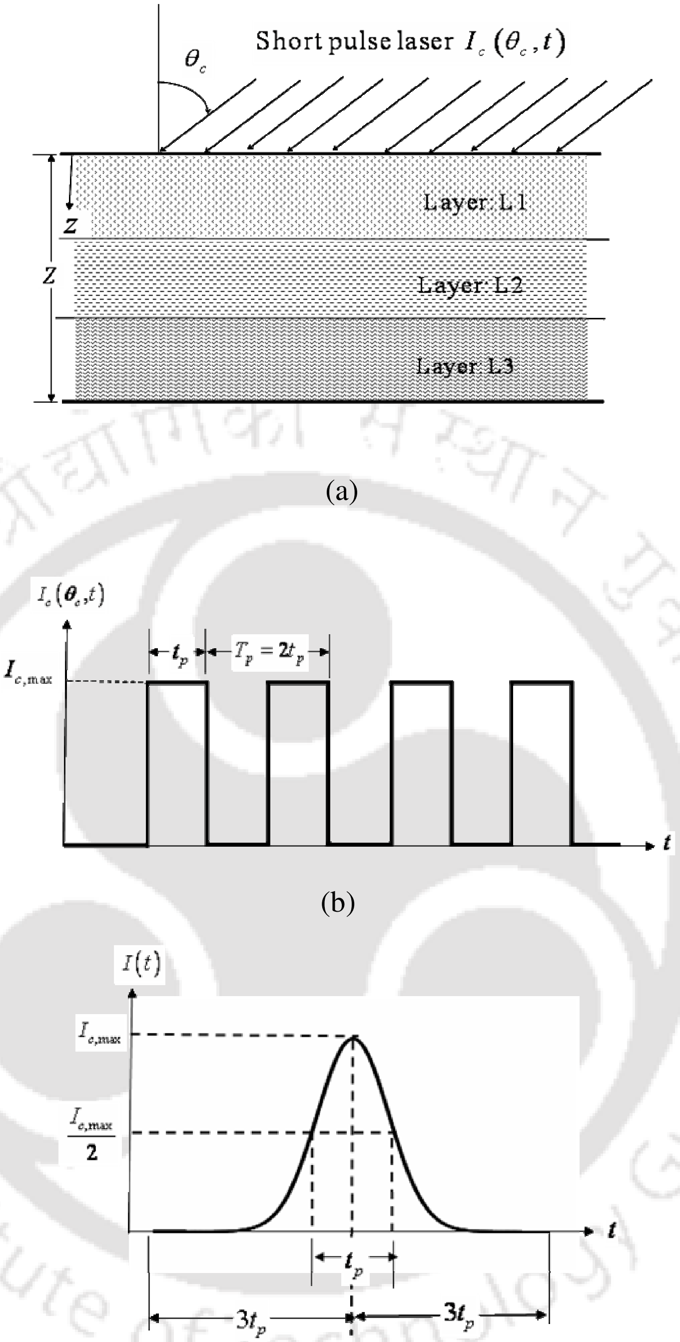

(a)

(b)

(c)

Figure 4.1: (a) 1-D planar participating inhomogeneous medium(b) step pulse train (c) pulse of Gaussian temporal profile.

4.2 Problem

We consider the north boundary of an inhomogeneous 1-D planar participating medium (Fig. 4.1a) subjected to a single or a train of 4 step laser pulses (Fig. 4.1b). The laser beam is directed normal to the boundary. Results of transmittance $q_t^*\left(Z,t^*\right)$ and reflectance $q_r^*\left(0,t^*\right)$ signals are analyzed for an inhomogeneous medium consisting of 2-3 layers. Inhomogeneities in the medium are caused because of the varying scattering albedo ω and optical depth $\left(\tau=\beta z\right)$ in different layers. Extinction coefficient β of different layers is the same.

4.3 Step Pulse- Results and Discussions

Towards validation of our results with an inhomogeneous medium, first we do comparison of our results for a single step-pulse laser with those available in the literature [106]. Next we present and analyze results for a single and a train of 4-step pulses for a 2-3 layer medium.

4.3.1 Validation of results

The 2-layer medium having optical depths $\tau_1=\tau_2=0.5$ is subjected to a single step-pulse laser of pulse width $t_p^*=0.3$. With physical depth of each layer being 0.5 m, the extinction coefficient β in both the layers is 1.0. The two layers have different scattering albedos.

In Figs 4.2a and 4.2b, reflectance $q_r^*\left(0,t^*\right)$ results of the present work for a single step-pulse laser are compared with those of Lu and Hsu [106]. In Fig. 4.2a, scattering albedos of layers 1 and 2 are $\omega_1=0.1$ and $\omega_2=0.9$, respectively. For results in Fig. 4.2b, scattering albedos of the two layers are reversed. Results of the present work are in good agreement with those reported in the literature [106].

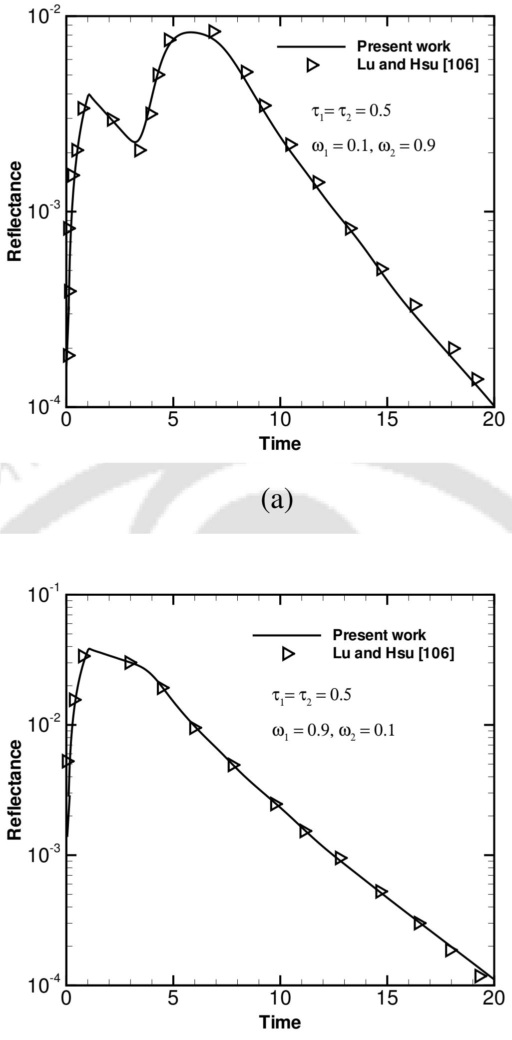

(a)

(b)

Figure 4.2: Comparison of reflectance $q_r^*\left(0,t^*\right)$ signals for a two-layer medium with $\tau_1 = \tau_2 = 1.0$ (a) $\omega_1 = 0.1, \omega_2 = 0.9$ and (b) $\omega_1 = 0.9, \omega_2 = 0.1$.

4.3.2 Results with 1- and 4-pulse laser train

In the following pages, transmittance $q_t^*\left(Z,t^*\right)$ and reflectance $q_r^*\left(0,t^*\right)$ results with a single and a train of 4-pulses are provided for a 2-3 layer medium in which optical depths τ and scattering albedo ω of different layers are different. These results are presented for pulse width $t_p^* = \beta c t_p = 0.3$ which corresponds to a pulse-width of one nano-second. The extinction coefficient $\beta = 1.0$ is considered in all the cases. The inhomogeneous medium is considered absorbing and isotropically scattering, and the diffuse-gray boundaries are black and cold.

It is to be noted that in the present work, sudden change in properties of the inhomogeneous medium is represented in the form of a discrete variation of optical properties such the optical depth τ and the scattering albedo ω. For example, a two-layer medium with $\tau_1 = 10.0$, $\omega_1 = 0.1$ and $\tau_2 = 1.0$, $\omega_2 = 0.9$ is highly absorbing and weakly scattering in the first layer, whereas low absorbing and strongly scattering in the second layer.

Figs. 4.3a-d show the transmittance $q_t^*\left(Z,t^*\right)$ and reflectance $q_r^*\left(0,t^*\right)$ signals for a 2-layer medium of total optical depth $\tau = 6.0$. Optical depths of layers 1 and 2 are 1.0 and 5.0, respectively. For results in Figs. 4.3a and 4.3b, scattering albedo ω of layers 1 and 2 are 0.1 and 0.9, respectively. A different case is studied in Figs. 4.3c and 4.3d by reversing the scattering albedos ω of layers 1 and 2.

In Figs. 4.3a and 4.3b, the first layer is low absorbing $\left(\tau_1 = 1.0\right)$ and weakly scattering $\left(\omega_1 = 0.1\right)$ while the second layer is highly absorbing $\left(\tau_2 = 5.0\right)$ and strongly scattering $\left(\omega_2 = 0.9\right)$. In Figs. 4.3c and 4.3d, the first layer is low absorbing $\left(\tau_1 = 1.0\right)$ and strongly scattering $\left(\omega_1 = 0.9\right)$ while the second layer is highly absorbing $\left(\tau_2 = 5.0\right)$ and weakly scattering $\left(\omega_2 = 0.1\right)$.

In Fig. 4.3a, the transmitted energy passes through the first layer without any considerable decay and scattering, but encounters high decay and a strong scattering in the layer 2. Accordingly, the transmittance $q_t^*\left(Z,t^*\right)$ signals remain available for a long period. But in the case of Fig. 4.3c, even though there is a strong scattering in layer 1, the dissipation of energy is less due to low decay of the incident energy. The energy passes from layer 1 to layer 2 without much extinction and then while traveling in the layer 2, it encounters inhomogeneities having high extinction and

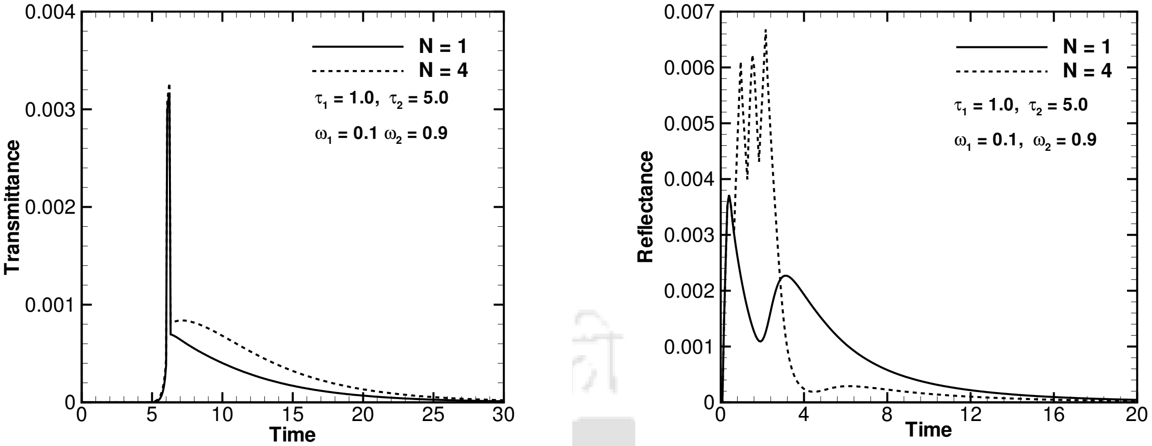

(a) $\tau_1 = 1.0,\ \tau_2 = 5.0;$ $\omega_1 = 0.1, \omega_2 = 0.9$

(b) $\tau_1 = 1.0,\ \tau_2 = 5.0;$ $\omega_1 = 0.1, \omega_2 = 0.9$

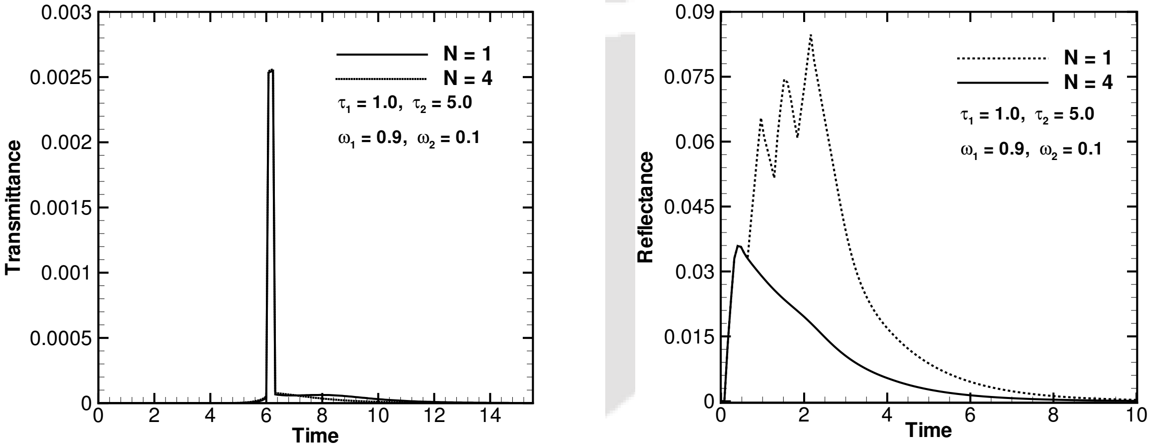

(c) $\tau_1 = 1.0,\ \tau_2 = 5.0;$ $\omega_1 = 0.9, \omega_2 = 0.1$

(d) $\tau_1 = 1.0,\ \tau_2 = 5.0;$ $\omega_1 = 0.9, \omega_2 = 0.1$

Figure 4.3: Transmittance $q_t^*\left(Z, t^*\right)$ signals and reflectance $q_r^*\left(0, t^*\right)$ signals for a two-layer medium.

weak scattering. Because of this, the transmittance $q_t^*\left(Z, t^*\right)$ signals are available for a shorter duration in comparison to the arrangement of inhomogeneities in case of Fig.

4.3a. In Fig. 4.3a, distinct temporal signatures for a single and 4-pulse laser train are observed. However, in Fig. 4.3c, the same are not distinct.

An observation of Figs. 4.3a and 4.3c show that the difference in the peak magnitudes of the transmittance $q_t^*\left(Z,t^*\right)$ signals is small. In both the cases (Figs. 4.3a and 4.3c), the total optical depth of the medium is the same $\left(\tau=\tau_1+\tau_2=6.0\right)$. For the case represented by Fig. 3c, the north boundary is adjacent to a strongly scattering layer. Hence, this boundary receives more diffuse energy from the medium. This accounts for the differences in the peak magnitudes (Figs. 4.3a and 4.3c) of the transmittance signals at the south boundary.

In case of Figs. 4.3b and 4.3d, a large difference in the peak magnitudes of the reflectance $q_r^*\left(0,t^*\right)$ signals is noticed for both a single-pulse and a 4-pulse laser train. In Fig. 4.3b, due to a high decay and strong scattering effects in layer 2, the reflectance $q_r^*\left(0,t^*\right)$ signal corresponding to that layer is spread broadly over time. But due to a low decay and low scattering in layer 1, a peak of almost twice the magnitude of energy corresponding to layer 2 is received for shorter duration. In the reflectance signals, with a 4-pulse train, the minima corresponding to its periodicity are observed in both Figs.4.3b and 4.3d. With a single pulse, the minimum which corresponds to the inhomogeneities in the medium is noticed only in case of Fig. 4.3b. However, the same is not noticed in Fig. 4.3d.

In Figs. 4.4a-d, a 2-layer medium of the same total optical depth $\tau=6.0$ as that of Fig. 4.3a-d is considered. Inhomogeneities in terms of the scattering albedo ω are also the same. In Fig. 4.4a, the temporal signatures in the case of a single and 4-pulse laser train do not show any visible difference. But in Fig. 4.4c, a noticeable difference in the peak values and the temporal profile is seen. This is due to the fact that the first layer corresponding to Fig. 4.4a is weakly scattering $\left(\omega_1=0.1\right)$ and while it is strongly scattering $\left(\omega_1=0.9\right)$ in Fig. 4.4c.

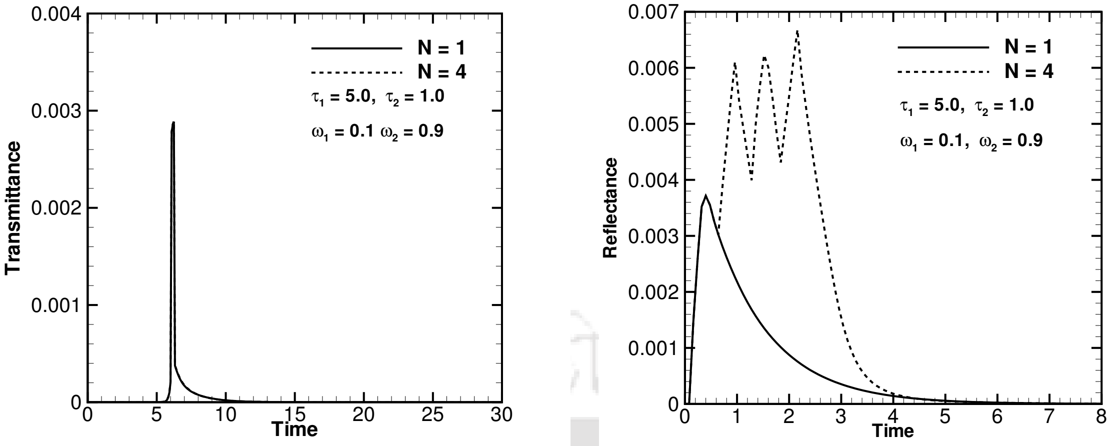

(a) $\tau_1 = 5.0,\ \tau_2 = 1.0; \omega_1 = 0.1, \omega_2 = 0.9$ (b) $\tau_1 = 5.0,\ \tau_2 = 1.0; \omega_1 = 0.1, \omega_2 = 0.9$

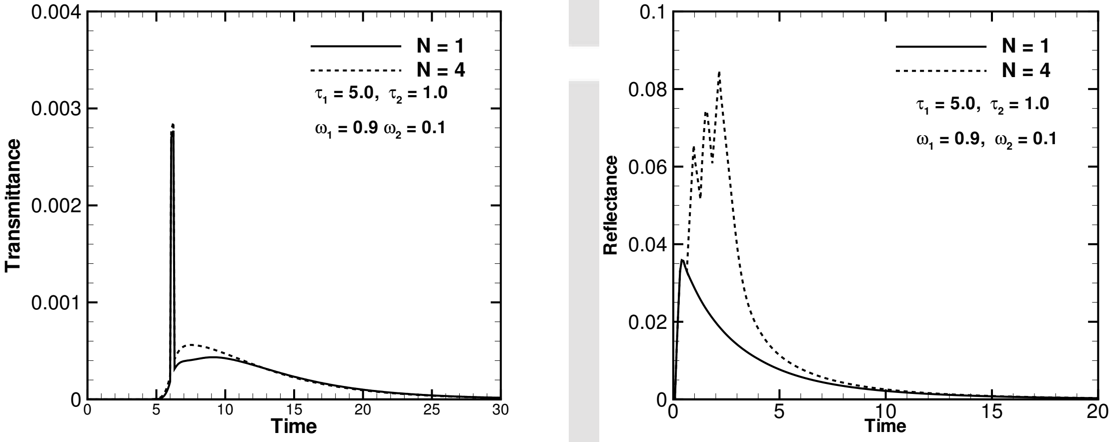

(c) $\tau_1 = 5.0,\ \tau_2 = 1.0; \omega_1 = 0.9, \omega_2 = 0.1$ (d) $\tau_1 = 5.0,\ \tau_2 = 1.0; \omega_1 = 0.9, \omega_2 = 0.1$

Figure 4.4: Transmittance $q_t^*\left(Z, t^*\right)$ signals and reflectance $q_r^*\left(0, t^*\right)$ signals for a two-layer medium.

In Fig. 4.4c, transmittance $q_t^*\left(Z, t^*\right)$ signals of almost the same magnitude of Fig. 4.4a is observed for longer time duration for almost three times that of Fig. 4.4a. This again can be attributed to the fact that the layer 1 is highly absorbing $\left(\tau_1 = 5.0\right)$ and

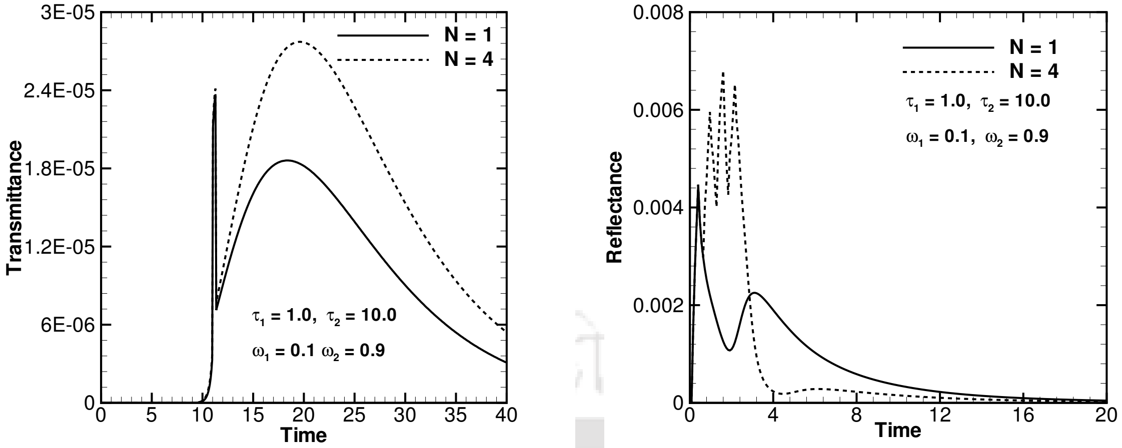

(a) $\tau_1 = 1.0,\ \tau_2 = 10.0; \omega_1 = 0.1, \omega_2 = 0.9$ (b) $\tau_1 = 1.0,\ \tau_2 = 10.0; \omega_1 = 0.1, \omega_2 = 0.9$

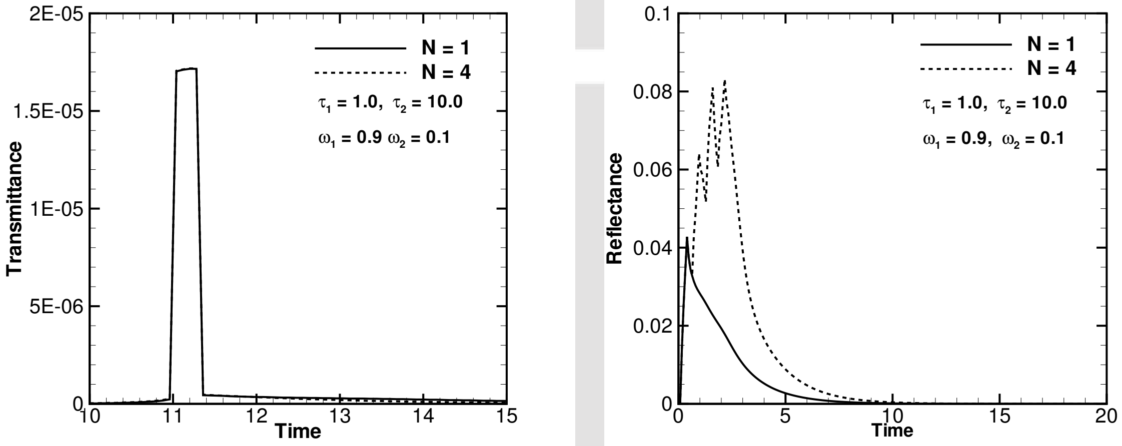

(c) $\tau_1 = 1.0,\ \tau_2 = 10.0; \omega_1 = 0.9, \omega_2 = 0.1$ (d) $\tau_1 = 1.0,\ \tau_2 = 10.0; \omega_1 = 0.9, \omega_2 = 0.1$

Figure 4.5: Transmittance $q_t^*\left(Z, t^*\right)$ signals and reflectance $q_r^*\left(0, t^*\right)$ signals for a two-layer medium.

highly scattering $\left(\omega_1 = 0.9\right)$. In Fig. 4.4d, the magnitudes of reflectance $q_r^*\left(0, t^*\right)$ signals of both a single and a 4-pulse laser train are one order higher than Fig. 4.4b.

Figs. 4.5a-d give results for a 2-layer medium in which the layer 1 is low absorbing $\left(\tau_1 = 1.0\right)$ and layer 2 is highly absorbing $\left(\tau_2 = 10.0\right)$. The transmittance

$q_t^*\left(Z,t^*\right)$ signals in Figs. 4.5a and 4.5c are both of very low magnitudes while the reflectance $q_r^*\left(0,t^*\right)$ signals in Fig. 4.5b and 4.5d are one order different. In Fig. 4.5a, due to both strong scattering $(\omega_2 = 0.9)$ and a very high decay in layer 2, the large amount of diffused energy in this layer is responsible for the transmittance $q_t^*\left(Z,t^*\right)$ signals for a very long duration. In Fig. 4.5c, the peak magnitude of transmittance $q_t^*\left(Z,t^*\right)$ signal is as low as half that of Fig. 4.5a. Due to a very high decay $(\tau_2 = 10.0)$ and weak scattering $(\omega_2 = 0.1)$ effects in layer 2, the temporal span of the transmittance $q_t^*\left(Z,t^*\right)$ signal is much shorter in comparison to Fig. 4.5a.

In Fig. 4.5c, the incident laser energy propagates through the low absorbing $(\tau_1 = 1.0)$ and weak scattering $(\omega_1 = 0.1)$ layer 1 due to which the back scattered intensities to the north boundary are lesser. Due to this, the reflectance $q_r^*\left(0,t^*\right)$ signals in both cases of a single and 4-pulse laser train are less than that of Fig. 4.5d. The first peak of 4-pulse and the peak of the single-pulse have a 1-1 correspondence due to the fact that the initial peak of any reflectance $q_r^*\left(0,t^*\right)$ signal depends only on the optical nature of the layer that lies adjacent to the north boundary.

Results for a 2-layer medium in which the layer 1 is very highly absorbing $(\tau_1 = 10.0)$ and layer 2 is low absorbing $(\tau_2 = 1.0)$ are presented in Figs.4.6a-d. In Figs. 4.6a and 4.6c, the magnitudes of transmittance $q_t^*\left(Z,t^*\right)$ signals are comparable whereas the temporal profiles are not. In Fig. 4.6a, in which the layer 1 is weak scattering $(\omega_1 = 0.1)$ and layer 2 is strongly scattering $(\omega_2 = 0.9)$, an initial peak of a comparably a very high magnitude than a latter maximum is observed. After a very high decay in layer 1, when the energy travels through layer 2, although there is a low decay in this layer, due to strong scattering effects, the contribution of the diffuse energy is high. This is the reason for the availability of transmittance $q_t^*\left(Z,t^*\right)$ signal

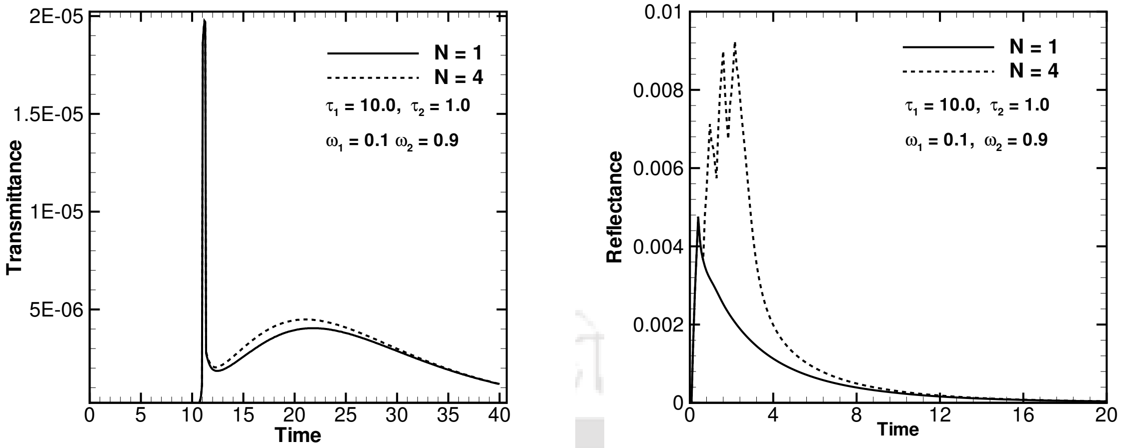

(a) $\tau_1 = 10.0,\ \tau_2 = 1.0; \omega_1 = 0.1, \omega_2 = 0.9$ (b) $\tau_1 = 10.0,\ \tau_2 = 1.0; \omega_1 = 0.1, \omega_2 = 0.9$

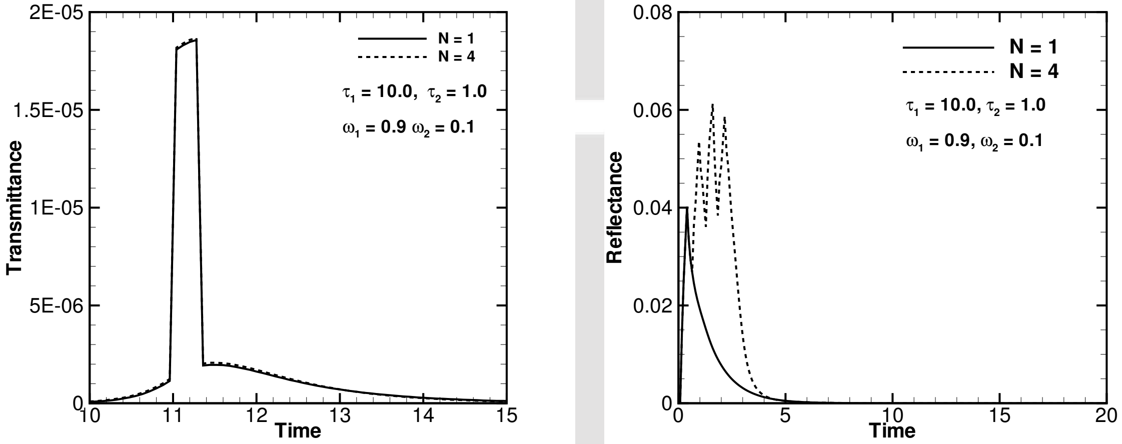

(c) $\tau_1 = 10.0,\ \tau_2 = 1.0; \omega_1 = 0.9, \omega_2 = 0.1$ (d) $\tau_1 = 10.0,\ \tau_2 = 1.0; \omega_1 = 0.9, \omega_2 = 0.1$

Figure 4.6: Transmittance $q_t^*\left(Z, t^*\right)$ signals and reflectance $q_r^*\left(0, t^*\right)$ signals for a two-layer medium.

for a very long duration. In Fig. 4.6c, since the layer 2 is weak scattering $\left(\omega_2 = 0.1\right)$, the presence of energy at the south boundary is limited as far as time is concerned.

In Fig. 4.6b as well as in Fig. 4.6d, any abrupt change in the trend of the reflectance $q_r^*\left(0, t^*\right)$ signal due to inhomogeneities of the medium is not observed. The

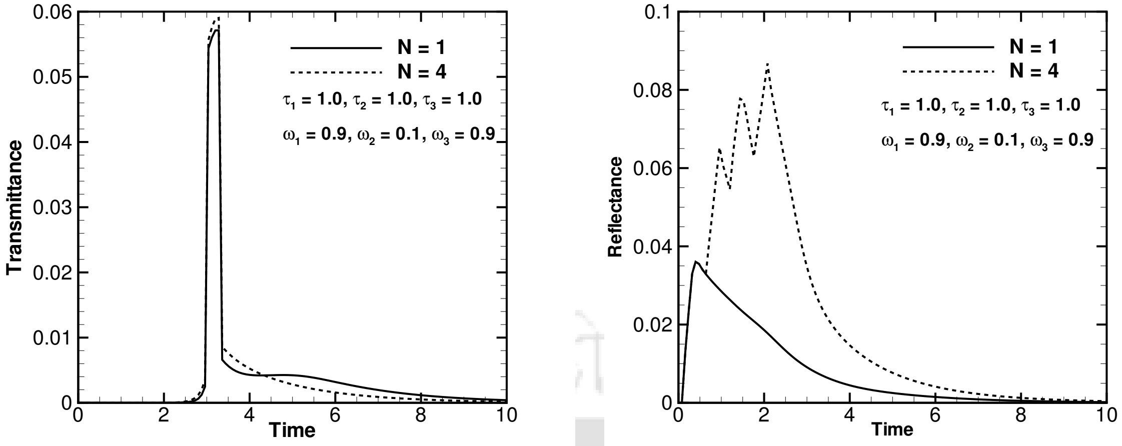

(a) $\tau_1 = 1.0,\ \tau_2 = 1.0, \tau_3 = 1.0$
$\omega_1 = 0.9, \omega_2 = 0.1, \omega_3 = 0.9$

(b) $\tau_1 = 1.0,\ \tau_2 = 1.0, \tau_3 = 1.0$
$\omega_1 = 0.9, \omega_2 = 0.1, \omega_3 = 0.9$

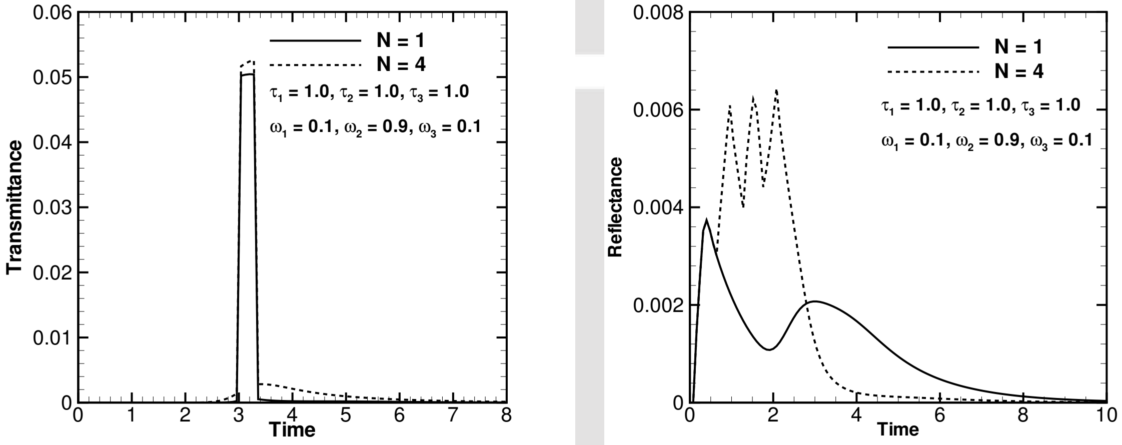

(c) $\tau_1 = 1.0,\ \tau_2 = 1.0, \tau_3 = 1.0$
$\omega_1 = 0.1, \omega_2 = 0.9, \omega_3 = 0.1$

(d) $\tau_1 = 1.0,\ \tau_2 = 1.0, \tau_3 = 1.0$
$\omega_1 = 0.1, \omega_2 = 0.9, \omega_3 = 0.1$

Figure 4.7: Transmittance $q_t^*\left(Z, t^*\right)$ signals and reflectance $q_r^*\left(0, t^*\right)$ signals for a three-layer medium.

magnitude of reflectance $q_r^*\left(0, t^*\right)$ signal in Fig. 4.6d is higher than that of Fig. 4.6c both for a single and 4-pulse laser train. This is due to strong scattering effects $\left(\omega_1 = 0.9\right)$ of layer 1 corresponding to Fig. 4.6d.

Figs. 4.7a-d present results for a 3-layer medium of total optical depth $\tau = 3.0$. The inhomogeneities are represented by considering distinct values of the scattering albedo in the three layers. The peak magnitudes of transmittance $q_t^*\left(Z,t^*\right)$ signal in Figs. 4.7a and 4.7c are comparable. In both the cases, due to a larger diffusion of energy, the magnitude of the transmittance $q_t^*\left(Z,t^*\right)$ signals with a 4-pulse laser train is a little higher than that for a single pulse. In Fig. 4.7a, for a single pulse, inhomogeneities can be observed by distinct maxima and minima in the transmittance $q_t^*\left(Z,t^*\right)$ signals. The first minimum corresponds to the interface of layer 2 and layer 3. Such distinct maxima or minima are not observed in the case of a 4-pulse train. Due to the stronger scattering $(\omega_3 = 0.9)$ effects of layer 3 in Fig. 4.7a, after the second maximum, the signal stays for a longer duration than in the case of Fig. 4.7c.

In case of Figs. 4.7a and 4.7c, the overall scattering nature of the medium is stronger $(\omega_1 = 0.9, \omega_2 = 0.1, \omega_3 = 0.9)$ than that of case represented in Fig. 4.7b and 4.7d $(\omega_1 = 0.1, \omega_2 = 0.9, \omega_3 = 0.1)$. Due to this, a considerably higher difference in the magnitudes of the reflectance $q_r^*\left(0,t^*\right)$ signal in Fig. 4.7d for both single and 4-pulse train is observed. This trend is analogous to cases discussed in Figs. 4.3-4.6.

Fig. 4.8 presents results for a 3-layer medium having a total optical depth $\tau = 11.0$. In Figs. 4.8a and 4.8b, the middle layer has a weak scattering $(\omega_2 = 0.1)$, and in Fig. 4.8c and 4.8d, it has a strong scattering $(\omega_2 = 0.9)$. The adjacent two layers in all the cases are low absorbing $(\tau_1 = \tau_3 = 1.0)$. The peak magnitudes of transmittance $q_t^*\left(Z,t^*\right)$ signals in Figs. 4.8a and 4.8c are comparable, but the temporal profile of Fig. 4.8c is totally different from that of Fig. 4.8a. In Fig. 4.8a, though the middle layer is highly absorbing $(\tau_2 = 9.0)$, due to its weak scattering nature $(\omega_2 = 0.1)$, it allows a higher amount of energy to propagate through it. But in Fig. 4.8c, due to the strong scattering effects $(\omega_2 = 0.9)$, the middle layer retains the energy for a very long duration.

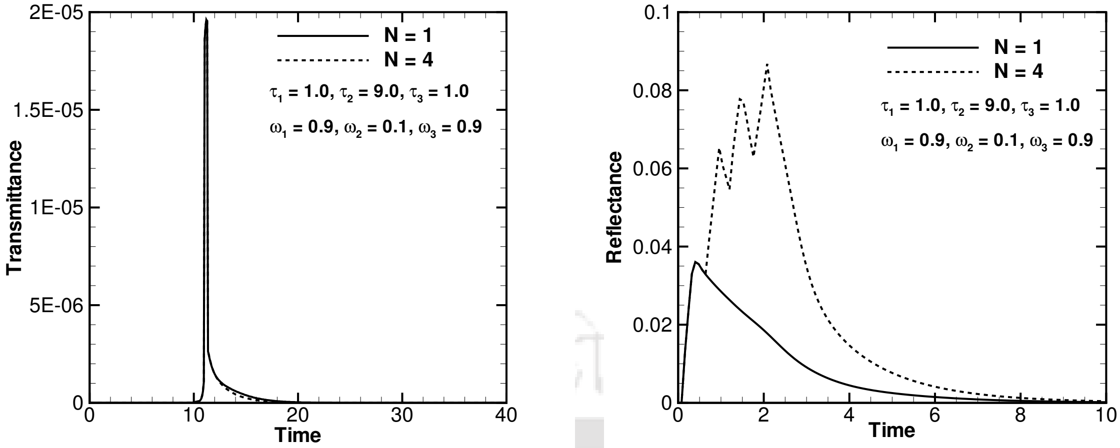

(a) $\tau_1 = 1.0,\ \tau_2 = 9.0, \tau_3 = 1.0$
$\omega_1 = 0.9, \omega_2 = 0.1, \omega_3 = 0.9$

(b) $\tau_1 = 1.0,\ \tau_2 = 9.0, \tau_3 = 1.0$
$\omega_1 = 0.9, \omega_2 = 0.1, \omega_3 = 0.9$

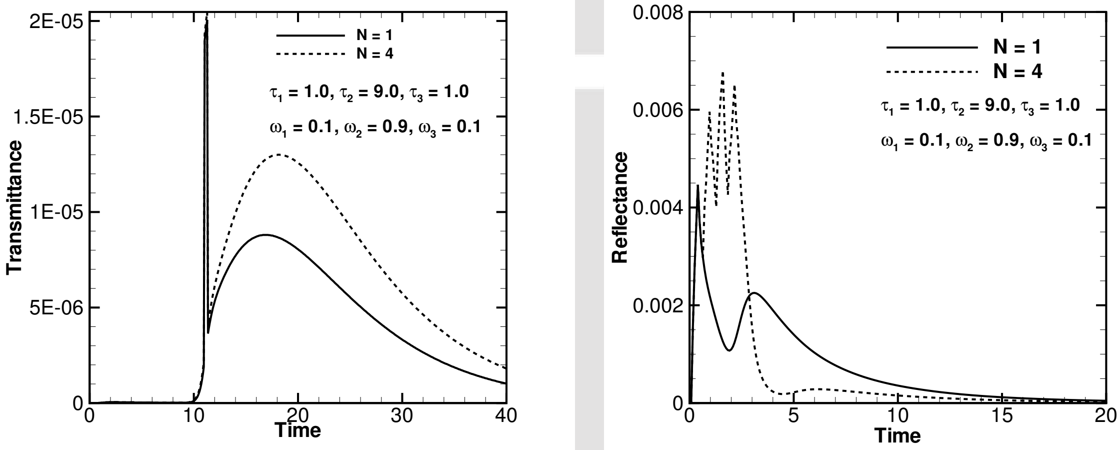

(c) $\tau_1 = 1.0,\ \tau_2 = 9.0, \tau_3 = 1.0$
$\omega_1 = 0.1, \omega_2 = 0.9, \omega_3 = 0.1$

(d) $\tau_1 = 1.0,\ \tau_2 = 9.0, \tau_3 = 1.0$
$\omega_1 = 0.1, \omega_2 = 0.9, \omega_3 = 0.1$

Figure 4.8: Transmittance $q_t^*\left(Z, t^*\right)$ signals and reflectance $q_r^*\left(0, t^*\right)$ signals for a three-layer medium.

4.4 Gaussian Pulse-Results and Discussions

As far as inhomogeneous medium is concerned, study on a short-pulse laser with a Gaussian temporal profile has not received much attention and the same has not been analyzed using the FVM. In [106], Lu and Hsu have done the analysis of interaction

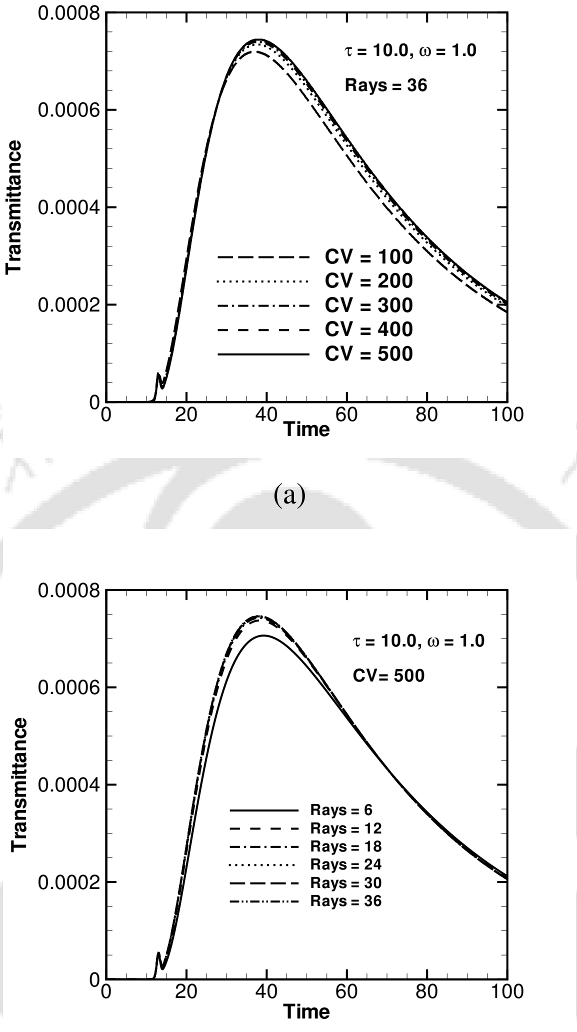

(b)

Figure 4.9: Grid and ray independency tests; effect of the number (a) of control volumes and (b) number of rays on transmittance $q_t^*\left(Z,t^*\right)$ signals for a homogeneous medium.

of short-pulse laser with a planar participating inhomogeneous medium. In their study they have used a short-pulse laser having step temporal profile. They did the analysis using the reverse MCM. Inhomogeneities were found to have significant effect on the transmittance and reflectance signals. A short-pulse laser with Gaussian temporal profile is more practical [15, 22-24] than that with a step temporal profile. Further, the MCM is the most time-consuming method and has the drawback of statistical errors. In case of a planar medium problem, Lu and Hsu [106] used 10^9

photons in their analysis. They have not reported the CPU time. Compared to the MCM, the FVM is computationally very fast.

We consider the north boundary subjected to the laser pulse. The laser beam is directed normal to the boundary. Temporal variation of any pulse is a Gaussian function (Fig.4.1c). Results of transmittance $q_t^*\left(Z,t^*\right)$ and reflectance $q_r^*\left(0,t^*\right)$ signals are presented for an inhomogeneous medium consisting of 2-3 layers (Fig.4.1a). The scattering albedo ω and optical depths $\left(\tau=\beta z\right)$ of different layers are different. Extinction coefficient β of different layers is the same.

For grid independent results, 500 equal size control volumes were used (Fig. 4.9a) and a maximum of 36 equally spaced directions in the polar space $\left(0\le\theta\le\pi\right)$ were found enough for the ray-independent solutions (Fig. 4.9b). 1000 divisions of the total time t^* domain were found sufficient for marching in the time dimension. Iteration was terminated when the maximum variation of the source at any location for a given direction between two consecutive time levels did not exceed 1.0×10^{-7}.

In Figs. 4.10-4.15, transmittance $q_t^*\left(Z,t^*\right)$ and reflectance $q_r^*\left(0,t^*\right)$ results for different arrangements of inhomogeneities in the medium are presented. In Figs. 4.10-4.14, variations in inhomogeneities in different layers are discrete, while for results in Fig. 4.15, the variation of the scattering albedo ω in the medium is a quadratic function of space. Two different quadratic profiles have been considered.

In Fig. 4.10, transmittance $q_t^*\left(Z,t^*\right)$ and reflectance $q_r^*\left(0,t^*\right)$ results have been presented for a two-layer medium. Four different combinations of optical depths τ and scattering albedo ω have been considered. Out of these, cases A01 and A02 represent a homogeneous medium. Though in both the cases, optical depths τ of the layers are the same, in case A01, the layers are weakly scattering $\left(\omega_1=\omega_2=0.1\right)$, while in case A02, the two layers are strongly scattering $\left(\omega_1=\omega_2=0.9\right)$. A two-layer inhomogeneous medium is represented by cases A03 and A04. In this, the

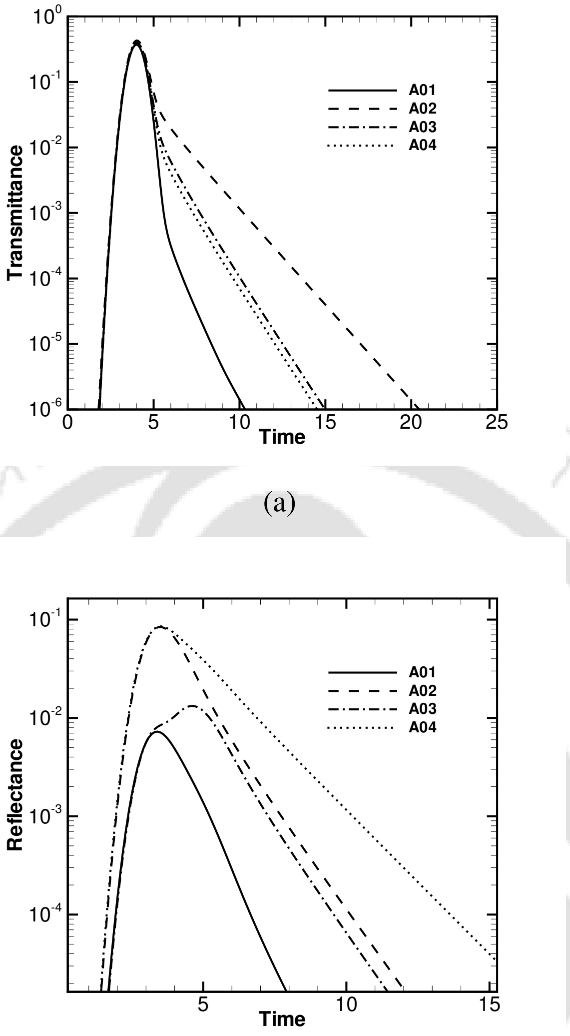

(a)

(b)

Figure 4.10: (a) Transmittance $q_t^*\left(Z,t^*\right)$ and (b) reflectance $q_r^*\left(0,t^*\right)$ signals for a two-layer medium.

Case	τ_1	τ_2	ω_1	ω_2
A01	0.5	0.5	0.1	0.1
A02	0.5	0.5	0.9	0.9
A03	0.5	0.5	0.1	0.9
A04	0.5	0.5	0.9	0.1

scattering albedos of the two layers are different. The weakly scattering layer is in contact with the boundary of incidence in case A03. Opposite is the situation in case A04.

Although in all the four cases, the total optical depth of the medium is the same, due to different scattering albedos of the layers, the time decay of the signals are different. The peak magnitudes of the transmittance $q_t^*\left(Z,t^*\right)$ signals are the same. Because of an overall weak scattering $\left(\omega_1=\omega_2=0.1\right)$ in case A01, the signal does not last long. However, in case A02, the medium is overall strongly scattering $\left(\omega_1=\omega_2=0.9\right)$ and thus the temporal duration is almost double than the case A01. Temporal spans of cases A03 and A04 are in between A01 and A02.

In Fig. 4.10b, the peak magnitudes of the reflectance signals for homogeneous medium case A01 and inhomogeneous medium case A03 are of the same order. The same is the situation with homogeneous medium case A02 and inhomogeneous medium case A04. In case A03, a minimum corresponding to the interface of the layers is observed. The temporal span of the reflectance signals for all the cases depend on the overall scattering nature of the medium.

All the four cases A11 to A14 in Fig. 4.11 have the same total optical depth $\left(\tau_1+\tau_2=11.0\right)$. Case A13 is for a medium consisting of layers that are swapped arrangements of the case A11. Similarly A14 is for a medium consisting of layers that are swapped arrangements of the case A12. In cases A11 and A14, the layers with high optical depth are strongly scattering, whereas, in cases A12 and A13, the layers with high optical depth are weakly scattering. Due to the presence of an optically very thick and strongly scattering layer adjacent to the south boundary in A11, the transmittance $q_t^*\left(Z,t^*\right)$ signals stay for a very long time. As seen in Fig. 4.11a, a minimum is observed in temporal profiles corresponding to cases A11 and A14. This is due to the sudden change of scattering albedo of the two layers. In cases A12 and A13, due to the overall weak scattering nature of the medium, the transmittance $q_t^*\left(Z,t^*\right)$ signals die out quickly. In case A14, the temporal decay is

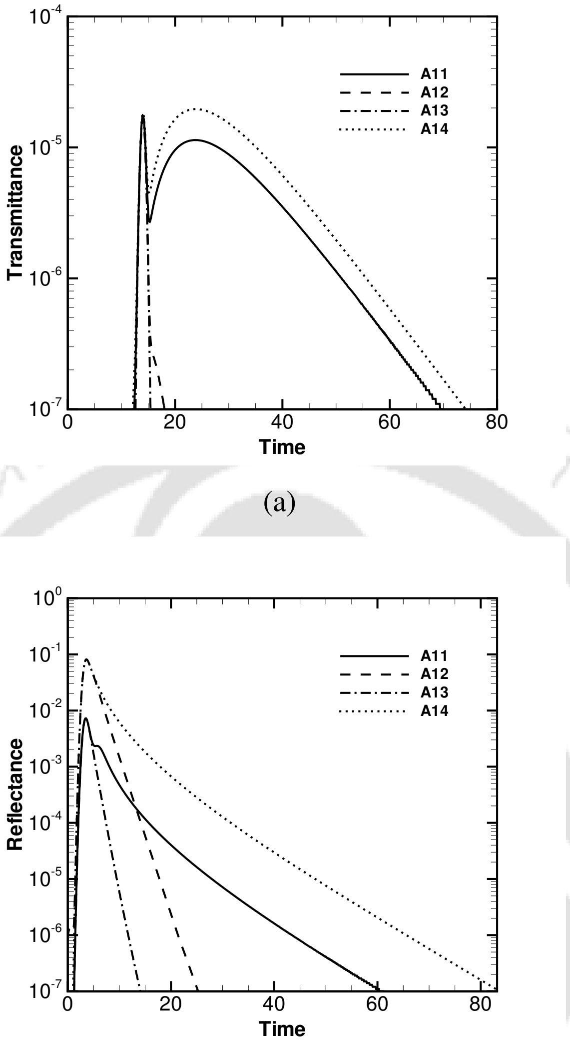

(a)

(b)

Figure 4.11: (a) Transmittance $q_t^*\left(Z,t^*\right)$ and (b) reflectance $q_r^*\left(0,t^*\right)$ signals for a two-layer medium.

Case	τ_1	τ_2	ω_1	ω_2
A11	1.0	10.0	0.1	0.9
A12	1.0	10.0	0.9	0.1
A13	10.0	1.0	0.1	0.9
A14	10.0	1.0	0.9	0.1

more gradual than the case A11. This is due to the presence of an optically very thick and strongly scattering layer close to the south boundary.

In Fig. 4.11b, the peak magnitudes of reflectance $q_r^*\left(0,t^*\right)$ signals for cases A11 and A13 are the same. Similarly, the peak magnitudes of cases A12 and A14 are the same. This is due to the reason that the scattering albedos of the two layers are the same while their optical depths are swapped. The relative magnitudes of the peak signals for cases A12 and A14 are one order magnitude higher than that for the cases A11 and A13. The temporal spans of the reflectance $q_r^*\left(0,t^*\right)$ signals for all the four cases have the same trend as that of the transmittance $q_t^*\left(Z,t^*\right)$ signals. However, in all the cases, the reflectance $q_r^*\left(0,t^*\right)$ signals stay for a longer duration.

In Fig. 4.12, cases A21 to A26 are in the descending order of the total $\left(\tau=\tau_1+\tau_2\right)$ optical thickness. In all the cases, the first layer is strongly $\left(\omega_1=0.9\right)$ scattering. Optical depth of layer 1 is the same in all cases $\left(\tau_1=1.0\right)$, while for the layer 2, it is decreasing from 10.0 to 0.25 from layers A21 to A26. Thus, the peak magnitudes of the transmittance $q_t^*\left(Z,t^*\right)$ signals are in ascending order from A21 to A26. Further, temporal spans of the signals are in ascending order from A21 to A26. Due to a wide variation of total optical depths from A21 to A26, the times of arrival of the transmittance $q_t^*\left(Z,t^*\right)$ signals at the south boundary are also different. In the case A21 in which the optical thickness is the maximum $\left(\tau_1+\tau_2=11.0\right)$, the signal appears at the south boundary later than any other case.

It is observed from Fig. 4.12b that for all the cases from A21 to A26, the peaks and the profiles of the reflectance $q_r^*\left(0,t^*\right)$ signals show no apparent difference. The reflectance $q_r^*\left(0,t^*\right)$ signals being mainly dependent on the nature of the medium adjacent to the boundary of incidence, a low absorbing and strongly scattering layer near the north boundary is the only influence on the peak magnitude. The second

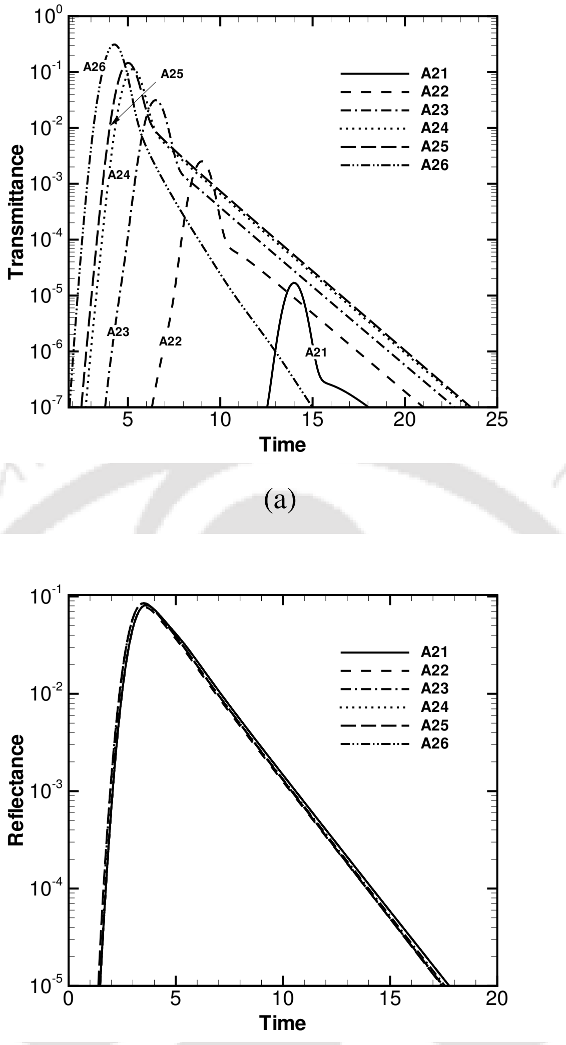

(a)

(b)

Figure 4.12: (a) Transmittance $q_t^*\left(Z,t^*\right)$ and (b) reflectance $q_r^*\left(0,t^*\right)$ signals for a two-layer medium.

Case	τ_1	τ_2	ω_1	ω_2
A21	1.0	10.0	0.9	0.1
A22	1.0	5.0	0.9	0.1
A23	1.0	2.5	0.9	0.1
A24	1	1.25	0.9	0.1
A25	1	1	0.9	0.1
A26	1.0	0.25	0.9	0.1

layer being weakly scattering in all the cases, no appreciable influence is visible either on the magnitude or the time span of the reflectance $q_r^*\left(0,t^*\right)$ signals.

Results in Figs. 4.13 and 4.14 are for a three-layer medium. The total optical depth of each case B01 to B04 is the same $\left(\tau_1+\tau_2+\tau_3=11.0\right)$. The three layers in cases B01 and B02 differ only in terms of scattering albedo. The same is the cases with layers in cases B03 and B04. The cases ordered as B04, B01, B02 and B03 represent descending nature of the overall scattering in the medium. For example, in case B04, the two layers adjacent to the boundaries are optically thick $\left(\tau_1=\tau_3=5.0\right)$ and these two layers are also strongly scattering $\left(\omega_1=\omega_3=0.9\right)$. In case B03, for the same total optical thickness, the two layers adjacent to the boundaries are optically thick $\left(\tau_1=\tau_3=5.0\right)$, but they are weakly scattering $\left(\omega_1=\omega_3=0.1\right)$.

The case B01 having an optically thick and strongly scattering middle layer is comparable with case A11 of Fig. 4.11a. Similarly, case B04 being strongly scattering for a high optical depth can be compared with case A14 of Fig. 4.11a. In the same way, B02 and B03 can be compared with A12 and A13 respectively in Fig. 4.11a.

In Fig. 4.14, in all the cases, scattering albedos of the three layers are the same. Further, layers 1 and 3 that are adjacent to the two boundaries and both of them are optically thin, and they have the same optical depth $\left(\tau_1=\tau_3=1.0\right)$. The middle layer in all the cases is weakly scattering $\left(\omega_2=0.1\right)$. Since the total optical depths of the cases B11 to B16 are of the decreasing order, the peak magnitudes of transmittance $q_t^*\left(Z,t^*\right)$ signals are accordingly increasing. In all these, the temporal trends have sudden change in slope. But the change in the slope decreases with a decrease in the optical depth. The middle layer is the most responsible for extinction and the layers 1 and 3 are the main contributors to scattering. Thus, in case B11, the signal undergoes a high absorption and weak scattering while traveling the interfaces of the layers. But this transport takes place in layers of widely varying optical properties. In case B16, the extinction nature of the medium remains the same throughout the three layers but the scattering behaviour is the same as B11.

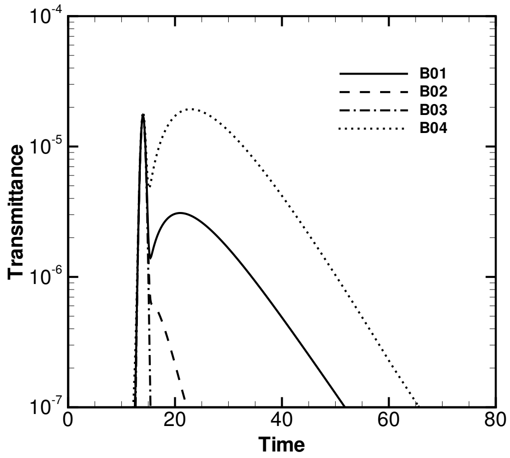

(a)

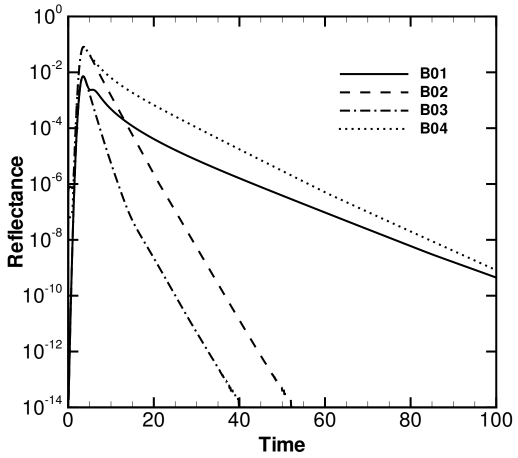

(b)

Figure 4.13: (a) Transmittance $q_t^*\left(Z,t^*\right)$ and (b) reflectance $q_r^*\left(0,t^*\right)$ signals for a three-layer medium.

Case	τ_1	τ_2	τ_3	ω_1	ω_2	ω_3
B01	1.0	9.0	1.0	0.1	0.9	0.1
B02	1.0	9.0	1.0	0.9	0.1	0.9
B03	5.0	1.0	5.0	0.1	0.9	0.1
B04	5.0	1.0	5.0	0.9	0.1	0.9

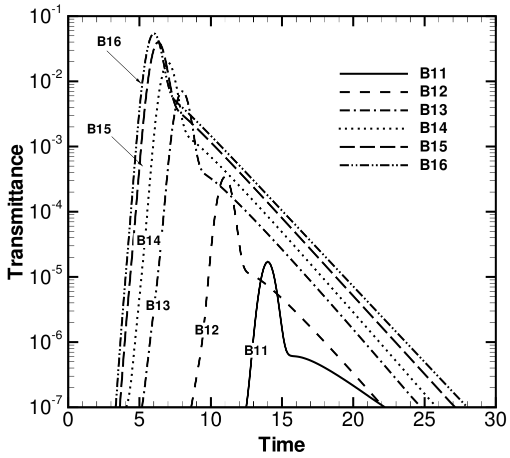

(a)

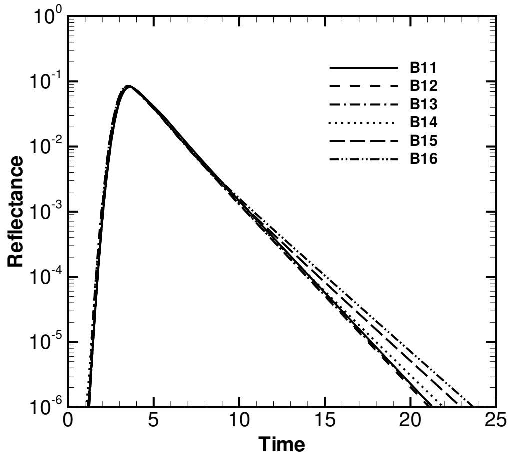

(b)

Figure 4.14: (a) Transmittance $q_t^*\left(Z,t^*\right)$ and (b) reflectance $q_r^*\left(0,t^*\right)$ signals for a three-layer medium.

Case	τ_1	τ_2	τ_3	ω_1	ω_2	ω_3
B11	1.0	9.0	1.0	0.9	0.1	0.9
B12	1.0	6.0	1.0	0.9	0.1	0.9
B13	1.0	3.0	1.0	0.9	0.1	0.9
B14	1.0	2.0	1.0	0.9	0.1	0.9
B15	1.0	1.3	1.0	0.9	0.1	0.9
B16	1.0	1.0	1.0	0.9	0.1	0.9

This difference in the optical properties between the cases B11 and B16, accounts for the difference in change in slopes between these two cases. In all the cases B11 to B16, the change in slope in transmittance $q_t^*\left(Z,t^*\right)$ signals is noticed to be gradually decreasing. The same reasoning can be attributed to this characteristic of the temporal trend.

In Fig. 4.14b, the peak magnitudes of the reflectance $q_r^*\left(0,t^*\right)$ signals in all the cases from B11 to B16 are equal. The time spans of the signals are found to be almost the same for all the cases. But with the decrease in the total optical depth, the time span of the signal increases slightly. The layer adjacent to the north boundary being the most contributing, the peak magnitudes of the reflectance $q_r^*\left(0,t^*\right)$ signals are the same in all the cases.

Effect of continuously varying scattering albedo ω on transmittance $q_t^*\left(Z,t^*\right)$ and reflectance $q_r^*\left(0,t^*\right)$ signals have been studied in Fig. 4.15. Following two cases have been considered:

C01: $$\tau = 5.0,\ \omega(z) = 0.175\left(\left(\frac{2z}{Z}\right)^2 + 1.0\right)$$

C02: $$\tau = 5.0,\ \omega(z) = 0.5\left(\left(\frac{2z}{Z}\right)\left(\frac{2z}{Z} - 2.0\right) + 2.0\right)$$

In both the cases C01 and C02, total optical depth of the medium is the same $(\tau = 5.0)$. However, in case C01, the scattering albedo of the medium is increasing from 0.175 at the north boundary to 0.875 at the south boundary. In case C02, scattering albedo profile is symmetric about the mid-plane $\left(\frac{z}{Z} = 0.5\right)$. It has the maximum value $(\omega = 1.0)$ at the two boundaries and the minimum $(\omega = 0.0)$ at the mid-plane. Since the mean scattering coefficient in the case C02 is higher than that of C01, considerable differences in transmittance $q_t^*\left(Z,t^*\right)$ and reflectance $q_r^*\left(0,t^*\right)$

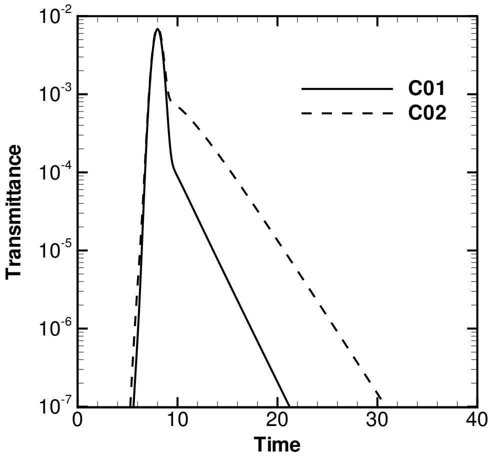

(a)

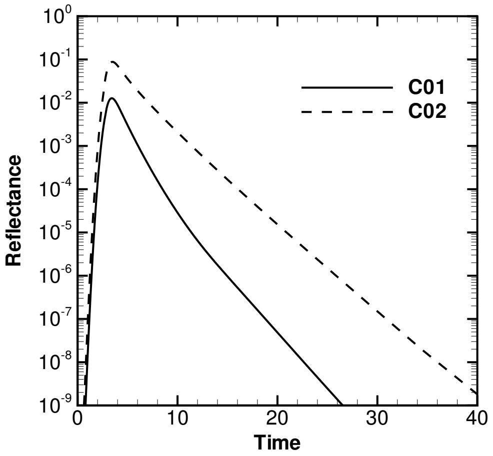

(b)

Figure 4.15: (a) Transmittance $q_t^*\left(Z,t^*\right)$ and (b) reflectance $q_r^*\left(0,t^*\right)$ signals for a medium of a scattering albedo profile;

$$\text{C01}: \tau = 5.0, \quad \omega(z) = 0.175\left(\left(\frac{2z}{Z}\right)^2 + 1.0\right)$$

$$\text{C02}: \ \tau = 5.0, \omega(z) = 0.5\left(\left(\frac{2z}{Z}\right)\left(\frac{2z}{Z} - 2.0\right) + 2.0\right).$$

signals are noticed. The peak magnitudes of transmittance $q_t^*\left(Z,t^*\right)$ signals being mainly dependent on the extinction nature of the medium, it remains the same in both the cases.

The time span of transmittance $q_t^*\left(Z,t^*\right)$ signals in case C02 is more than that of C01. The case C01 can be considered as a medium consisting of a large number of layers with increasing scattering albedos from the north to the south boundaries. The change in the slope of the transmittance $q_t^*\left(Z,t^*\right)$ signal occurs at the same time for both the cases C01 and C02. In the case of reflectance $q_r^*\left(0,t^*\right)$ as well, the magnitude and the temporal profiles of the signal are considerably different. This again can be attributed to the fact that the mean scattering coefficient of C02 is greater than C01. In case of C02, the layers of the medium lying adjacent to the north boundary are moderately scattering, while, in the case C01, they are very weakly scattering. Since the peak magnitude of the reflectance signals depends primarily upon the properties of the medium adjacent to the boundary of incidence, the reflectance $q_r^*\left(0,t^*\right)$ signals are one order higher in the case C02.

To have an idea of the computational time, the CPU times were recorded for all the combinations. Runs were taken on Xeon 300 dual processor 800 MHz computer. The CPU times for optically thin $(\tau = 1.0)$ to thick $(\tau = 11.0)$ situations ranged from 30 seconds to 218 seconds, respectively.

4.5 Summary

The radiative transport of a short-pulse radiation through an inhomogeneous participating medium was analyzed. The absorbing and scattering participating medium was considered to be consisting of 2-3 layers having different optical properties. Analysis was done for a single and a 4-pulse laser train of either a step or a Gaussian temporal profile. The temporal variations of transmittance and reflectance signals for different cases were studied. The peak magnitudes of the transmittance signals were found to depend mainly on the total optical depth of the medium. But the peak magnitudes of the reflectance signals were found to depend mostly on the scattering nature of the layer adjacent to the boundary of incidence.

The time spans of the transmittance signals were found to depend on both the optical depth and the scattering albedo. However, the time span of the reflectance signals were found to depend more on the scattering albedo of the layer adjacent to the north boundary. Depending upon whether the highly absorbing and/or highly scattering layer the radiation encounters first, different transmittance and reflectance signals were found. These signals depend strongly on the radiative properties of the layers and locations of the layer with respect to the boundary of incidence. For a given total optical depth of the medium, irrespective of the scattering albedo of the various layers, the magnitudes of the peaks of the transmittance signals were found to be of the same order. However, time span of the transmittance signals showed heavy dependence on the scattering albedos of the layers. On the other hand, for a given total optical depth of the medium, the peak magnitudes of the reflectance signals for both single pulse and 4-pulse train were found to depend on the scattering albedos of the layers. If the layer adjacent to the boundary of incidence is strongly scattering, the magnitudes of the reflectance were observed to be one order higher than the case in which the layer adjacent to the boundary was weak in scattering.

Having analyzed transport of a short-pulse radiation through an inhomogeneous medium in Chapters 3 and 4, in the following chapters, analyses are made for the thermal signatures obtained because of transport of short pulse radiation in a 2-D rectangular participating medium.

CHAPTER 5

Effects of the Incidence of a Short-Pulse Laser Wave on a 2-D Rectangular Homogeneous Participating Medium

---

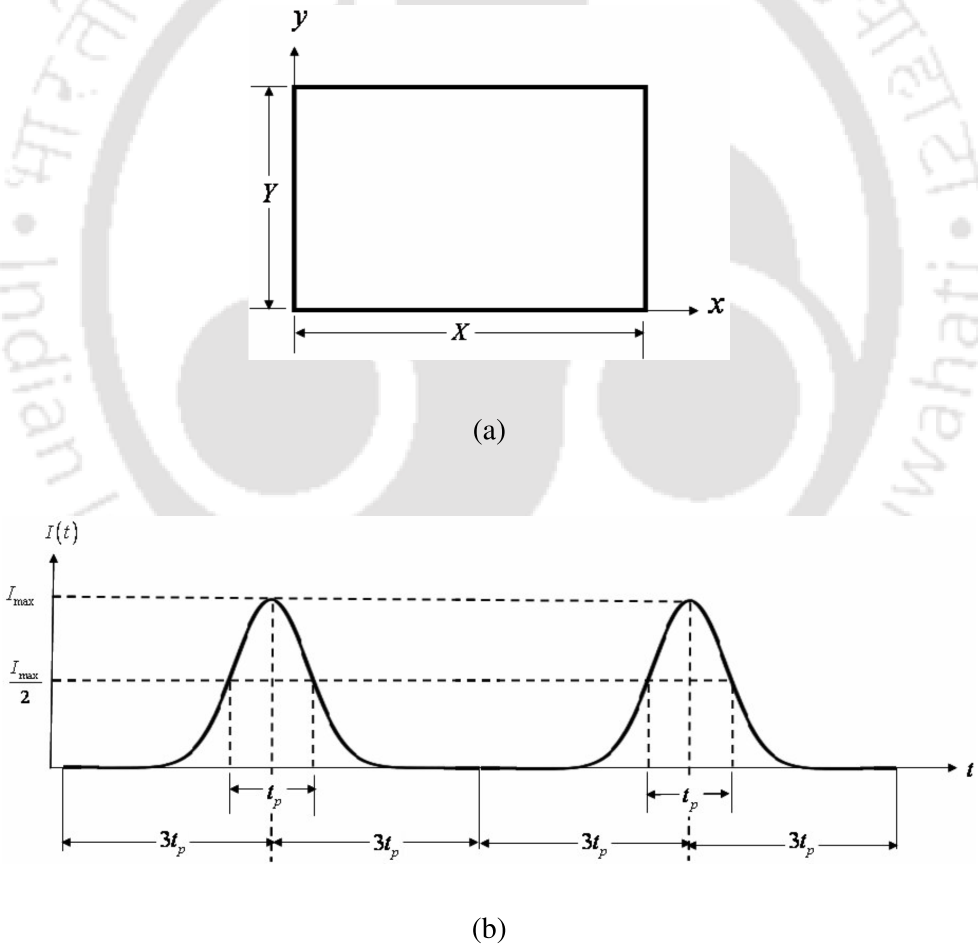

Figure (a) 2-D Geometry and the coordinate system under consideration (b) Gaussian 2- pulse train.

5.1 Introduction

A 2-D geometry represents a more realistic situation, but on the other hand, it brings additional mathematical complexities. As far as the 2-D rectangular geometries are concerned, so far no work has been focused on the study of the effect of multiple pulses on transmittance and reflectance signals. The work in Chapter 5 deals with the analysis of interaction of a short-pulse laser train in a 2-D rectangular homogeneous participating medium. One of the boundaries of the medium is subjected to either a diffuse or a collimated radiation. Temporal profile of the short-pulse radiation at the boundary of incidence is a step or a Gaussian function. Transmittance and reflectance signals are analyzed for the effects of the extinction coefficient and the scattering albedo. Heat flux distributions inside the medium are also studied. In this chapter, formulation specific to transport of a pulse radiation through a 2-D participating medium is also presented.

5.2 Problem

We consider the south boundary of the 2-D rectangular (Fig. 5.1a) absorbing, emitting and scattering participating medium subjected to a pulse radiation. As shown in Figs. 1b and 1c, the pulse radiation at the south boundary can either be diffuse or collimated. The temporal profile of the pulse radiation is a step function (Fig. 1d). The pulse train consists of 1-4 pulses. The pulse-width t_p of the incident radiation is $O\left(10^{-9}\text{s}\right)$. The half-time period of the pulse train is taken the same as the pulse width t_p (Fig. 1d).

5.3 Formulation

The radiation signals at any point in the medium including the boundaries are thus short-lived and their magnitudes are strong functions of time. In this situation, the radiative transfer equation (RTE) is given by

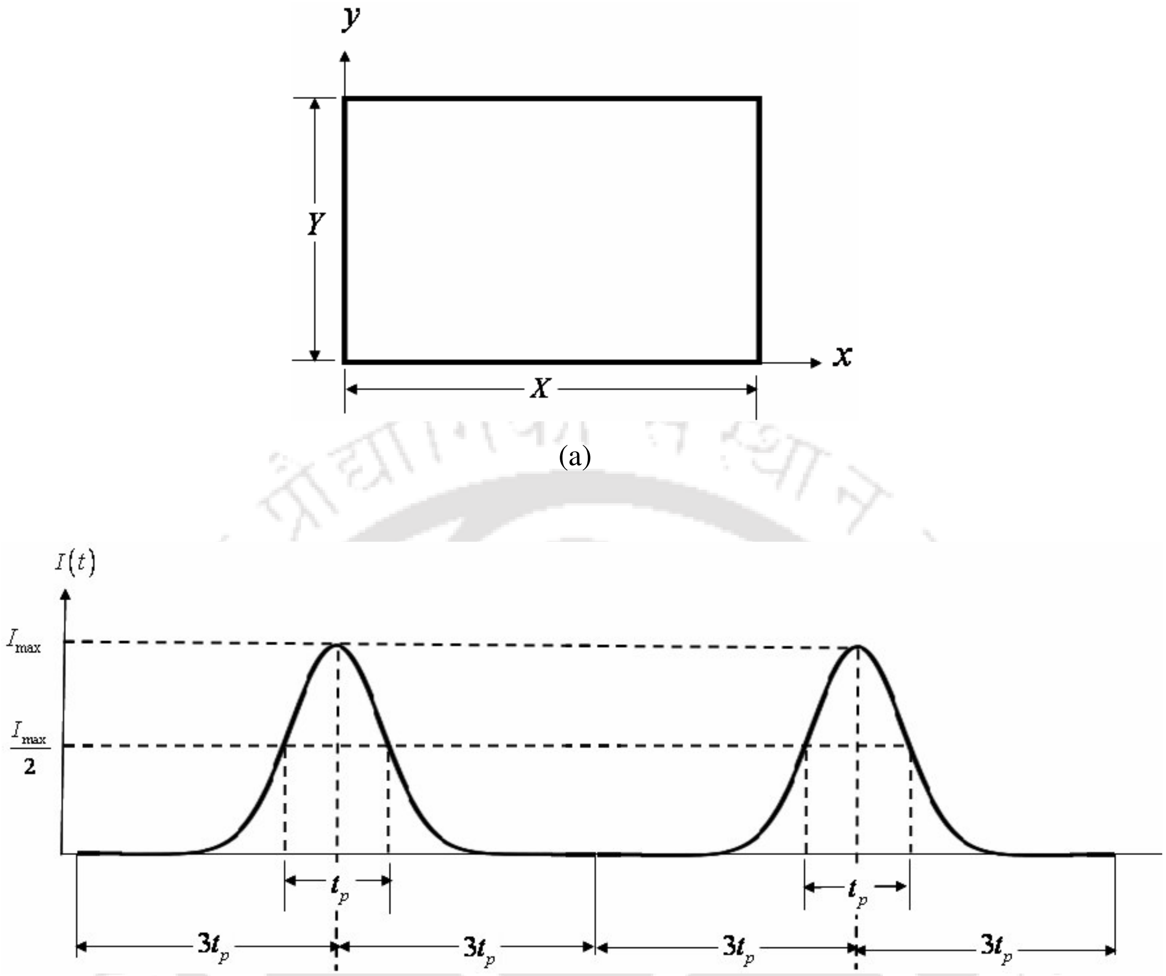

(a)

(b)

Figure 5.1: (a) 2-D Geometry and the coordinate system under consideration (b) Gaussian 2- pulse train.

$$\left(\frac{1}{c}\right)\frac{\partial I}{\partial t}+\frac{\partial I}{\partial s}=-\beta I+\kappa_a I_b+\frac{\sigma_s}{4\pi}\int_{4\pi} I\, p\left(\Omega,\Omega'\right)d\Omega' \tag{5.1}$$

where s is the geometric distance in the direction $\hat{s}=\left(\sin\theta\cos\phi\right)\hat{i}+\left(\sin\theta\sin\phi\right)\hat{j}+\cos\theta\hat{k}$, k_a is the absorption coefficient, β is the extinction coefficient, σ_s is the scattering coefficient and p is the scattering phase function. In the present work, we have considered the south boundary of the 2-D medium subjected to either a diffuse or a collimated radiation. In the following pages, we provide a formulation for the latter case which is more general. The change in the formulation for the diffuse radiation is highlighted wherever it is necessary.

The transport of the collimated radiation in the medium and its decay results in diffuse radiation. Thus within the medium, the intensity I is composed of two components, *viz.*, the collimated intensity I_c and the diffuse intensity I_d.

$$I = I_c + I_d \tag{5.2}$$

The change of the collimated intensity I_c in the medium is governed by

$$\left(\frac{1}{c}\right)\frac{\partial I_c}{\partial t} + \frac{\partial I_c}{\partial s} = -\beta I_c \tag{5.3}$$

From Eqs. (5.1) – (5.3), we get

$$\left(\frac{1}{c}\right)\frac{\partial I_d}{\partial t} + \frac{\partial I_d}{\partial s} = -\beta I_d + S_c + S_d = -\beta I_d + S_t \tag{5.4}$$

where S_c and S_d are the source terms resulting from the collimated and the diffuse components of radiation, respectively. In Eq. (4), $S_t = S_c + S_d$ is the total source term. The source term S_c resulting from the collimated radiation I_c, in terms of the incident radiation G_c and heat flux q_c, for a linear anisotropic phase function $p(\Omega,\Omega') = 1 + a\cos\theta\cos\theta'$ is given by

$$\begin{aligned} S_c(t) &= \frac{\sigma_s}{4\pi}\int_{\Omega'=0}^{4\pi} I_c(\Omega,t)\,p(\Omega,\Omega')\,d\Omega' \\ &= \frac{\sigma_s}{4\pi}\left[G_c(t) + a\cos\theta\, q_c(t)\right] \end{aligned} \tag{5.4a}$$

In Eq. (5.4a), G_c and q_c are given by

$$G_c(t) = I_c(\theta,\phi,t) \tag{5.5}$$

$$q_c(t) = I_c(\theta,\phi,t)\cos\theta \tag{5.6}$$

where

$$I_c(\theta,\phi,t) = I_{c,\max}(\theta,\phi,t)\exp(-\beta s_c) \times \begin{bmatrix} H\left\{\beta\left(ct-(N-1)T_p - s_c\right)\right\} \\ -H\left\{\beta\left(ct-(N-1)T_p-s_c\right)-\beta c t_p\right\}\end{bmatrix} \times\delta(\theta-\theta_c)\times\delta(\phi-\phi_c) \tag{5.7a}$$

where in Eq. (5.7a), $I_{c,\max}$ is the collimated intensity at the south boundary, s_c is the geometric distance in the direction (θ_c,ϕ_c) of the collimated radiation, δ is the Dirac-delta function and H is the Heaviside function. For a Gaussian pulse train the collimated intensity is given by

$$I_c(\theta,\phi,t) = I_{c,\max}(\theta,\phi,t)\exp(-\beta s_c)\times \exp\left[-4\left(\frac{t-\frac{s_c}{c}-t_c-(N-1)T_P}{t_p}\right)^2 \ln 2\right] \times\delta(\theta-\theta_c)\times\delta(\phi-\phi_c), \quad 0<t<2t_c \tag{5.7b}$$

If $t^* = \beta c t$ and $t_p^* = \beta c t_p$ are the dimensionless times, Eq. (5.7) can be written as

$$I_c\left(\theta,\phi,t^*\right) = I_{c,\max}\left(\theta,\phi,t^*\right)\exp(-\beta s_c) \times\left[H\left\{t^*-(N-1)T_p^*-\beta s_c\right\}-H\left\{t^*-\beta s_c-(N-1)T_p^*-t_p^*\right\}\right] \times\delta(\theta-\theta_c)\times\delta(\phi-\phi_c) \tag{5.8a}$$

$$I_c(\theta,\phi,t) = I_{c,\max}(\theta,\phi,t)\exp(-\beta s_c)\times \exp\left[-4\left(\frac{t^*-\beta s_c-t_c^*-(N-1)T_p^*}{t_p^*}\right)^2 \ln 2\right] \times\delta(\theta-\theta_c)\times\delta(\phi-\phi_c), \quad 0<t^*<2t_c^* \tag{5.8b}$$

where in Eq. (5.8), N is the number of pulses and $T_p^* = \beta c T_p$ is the dimensionless time period of the pulse train.

In Eq. (5.4), for the linear anisotropic phase function $p(\Omega,\Omega') = 1 + a\cos\theta\cos\theta'$, the source term S_d in terms of incident radiation G_d and heat flux q_d resulting from the diffuse radiation I_d is given by

$$S_d\left(t^*\right) = \kappa_a I_b\left(t^*\right) + \frac{\sigma_s}{4\pi}\left[G_d\left(t^*\right) + a\cos\theta\, q_d\left(t^*\right)\right] \tag{5.9}$$

In Eq. (5.9), G_d and q_d are given by and numerically computed from [35]

$$G_d\left(t^*\right) \approx \sum_{l=1}^{M_\phi}\sum_{k=1}^{M_\theta} I_d(\theta_k^m,\phi_l^m,t^*)\,2\sin\theta_k^m \sin\left(\frac{\Delta\theta_k^m}{2}\right)\Delta\phi_l^m \tag{5.10}$$

$$q_d\left(t^*\right) \approx \sum_{l=1}^{M_\phi}\sum_{k=1}^{M_\theta} I_d(\theta_k,\phi_l,t^*)\sin\theta_k^m\ \cos\theta_k^m\ \sin\Delta\theta_k^m\ \Delta\phi_l^m \tag{5.11}$$

where M_θ and M_ϕ are the number of discrete points considered over the complete span of the polar angle $\left(0\le\theta\le\pi\right)$ and azimuthal angle $\left(0\le\phi\le 2\pi\right)$, respectively. Therefore, $M_\theta\times M_\phi$ constitute the number of discrete directions in which intensities are considered at any point.

For a boundary having temperature T_w and emissivity ε_w, the boundary intensity $I_d\left(r_w,t^*\right)$ is given by and computed from

$$I_d\left(r_w,t^*\right)\approx\frac{\varepsilon_w\sigma T_w^4}{\pi}+\left(\frac{1-\varepsilon_w}{\pi}\right)\sum_{l=1}^{M_\phi}\sum_{k=1}^{M_\theta/2}\left[I_{d,w}\left(\theta_k^m,\phi_l^m,t^*\right)+I_{c,w}\left(\theta_k^m,\phi_l^m,t^*\right)\right] \times\sin\theta_k^m\cos\theta_k^m\sin\Delta\theta_k^m\Delta\phi_l^m \tag{5.13}$$

where in Eq. (5.13), the first and the second terms represent emitted and reflected components of the boundary intensity, respectively.

In terms of non-dimensional time t^*, the RTE given in Eq. (5.4) for a discrete direction $\left(\theta_k^m,\phi_l^m\right)$ with index m is now written as

$$\beta\frac{\partial I_d^m}{\partial t^*}+\frac{\partial I_d^m}{\partial s^m}+\beta I_d^m=S_t^m \tag{5.14}$$

Using backward differencing scheme in time, Eq. (5.14) becomes

$$\beta\frac{I_d^m\left(t^*\right)-I_d^m\left(t^*-\Delta t^*\right)}{\Delta t^*}+\frac{\partial I_d^m\left(t^*\right)}{\partial s^m}+\beta I_d^m\left(t^*\right)=S_t^m\left(t^*\right) \tag{5.15}$$

Equation (5.15) is written in simplified form as

$$B\frac{\partial I_d^m\left(t^*\right)}{\partial s^m}+\beta I_d^m\left(t^*\right)=BS_t^m\left(t^*\right)+CI_d^m\left(t^*-\Delta t^*\right) \tag{5.16}$$

where $B=\dfrac{\Delta t^*}{(1+\Delta t^*)}$ and $C=\dfrac{\beta}{1+\Delta t^*}$.

Below the formulation and methodology to solve Eq. (5.16) using the FVM is presented briefly.

Resolving Eq. (5.16) in $x-$ and $y-$ Cartesian coordinate directions and integrating it over the elemental solid angle $\Delta\Omega^m$, we get

$$B\left[\frac{\partial I_d^m\left(t^*\right)}{\partial x}D_x^m+\frac{\partial I_d^m\left(t^*\right)}{\partial y}D_y^m\right]+\beta I_d^m\left(t^*\right)=\left[BS_t^m\left(t^*\right)+CI_d^m\left(t^*-\Delta t^*\right)\right]\Delta\Omega^m \tag{5.17}$$

When the outward normal $\hat{n}$ is pointing towards one of the positive coordinate directions, D_x^m and D_y^m are given by Mishra and Roy [103]

$$D_x^m=\cos\phi^m\sin\left(\frac{\Delta\phi^m}{2}\right)\left[\Delta\theta^m-\cos 2\theta^m\sin\left(\Delta\theta^m\right)\right] \tag{5.18}$$

$$D_y^m=\sin\phi^m\sin\left(\frac{\Delta\phi^m}{2}\right)\left[\Delta\theta^m-\cos 2\theta^m\sin\left(\Delta\theta^m\right)\right] \tag{5.19}$$

For $\hat{n}$ pointing towards the negative coordinate directions, signs of D_x^m and D_y^m are negative. In Eq. (5.17), $\Delta\Omega^m$ is given by

$$\Delta\Omega^m=2\sin\theta^m\sin\left(\frac{\Delta\theta^m}{2}\right)\Delta\phi^m \tag{5.20}$$

Integrating Eq. (18) over the 2-D control volume $\left(dV=dx\times dy\times 1\right)$, we get

$$\begin{aligned}\left[I_{d,E}^m\left(t^*\right)-I_{d,W}^m\left(t^*\right)\right]A_xD_x^m+\left[I_{d,N}^m\left(t^*\right)-I_{d,S}^m\left(t^*\right)\right]A_yD_y^m\\=\left[-\frac{\beta}{B}I_{d,P}^m\left(t^*\right)+S_{t,P}^m+\frac{C}{B}I_{d,P}^m\left(t^*-\Delta t^*\right)\right]dV\Delta\Omega^m\end{aligned} \tag{5.21}$$

where A_x and A_y are the areas of the x- and y-faces of the 2-D control volume, respectively. In Eq. (5.21), I with suffixes E, W, N and S designate east, west, north and south control surface average intensities, respectively. On the right-hand side of Eq. (14), I_P^m and S_P^m are the volume averaged intensity and source term at the cell centre P, respectively.

To reduce the number of unknowns in Eq. (5.21), in a given direction, in a control volume, a relationship is sought among surface average intensities and the volume averaged intensity. The common practice in the FVM is to use a diamond differencing scheme. For 2-D control volumes considered in the present problem, thus we have:

$$I_{d,P}^{m} = \frac{I_{d,N}^{m} + I_{d,S}^{m}}{2} = \frac{I_{d,E}^{m} + I_{d,W}^{m}}{2} \tag{5.22}$$

From Eqs. (5.21) and (5.22), a general expression of $I_{d,P}^{m}(t^{*})$ in terms of known surface average intensities and source terms is written as [35]

$$I_{d,P}^{m}(t^{*}) = \frac{\left[\begin{array}{r} \left|D_x^m\right| A_x I_{d,x_i}^{m}(t^{*}) + \left|D_y^m\right| A_y I_{d,y_i}^{m}(t^{*}) \\ + \left(\dfrac{V\Delta\Omega^m}{2}\right) S_{t,P}^{m}(t^{*}) + \left(\dfrac{CV\Delta\Omega^m}{2B}\right) I_{d,P}^{m}(t^{*} - \Delta t^{*}) \end{array}\right]}{\left|D_x^m\right| A_x + \left|D_y^m\right| A_y + \left(\dfrac{\beta V\Delta\Omega^m}{2B}\right)} \tag{5.23}$$

where in Eq. (5.23), x_i and y_i suffixes over I_d^m are for the intensities entering the control volume through x-, and y-faces, respectively.

Temporal signals at the boundary of incidence and the opposite boundary termed as reflectance $q_r^{*}\left(\frac{x}{X}, 0, t^{*}\right)$ and transmittance $q_t^{*}\left(\frac{x}{X}, 1, t^{*}\right)$, respectively. As described elsewhere before in this thesis, these are the two important signals normally analyzed and they are the radiative fluxes at the respective boundaries because of the radiative contributions from the medium. Further, heat flux $q^{*}\left(\frac{x}{X}, \frac{y}{Y}, t^{*}\right)$ distributions inside the medium also provide some useful information. For any dimensionless time t^{*}, in non-dimensional form, they are defined as

$$\text{Reflectance: } q_r^{*}\left(\frac{x}{X}, 0, t^{*}\right) = \frac{q_d\left(\frac{x}{X}, 0, t^{*}\right)}{q_{in}\left(\frac{x}{X}, 0, t^{*}\right)} \tag{5.24}$$

$$\text{Transmittance: } q_t^{*}\left(\frac{x}{X}, 1, t^{*}\right) = \frac{q_c\left(\frac{x}{X}, 1, t^{*}\right) + q_d\left(\frac{x}{X}, 1, t^{*}\right)}{q_{in}\left(\frac{x}{X}, 0, t^{*}\right)} \tag{5.25}$$

Heat flux: $$q^*\left(\frac{x}{X},\frac{y}{Y},t^*\right)=\frac{q_c\left(\frac{x}{X},\frac{y}{Y},t^*\right)+q_d\left(\frac{x}{X},\frac{y}{Y},t^*\right)}{q_{in}\left(\frac{x}{X},0,t^*\right)} \tag{5.26}$$

where $q_{in}\left(\frac{x}{X},0,t^*\right)$ is the flux input to the medium at the boundary of incidence (south boundary).

5.4 Results and Discussion – Step pulse train

For grid independent situation, 50×50 equal size control volumes were used, and a maximum of 120 directions covering the 4π solid angle were found enough for the ray-independent solutions. 1000 divisions of the total time t^* domain were found sufficient for marching in time. At every time step, the iteration was set to $\left|S^m_{t,\text{old},P}-S^m_{t,\text{new},P}\right|\leq1.0\times10^{-7}$.

5.4.1 Validation of results

First we validate the results of the present work for a single pulse with those available in the literature. For a square medium $\left(\frac{X}{Y}=1\right)$ subjected to a single collimated radiation (laser) pulse, Figs. 5.2a and 5.2b show comparison of the present results with those of Sakami et al. [100] obtained using the discrete ordinates method with high order upwind piecewise parabolic interpolation scheme. In Fig. 5.2c and 5.2d, transmittance results of the present 2-D code have been compared with those from Mishra et al. [97] and exact results [1] for the 1-D case. In the 2-D case, these results are computed at the centre $(0.5,1.0)$ of the north boundary. To compare the results of the 2-D code with that for 1-D case with collimated radiation, for results in Fig. 2c, the aspect ratio $\frac{X}{Y}=100$ was considered and the domain was divided into 500×10 control volumes. With diffuse radiation (Fig. 5.2d), the aspect ratio $\frac{X}{Y}=10$ was

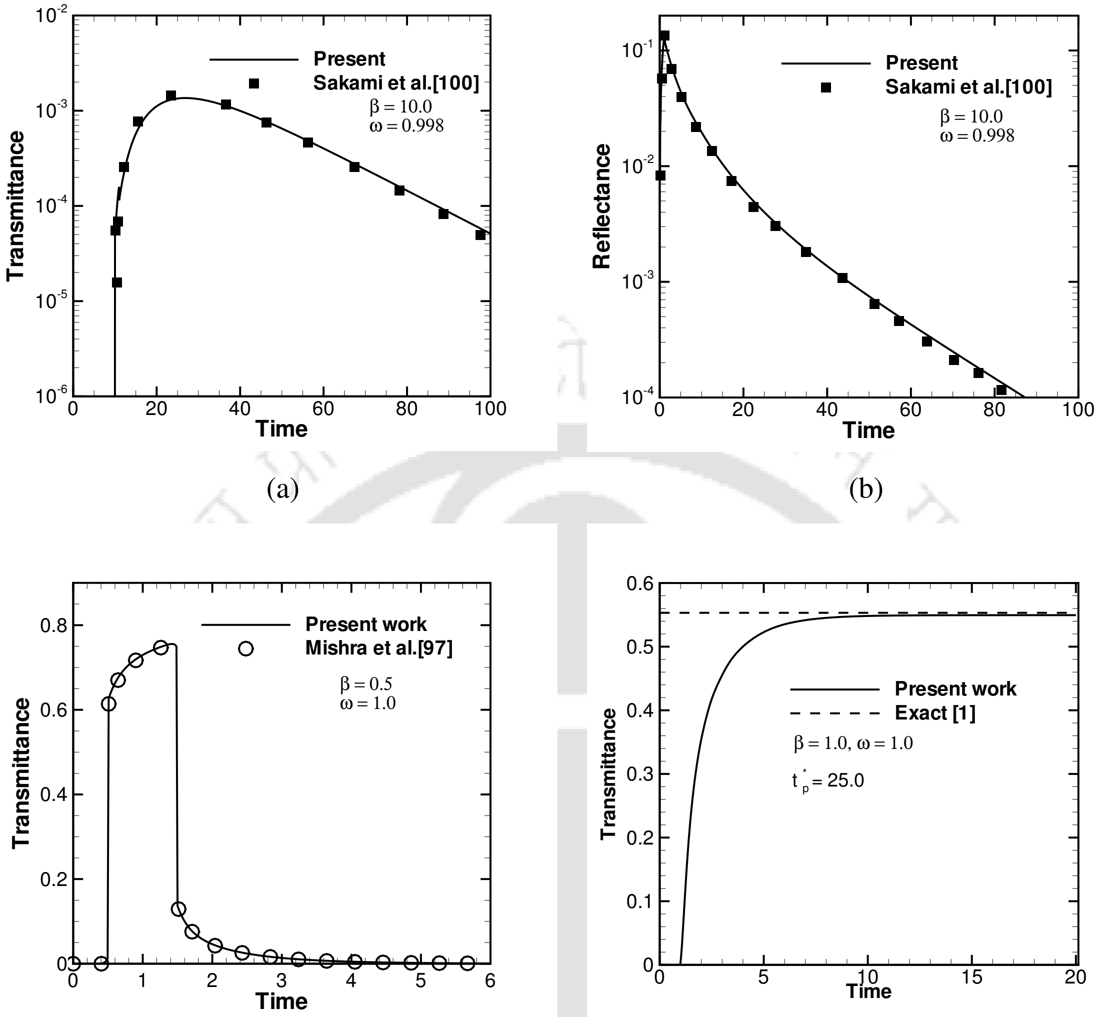

(a) (b)

(c) (d)

Figure 5.2: Comparison of (a) transmittance $q_t^*\left(0.5,1.0,t^*\right)$ for $\frac{X}{Y}=1$, (b) reflectance $q_r^*\left(0.5,0.0,t^*\right)$ for $\frac{X}{Y}=1$ and (c) transmittance $q_t^*\left(0.5,1.0,t^*\right)$ for $\frac{X}{Y}=100$ signals in a 2-D medium with a collimated pulse (d) transmittance $q_t^*\left(0.5,1.0,t^*\right)$ for $\frac{X}{Y}=10$ signals in a 2-D medium with a diffuse pulse.

found sufficient. A higher value of $\frac{X}{Y}$ in case of collimated radiation is attributed to strong directional dependency. It is seen from Figs. 5.2a-5.2d that in all the case, results of the present work with single pulse are in good agreement with those available in the literature. It is to be noted that in Fig. 5.2d, pulse-width of the single-pulse has been taken as $t_p^* = 25$. For this large pulse width and with aspect ratio $\frac{X}{Y} = 10$, result of the 2-D transient code were found to match with the 1-D steady-state results.

5.4.2 Results with 1-4 pulse train

In the following pages, we provide results for a square medium $\left(\frac{X}{Y} = 1\right)$ with its south boundary subjected to either diffuse or collimated pulses. The pulse train is considered consisting of 1-4 pulses.

With the south boundary subjected to a diffuse pulse train, Figs. 5.3a-f show transmittance $q_t^*\left(0.5, 1.0, t^*\right)$ and reflectance $q_r^*\left(0.5, 1.0, t^*\right)$ at the middle of the south and the north boundaries, respectively. With scattering albedo $\omega = 1.0$, for 1-4 pulses, these results are shown for three values of the extinction coefficient β. It is seen from Figs. 5.3a-c that the magnitudes of the signal peaks decrease with increasing β. It is also observed that troughs that are present in 2-4 pulse trains in Fig. 5.3a for $\beta = 1.0$, vanish for higher values of β (Figs. 5.3b and 5.3c). Observations of Figs. 5.3a-c show that the peaks of different pulse-trains are more aligned for higher β, and temporal spreads in the signals are more spread for higher β. A distinct difference in the peak magnitudes of the signals for multiple pulses are observed for $\beta = 5.0$ and 10.0. Further, since radiation takes $t^* = \beta ct = \beta Y$ to reach the opposite (north boundary), with $Y = 1.0$, in Figs. 5.3a-c, the transmittance signals start appearing at $t^* = \beta$.

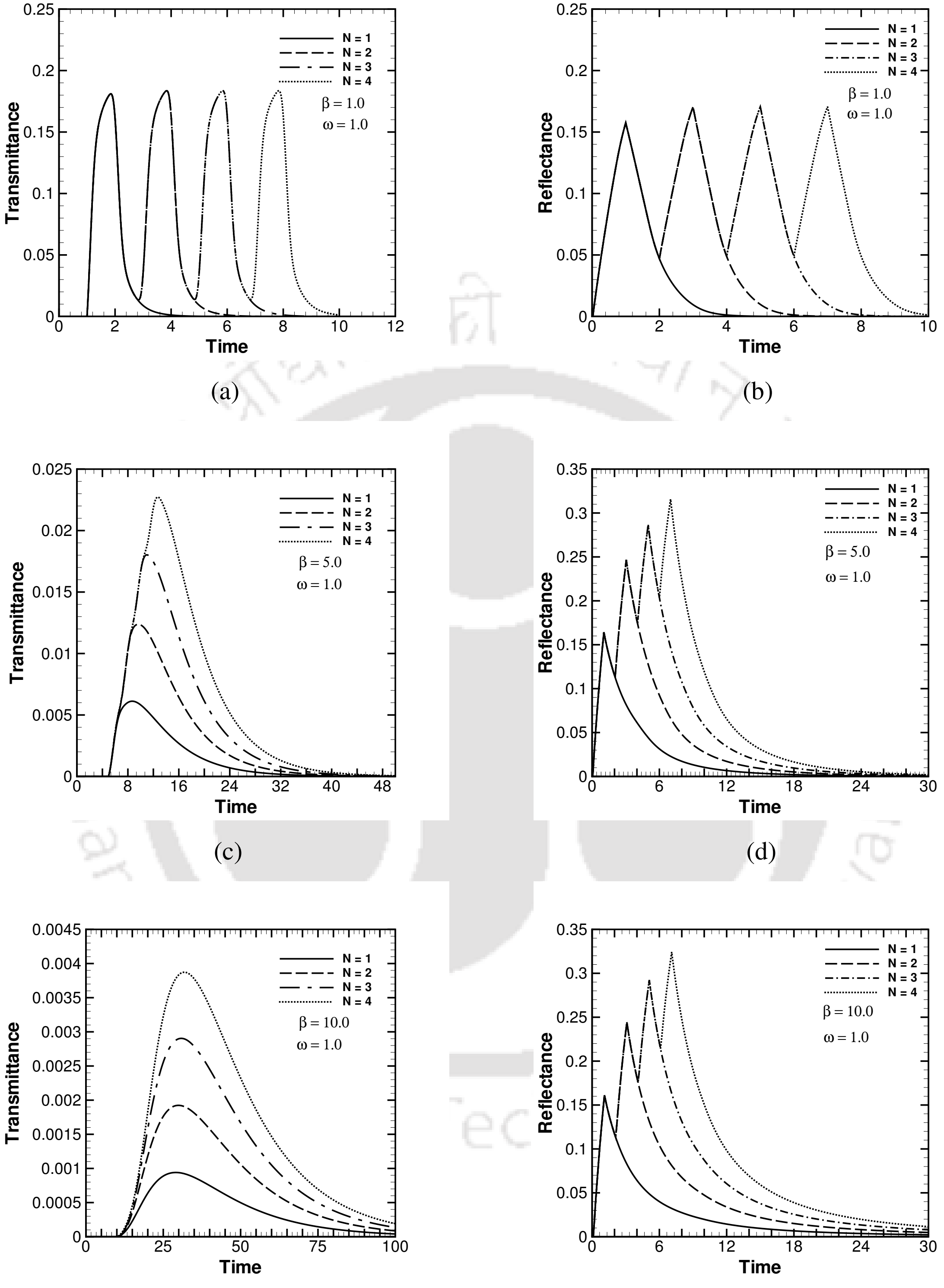

(a) (b)

(c) (d)

(e) (f)

Figure 5.3: Transmittance $q_t^*\left(0.5,1.0,t^*\right)$ signals and reflectance $q_r^*\left(0.5,0.0,t^*\right)$ signals for 1-4 pulses The south boundary subjected to diffuse radiation.

For the corresponding cases, reflectance $q_r^*\left(0.5,0.0,t^*\right)$ results are shown in Figs. 5.3d-f. Unlike transmittance $q_t^*\left(0.5,1.0,t^*\right)$, the peak magnitudes of the reflectance $q_r^*\left(0.5,0.0,t^*\right)$ signals increase with increase in β, and also different crests and troughs are distinct for all values of β. Like transmittance $q_t^*\left(0.5,1.0,t^*\right)$ (Fig. 5.3a), the reflectance $q_r^*\left(0.5,0.0,t^*\right)$ signals (Fig. 5.3d) do not last long for $\beta = 1.0$, and for $\beta = 5.0$ and 10.0, they last longer (Figs. 5.3e and 5.3f). However, their temporal spans are shorter than the transmittance $q_t^*\left(0.5,1.0,t^*\right)$ signals (Figs. 5.3b and 5.3c). Since the south boundary starts getting radiation the time the radiation enters the medium, the reflectance signals are seen to start with $t^* = 0.0$ (Figs. 5.3d-f).

Transmittance $q_t^*\left(0.5,1.0,t^*\right)$ and reflectance $q_r^*\left(0.5,0.0,t^*\right)$ results with collimated pulses are shown in Figs. 5.4a-f. With scattering albedo $\omega = 1.0$, for 1-4 pulses, these results are shown for three values of the extinction coefficient $\beta = 1.0, 5.0$ and 10.0. For $\beta = 1.0$, trends of the two signals (Figs. 5.4a and 5.4d) are similar to that of diffuse pulse train (Figs. 5.3a and 5.3d). For 1-3 pulses, the transmittance signals with $\beta = 5.0$ have a distinct peak and a sharp decline leading to another well distributed maxima (Fig. 5.4c). The sharp peak is attributed to the arrival of the collimated component of the incident radiation much earlier than the diffuse radiations from the medium. Though the troughs in the curves occur at the same time for 1-4 pulses (Fig. 5.4b), a large difference in their magnitude is observed. With $\beta = 10.0$ (Fig. 5.4c), unlike $\beta = 5.0$ (Fig. 5.4b), distinct crests and troughs at an early stage are not prominent. Like diffuse radiation (Fig. 5.3c), for $\beta = 10.0$, the signals are characterized by a single crest for any number of pulses. The reflectance $q_r^*\left(0.5,0.0,t^*\right)$ results with $\beta = 1.0, 5.0$ and 10.0 for 1-4 pulses are shown in Figs.5. 4d-f, respectively. Profiles of these signals are the same as that for the diffuse pulse train (Figs. 5.3d-f) except for $\beta = 5.0$ and 10.0, narrow crests and troughs are visible for a single and a 2-pulse train.

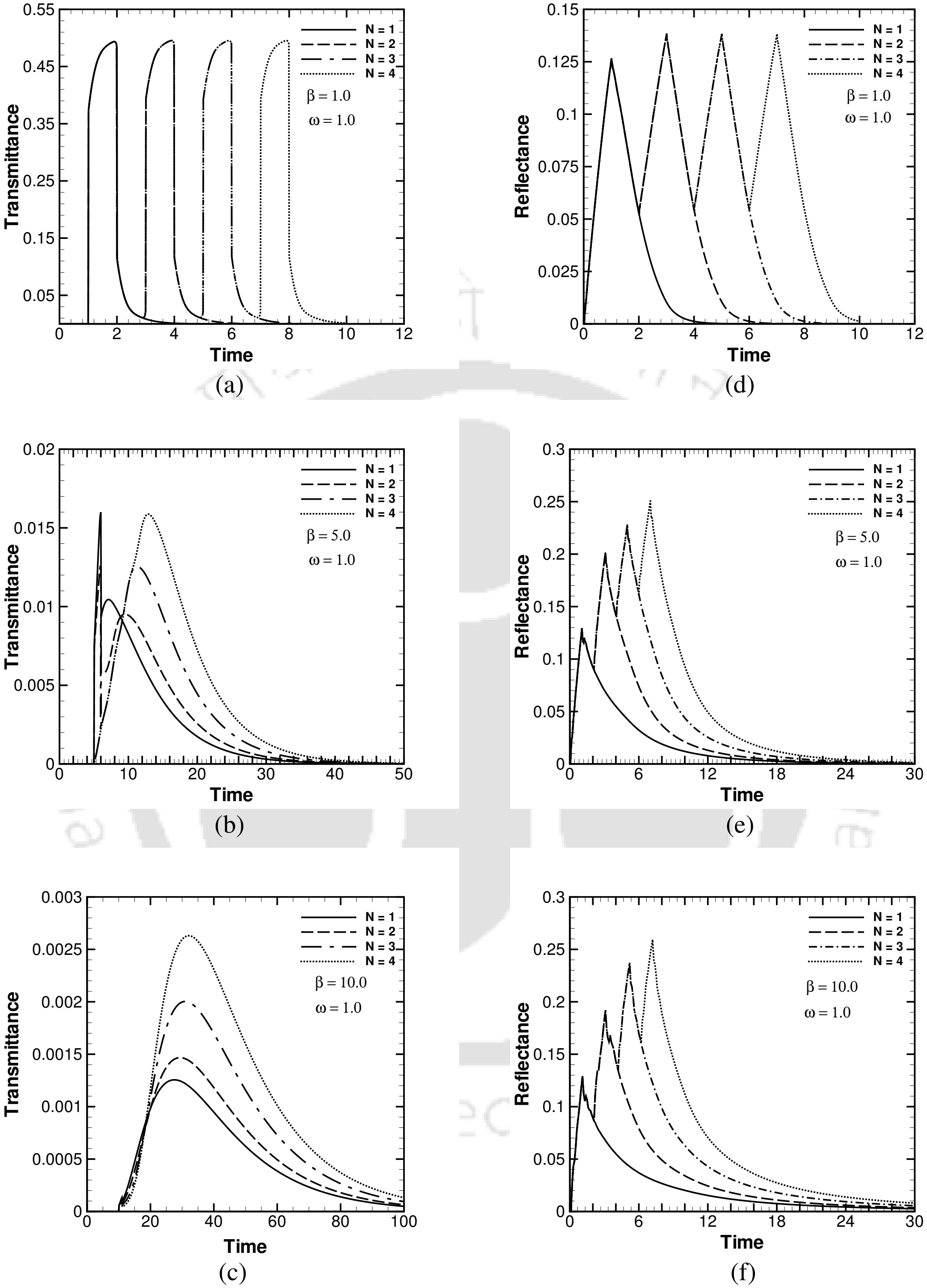

Figure 5.4: Transmittance $q_t^*\left(0.5,1.0,t^*\right)$ signals and reflectance $q_r^*\left(0.5,0.0,t^*\right)$ signals for 1-4 pulses for three different values of extinction coefficient β. The south boundary subjected to collimated radiation.

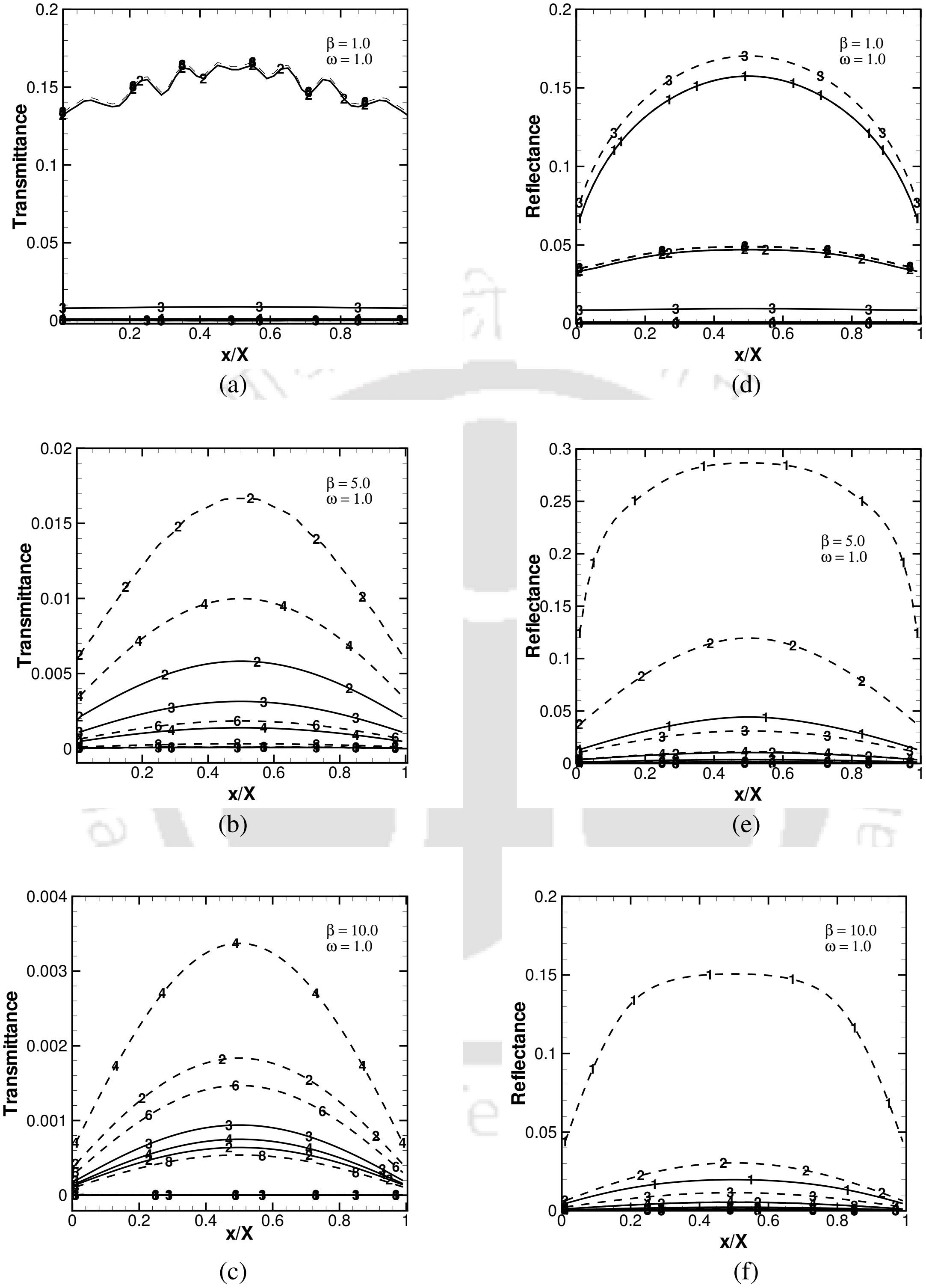

Figure 5.5: Time evolution of the distribution of transmittance $q_t^*\left(x/X,1.0,t^*\right)$ and reflectance $q_r^*\left(x/X,0.0,t^*\right)$ signals along the boundaries. The digit n on any curve indicates the distribution of the signal at $n\times100^{\text{th}}$ time step. Solid and dash lines are results for 1- and 4-pulse diffuse radiation.

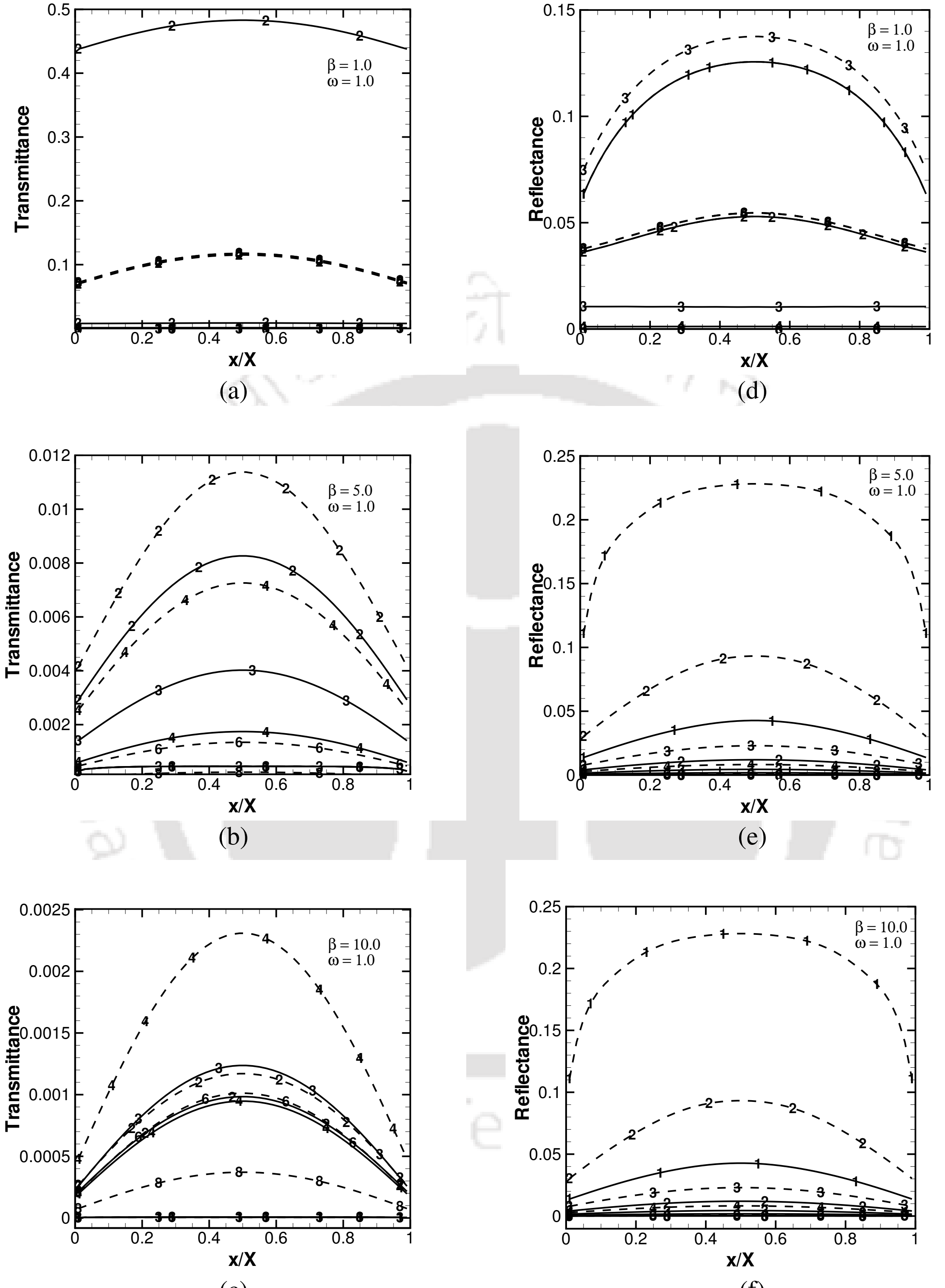

(a) (d)

(b) (e)

(c) (f)

Figure 5.6: Time evolution of the distribution of transmittance $q_t^*\left(x/X, 1.0, t^*\right)$ and reflectance $q_r^*\left(x/X, 0.0, t^*\right)$ signals along the boundaries. The digit n on any curve indicates the distribution of the signal at $n \times 100^{\text{th}}$ time step. Solid and dash lines are results for 1- and 4-pulse collimated radiation.

In Figs. 5.5 and 5.6, for a single and a 4-pulse train, distributions of transmittance $q_t^*\left(\frac{x}{X},1.0,t^*\right)$ and reflectance $q_r^*\left(\frac{x}{X},0.0,t^*\right)$ results along the boundaries, have been plotted for diffuse and collimated radiations, respectively. With $\omega = 1.0$, these distributions are shown for the extinction coefficient $\beta = 1.0, 5.0$ and 10.0. For a given β, these distributions are plotted at 6 time levels, viz. $\frac{t^*}{\Delta t^*} = 100, 200, 300, 400, 600$ and 800.

It is seen from Figs. 5.5a and 5.6a that when the medium is less participating $(\beta = 1.0)$, the transmittance $q_t^*\left(\frac{x}{X},1.0,t^*\right)$ results for a single and a 4-pulse train almost coincide with each other at all times. However, the reflectance $q_r^*\left(\frac{x}{X},0.0,t^*\right)$ signals are more distinct at almost all times for a single and a 4-pulse train. For $\beta = 5.0$ and 10.0, the transmittance $q_t^*\left(\frac{x}{X},1.0,t^*\right)$ signals at all time levels are well separated. However, it is observed that for any value of β, at an early stage $\frac{t^*}{\Delta t^*} = 100$ since the magnitudes of the signals are very small, they are not noticeable. This can be verified from Figs. 5.3a-c, and 5.4a-c, where the time evolution of the transmittance signals in the middle of the north boundary $(0.5, 1.0)$ have been plotted.

It is observed from Figs. 5.5c and 5.6c that for $\beta = 1.0$ at $\frac{t^*}{\Delta t^*} = 100$, for both diffuse and collimated pulses, profiles of the reflectance $q_r^*\left(\frac{x}{X},0.0,t^*\right)$ signals coincide for both a single and a 4-pulse train. However, at $\frac{t^*}{\Delta t^*} = 300$, the $q_r^*\left(\frac{x}{X},0.0,t^*\right)$ is considerably higher for a 4-pulse train. At later times, they are close with each other. For $\beta = 5.0$ and 10.0, (Figs. 5.5b, 5.5c, 5.6e and 5.6f), profiles of $q_r^*\left(\frac{x}{X},0.0,t^*\right)$ at the first two time levels are far too distinct for a 4-pulse train. However, for a single-pulse, their magnitudes are less. At later time levels, for both a single-pulse and a 4-pulse train, results are close to each other.

Figures 5.7-5.10 provide heat flux contours in the medium for a single and a 4-pulse train. In each of these figures, the contours are plotted at three time levels, viz $\frac{t^*}{\Delta t^*} = 50, 200$ and 800. In these figures, results for a single-pulse are given in Figs. (5.7-5.10)a-c, whereas the same for a 4-pulse train are given in Figs. (5.7-5.10)d-f. For $\omega = 1.0$ and $\beta = 1.0$, heat flux contours are given in Figs. 5.7 and 5.8 for diffuse and collimated pulses, respectively. In Figs. 5.9 and 5.10, heat flux contours are presented for diffuse and collimated pulses, respectively for $\omega = 1.0$ and $\beta = 10.0$.

From Figs. 5.7a and 5.7d it is observed that for a single-pulse, at $\frac{t^*}{\Delta t^*} = 50$, the negative heat flux $q^*\left(\frac{x}{X}, \frac{y}{Y}, t^*\right)$ appears near the south boundary. It is to be noted that the negative heat flux contributes towards the reflectance $q_r^*\left(\frac{x}{X}, 0.0, t^*\right)$ signals. For a 4-pulse train, from Fig. 5.7d it is observed that at $\frac{t^*}{\Delta t^*} = 50$, like Fig. 5.7a, for a single-pulse, the radiation has not reached the north boundary, but the positive heat flux towards the north boundary is more prominent.

At $\frac{t^*}{\Delta t^*} = 200$, it is observed from Figs. 5.7b and 5.7c, and 5.7e and 5.7f that both negative and positive heat fluxes remain in the medium for a single and a 4-pulse train. The region of negative heat flux is observed to be more for a single-pulse. Further it is observed that the peak magnitudes of the heat flux are still found inside the medium in the neighborhood of the north boundary. But as time progresses $\left(\frac{t^*}{\Delta t^*} = 800\right)$, the maximum magnitude of the heat flux is found to be concentrated around the middle of the south and the north boundaries. This observation is substantiated with Figs. 5.5a and 5.5d.

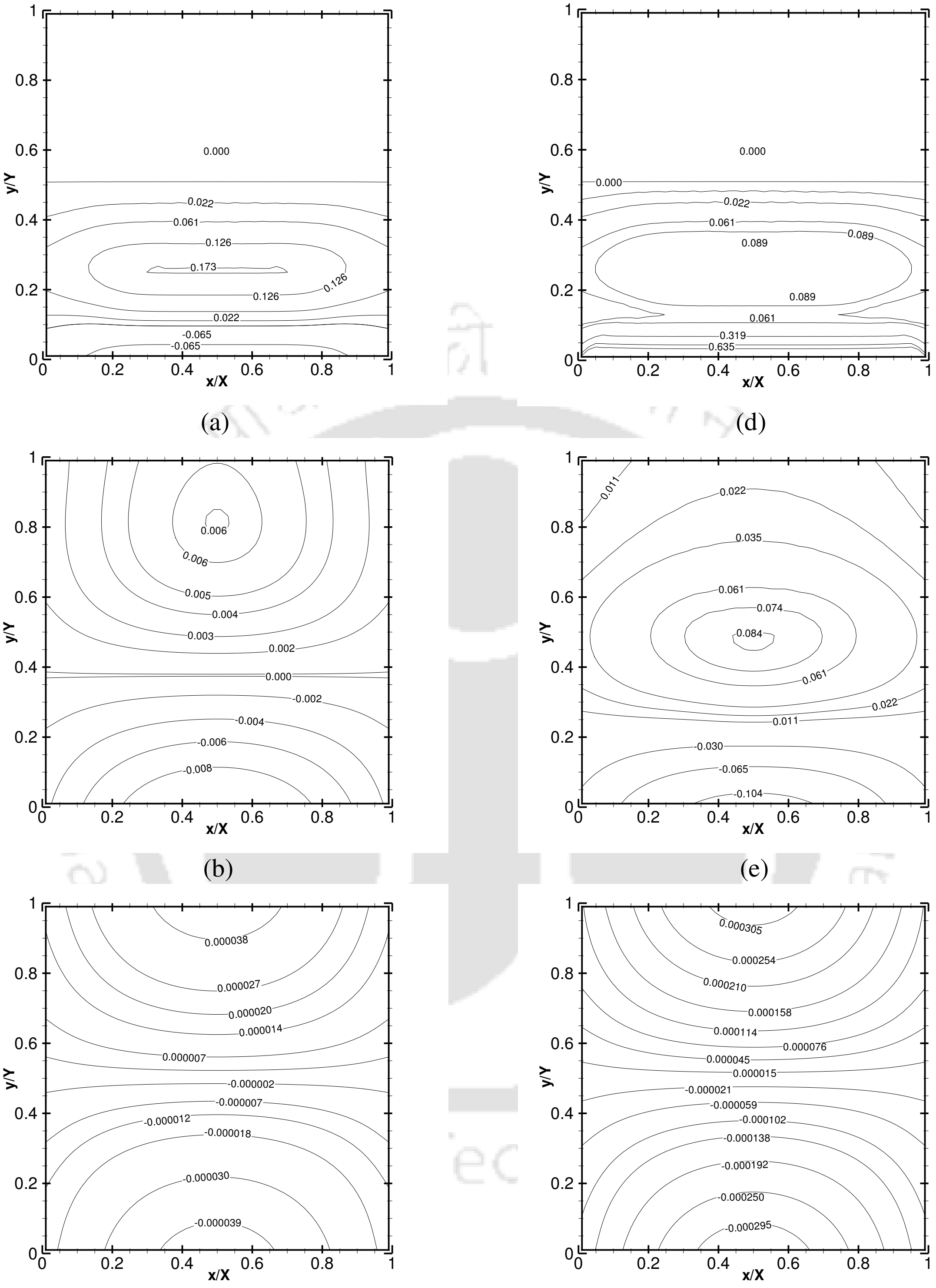

(a) (d)

(b) (e)

(c) (f)

Figure 5.7: Heat flux contours in the medium at time $\frac{t^*}{\Delta t^*}$ (a) = 50, (b) = 200, (c) 800 for a single-pulse, (d) = 50, (e) = 200, (f) 800 for a 4-pulse train. The south boundary subjected to diffuse radiation. $\beta = 1.0, \omega = 1.0$.

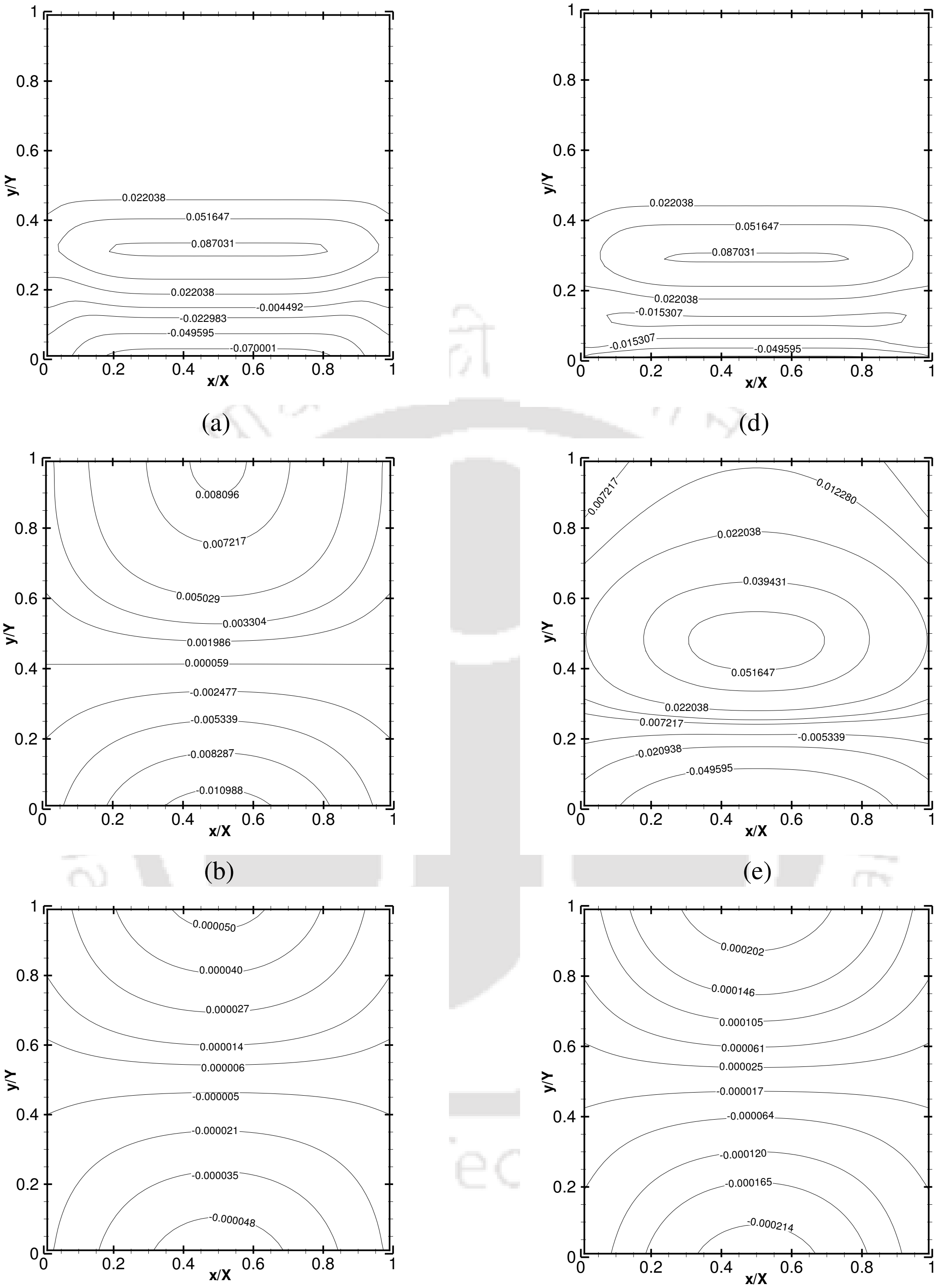

(a) (d)

(b) (e)

(c) (f)

Figure 5.8: Heat flux contours in the medium at time $\frac{t^*}{\Delta t^*}$ (a) = 50, (b) = 200, (c) 800 for a single-pulse, (d) = 50, (e) = 200, (f) 800 for a 4-pulse train. The south boundary subjected to collimated radiation. $\beta = 1.0, \omega = 1.0$.

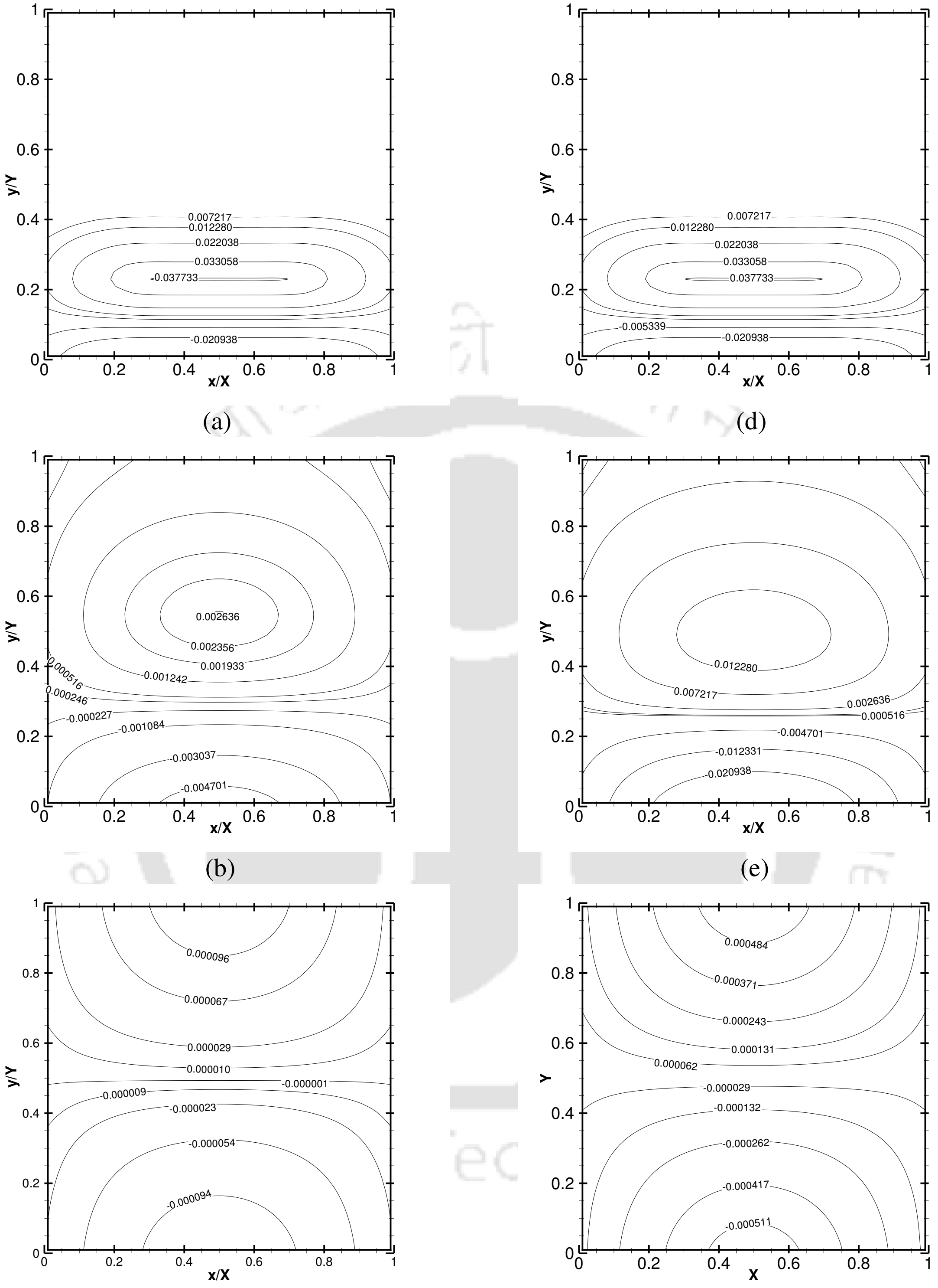

(a) (d)

(b) (e)

(c) (f)

Figure 5.9: Heat flux contours in the medium at time $\frac{t^*}{\Delta t^*}$ (a) = 50, (b) = 200, (c) 800 for a single-pulse, (d) = 50, (e) = 200, (f) 800 for a 4-pulse train. The south boundary subjected to diffuse radiation. $\beta = 10.0, \omega = 1.0$.

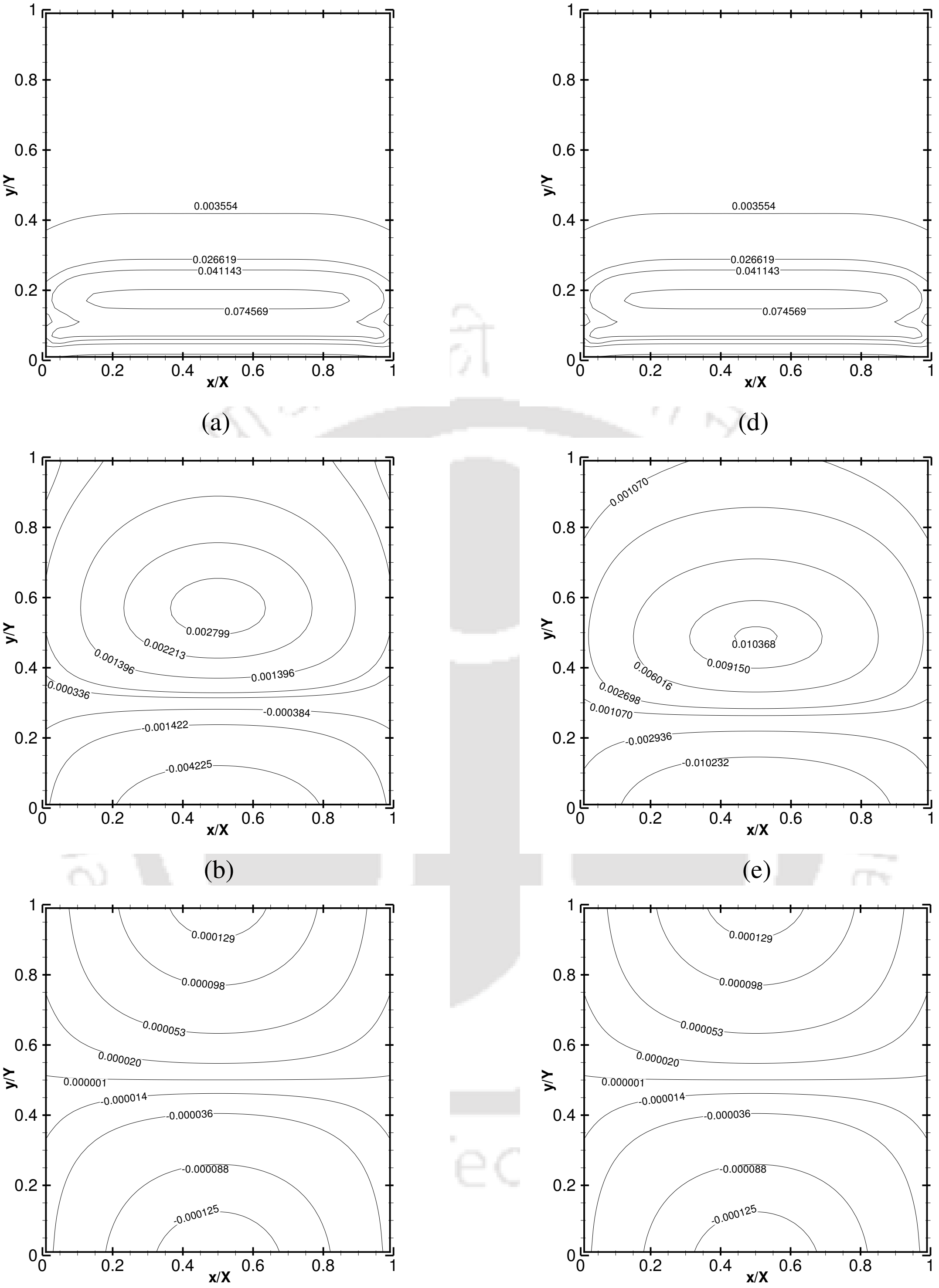

(a) (d)

(b) (e)

(c) (f)

Figure 5.10: Heat flux contours in the medium at time $\frac{t^*}{\Delta t^*}$ (a) = 50, (b) = 200, (c) 800 for a single-pulse, (d) = 50, (e) = 200, (f) 800 for a 4-pulse train. The south boundary subjected to collimated radiation. $\beta = 10.0, \omega = 1.0$.

A comparison of Figs. 5.7b and 5.8b show that the heat flux concentration around the middle of the north boundary is already established at $\frac{t^*}{\Delta t^*} = 200$ in the case of collimated single-pulse (Fig. 5.8b). Though the medium is low absorbing $(\beta = 1.0)$, in case of collimated radiation, since radiation is more directional than the diffuse, the heat flux packet is found much earlier at the north boundary (Fig. 5.8b).

Heat flux contours in Figs. 5.9a and 5.9c for diffuse radiation for a single-pulse and a 4-pulse train for $\beta = 10.0$ look similar at $\frac{t^*}{\Delta t^*} = 50$. A similar trend is also observed in Figs. 5.10a and 5.10c for the collimated radiation.

At $\frac{t^*}{\Delta t^*} = 200$, a smooth distribution of heat flux varying from a minimum near the boundaries to a maximum near the geometric centre of the medium is seen from Figs. 5.9b, 5.9e, 5.10b and 5.10e. The magnitude of the maximum is much higher in the case of Figs. 5.9e and 5.10e due to more energy contained with a 4-pulse train. The low gradient of heat flux inside the medium accounts for a longer life of both the signals with $\beta = 10.0$.

At $\frac{t^*}{\Delta t^*} = 800$, in Figs. 5.9c, 5.9f, 5.10c and 5.10f, the heat flux concentrations at the boundaries are widely distributed around the middle of the north and the south boundaries. The curves marked 8 in Figs. 5.5e, 5.5f, 5.6e and 5.6f are analogous to this observation.

With extinction coefficient $\beta = 1.0$, for 1-4 pulse trains, transmittance $q_t^*\left(0.5, 1.0, t^*\right)$ and reflectance $q_r^*\left(0.5, 0.0, t^*\right)$ signals for three different values of the scattering albedo ω are shown in Figs. 5.11 and 5.12 for diffuse and collimated radiations, respectively. It is seen from these figures (Fig. 5.11a-5.11c and 5.12a-5.12c) that when the scattering is less $(\omega = 0.1)$, transmittance $q_t^*\left(0.5, 1.0, t^*\right)$ signals for a N-pulse train lasts for a shorter duration, their peaks are flattened and magnitudes of the

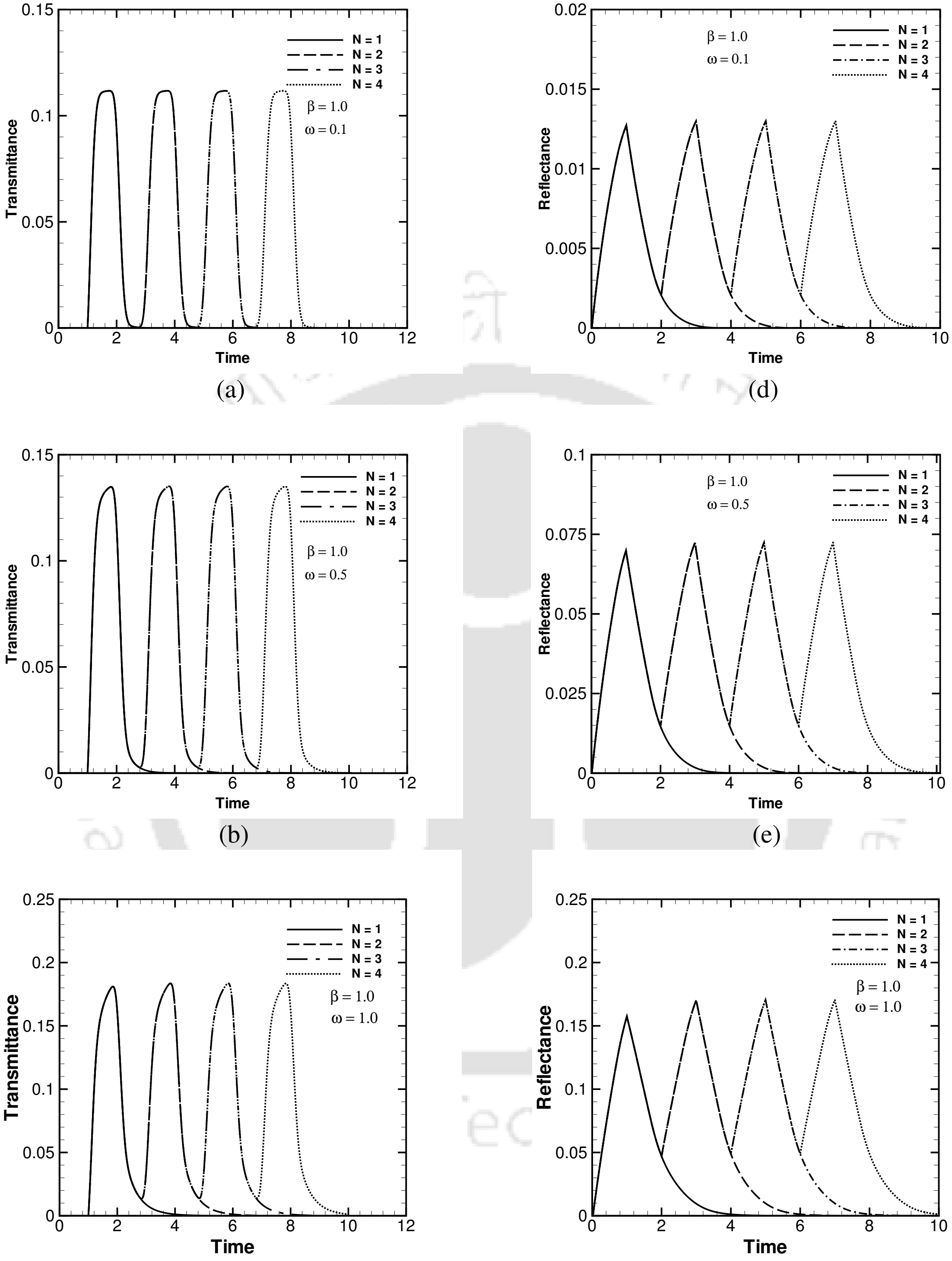

(a) (d)

(b) (e)

(c) (f)

Figure 5.11: Transmittance $q_t^*\left(0.5,1.0,t^*\right)$ signals and reflectance $q_r^*\left(0.5,0.0,t^*\right)$ signals for 1-4 pulses for three different values of scattering albedo ω. The south boundary subjected to diffuse radiation.

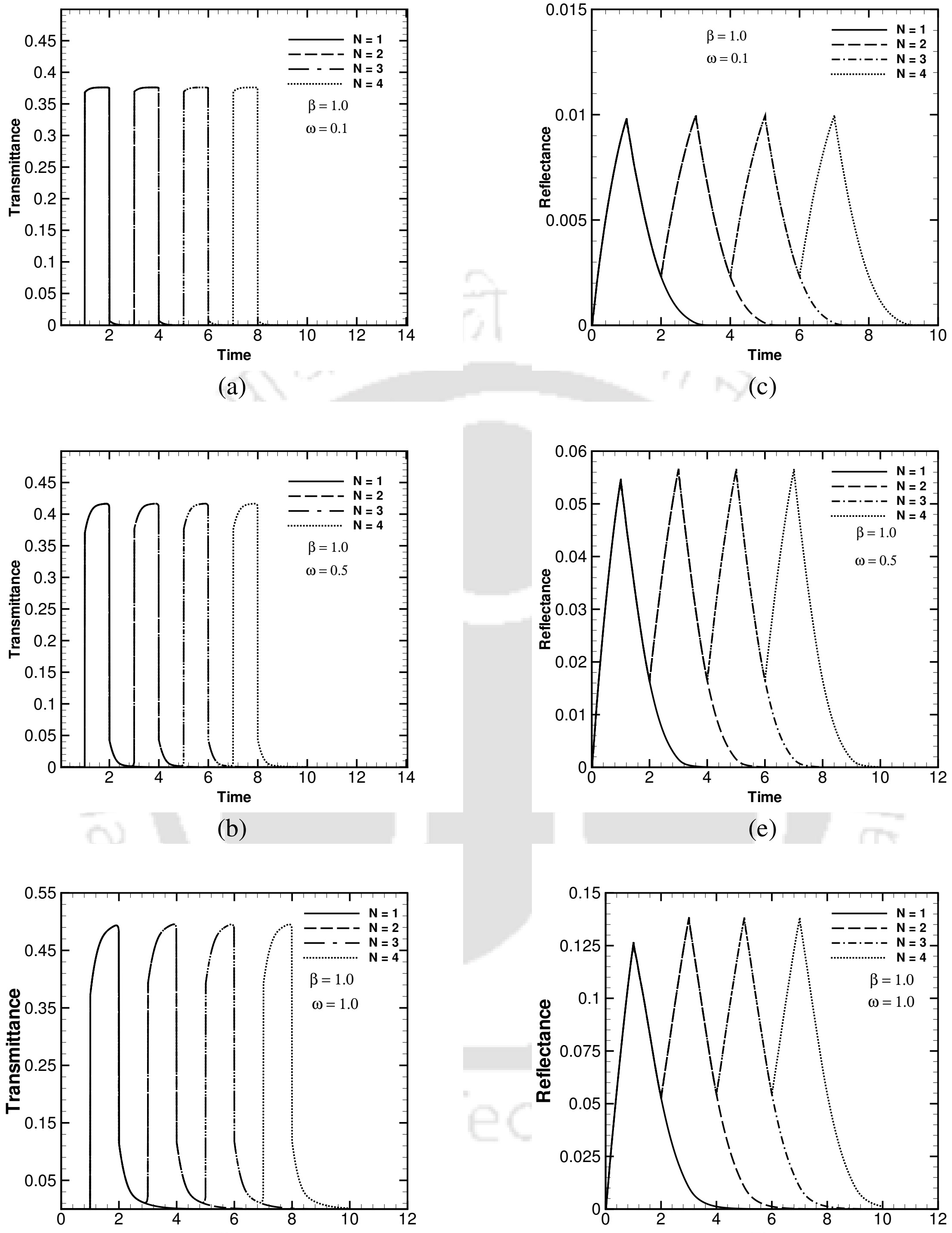

(a) (c)

(b) (e)

(c) (f)

Figure 5.12: Transmittance $q_t^*\left(0.5,1.0,t^*\right)$ signals and reflectance $q_r^*\left(0.5,0.0,t^*\right)$ signals for 1-4 pulses for three different values of scattering albedo ω. The south boundary subjected to collimated radiation.

peaks are less. A comparison of reflectance $q_r^*\left(0.5,0.0,t^*\right)$ signals show, no visible effect of ω on the shape of the peaks and temporal spans for any pulse train. Like transmittance, the magnitudes of the reflectance signals too are found to increase with increase in ω. A comparison of Figs. 5.11 and 5.12 shows that in case of collimated radiation, the transmittance signals are the replicas of the incident square pulse but with a considerable reduction in magnitude. Since the collimated radiation is more directional, the shape of the transmittance signals (Fig. 5.12a) for a lower value of β and a small value of ω is more or less like that of the incident pulses (Fig. 4.1b). However, in case of diffuse radiation, the incident energy is equally distributed in all directions, the signal profiles are of diffuse nature.

5.5 Results and Discussion – Gaussian pulse train

5.5.1 Validation of results

First we validate the present code for the 2-D case with Gaussian multiple pulses by comparing its results with the 1-D case with single and/or a multiple pulse reported in the literature [88,101]. For this, the $x-$dimension in the 2-D code was stretched and the transmittance signal at the centre $\left(0.5,1.0\right)$ of the north boundary was compared with the results for the 1-D case reported in the literature. For this purpose, in the 2-D code, aspect ratios $\frac{X}{Y}=10$ and 100 were found sufficient for diffuse and collimated radiation, respectively. Runs were taken for 10×500 control volumes and 120 directions. It is to be noted that a higher value of $\frac{X}{Y}$ in case of collimated radiation is attributed to strong directional dependency.

Fig. 5.13a shows comparison of the transmittance $q_t^*\left(0.5,1.0,t^*\right)$ signals from the present 2-D code for collimated single-pulse with the 1-D results reported by Okutucu and Yener [101]. This comparison is shown for the extinction coefficient $\beta=0.5$ and scattering albedo $\omega=0.998$. With $\beta=1.0$ and $\omega=1.0$, for a 4-pulse train, transmittance $q_t^*\left(0.5,1.0,t^*\right)$ signals obtained from the present 2-D code have been

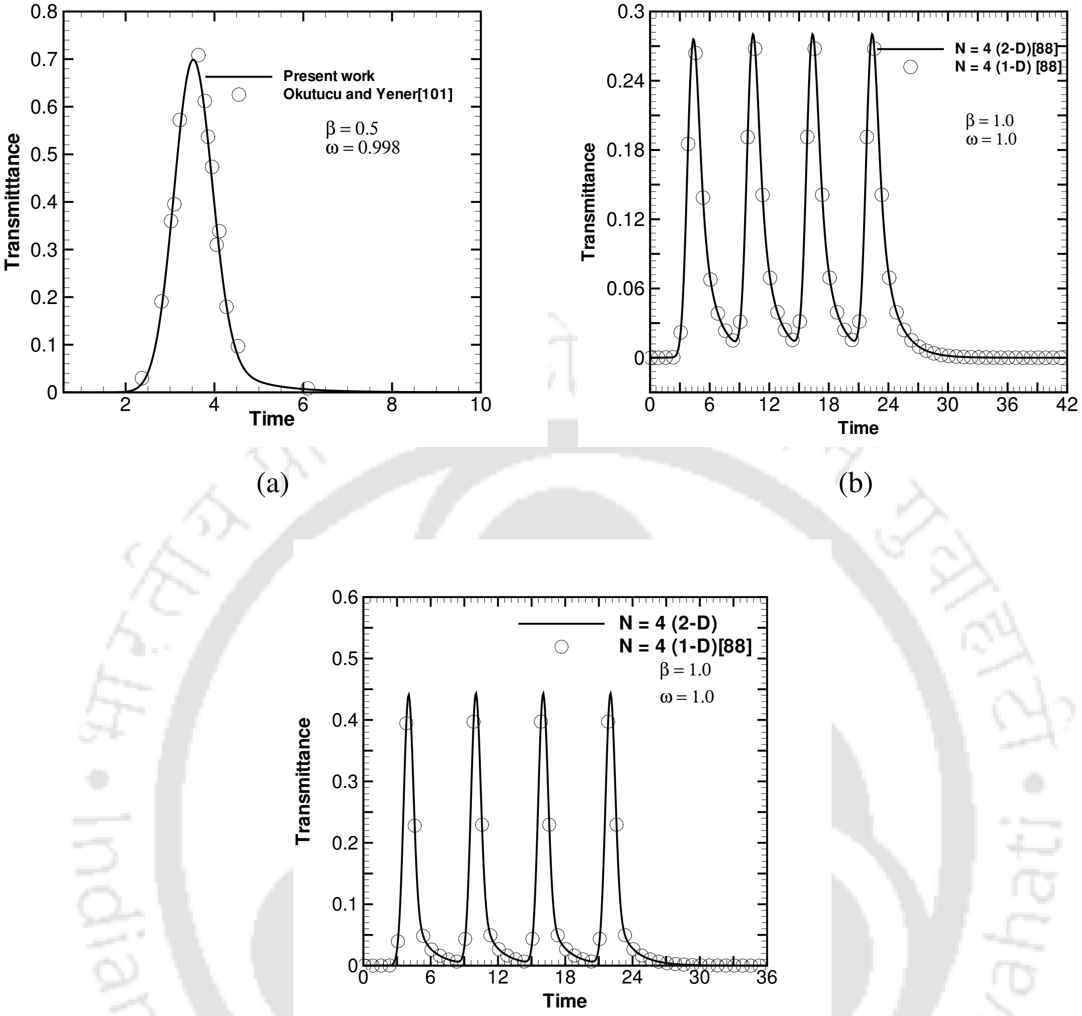

(a) (b)

(c)

Figure 5.13: Comparison of transmittance $q_t^*\left(0.5,1.0,t^*\right)$ signals for (a) a single-pulse collimated radiation with $\frac{X}{Y}=100$ (b) a 4-pulse collimated radiation with $\frac{X}{Y}=100$ and (c) 4-pulse diffuse radiation with $\frac{X}{Y}=10$.

compared for collimated and diffuse radiation in Figs. 5.13b and 5.13c, respectively with 1-D results reported in [88]. It is seen from Figs. 5.13a-c that in all the case, results of the present work with a single or a 4-pulse are in good agreement with those available in the literature [26, 32].

5.5.2 Results with 1-4 pulse train

In the following pages, results for a square medium $\left(\frac{X}{Y}=1\right)$ with its south boundary subjected to either diffuse or collimated pulses are provided. The pulse train consists of 1-4 pulses.

With the south boundary subjected to a diffuse pulse train, Figs. 5.14a-f show transmittance $q_t^*\left(0.5,1.0,t^*\right)$ and reflectance $q_r^*\left(0.5,1.0,t^*\right)$ at the middle of the south and the north boundaries, respectively. Results are shown for 1-4 pulses. With scattering albedo $\omega=1.0$, these results are presented for the extinction coefficient $\beta=1.0,5.0$ and 10.0.

It is seen from Figs. 5.14a-c that the magnitudes of the transmittance $q_t^*\left(0.5,1.0,t^*\right)$ signal peaks decrease by an order of magnitude with increasing β. Observations of Figs. 5.14a-c show that the peaks of different pulse-trains are time-wise more aligned and further signals last longer for higher β. Peaks of increasing magnitudes are observed for multiple pulses for $\beta=5.0$ and 10.0. Relative difference in magnitudes of the successive peaks increases with increase in β. Further, since radiation takes $t^*=\beta ct=\beta Y$ to reach the opposite (north boundary), with $Y=1.0$, in Figs. 3a-c, the transmittance signals $q_t^*\left(0.5,1.0,t^*\right)$ start appearing after $t^*=\beta$. Since the magnitude of the incident pulse is Gaussian function, a gradual increase in the signal is noticed.

Reflectance $q_r^*\left(0.5,0.0,t^*\right)$ results for the corresponding cases of Figs. 5.14a-c are shown in Figs. 5.14d-f. Unlike transmittance $q_t^*\left(0.5,1.0,t^*\right)$**,** the peak magnitudes of the reflectance $q_r^*\left(0.5,0.0,t^*\right)$ signals increase with increase in β, and also different crests and troughs are distinct for all values of β. Like transmittance $q_t^*\left(0.5,1.0,t^*\right)$

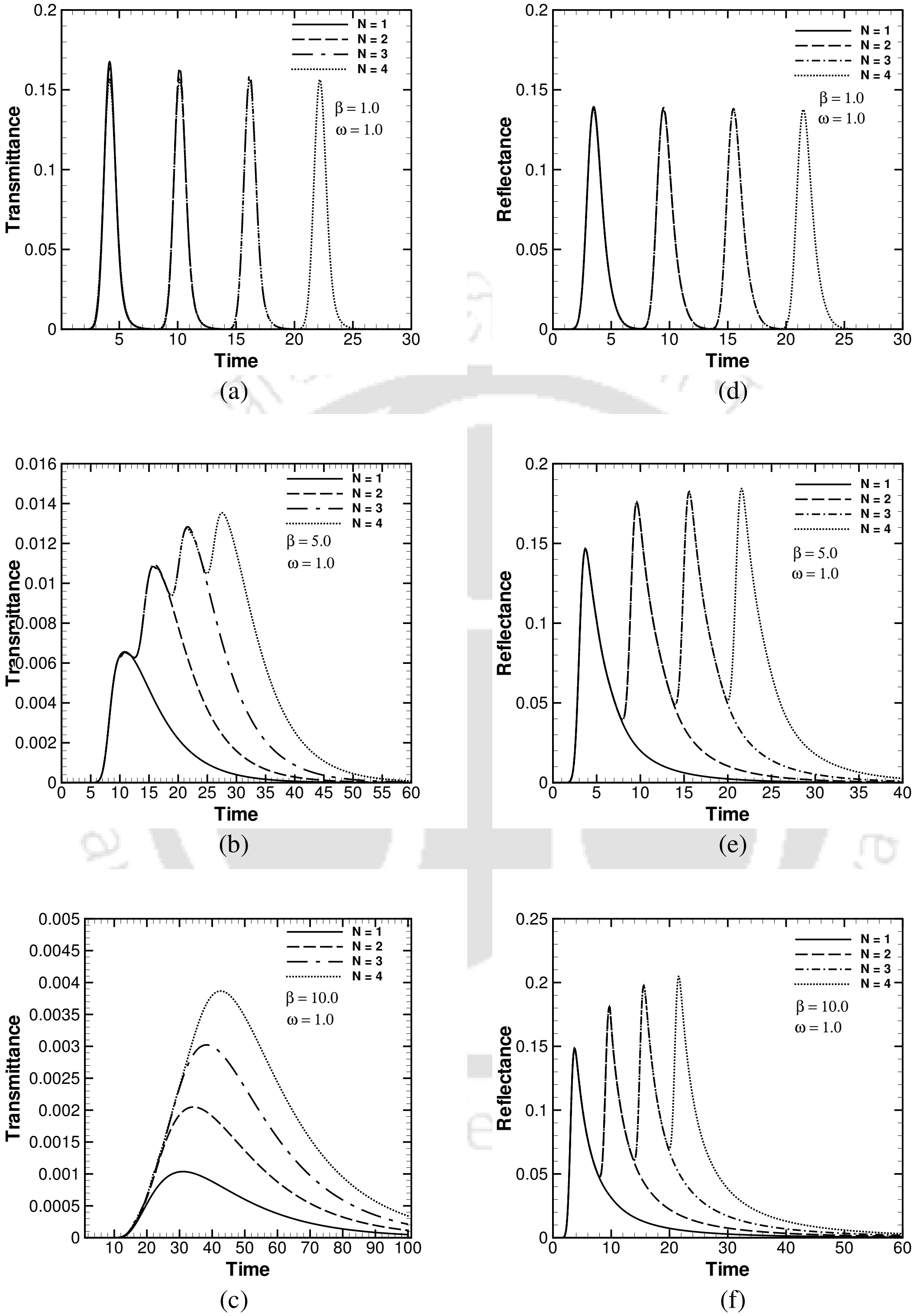

Figure 5.14: Transmittance $q_t^*\left(0.5,1.0,t^*\right)$ signals and reflectance $q_r^*\left(0.5,0.0,t^*\right)$ signals for 1-4 pulses for three different values of extinction coefficient β. The south boundary is subjected to diffuse radiation.

(Fig. 5.14a), the reflectance $q_r^*\left(0.5, 0.0, t^*\right)$ signals (Fig. 5.14d) do not last long for $\beta = 1.0$. Both of them exist for approximately the same time, $t^* = 25.0$. With $\beta = 5.0$ and 10.0, they last longer (Figs. 5.14e and 5.14f). However, their temporal spans are shorter than the transmittance $q_t^*\left(0.5, 1.0, t^*\right)$ signals (Figs. 5.14b and 5.14c). Since the south boundary starts getting radiation much earlier than the north boundary, the reflectance $q_r^*\left(0.5, 0.0, t^*\right)$ signals are seen to start earlier than the transmittance $q_t^*\left(0.5, 1.0, t^*\right)$ signals (Figs. 5.14d-f).

Figs. 5.15a-f show transmittance $q_t^*\left(0.5, 1.0, t^*\right)$ and reflectance $q_r^*\left(0.5, 0.0, t^*\right)$ results with collimated pulses. With scattering albedo $\omega = 1.0$, these results are shown for the extinction coefficient $\beta = 1.0, 5.0$ and 10.0. For $\beta = 1.0$, trends of the two signals (Figs. 5.15a and 5.15d) are similar to that of diffuse pulse train (Figs. 5.14a and 5.14d). However, magnitudes of $q_t^*\left(0.5, 1.0, t^*\right)$ are higher and that of $q_r^*\left(0.5, 0.0, t^*\right)$ lower than the diffuse pulse-train. Since the direction of incidence is normal, a higher magnitude of the $q_t^*\left(0.5, 1.0, t^*\right)$ signals in case of collimated radiation is attributed to increased concentration of energy with less attenuation that reaches the north boundary.

The transmittance signals with $\beta = 5.0$ for a single pulse is observed to have a distinct peak and a sharp decline leading to another well distributed maximum (Fig. 5.15b). The sharp peak is attributed to the arrival of the collimated component of the incident radiation much earlier than the diffuse radiations from the medium. For 2-4 pulses, a trend similar to diffuse radiation (Fig. 5.14b) is noticed. Though the troughs in the curves occur at the same time for 1-4 pulses (Fig. 5.15b), a considerable difference in their magnitude is observed.

With $\beta = 10.0$ (Fig. 5.15c), unlike $\beta = 5.0$ (Fig. 5.15b), distinct crests and troughs corresponding to 1-4 pulses are not observed. Like diffuse pulse (Fig. 5.14c), for $\beta = 10.0$, the signals are characterized by a single crest for any number of pulses.

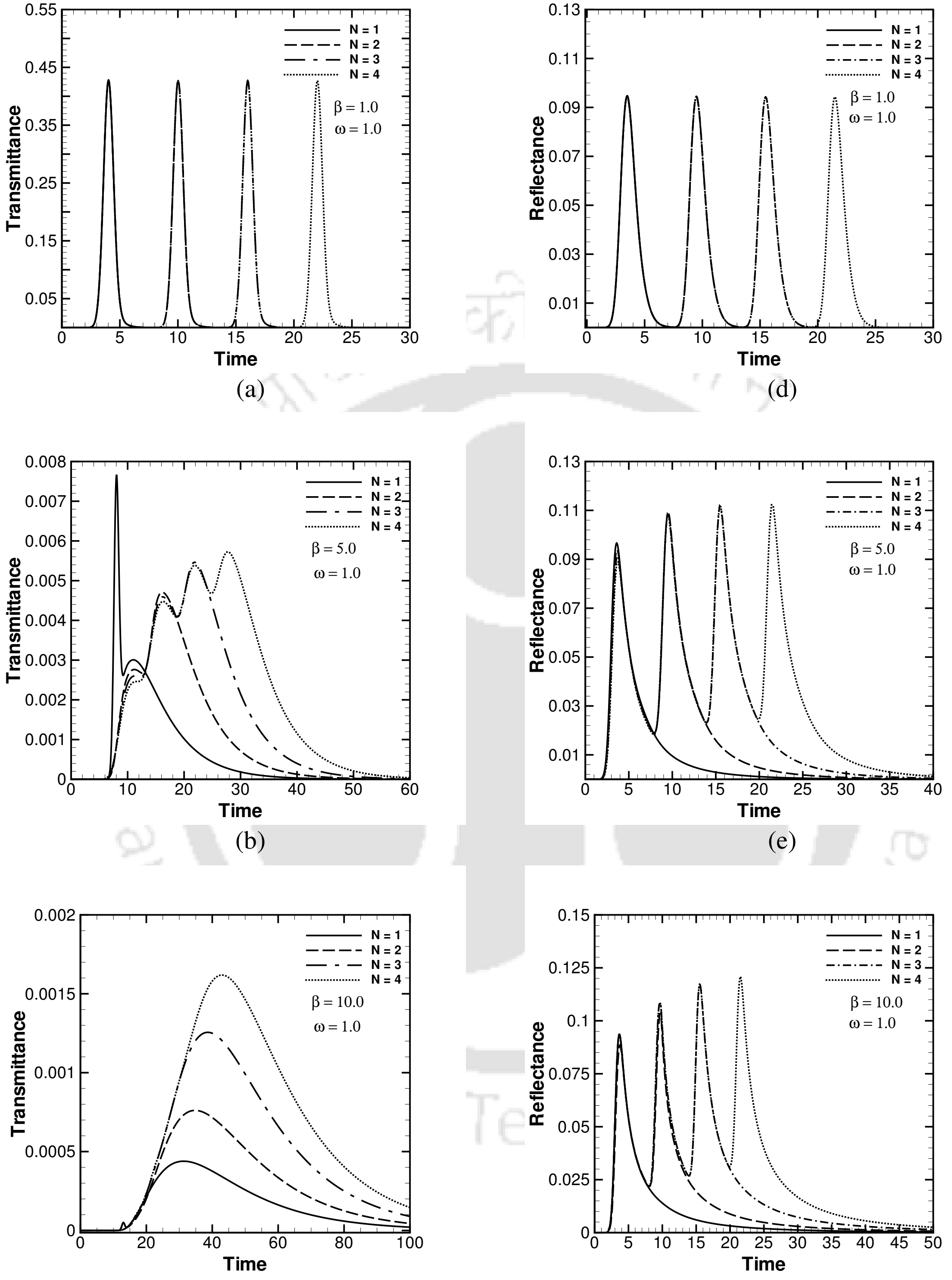

(a) (d)

(b) (e)

(c) (f)

Figure 5.15: Transmittance $q_t^*\left(0.5,1.0,t^*\right)$ signals and reflectance $q_r^*\left(0.5,0.0,t^*\right)$ signals for 1-4 pulses for three different values of extinction coefficient β. The south boundary is subjected to collimated radiation.

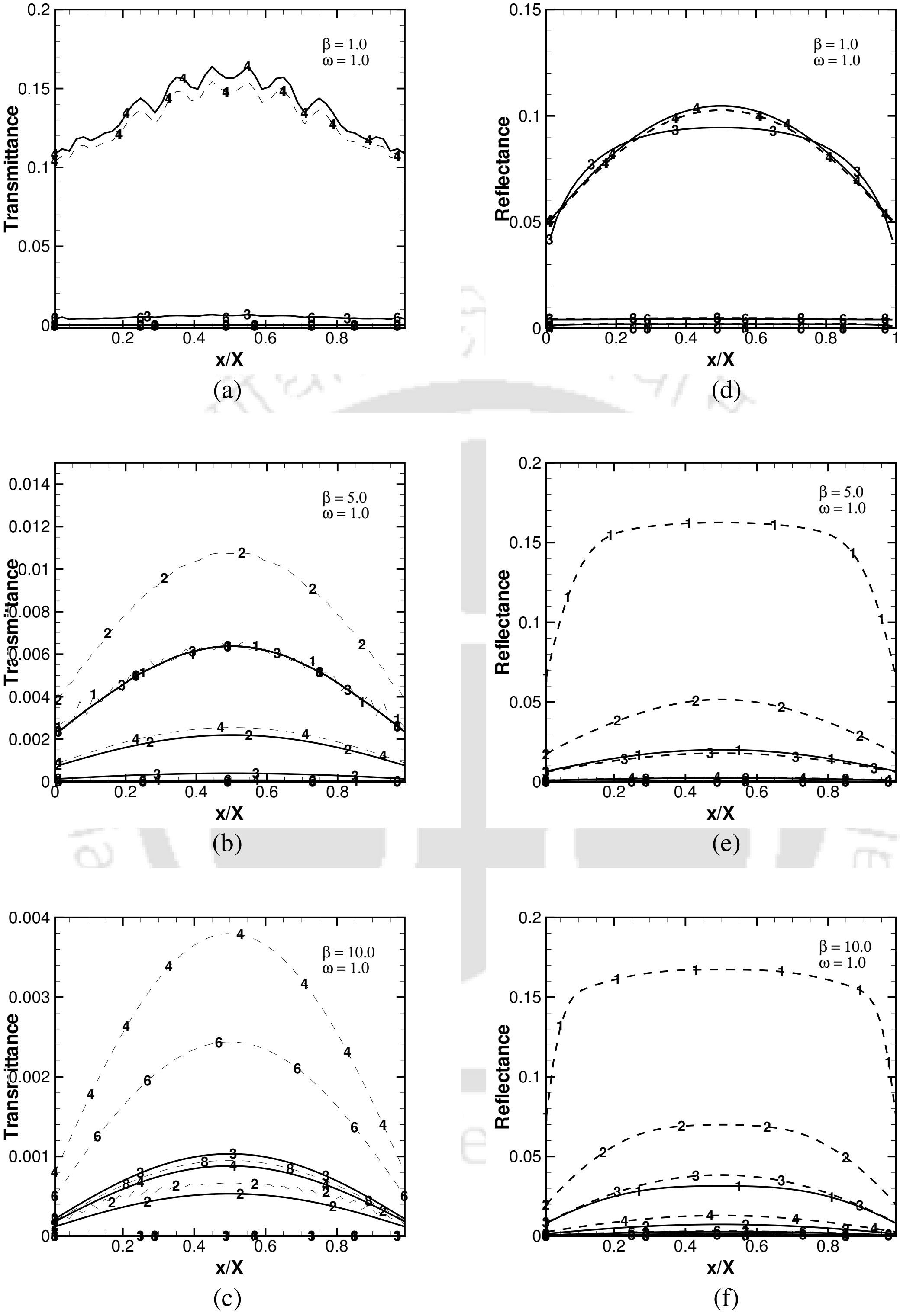

(a) (d)

(b) (e)

(c) (f)

Figure 5.16: Time evolution of the distribution of transmittance $q_t^*\left(x/X,1.0,t^*\right)$ and reflectance $q_r^*\left(x/X,0.0,t^*\right)$ signals along the boundaries. The digit n on any curve indicates the distribution of the signal at $n\times100^{\text{th}}$ time step. Solid and dash lines are results for 1- and 4-pulse diffuse radiation.

Observation of Figs. 5.15b and 5.15c shows that the magnitudes of the peak $q_t^*\left(0.5,1.0,t^*\right)$ signals are less than that for the $q_t^*\left(0.5,1.0,t^*\right)$ signals resulting from diffuse pulse cases given in Figs. 5.14b and 5.14c. Although in this case, the collimated energy is more concentrated, unlike $\beta=1.0$ in Fig. 5.15a, for $\beta=5.0$ and 10.0 in Figs. 5.15b and 5.15c, because of very high attenuation, the magnitudes of $q_t^*\left(0.5,1.0,t^*\right)$ signals are lower than those given in Figs. 5.14b and 5.14c. In Figs. 5.14b and 5.15b, and also Figs. 5.14c and 5.15c, although the extinction coefficient β values are the same, overall attenuation is less in case of Figs. 5.14b and 5.14c because of diffuse nature of the pulse.

The reflectance $q_r^*\left(0.5,0.0,t^*\right)$ results with $\beta=1.0,5.0$ and 10.0 for 1-4 pulses are shown in Figs. 5.15d-f, respectively. Profiles of these signals are the same as that for the diffuse pulse train (Figs. 5.14d-f).In Figs. 5.15 and 5.17, for a single and a 4-pulse train, distributions of transmittance $q_t^*\left(\frac{x}{X},1.0,t^*\right)$ and reflectance $q_r^*\left(\frac{x}{X},0.0,t^*\right)$ results along the boundaries, have been plotted for diffuse and collimated pulses, respectively. With $\omega=1.0$, these distributions are shown for the extinction coefficient $\beta=1.0,5.0$ and 10.0. For a given β, these distributions are plotted at 6 time levels, viz. $\frac{t^*}{\Delta t^*}=100,200,300,400,600$ and 800.

It is seen from Figs. 5.16a and 5.17a that when the medium is less participating $(\beta=1.0)$, the transmittance $q_t^*\left(\frac{x}{X},1.0,t^*\right)$ results for a single and a 4-pulse train almost coincide with each other at all times. The same is the case with the reflectance $q_r^*\left(\frac{x}{X},0.0,t^*\right)$ signals. For $\beta=5.0$ and 10.0, the transmittance $q_t^*\left(\frac{x}{X},1.0,t^*\right)$ signals at all time levels are well separated. This can be verified from Figs. 5.14a-c, and 5.15a-c, where the time evolution of the transmittance signals in the middle of the north boundary $(0.5,1.0)$ have been plotted.

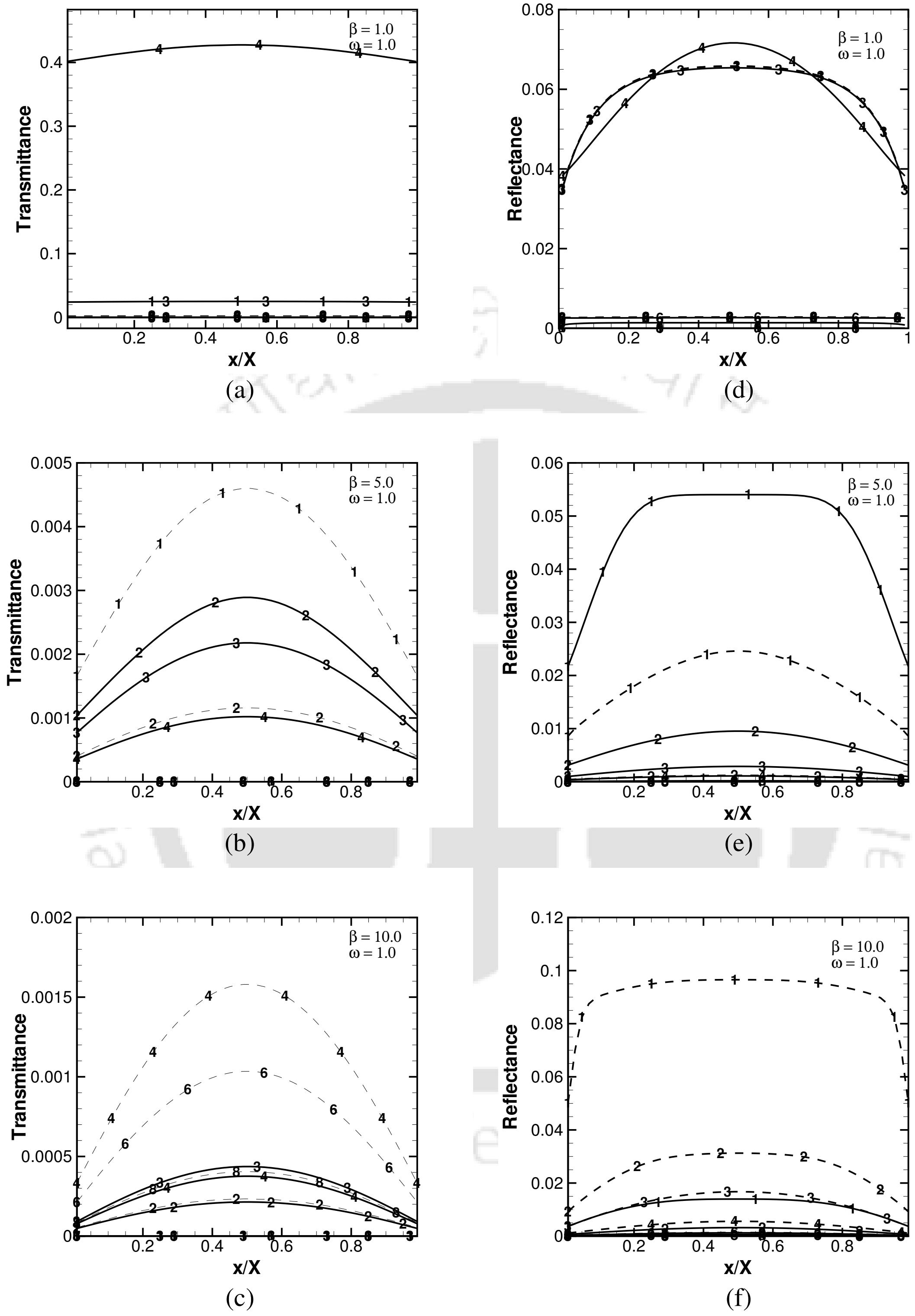

Figure 5.17: Time evolution of the distribution of transmittance $q_t^*\left(x/X,1.0,t^*\right)$ and reflectance $q_r^*\left(x/X,0.0,t^*\right)$ signals along the boundaries. The digit n on any curve indicates the distribution of the signal at $n\times100^{\text{th}}$ time step. Solid and dash lines are results for 1- and 4-pulse collimated radiation.

Figures 5.18-5.21 provide heat flux contours in the medium for a single and a 4-pulse train. In each of these figures, the contours are plotted at three time levels, viz $\frac{t^*}{\Delta t^*} = 50, 200$ and 800. In these figures, results for a single-pulse are given in Figs. (5.18-5.21)a-c, whereas the same for a 4-pulse train are given in Figs. (5.18-5.21)d-f. For $\omega = 1.0$ and $\beta = 5.0$, heat flux contours are given in Figs. 5.18 and 5.19 for diffuse and collimated pulses, respectively. In Figs. 5.20 and 5.21, heat flux contours are presented for diffuse and collimated pulses, respectively for $\omega = 1.0$ and $\beta = 10.0$.

From Figs. 5.18a and 5.18d it is observed that for a single-pulse, at $\frac{t^*}{\Delta t^*} = 50$, the negative heat flux $q^*\left(\frac{x}{X}, \frac{y}{Y}, t^*\right)$ appears near the south boundary. It is to be noted that the negative heat flux contributes towards the reflectance $q_r^*\left(\frac{x}{X}, 0.0, t^*\right)$ signals. For a 4-pulse train, from Fig. 5.18d it is observed that at $\frac{t^*}{\Delta t^*} = 50$, like Fig. 5.18a, for a single-pulse, the radiation has not reached the north boundary, but the positive heat flux towards the north boundary is more prominent.

At $\frac{t^*}{\Delta t^*} = 200$, it is observed from Figs. 5.18b and 5.18c, and 5.18e and 5.18f that both negative and positive heat fluxes remain in the medium for a single and a 4-pulse train. The region of negative heat flux is observed to be more for a single-pulse. Further it is observed that the peak magnitudes of the heat flux are still found inside the medium in the neighborhood of the north boundary. But as time progresses $\left(\frac{t^*}{\Delta t^*} = 800\right)$, the maximum magnitude of the heat flux is found to be concentrated around the middle of the south and the north boundaries. This observation is substantiated with Figs. 5.16a and 5.16d.

A comparison of Figs. 5.18b and 5.19b show that the heat flux concentration around the middle of the north boundary is already established at $\frac{t^*}{\Delta t^*} = 200$ in the case of

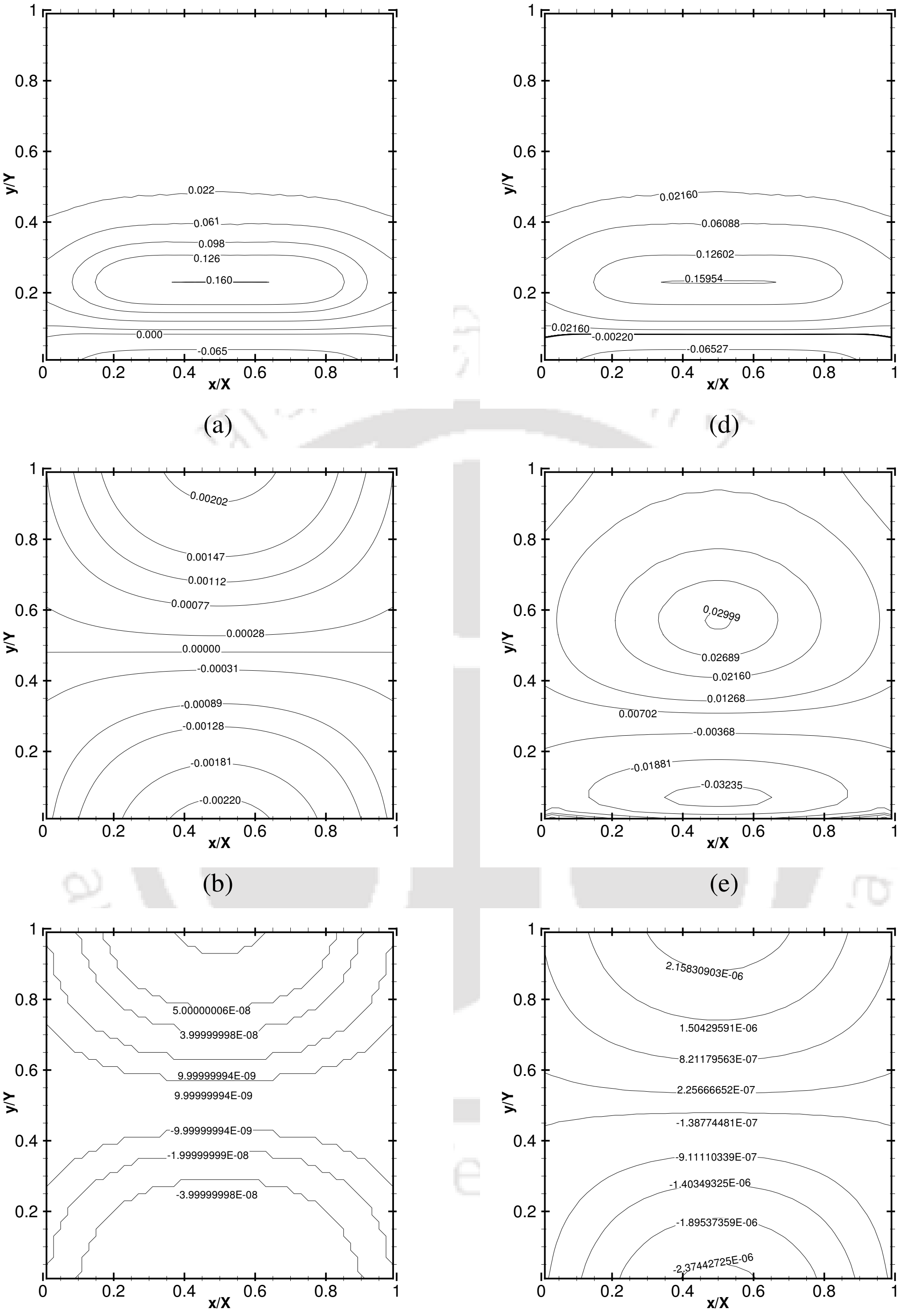

(a) (d)

(b) (e)

(c) (f)

Figure 5.18: Heat flux contours in the medium at time $\frac{t^*}{\Delta t^*}$ (a) = 50, (b) = 200, (c) = 800 for a single-pulse, (d) = 50, (e) = 200, (f) = 800 for a 4-pulse train. The south boundary is subjected to diffuse radiation. $\beta = 5.0, \omega = 1.0$.

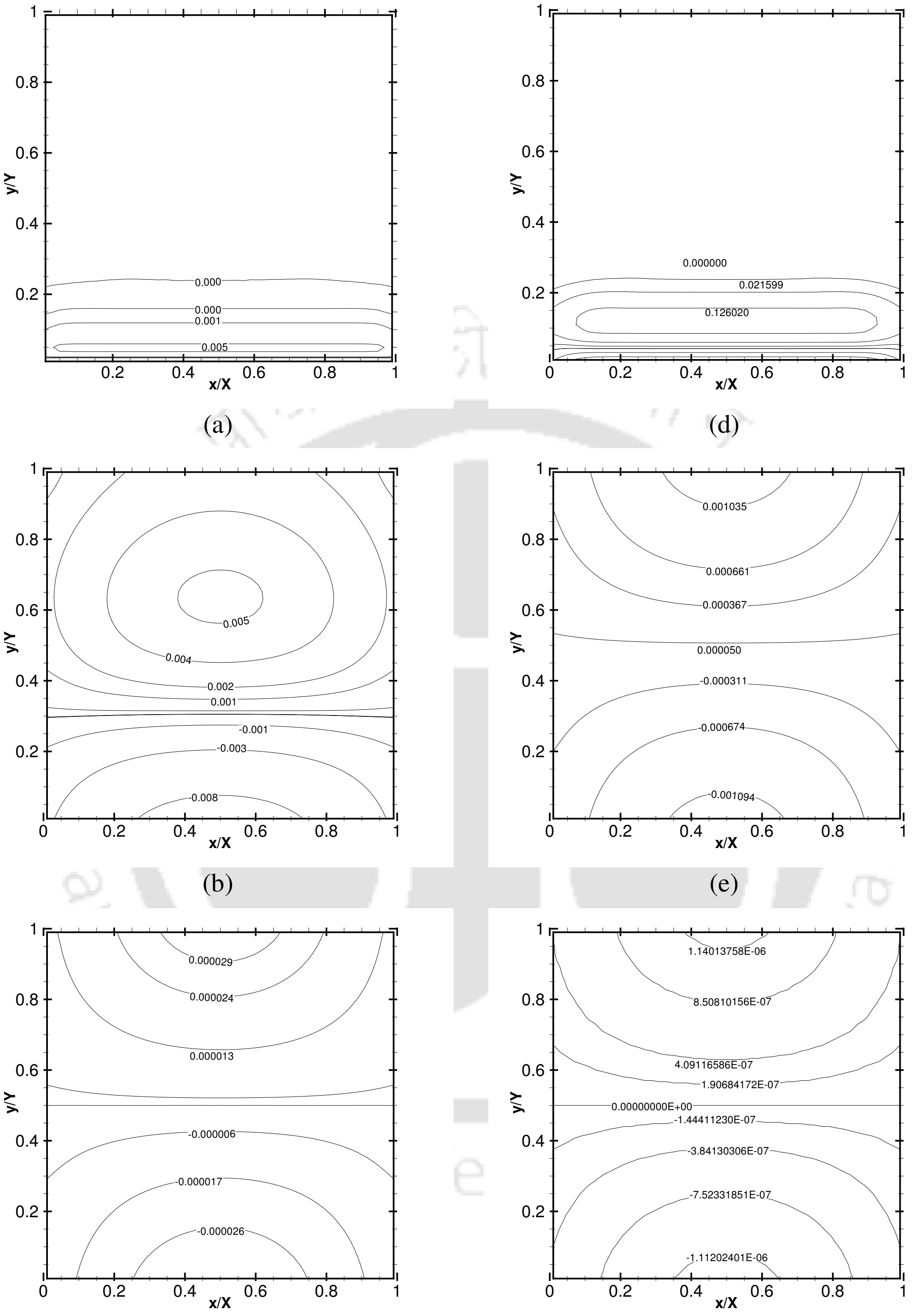

(a) (d)

(b) (e)

(c) (f)

Figure 5.19: Heat flux contours in the medium at time $\frac{t^*}{\Delta t^*}$ (a) = 50, (b) = 200, (c) = 800 for a single-pulse, (d) = 50, (e) = 200, (f) = 800 for a 4-pulse train. The south boundary is subjected to collimated radiation. $\beta = 5.0, \omega = 1.0$.

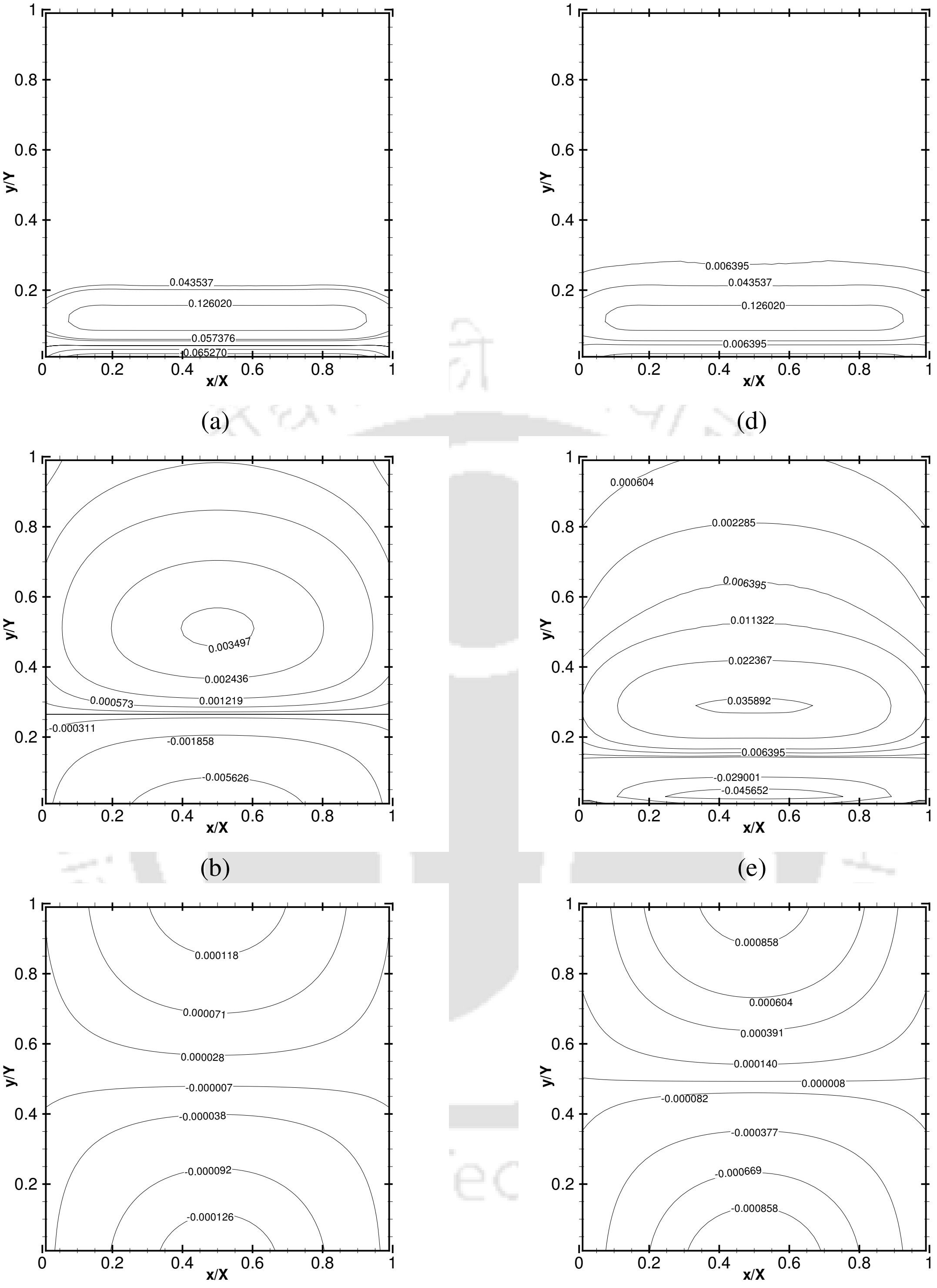

(a) (d)

(b) (e)

(c) (f)

Figure 5.20: Heat flux contours in the medium at time $\frac{t^*}{\Delta t^*}$ (a) = 50, (b) = 200, (c) = 800 for a single-pulse, (d) = 50, (e) = 200, (f) = 800 for a 4-pulse train. The south boundary is subjected to diffuse radiation. $\beta = 10.0, \omega = 1.0$.

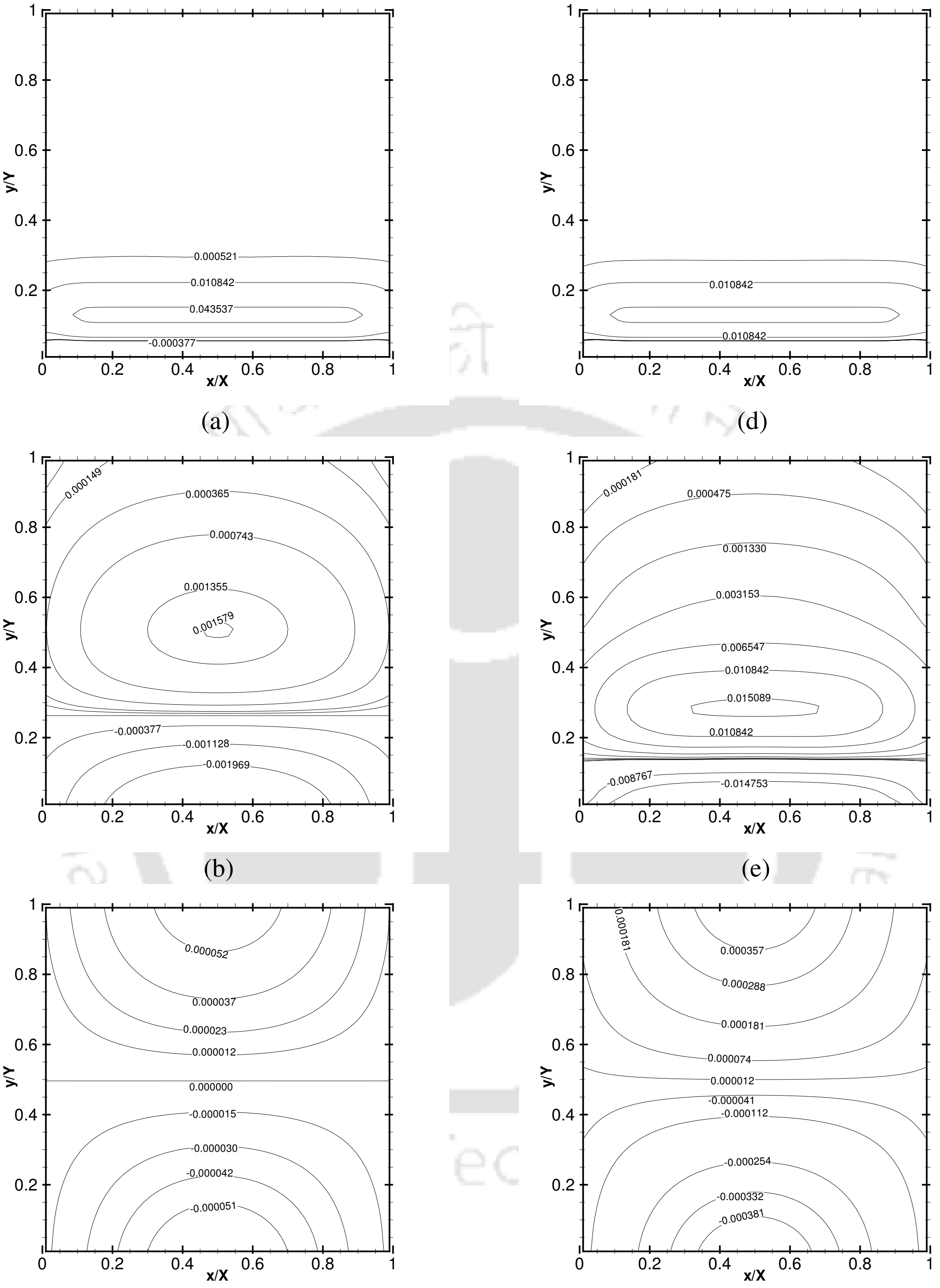

(a) (d)

(b) (e)

(c) (f)

Figure 5.21: Heat flux contours in the medium at time $\frac{t^*}{\Delta t^*}$ (a) = 50, (b) = 200, (c) =800 for a single-pulse, (d) = 50, (e) = 200, (f) = 800 for a 4-pulse train. . The south boundary is subjected to collimated radiation. $\beta = 10.0, \omega = 1.0$.

diffuse single-pulse (Fig. 5.18b). Though the medium is highly absorbing $(\beta = 5.0)$, in case of diffuse radiation, the heat flux packet is found much earlier at the north boundary (Fig. 5.18b).

It is observed from Figs. 5.20 and 5.21 that heat flux contours for both diffuse and collimated radiation for a single-pulse and a 4-pulse train for $\beta = 10.0$ look similar at various time levels.

At $\frac{t^*}{\Delta t^*} = 200$, a smooth distribution of heat flux varying from a minimum near the boundaries to a maximum near the geometric centre of the medium is seen from Figs. 5.20b, 5.20e, 5.21b and 5.21e. The magnitude of the maximum is higher in the case of Figs. 5.20e and 5.21e due to more energy contained with a 4-pulse train. The low gradient of heat flux inside the medium accounts for a longer life of both the signals with $\beta = 10.0$.

At $\frac{t^*}{\Delta t^*} = 800$, in Figs. 5.20c, 5.20f, 5.21c and 5.21f, the heat flux concentrations at the boundaries are widely distributed around the middle of the north and the south boundaries.

Figures 5.22 and 5.23 show transmittance $q_t^*\left(0.5, 1.0, t^*\right)$ and reflectance $q_r^*\left(0.5, 0.0, t^*\right)$ signals for the scattering albedo $\omega = 0.1, 0.5$ and 1.0. With extinction coefficient $\beta = 1.0$, these results are given for 1-4 pulse trains for diffuse and collimated radiations, in Figs. 5.22 and 5.23, respectively. It is seen from these figures (Fig. 5.22 a-c and 5.23 a-c) that when the scattering is less $(\omega = 0.1)$, transmittance $q_t^*\left(0.5, 1.0, t^*\right)$ signals for a N-pulse train lasts for a shorter duration, their peaks are flattened and magnitudes of the peaks are less. A comparison of reflectance $q_r^*\left(0.5, 0.0, t^*\right)$ signals show, no visible effect of ω on the shape of the peaks and temporal spans for any pulse train. Like transmittance, the magnitudes of the reflectance signals too are found to increase with increase in ω. A comparison of

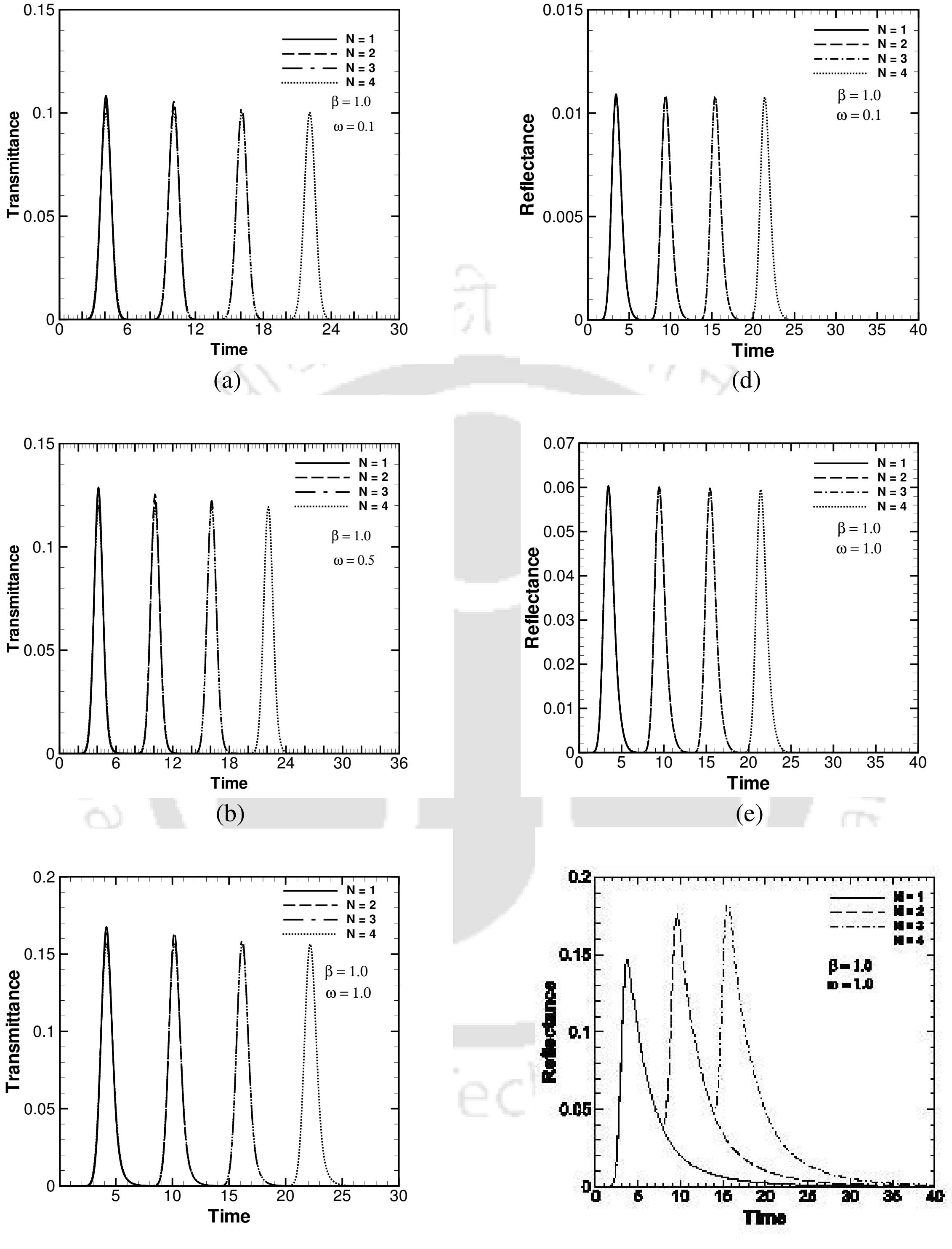

(a) (d)

(b) (e)

(c) (f)

Figure 5.22: Transmittance $q_t^*\left(0.5,1.0,t^*\right)$ signals and reflectance $q_r^*\left(0.5,0.0,t^*\right)$ signals for 1-4 pulses for three different values of scattering albedo ω. The south boundary is subjected to diffuse radiation.

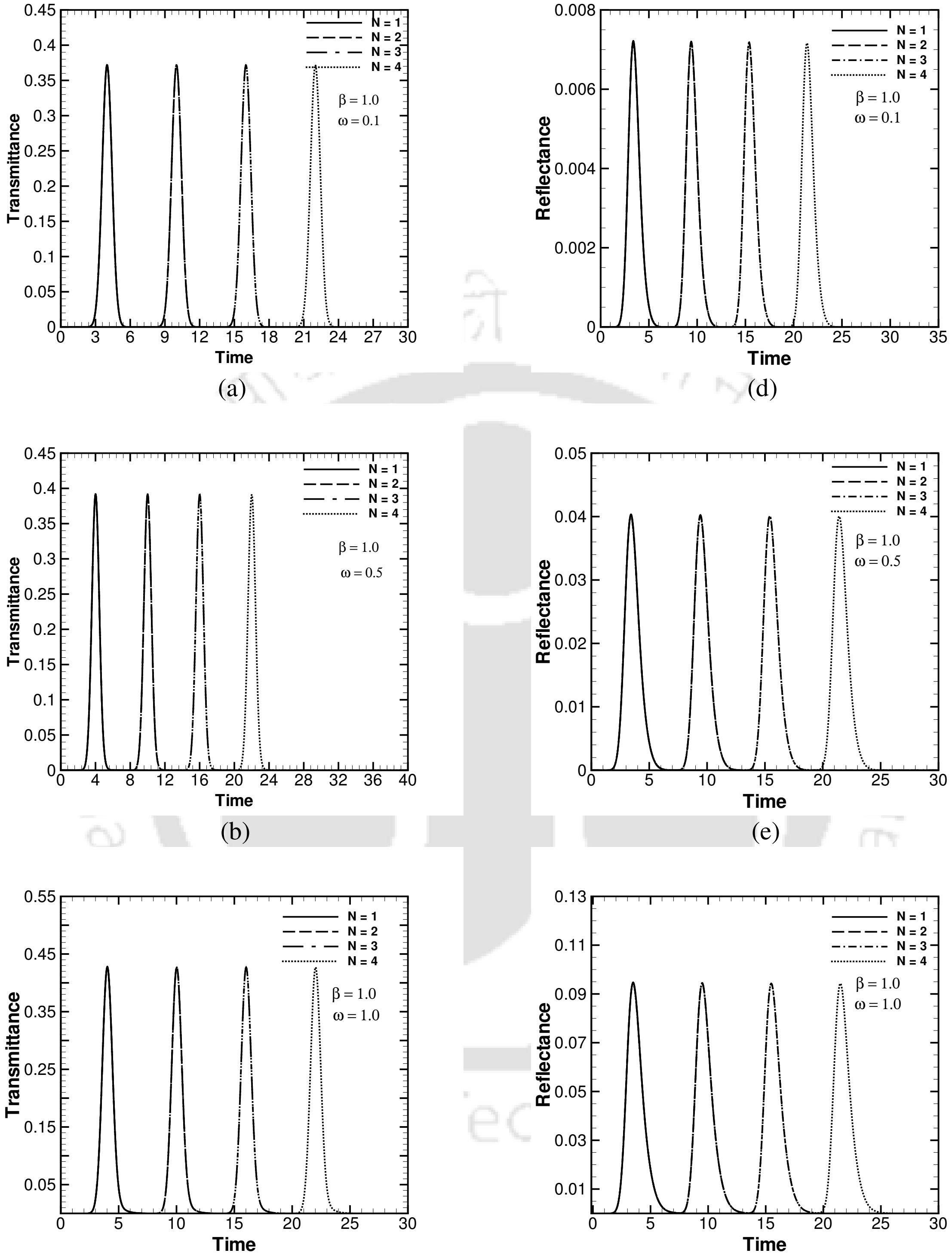

(a) (d)

(b) (e)

(c) (f)

Figure 5.23: Transmittance $q_t^*\left(0.5, 1.0, t^*\right)$ signals and reflectance $q_r^*\left(0.5, 0.0, t^*\right)$ signals for 1-4 pulses for three different values of scattering albedo ω. The south boundary is subjected to collimated radiation.

Figs. 5.22 and 5.23 shows that in case of both diffuse and collimated pulses, the transmittance signals are the replicas of the incident pulses having Gaussian temporal profile but with a considerable reduction in magnitude. Each segment of the signal is seen to last for $t^* = 6t_p^*$.

5.6 Summary

Transport of a train of short-pulse radiation through a 2-D rectangular participating medium was studied. The analysis was done by considering the south boundary of the medium subjected to a short-pulse radiation. Both diffuse and collimated radiations were considered. The temporal profile of the pulse radiation was a step or Gaussian function and the pulse train consisted of 1-4 pulses. The homogeneous participating medium was absorbing and scattering. The transmittance and reflectance signals were studied for the effects of the extinction coefficient and the scattering albedo. Heat flux distributions inside the medium were also studied. With a single pulse, results were compared with those available in the literature for the 2-D case. The 1-D results from the 2-D code were also validated against 1-D results available in the literature. In all the cases, very good comparisons were obtained. Results with 1-4 pulses were found to have significant effects of the extinction coefficient and the scattering albedo.

The next chapter deals with the transport of a short-pulse laser through a 2-D participating medium containing square shaped inhomogeneties.

CHAPTER 6

Effects of the Incidence of a Short-Pulse Radiation Transport through a 2-D Rectangular Inhomogeneous Participating Medium

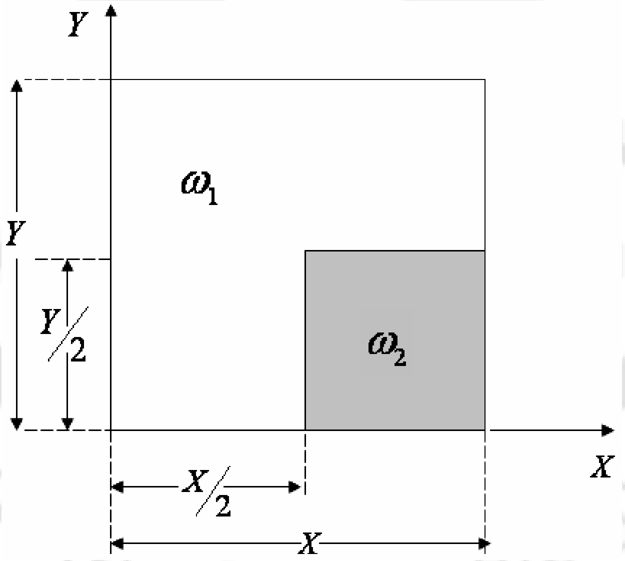

Figure: 2-D geometry and the coordinate system under consideration

6.1 Introduction

Though a few studies involving presence of inhomogeneities in 2-D rectangular participating media are found in the literature [17, 30, 35, 46, 51, 70, 76, 119, 120, 121], studies on the effects of multiple pulses on 2-D geometries with a local inhomogeneity and hence its thermal signatures viz., transmittance and reflectance have never been done so far. Further the effect of the location of the inhomogeneity in the medium has also not been reported either for a single or a multiple pulses. An investigation of the transport of a train of short-pulse radiation through a 2-D rectangular participating medium consisting of local inhomogeneities is presented in this chapter. A collimated beam of step or Gaussian temporal-profile is considered. The incident radiation consists of 1 and 4 pulses. The absorbing and scattering participating medium contains a square-shaped local inhomogeneity. The inhomogeneity differs from the rest of the medium by its scattering albedo.

The pulse-width and the period of the incident radiation are of the order of a nano-second. Transmittance and reflectance signals are analyzed for the effects of the extinction coefficient and the scattering albedo. Heat flux distributions inside the medium are also studied. The formulation for the problems considered in this chapter is the same as that presented in the Chapter 5.

6.2 Problem

Figs 6.1a-c show the positions of the square-shaped inhomogeneity in the medium. Two different combinations of the extinction coefficient β and the scattering albedo ω of the medium and its inhomogeneity are considered for each of the three different locations of the inhomogeneity. The volume of the inhomogeneity is one-fourth of that of the medium. The south boundary is subjected to collimated radiation.

In Case 1 (Fig. 6.1a), inhomogeneity is located centrally in the medium. In Case 2, the inhomogeneity is at the top-left corner of the medium (Fig.6.1b) while in Case 3, it is located at the bottom-right corner of the (Fig. 6.1c). By switching the scattering albedo of the medium and its inhomogeneities three more cases viz., Case 4, Case 5, Case 6 are considered and analyzed. The medium and its inhomogeneity are considered to have the same extinction coefficient β. For three values of $\beta = 1.0, 5.0$ and 10.0 considered in the present work, the cases considered are shown in the Table 6.1.

Case	Scattering albedo of medium ω_1	Scattering albedo of inhomogeneity ω_2	location of the inhomogeneity as shown in
1	0.998	0.1	Fig. 6.1a
2	0.998	0.1	Fig. 6.1b
3	0.998	0.1	Fig. 6.1c
4	0.1	0.998	Fig. 6.1a
5	0.1	0.998	Fig. 6.1b
6	0.1	0.998	Fig. 6.1c

Table 6.1: Various inhomogeneous cases discussed in Chapter 6

6.3 Results and Discussion – Step pulse train

For grid independent, 50×50 equal size control volumes were used and a maximum of 120 directions covering the 4π solid angle were found enough for the ray-independent solutions. 1000 divisions of the total time t^* domain were found sufficient for marching in the time dimension. At every time step, the iteration was set to $\left| S^m_{t,\mathrm{old},P} - S^m_{t,\mathrm{new},P} \right| \le 1.0 \times 10^{-7}$.

With the extinction coefficient $\beta = 10.0$, for a square medium $\left(\frac{X}{Y} = 1 \right)$ subjected to a single pulse laser, we first validate our results for homogeneous and inhomogeneous cases with those available in the literature [100]. With the scattering albedo

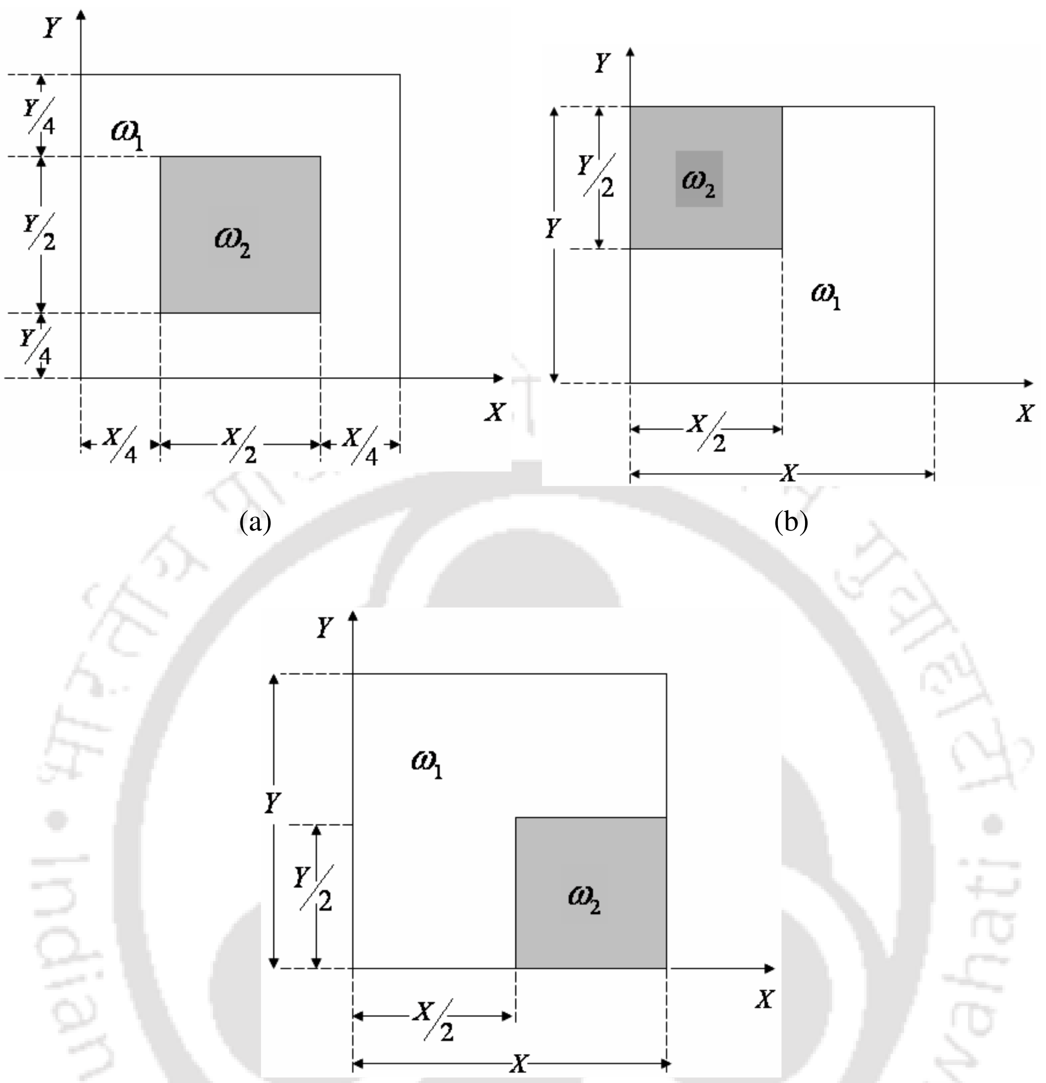

(a) (b)

(c)

Figure 6.1: (a) (b)(c) 2-D Geometries and the coordinate system under consideration

$\omega = 0.998$, for a homogeneous medium, transmittance $q_t^*\left(0.5, 1.0, t^*\right)$ and reflectance $q_r^*\left(0.5, 0.0, t^*\right)$ at the middle of the south and the north boundaries have been compared in Figs. 6.2a and 6.2b respectively with those of Sakami et al. [100] obtained using the DOM with high order upwind piecewise parabolic interpolation scheme.

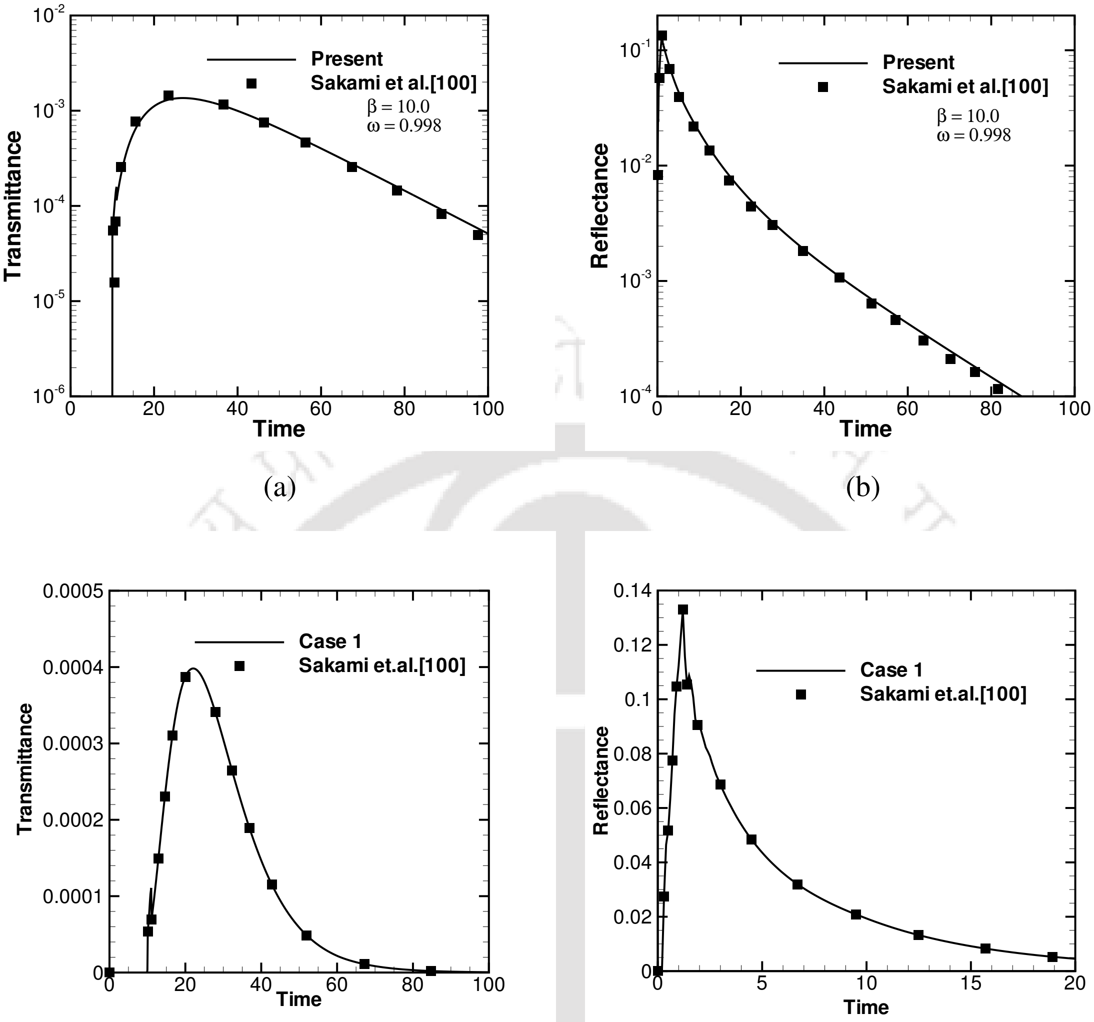

(a) (b)

(c) (d)

Figure 6.2: Comparison of (a) transmittance $q_t^*\left(0.5,1.0,t^*\right)$ (b) reflectance $q_r^*\left(0.5,0.0,t^*\right)$ for a homogeneous medium and (c) transmittance $q_t^*\left(0.5,1.0,t^*\right)$ (d) reflectance $q_r^*\left(0.5,0.0,t^*\right)$ for an inhomogeneous medium(Case 1)

With a localized inhomogeneity representing the case 1 above, Figs. 6.2c and 6.2d show comparison of transmittance and reflectance results of the present work with those of Sakami et al. [100]. It is seen from Figs. 6.2a-6.2d that in all the cases, results of the present work with a single pulse are in good agreement with those available in the literature [100].

In the following pages, we provide results for a square medium $\left(\frac{X}{Y}=1\right)$ containing a square shaped inhomogeneity. With $\beta = 1.0, 5.0$ and 10.0, results are presented for six different cases considered above. The south boundary of the 2-D medium is subjected to a short-pulse laser incident normal to the boundary. Effects due to a single pulse and a 4-pulse laser train are studied.

Transmittance $q_t^*\left(0.5, 1.0, t^*\right)$ and reflectance $q_r^*\left(0.5, 0.0, t^*\right)$ results for case 1 (Fig 6.1a), case 2 (Fig 6.1b) and case 3 (Fig 6.1c) for three different values of the extinction coefficient $\beta = 1.0, 5.0$ and 10.0 for a single-pulse are shown in Figs. 6.3a-f. For all three values of β, the trends of the transmittance $q_t^*\left(0.5, 1.0, t^*\right)$ (Fig 6.3a, 6.3c and 6.3e) and reflectance $q_r^*\left(0.5, 0.0, t^*\right)$ (Fig 6.3b, 6.3d and 6.3f) signals resemble the trends of the 1-D planar medium, but their temporal spans are much shorter [97].

With $\beta = 1.0$, the peak magnitudes of the signals are also close to that of the 1-D case while for $\beta = 5.0$ and 10.0, they are quite different [97]. It is observed Figs. 6.3a, 6.3c and 6.3d that with increase in β, the location of the inhomogeneity has pronounced effect on transmittance $q_t^*\left(0.5, 1.0, t^*\right)$. However, it is seen from Figs. 6.3b, 6.3d and 6.3f that location of the inhomogeneity has less effect on the reflectance $q_r^*\left(0.5, 1.0, t^*\right)$.

In cases 1-3, the large (3/4th) volume of the medium is strongly scattering $(\omega_1 = 0.998)$ and the inhomogeneity which occupies 1/4th of the volume is weak scattering $(\omega_2 = 0.1)$. When the medium is less participating $(\beta = 1.0)$, the location of the inhomogeneity has almost no effect on the transmittance $q_t^*\left(0.5, 1.0, t^*\right)$ (Fig 6.3a) and reflectance $q_r^*\left(0.5, 0.0, t^*\right)$ signals captured at the middle of the boundaries. But when the medium becomes more and more participating $(\beta = 5.0, 10.0)$, the

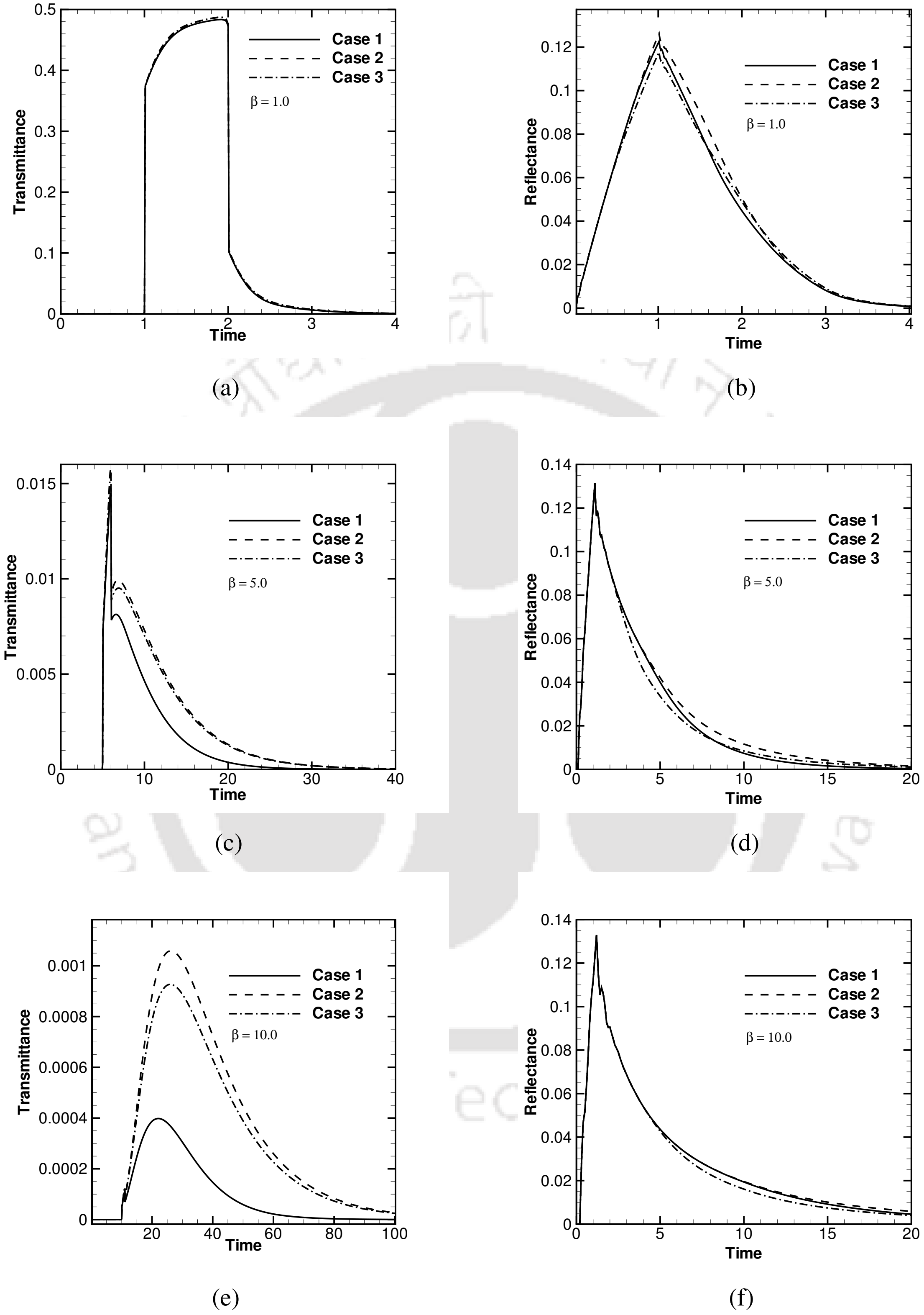

(a) (b)

(c) (d)

(e) (f)

Figure 6.3: Transmittance $q_t^*\left(0.5,1.0,t^*\right)$ signals and reflectance $q_r^*\left(0.5,0.0,t^*\right)$ signals for a single pulse for cases 1, 2, 3.

location of the inhomogeneity has more effect on the transmittance $q_t^*\left(0.5,1.0,t^*\right)$ signals.

With $\beta = 5.0$ and 10.0, for the situation representing case 1, the centrally located (Fig. 6.1a) weakly-scattering $(\omega_2 = 0.1)$ inhomogeneity is responsible for the low value of transmittance $q_t^*\left(0.5,1.0,t^*\right)$ at the center of the north boundary. Whereas in cases 2 and 3, since the weakly-scattering inhomogeniety is offset from the center (Figs. 6.1b and 6.1c), the middle portion of the north boundary receives much higher energy than that of the case 1. Further due to the presence of the weakly-scattering inhomogeneity at the north-west corner (case 2, Fig. 6.1b) of the medium, radiation encounters energy-damping during a later stage of its travel. Opposite is the case with situation represented by case 3 (Fig. 6.1c).

Transmittance $q_t^*\left(0.5,1.0,t^*\right)$ and reflectance $q_r^*\left(0.5,0.0,t^*\right)$ results for cases 4-6 for three different values of the extinction coefficient β for a single-pulse are shown in Figs. 6.4a-f. The scattering albedo of the medium and its inhomogeneity are opposite to that for the results in Figs. 6.3a-f (cases 1-3). In this situation, scattering albedo of the medium and is inhomogeneity are $\omega_1 = 0.1$ and $\omega_2 = 0.998$, respectively. Thus in cases 4-6, the medium is weakly scattering and the inhomogeneity is strongly scattering.

From Figs. 6.4a-f it is seen that for situations representing cases 4-6, transmittance $q_t^*\left(0.5,1.0,t^*\right)$ is less affected by the location of the inhomogeneity. Whereas, for low value of the extinction coefficient $(\beta = 1.0)$, the reflectance $q_r^*\left(0.5,0.0,t^*\right)$ signal depend heavily on the location of the inhomogeneity. Observations in Figs. 6.4a-f are opposite to that of Figs. 6.3a-f.

It is observed from Figs. 6.4a, 6.4c and 6.4e that the temporal profile of the transmittance $q_t^*\left(0.5,1.0,t^*\right)$ signal resembles the incident square pulse. But its peak

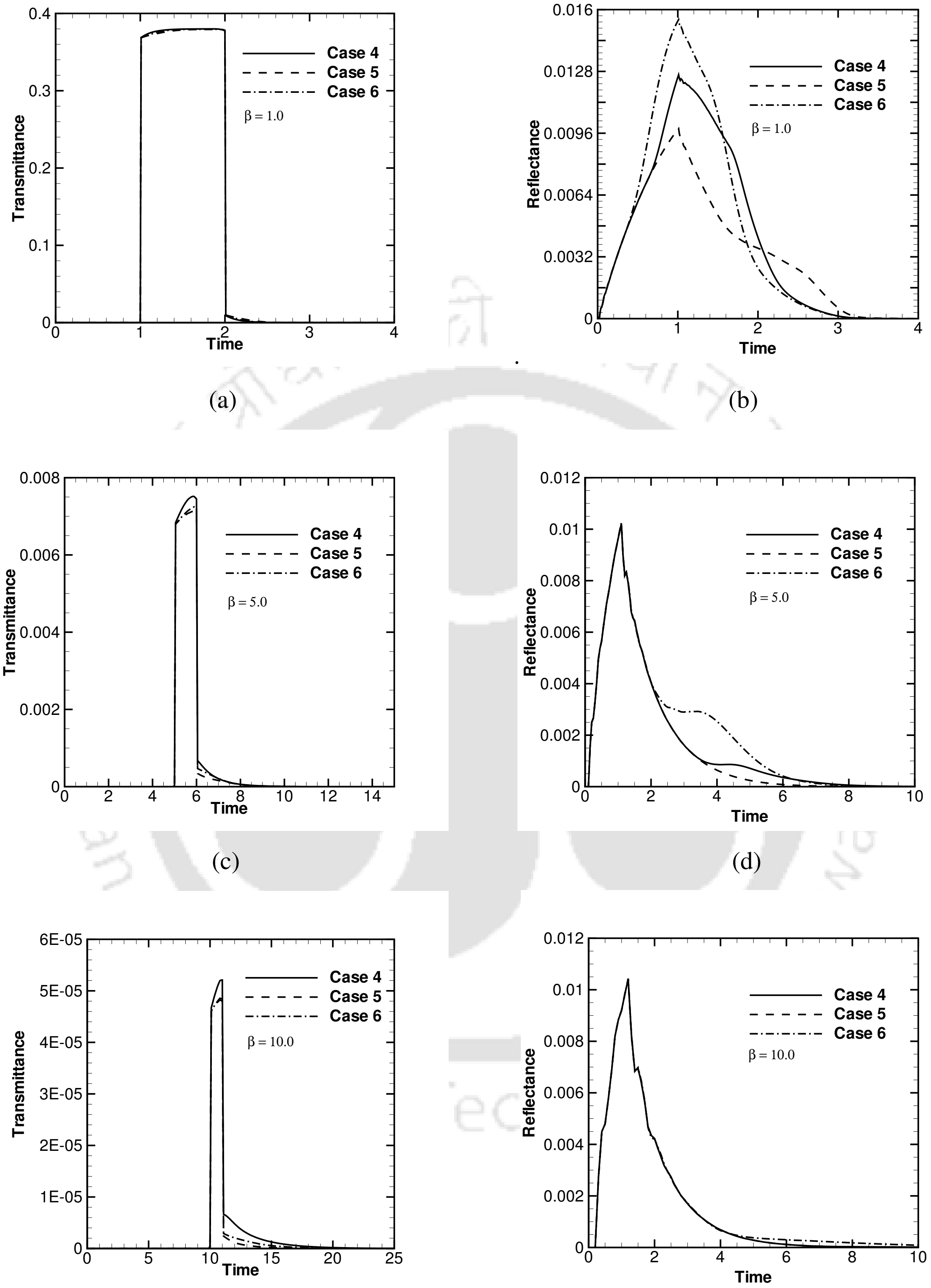

(a) (b)

(c) (d)

(e) (f)

Figure 6.4: Transmittance $q_t^*\left(0.5, 1.0, t^*\right)$ signals and reflectance $q_r^*\left(0.5, 0.0, t^*\right)$ signals for a single pulse for cases 1, 2, 3.

In Figs. 6.5a-f, for cases 1-3, distributions of transmittance $q_t^*\left(\frac{x}{X},1.0,t^*\right)$ and reflectance $q_r^*\left(\frac{x}{X},0.0,t^*\right)$ results along the boundaries have been plotted for three different values of the extinction coefficient $\beta = 1.0.5.0,10.0$. For a given β, these distributions are plotted at 6 time levels, viz. $\frac{t^*}{\Delta t^*} = 100, 200, 300, 400, 600$ and 800. The various cases are differentiated by line types in these figures.

It is seen from Figs. 6.5a-f that for case 1 (Fig. 6.1a), the spatial distributions of transmittance $q_t^*\left(\frac{x}{X},1.0,t^*\right)$ and reflectance $q_r^*\left(\frac{x}{X},0.0,t^*\right)$ signals at all time levels are symmetric about the mid-plane $\left(\frac{X}{2},y\right)$. In Fig.6.5a, for the cases 1-3, due to the low absorption $(\beta = 1.0)$ and strong-scattering $(\omega_1 = 0.998)$ of the medium, the spatial distribution of the transmittance at any time level is almost uniform. But as shown in Fig. 6.5b, the variation in spatial distribution of reflectance $q_r^*\left(\frac{x}{X},0.0,t^*\right)$ at the initial stages is much higher than in the later stages. Due to the presence of a weak-scattering inhomogeneity near the east boundary, the curve corresponding to case 3 (Fig. 6.1c) in Fig. 6.5b is skewed heavily towards the west boundary. A similar trend in the reflectance signals can also be observed for $\beta = 5.0$ in Fig.6.5d and $\beta = 10.0$ in Fig. 6.5f. A sharp skew is observed for a higher value of the extinction coefficient β. This trend is attributed to more diffusion of energy near the middle portion of the south boundary in comparison to the portions close to the east and the west boundaries. In Fig. 6.5c, for case 2, the spatial distribution of transmittance is found to be skewed towards the east boundary. This is due to the presence of a weakly-scattering inhomogeneity at the north-west corner. The skew also tends to get sharper with increasing extinction coefficient (Fig.6.5e). From the above results, it is inferred that an inhomogeneity near a particular boundary exerts more influence on the spatial distribution of a temporal signal at that boundary. The centrally located inhomogeneity does not have much effect on distributions of temporal signals.

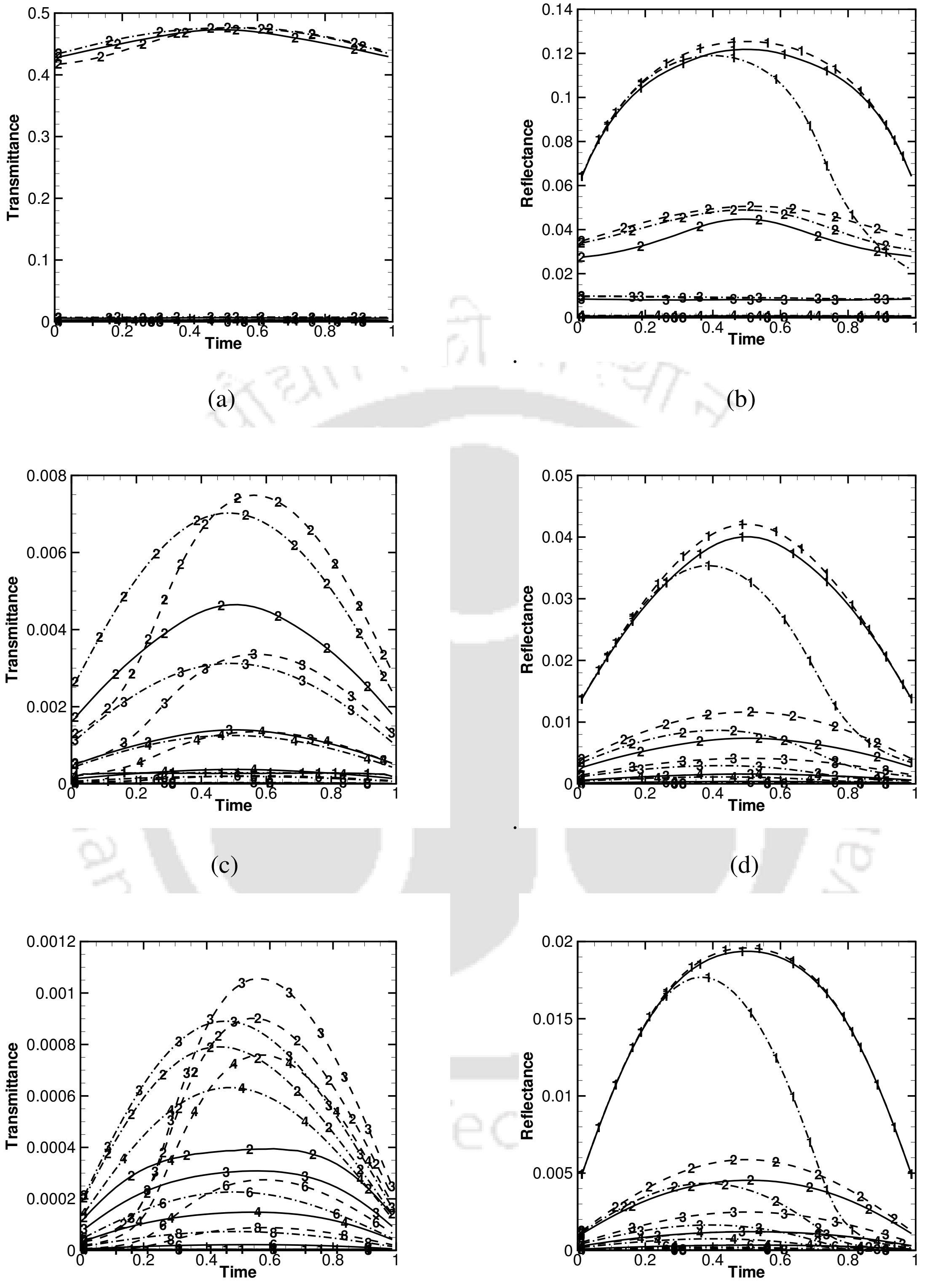

(a) (b)

(c) (d)

(e) (f)

Figure 6.5: Time evolution of the distribution of transmittance $q_t^*\left(x/X,1.0,t^*\right)$ and reflectance $q_r^*\left(x/X,0.0,t^*\right)$ signals along the boundaries. The digit n on any curve indicates the distribution of the signal at $n\times100^{\text{th}}$ time step. Solid, dashed and dotted lines represent cases 1, 2 and 3

In Figs. 6.6a-f, for cases 4-6, distributions of transmittance $q_t^*\left(\frac{x}{X},1.0,t^*\right)$ and reflectance $q_r^*\left(\frac{x}{X},0.0,t^*\right)$ results along the boundaries have been plotted for different values of the extinction coefficient $\beta = 1.0.5.0,10.0$. For a given β, these distributions are plotted at 6 time levels, viz. $\frac{t^*}{\Delta t^*} = 100,200,300,400,600$ and 800. The various cases are differentiated by line types in these figures. For results in Figs. 6.6a-f, the scattering albedo ω of the medium and is inhomogeneity are 0.1 and 0.998, respectively.

Results for cases 4-6 given in Figs. 6.6a-f represent an overall weakly scattering media. In Fig. 6.6a for $\beta = 1.0$ (low absorption), like results in Fig. 6.5a, the spatial distribution of transmittance $q_t^*\left(\frac{x}{X},1.0,t^*\right)$ is almost uniform throughout the boundary at all time levels. The trends are also the same for all the cases. In the present case since the medium and its inhomogeneity are low absorbing $(\beta = 1.0)$ and the medium is weakly scattering $(\omega_1 = 0.1)$, the location of a strongly-scattering inhomogeneity does not influence the distribution of temporal signals along the north boundary.

In Figs. 6.6c and 6.6e, with $\beta = 5.0$ and 10.0 (high absorption), for case 5, the transmittance towards the west side of the north boundary is much higher than that near the east side. The presence of a strongly- scattering inhomogeneity near the north-west corner is responsible for such a difference. similar to situation when $\beta = 1.0$, in Fig.6.6d, A skew towards the east boundary is observed in the trend corresponding to the case 6, due to the presence of a strongly-scattering inhomogeneity at the bottom-right corner of the geometry. Effects of the locations of inhomogeneity represented by cases 4-6 on reflectance $q_r^*\left(\frac{x}{X},0.0,t^*\right)$ signals for three values β have been shown in Figs. 6.6b, 6.6d and 6.6f. For all locations of the inhomogeneity, at all instants, the effect on reflectance signal is found

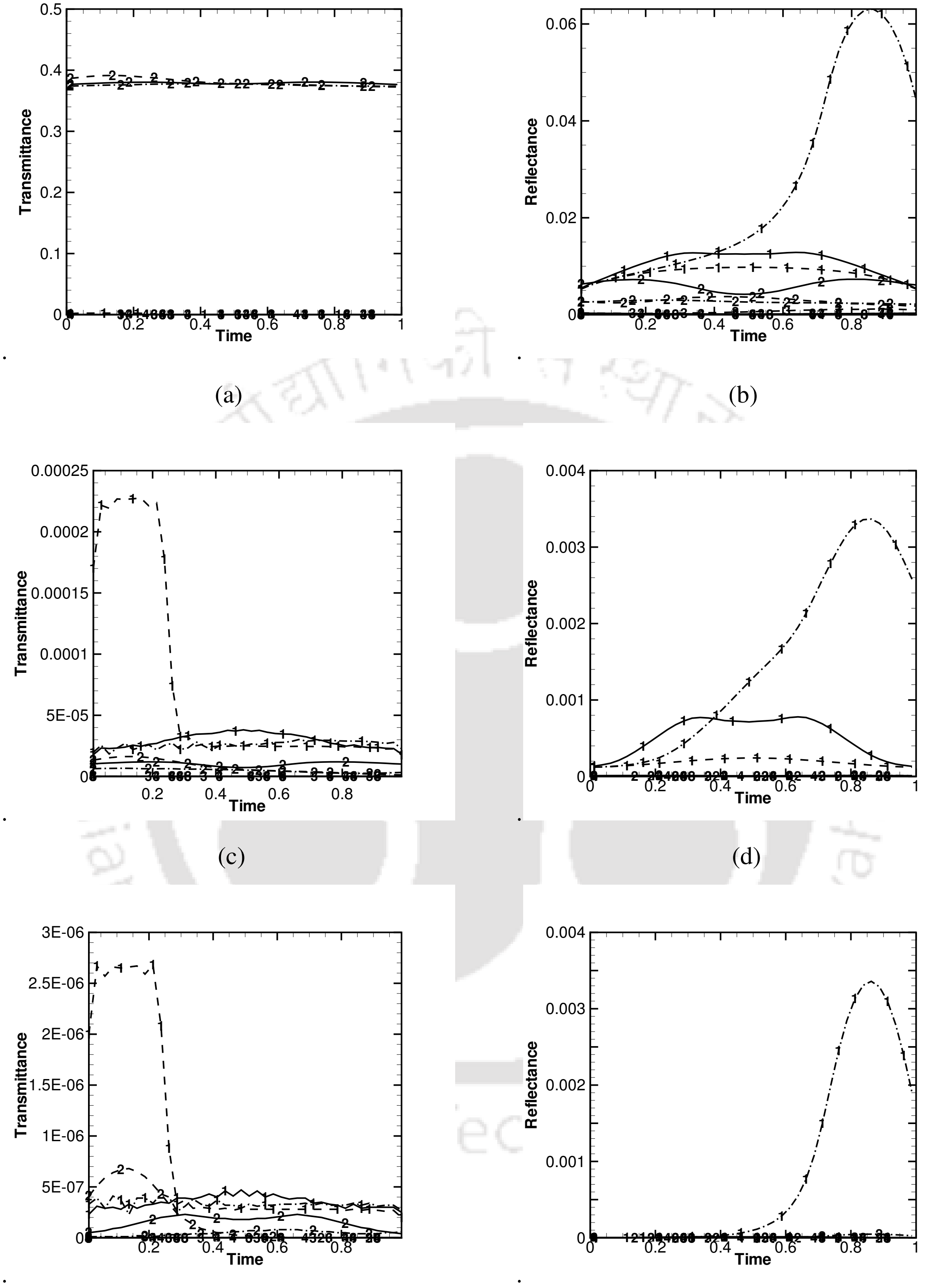

(a) (b)

(c) (d)

(e) (f)

Figure 6.6: Time evolution of the distribution of transmittance $q_t^*\left(x/X,1.0,t^*\right)$ and reflectance $q_r^*\left(x/X,0.0,t^*\right)$ signals along the boundaries. The digit n on any curve indicates the distribution of the signal at $n\times100^{\text{th}}$ time step. Solid, dashed and dotted lines are results for cases 4, 5 and 6.

to decrease with increase in β. With inhomogeneity located in the south-east corner (case 6, Fig. 6.1c), reflectance signals at an early instant $\left(\frac{t^*}{\Delta t^*}=100\right)$ are more prominent. At other times, magnitudes of the signals decrease.

Figures 6.7-6.12 provide heat flux $q^*\left(\frac{x}{X},\frac{y}{Y},t^*\right)$ contours in the medium for cases 1-6, respectively. In each of these figures, the contours have plotted at six time levels, viz. $\frac{t^*}{\Delta t^*}=50,100,200,400,600\,\text{and}\,800$. With a single pulse incident on the south boundary, in Figs. 6.7-6.9, results are presented for cases 1, 2 and 3, respectively. With $\beta=5.0$ and a 4-pulse train incident on the south boundary, flux contours have been plotted for cases 4, 5 and 6 in Figs. 6.10, 6.11 and 6.12, respectively.

Figures 6.7a-f show heat flux $q^*\left(\frac{x}{X},\frac{y}{Y},t^*\right)$ contours at six time levels $\frac{t^*}{\Delta t^*}=50,100,200,400,600\,\text{and}\,800$, respectively for a centrally located inhomogeneity (Case 1, Fig. 6.1a). From Figs. 6.7a and 6.7b, it is observed that for a single-pulse, at $\frac{t^*}{\Delta t^*}=50$ and 100, negative heat flux appears near the south boundary. It is to be noted that the negative heat flux contributes towards the reflectance $q_r^*\left(\frac{x}{X},0.0,t^*\right)$ signals. From Figs. 6.7a and 6.7b, a high heat flux values are observed in and around the central inhomogeneity. At $\frac{t^*}{\Delta t^*}=200$, it is observed from Fig. 6.7c that a negative heat flux which contributes towards reflectance is well established within the medium. A central region of negative heat flux is seen in the vicinity of the inhomogeneity. As the time progresses, as is seen from Figs. 6.7d-f, magnitude of heat flux decreases and its distribution is homogeneous. At $\frac{t^*}{\Delta t^*}=800$, the signal has died

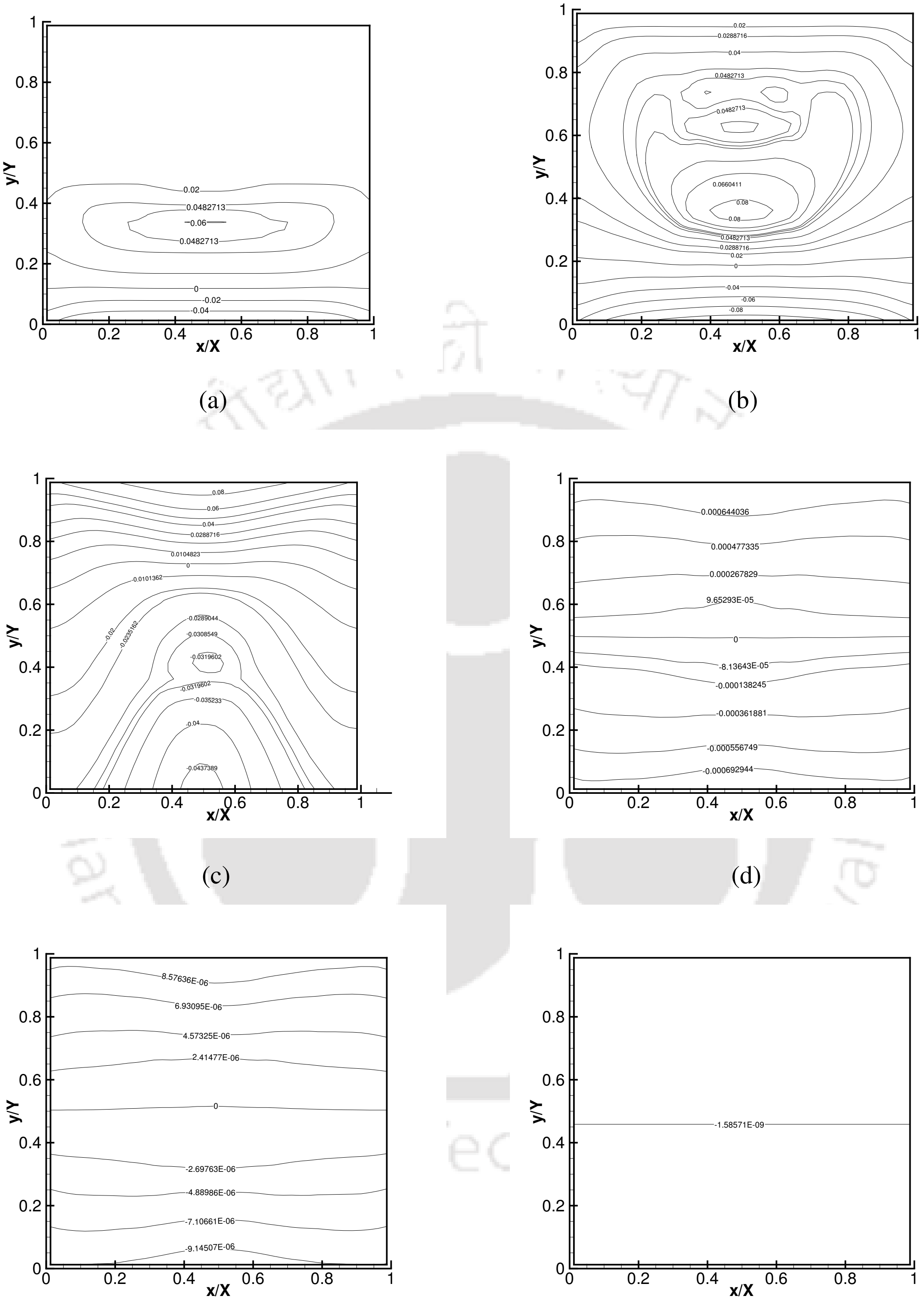

(a) (b)

(c) (d)

(e) (f)

Figure 6.7: Heat flux contours in the medium at time $\frac{t^*}{\Delta t^*}$ (a) = 50, (b) = 100, (c) = 200, (d) = 400 (e) = 600 (f) = 800 for β=1.0 and a single-pulse for Case 1.

With an inhomogeneity located in the north-west corner (Fig. 6.1b) for case 2, Figs 6.8a-f show heat flux contours at $\frac{t^*}{\Delta t^*} = 50, 100, 200, 400, 600 \text{ and } 800$, respectively. With $\beta = 1.0$, at $\frac{t^*}{\Delta t^*} = 50$, radiation reaches only half-way in the medium. Thus unlike a centrally located inhomogeneity (Fig. 6.7a), the inhomogeneity located in the north-west corner is not seen to have any effect on the heat flux contours.

At $\frac{t^*}{\Delta t^*} = 100$, radiation has just reached the other boundary and has also encountered the inhomogeneity, the heat flux contours are seen to be most affected in and around the north-west corner. As time has progressed, it is seen from Fig.6.8c that at $\frac{t^*}{\Delta t^*} = 200$, the negative heat flux extends beyond the central region and effect of inhomogeneity remain more in the north-west corner. With further passage of time, the domain of negative heat flux shifts towards the south boundary and magnitude of both positive and negative heat fluxes decrease with time. At $\frac{t^*}{\Delta t^*} = 800$, it is seen from Fig. 6.8f that the signal vanishes.

Effect of a localized inhomogeneity present in the south-east corner (case 3, Fig. 6.1c) on heat flux contours has been shown in Figs. 6.9a-f at $\frac{t^*}{\Delta t^*} = 50, 100, 200, 400, 600 \text{ and } 800$, respectively. Since in this case, unlike the case of Fig. 6.8a, at $\frac{t^*}{\Delta t^*} = 50$, radiation has already encountered the inhomogeneity, heat flux contours in the vicinity of the inhomogeneity is affected at an early stage. Like Fig. 6.9a, in Fig. 6.9b which shows results at $\frac{t^*}{\Delta t^*} = 100$, the effect is more prominent in the south-east corner. It is seen from Figs. 6.9c-e that with the passage of time, the influence of the inhomogeneity decreases, magnitude of the heat flux decreases and its distribution in the medium is more uniform. Like other two cases (Figs. 6.7f and 6.8f), at $\frac{t^*}{\Delta t^*} = 800$, the signal dies out.

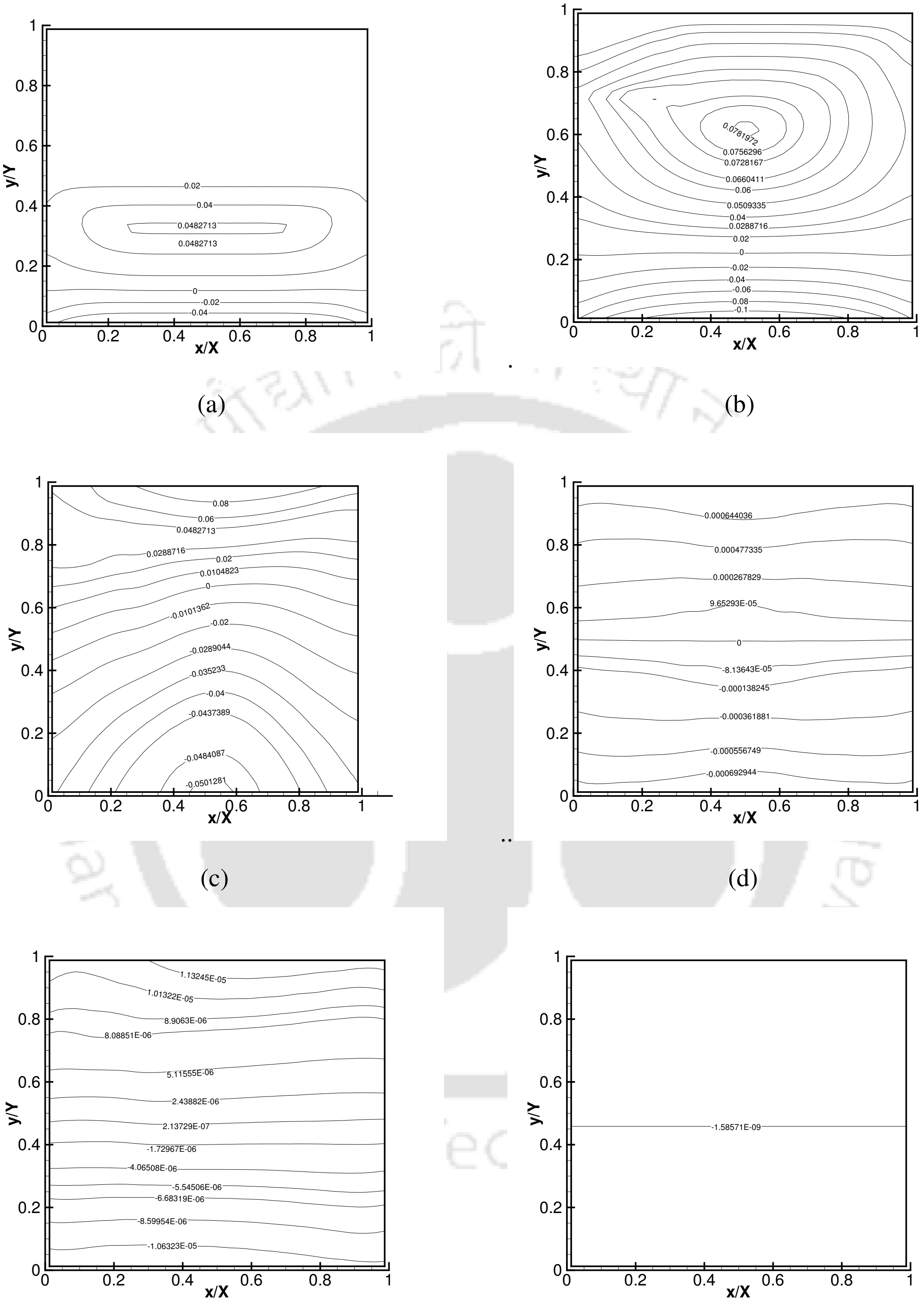

(a) (b)

(c) (d)

(e) (f)

Figure 6.8: Heat flux contours in the medium at time $\frac{t^*}{\Delta t^*}$ (a) = 50, (b) = 100, (c) = 200, (d) = 400 (e) = 600 (f) = 800 for β=1.0 and a single-pulse for Case 2.

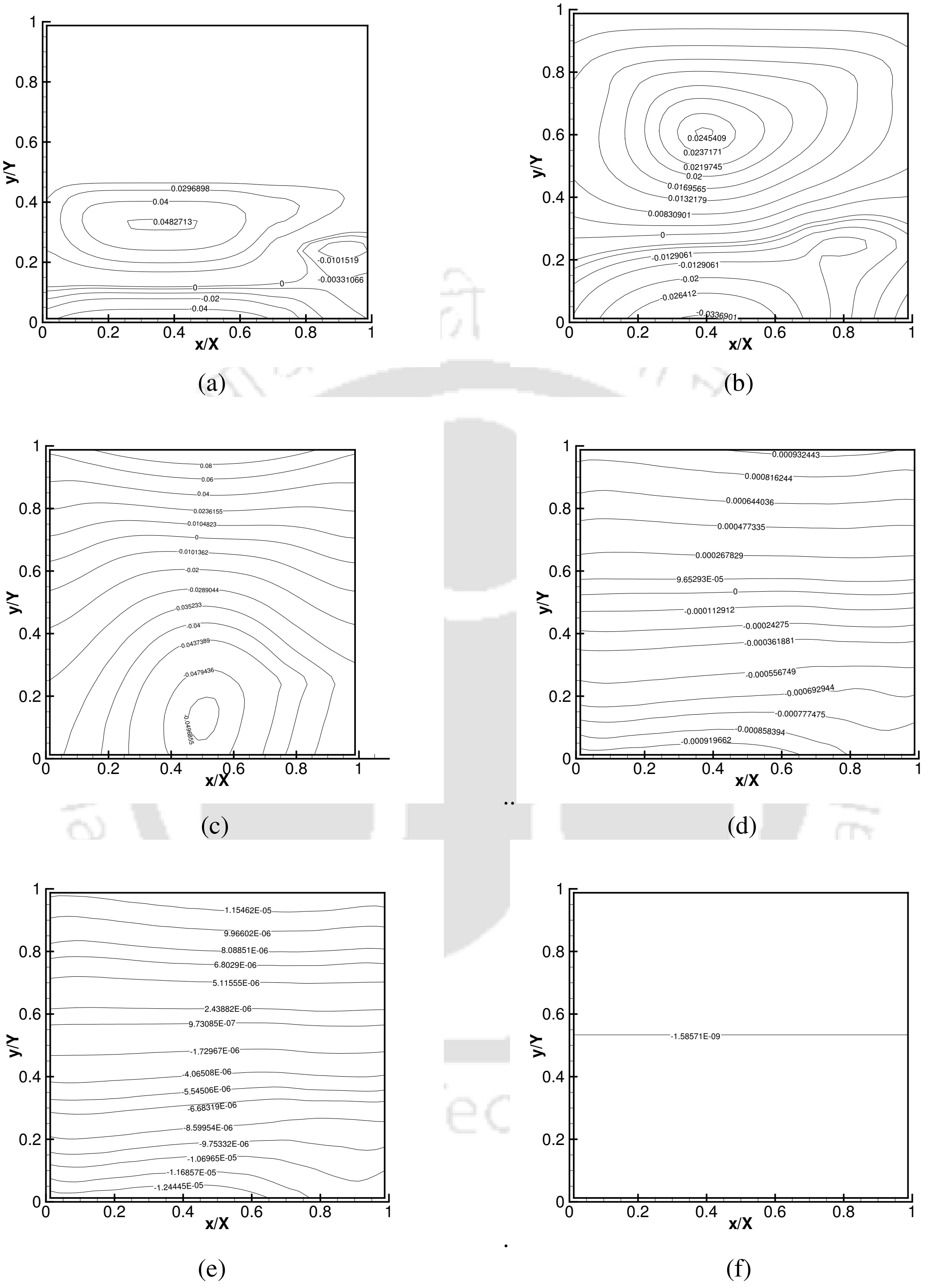

(a) (b)

(c) (d)

(e) (f)

Figure 6.9: Heat flux contours in the medium at time $\frac{t^*}{\Delta t^*}$ (a) = 50, (b) = 100, (c) = 200, (d) = 400 (e) = 600 (f) = 800 for β=1.0 and a single-pulse for Case 3.

Observation of Figs. 6.7-6.9 shows that at an early stage $\left(\frac{t^*}{\Delta t^*}=50\right)$, unless radiation reaches inhomogeneity, no noticeable effect is found. At $\frac{t^*}{\Delta t^*}=100$, radiation reaches the north boundary, in all three cases, localized inhomogeneity is seen to have influence over heat flux contours. The effect is seen to be the maximum in case 3 in which case radiation is more intense when it encounters the inhomogeneity. When the inhomogeneity is located in the north-west corner, effect is seen to be minimal. In all three cases, signal is seen to die at $\frac{t^*}{\Delta t^*}=800$.

With extinction coefficient $\beta=5.0$ and a 4-pulse train incident normal to the south boundary, for cases 4-6, heat flux contours have been shown in Figs. 6.10-6.12 respectively. Like results in Figs. 6.7-6.9, here too, heat flux contours have been studied at six time levels, viz., $\frac{t^*}{\Delta t^*}=50, 100, 200, 400, 600 \text{ and } 800$. Unlike situations considered in Figs. 6.7-6.9 for cases 1-3, results in Figs.6.10-6.12 corresponding to cases 4-6 are for strongly scattering $(\omega=0.998)$ inhomogeneity and weakly scattering medium $(\omega=0.1)$.

It is seen from Figs. 6.10a, 6.11a and 6.12a that at an early stage $\frac{t^*}{\Delta t^*}=50$, the heat flux contours are concentrated in the lower half portion and inhomogeneity placed in the south-east corner has more influence. Since at $\frac{t^*}{\Delta t^*}=50$, radiation has not gone beyond the middle portion of the medium, no heat flux is visible in the upper half region.

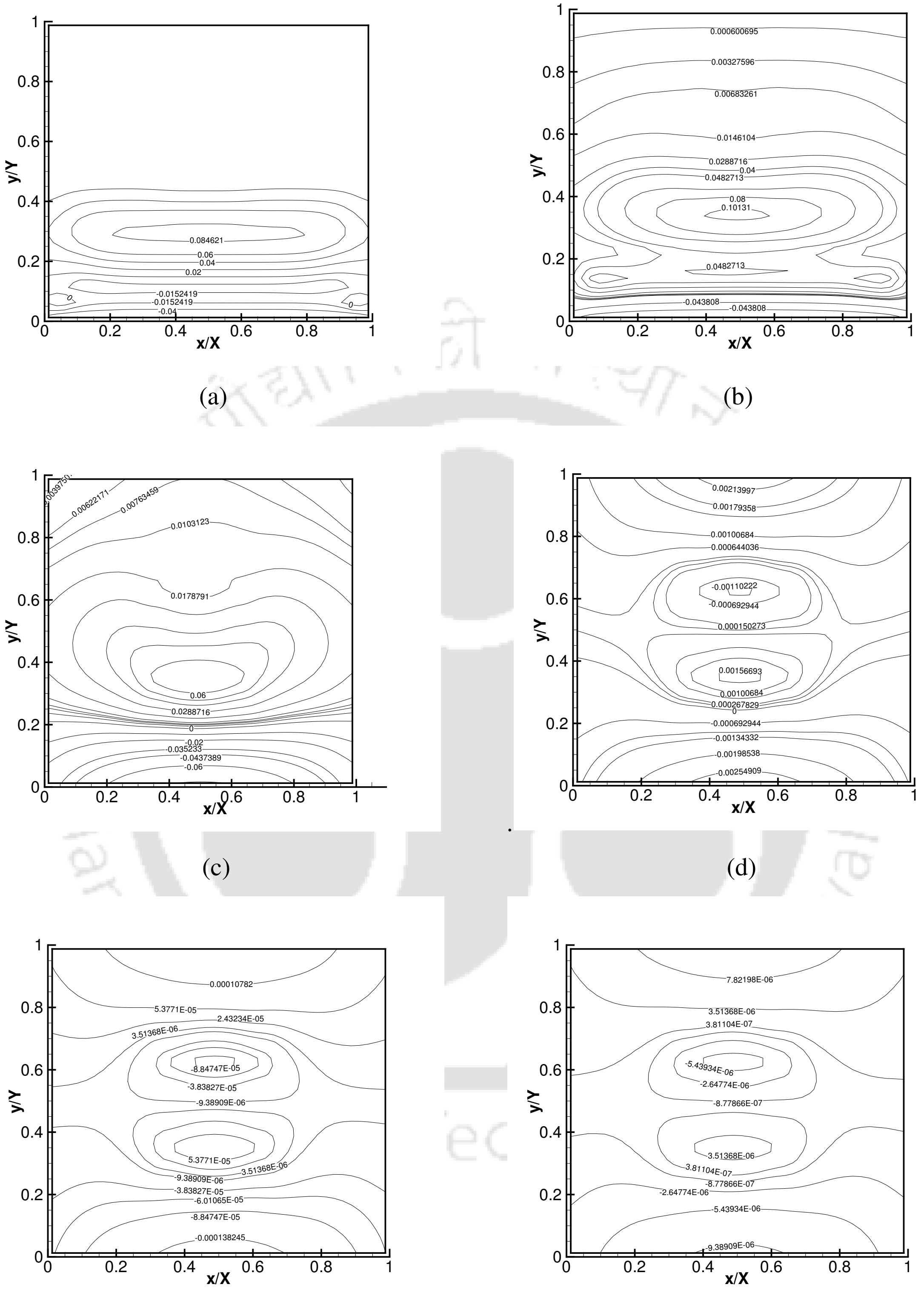

(a) (b)

(c) (d)

(e) (f)

Figure 6.10: Heat flux contours in the medium at time $\frac{t^*}{\Delta t^*}$ (a) = 50, (b) = 100, (c) = 200, (d) = 400 (e) = 600 (f) = 800 for $\beta = 5.0$ and a 4-pulse for Case 4.

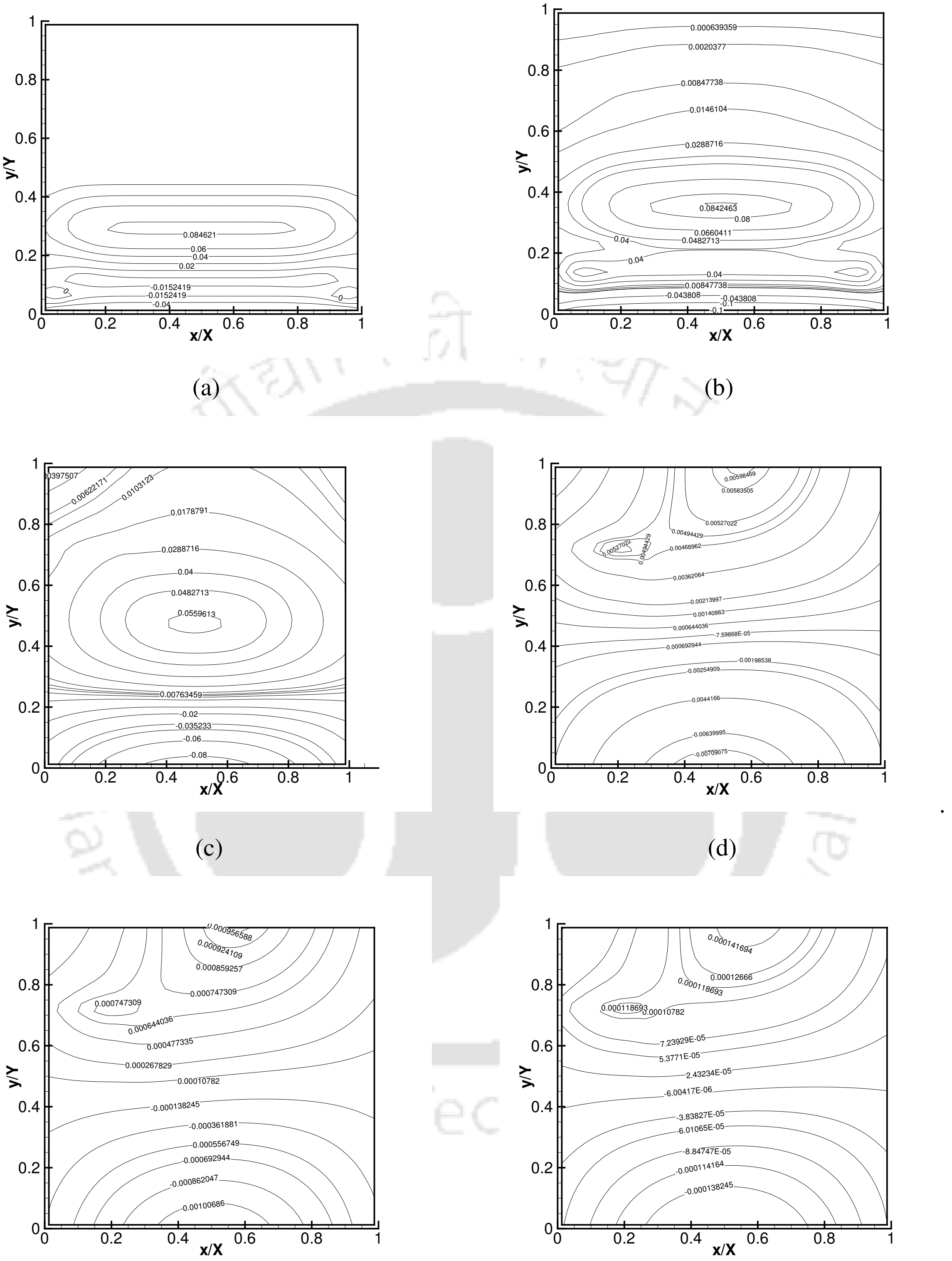

(a) (b)

(c) (d)

(e) (f)

Figure 6.11: Heat flux contours in the medium at time $\frac{t^*}{\Delta t^*}$ (a) = 50, (b) = 100, (c) = 200, (d) = 400 (e) = 600 (f) = 800 for $\beta = 5.0$ and a 4-pulse for Case 5.

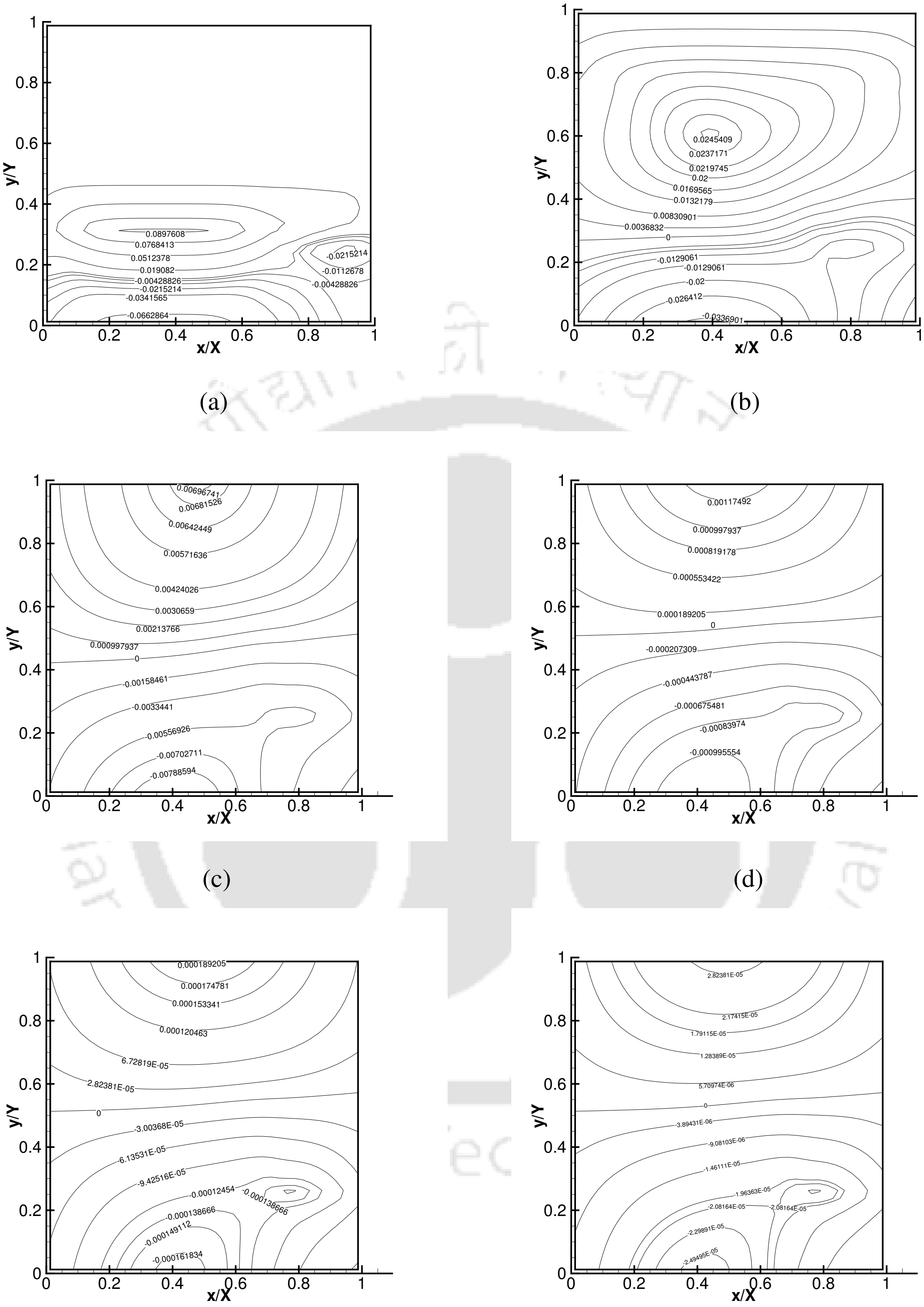

(a) (b)

(c) (d)

(e) (f)

Figure 6.12: Heat flux contours in the medium at time $\frac{t^*}{\Delta t^*}$ (a) = 50, (b) = 100, (c) = 200, (d) = 400 (e) = 600 (f) = 800 for $\beta = 5.0$ and a 4-pulse for Case 6.

At $\frac{t^*}{\Delta t^*} = 100$, it is seen from Figs. 6.10b, 6.11b and 6.12b that inhomogeneities have more influence near the south boundary. The influence is symmetric about the mid-plane in Figs. 6.10b and 6.11b. In case of Fig. 6.12b when the inhomogeneity is located in the south-east corner, heat flux contours are skewed in the region housing inhomogeneity. In all three figures, the region of the negative heat flux is seen concentrated near the south boundary.

At $\frac{t^*}{\Delta t^*} = 200, 400$ and 600, heat flux contours for cases 4-6 have been shown in Figs. 6.10c-e, 6.11c-e and 6.12c-e, respectively. From Figs. 6.10c-e, it is seen that with the passage of time, in the central region where the inhomogeneity is located, zones of negative and positive heat fluxes originate. An alternate zone of negative and positive heat fluxes are seen in Figs. 6.10d and 6.10e. In Figs. 6.11c-e, the fluxes arising from the inhomogeneity at the $\frac{t^*}{\Delta t^*} = 200, 400$ and 600 are positive and contribute towards the transmittance. This is due to the strong scattering nature of the inhomogeneity. From Figs. 6.12c-e, it is observed that the fluxes emanating due to inhomogeneity at the south-east corner of the medium are negative at $\frac{t^*}{\Delta t^*} = 200, 400$ and 600 and they contribute towards the reflectance.

At $\frac{t^*}{\Delta t^*} = 800$, it is observed from Figs. 6.10f, 6.11f and 6.12f that unlike the cases considered in Figs. 6.7f, 6.8f and 6.10f, the heat flux remain available throughout the medium and the effect of the location of inhomogeneity is obvious. Since in this case, the medium is more participating $(\beta = 5)$ and the energy content in the incident pulse is also more, signals exist for a longer duration.

6.4 Results and Discussion – Gaussian pulse train

The same validation that is done for the multi-pulse of step profile holds good for a Gaussian multi-pulse. Therefore, in the following pages, results for a square medium $\left(\frac{X}{Y}=1\right)$ containing a square shaped inhomogeneity are discussed. The cases involved are the same.

The trends of the transmittance $q_t^*\left(0.5,1.0,t^*\right)$ (Fig 6.13a, 6.13c and 6.13e) and reflectance $q_r^*\left(0.5,0.0,t^*\right)$ (Fig 6.13b, 6.13d and 6.13f) signals resemble the trends of the 1-D planar participating medium for all the values of extinction coefficient $\beta=1.0,5.0$ and 10.0. For all three values of β, the trends of the transmittance $q_t^*\left(0.5,1.0,t^*\right)$ (Fig 6.13a, 6.13c and 6.13e) and reflectance $q_r^*\left(0.5,0.0,t^*\right)$ (Fig 6.13b, 6.13d and 6.13f) signals resemble the trends of the 1-D planar medium, but their temporal lives are much shorter [101]. With $\beta=1.0$, the peak magnitudes of the signals are also approach that of the 1-D case while for $\beta=5.0$ and 10.0, they are quite different [101]. It is observed Figs. 6.13a, 6.13c and 6.13d that with increase in β, the location of the inhomogeneity has a marked effect on transmittance $q_t^*\left(0.5,1.0,t^*\right)$. However, it is seen from Figs. 6.13b, 6.13d and 6.13f that location of the inhomogeneity has only effect on the reflectance $q_r^*\left(0.5,1.0,t^*\right)$.

In Cases 1-3, a large (3/4th) volume of the medium is strongly scattering $\left(\omega_1=0.998\right)$ and the inhomogeneity which occupies 1/4th of the volume is weak scattering $\left(\omega_2=0.1\right)$. When the medium is less participating $\left(\beta=1.0\right)$, the location of the inhomogeneity has almost no effect on the transmittance $q_t^*\left(0.5,1.0,t^*\right)$ (Fig 6.13a) and reflectance $q_r^*\left(0.5,0.0,t^*\right)$ signals (Fig 6.13b) captured at the middle of the boundaries. But when the medium becomes more absorbing $\left(\beta=5.0,10.0\right)$, the

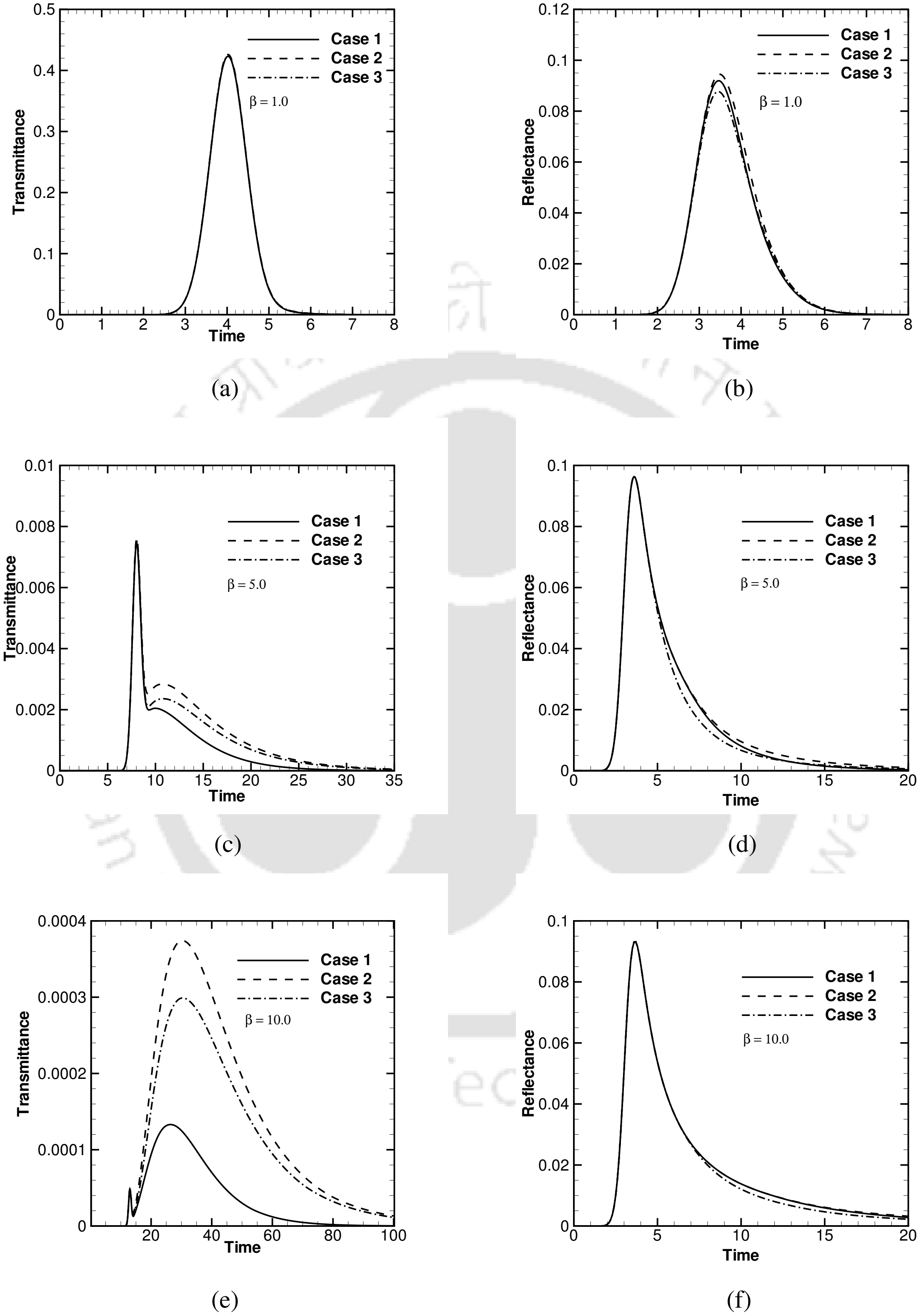

Figure 6.13: Transmittance $q_t^*\left(0.5,1.0,t^*\right)$ signals and reflectance $q_r^*\left(0.5,0.0,t^*\right)$ signals for a single pulse for cases 1, 2, 3.

location of the inhomogeneity has more effect on the transmittance $q_t^*\left(0.5,1.0,t^*\right)$ signals as seen from Figs. 6.13c and 6.13e.

With $\beta = 5.0$ and 10.0, for the situation representing Case 1, the centrally located (Fig. 6.1a) weakly-scattering $\left(\omega_2 = 0.1\right)$ inhomogeneity is responsible for the low magnitude of transmittance $q_t^*\left(0.5,1.0,t^*\right)$ at the center of the north boundary. Whereas in cases 2 and 3, since the weakly-scattering inhomogeniety is offset from the center (Figs. 6.1b and 6.1c), the middle portion of the north boundary receives considerably more energy than that of the case 1. Further due to the presence of the weakly-scattering inhomogeneity at the north-west corner (case 2, Fig. 6.1b) of the medium, radiation encounters energy-damping during a later stage of its travel. Opposite is the case with situation represented by case 3 (Fig. 6.1c).

Transmittance $q_t^*\left(0.5,1.0,t^*\right)$ and reflectance $q_r^*\left(0.5,0.0,t^*\right)$ results for Cases 4-6 for three different values of the extinction coefficient β for a single-pulse are shown in Figs. 6.14a-f. The inhomogeneities in these Cases are strongly-scattering. In this situation, scattering albedo of the medium and is inhomogeneity are $\omega_1 = 0.1$ and $\omega_2 = 0.998$, respectively.

From Figs. 6.14a-f it is seen that for situations representing cases 4-6, transmittance $q_t^*\left(0.5,1.0,t^*\right)$ is less affected by the location of the inhomogeneity. Whereas, for a medium of less attenuation $\left(\beta = 1.0\right)$, the reflectance $q_r^*\left(0.5,0.0,t^*\right)$ signal depend heavily on the location of the inhomogeneity. It is observed from Figs. 6.14a, 6.14c and 6.14e that the temporal profile of the transmittance $q_t^*\left(0.5,1.0,t^*\right)$ signals resemble the incident Gaussian pulse. But their peak magnitudes decrease with increase in β. It can also be observed that the temporal spans of the transmittance $q_t^*\left(0.5,1.0,t^*\right)$ signals remain almost the same for all values of β and it is equal to the temporal stay of the Gaussian pulse $2\,t_c^* = 6t_p^* = 6.0$.The above trend of the transmittance signals is attributed to the strongly-scattering inhomogeneity.

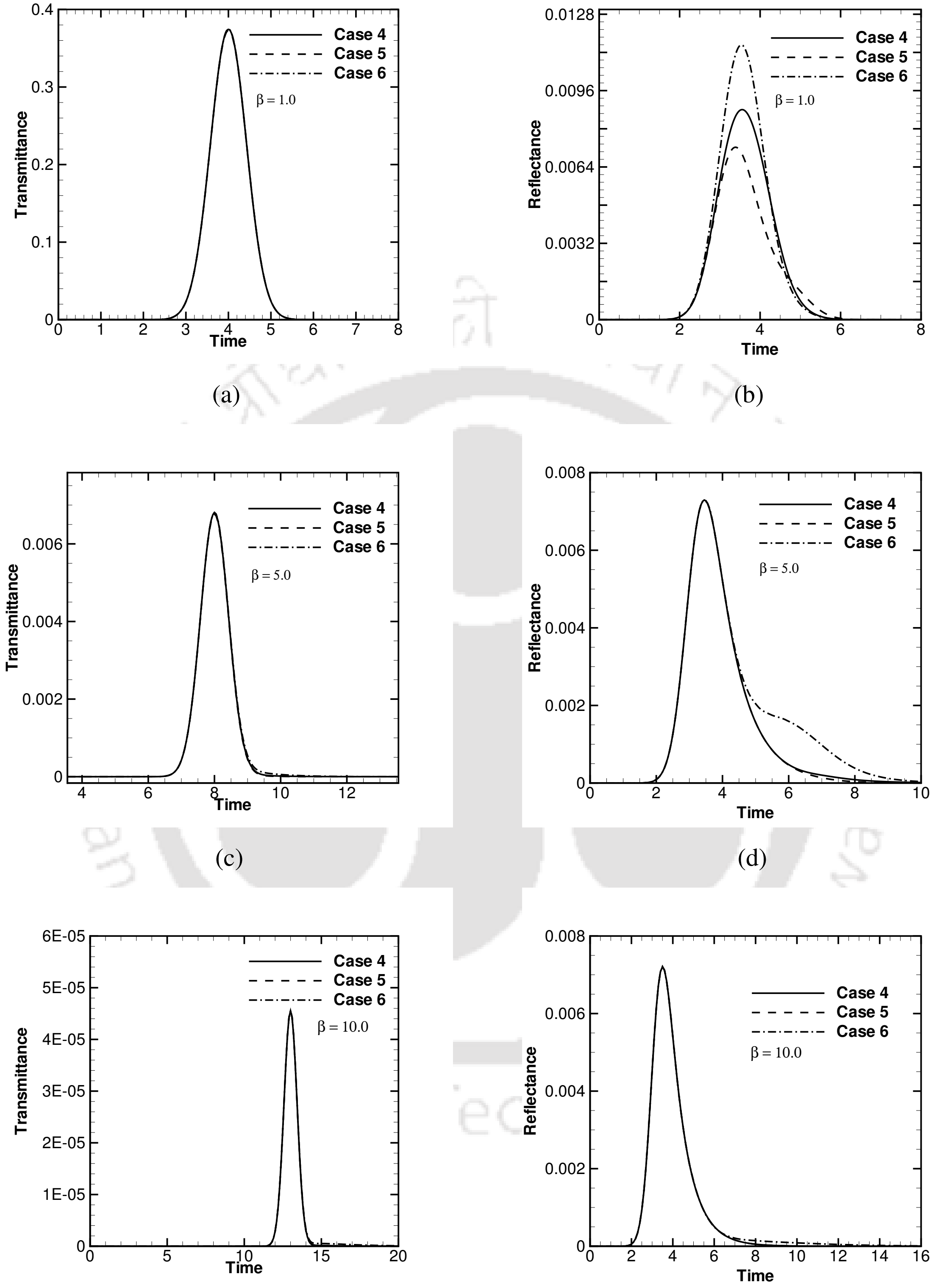

(a) (b)

(c) (d)

(e) (f)

Figure 6.14: Transmittance $q_t^*\left(0.5, 1.0, t^*\right)$ signals and reflectance $q_r^*\left(0.5, 0.0, t^*\right)$ signals for a single pulse for cases 1, 2, 3.

In Figs. 6.15a-f, for cases 1-3, distributions of transmittance $q_t^*\left(\frac{x}{X},1.0,t^*\right)$ and reflectance $q_r^*\left(\frac{x}{X},0.0,t^*\right)$ results along the boundaries have been plotted for three different values of the extinction coefficient $\beta=1.0.5.0,10.0$. For a given β, these distributions are plotted at 6 time levels, viz. $\frac{t^*}{\Delta t^*}=100,200,300,400,600$ and 800. The various cases are differentiated by line-types in these figures. The digit n on any curve indicates the distribution of the signal at $n\times100^{\text{th}}$ time step. Solid, dashed and dotted lines are results for cases 4, 5 and 6 respectively.

It is seen from Figs. 6.15a-f that for Case 1 (Fig. 6.1a), the spatial distributions of transmittance $q_t^*\left(\frac{x}{X},1.0,t^*\right)$ and reflectance $q_r^*\left(\frac{x}{X},0.0,t^*\right)$ signals at all time levels are symmetric about the mid-plane $\left(\frac{X}{2},y\right)$. In Fig.6.15a, for the Cases 1-3, due to the low absorption $(\beta=1.0)$ and strong-scattering $(\omega_1=0.998)$ of the medium, the spatial distribution of the transmittance at any time level is almost uniform. But as shown in Fig. 6.15b, the variation in spatial distribution of reflectance $q_r^*\left(\frac{x}{X},0.0,t^*\right)$ at the initial stages is much higher than in the later stages.

Due to the presence of a weak-scattering inhomogeneity near the east boundary, the curve corresponding to Case 3 (Fig. 6.1c) in Fig. 6.15b is skewed heavily towards the west boundary. A similar trend in the reflectance signals can also be observed for $\beta=5.0$ in Fig.6.15d and $\beta=10.0$ in Fig. 6.15f. A sharp skew is noticed for a higher value of the extinction coefficient β. This trend is attributed to more diffusion of energy near the middle portion of the south boundary in comparison to the portions close to the east and the west boundaries. In Fig. 6.15c, for Case 3, the spatial distribution of transmittance is found to be skewed towards the west boundary. This is due to the presence of a weakly-scattering inhomogeneity at the south-east corner. The skew also tends to get sharper with increasing extinction coefficient (Fig.6.15e).

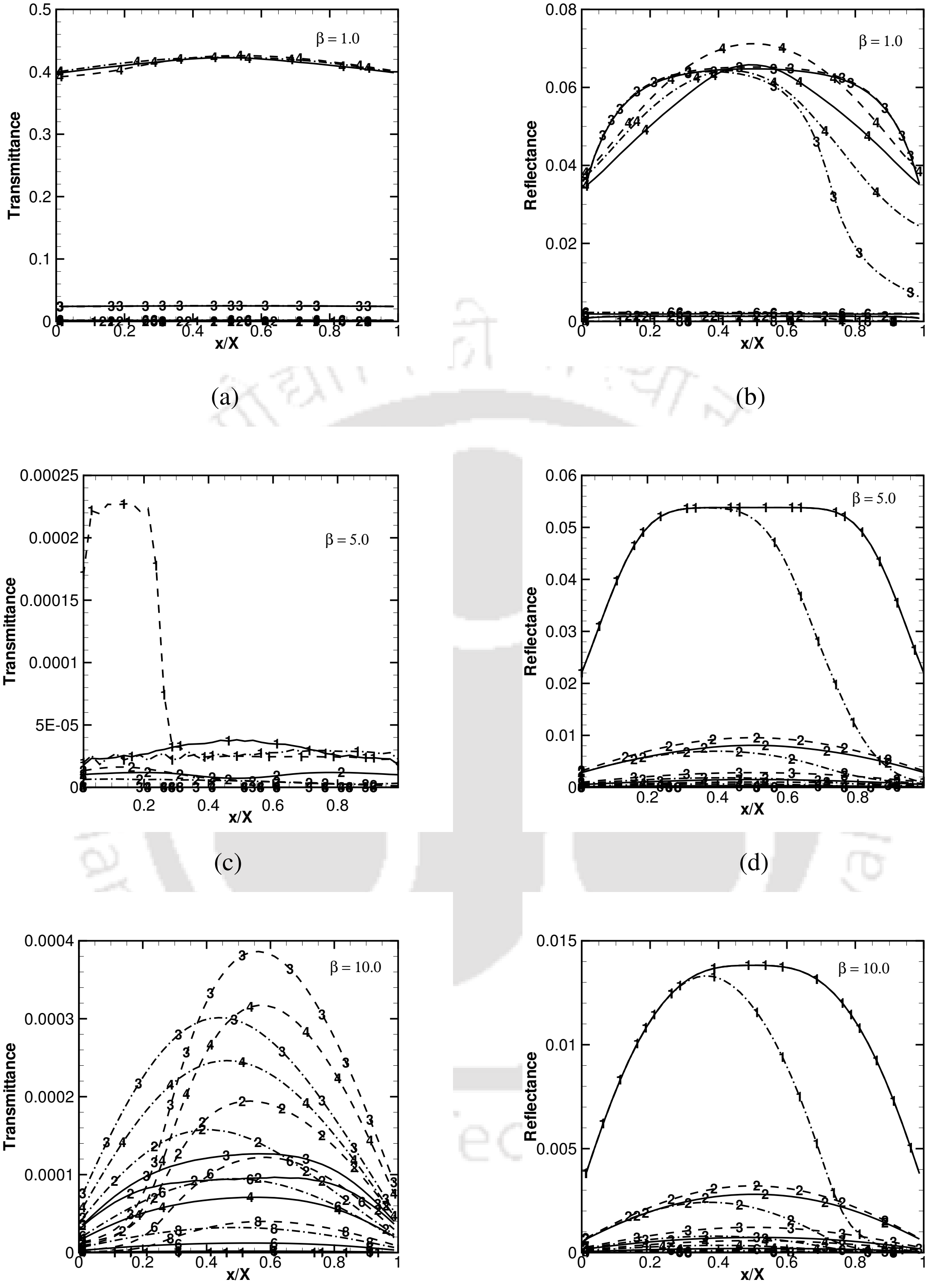

(a) (b)

(c) (d)

(e) (f)

Figure 6.15: Time evolution of the distribution of transmittance $q_t^*\left(x/X,1.0,t^*\right)$ and reflectance $q_r^*\left(x/X,0.0,t^*\right)$. The digit n on any curve indicates the distribution of the signal at $n\times100^{\text{th}}$ time step. Solid, dashed and dotted lines are results for cases 1, 2 and 3 respectively.

From the above results, it is inferred that an inhomogeneity near a particular boundary wield more effect on the spatial distribution of a temporal signal at that boundary. The centrally located inhomogeneity tends to distribute the temporal signals symmetrically about the mid-plane.

In Figs. 6.16a-f, for Cases 4-6, distributions of transmittance $q_t^*\left(\frac{x}{X},1.0,t^*\right)$ and reflectance $q_r^*\left(\frac{x}{X},0.0,t^*\right)$ results along the boundaries have been plotted for different values of the extinction coefficient $\beta = 1.0.5.0,10.0$. For a given β, these distributions are plotted at 6 time levels, viz. $\frac{t^*}{\Delta t^*} = 100, 200, 300, 400, 600$ and 800. Similar to Figs.6.15a-f , the various cases are differentiated by line types in these figures. For results in Figs. 6.16a-f, the scattering albedo ω of the medium and is inhomogeneity are 0.1 and 0.998, respectively.

Results for cases 4-6 given in Figs. 6.16a-f represent an overall weakly scattering media. In Fig. 6.16a for $\beta = 1.0$ (low absorption), like results in Fig. 6.15a, the spatial distribution of transmittance $q_t^*\left(\frac{x}{X},1.0,t^*\right)$ is observed to be almost uniform throughout the boundary at all time levels. The trends are also the same for all the cases. In the present case since both the medium and its inhomogeneity are low absorbing $(\beta = 1.0)$ and the medium is weakly scattering $(\omega_1 = 0.1)$, the location of a strongly-scattering inhomogeneity does not influence the distribution of temporal signals along the north boundary.

In Figs. 6.16c and 6.16d, with $\beta = 5.0$ (moderate absorption) and 10.0 (high absorption), for case 5, the transmittance towards the west side of the north boundary is much higher than that near the east side. The presence of a strongly- scattering inhomogeneity near the north-west corner is responsible for such a difference.
Due to the presence of a strongly scattering inhomogeneity at the bottom-right corner of the geometry, a trend with a skew towards the east boundary similar to Fig.6.16b is

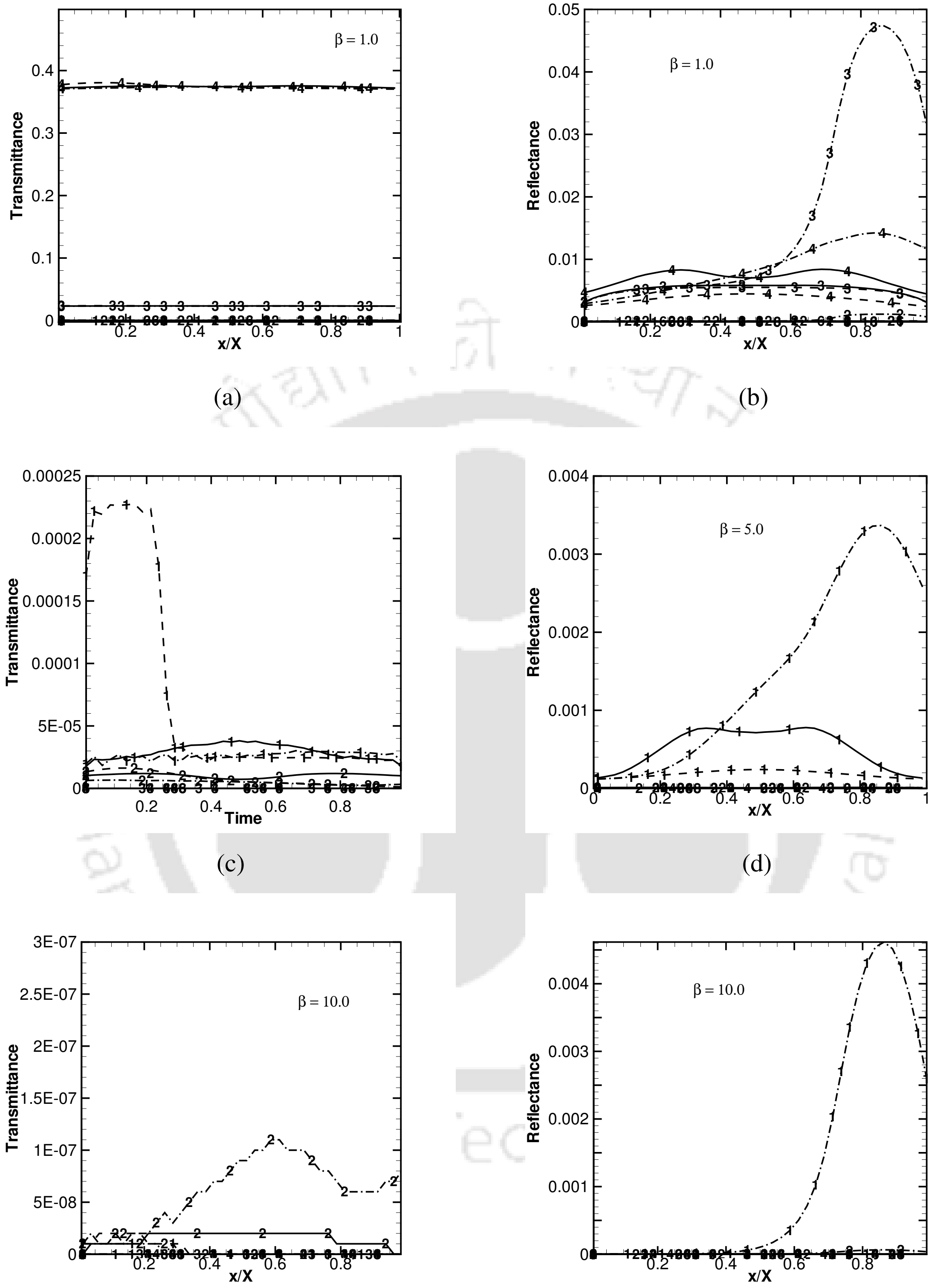

(a) (b)

(c) (d)

(e) (f)

Figure 6.16: Time evolution of the distribution of transmittance $q_t^*\left(x/X, 1.0, t^*\right)$ and reflectance $q_r^*\left(x/X, 0.0, t^*\right)$ signals along the boundaries. The digit n on any curve indicates the distribution of the signal at $n\times100^{\text{th}}$ time step. Solid, dashed and dotted lines are results for cases 4, 5 and 6 respectively.

observed in Fig. 6.16d. From Figs.6.16b, 6.16d and 6.16f the effects of the locations of inhomogeneity represented by Cases 4-6 on reflectance $q_r^*\left(\frac{x}{X}, 0.0, t^*\right)$ signals for three values β can be observed. Irrespective of the location of the inhomogeneity, at all instants, the effect of reflectance signal is found to decrease with the increase in β. With inhomogeneity located in the south-east corner (case 6, Fig. 6.1c), reflectance signals at an early instant $\left(\frac{t^*}{\Delta t^*} = 100\right)$ are more prominent. At other times, magnitudes of the signals decrease.

Figures 6.17-6.19 provide heat flux $q^*\left(\frac{x}{X}, \frac{y}{Y}, t^*\right)$ contours in the medium for cases 1-3, respectively. In each of these figures, the contours have been plotted at six time levels, viz. $\frac{t^*}{\Delta t^*} = 50, 100, 200, 400, 600 \text{ and } 800$ for a single-pulse and $\beta = 1.0$. Figures 6.17a-f show heat flux $q^*\left(\frac{x}{X}, \frac{y}{Y}, t^*\right)$ contours at six time levels $\frac{t^*}{\Delta t^*} = 50, 100, 200, 400, 600 \text{ and } 800$, respectively for a centrally located inhomogeneity (Case 1, Fig. 6.1a). From Figs. 6.17a and 6.17b, it is observed that for a single-pulse, at $\frac{t^*}{\Delta t^*} = 50$ and 100, negative heat flux appears near the south boundary. It is to be noted that the negative heat flux contributes towards the reflectance $q_r^*\left(\frac{x}{X}, 0.0, t^*\right)$ signals. From Figs. 6.17a and 6.17b, a high heat flux values are observed in and around the central inhomogeneity.

At $\frac{t^*}{\Delta t^*} = 200$, it is observed from Fig. 6.17c that a negative heat flux which contributes towards reflectance is well established. A central region of negative heat flux is seen in the proximity of the inhomogeneity. As the time progresses, as is seen from Figs. 6.17d-f, magnitude of heat flux decreases and its distribution is homogeneous. At $\frac{t^*}{\Delta t^*} = 800$, the signal is almost extinct.

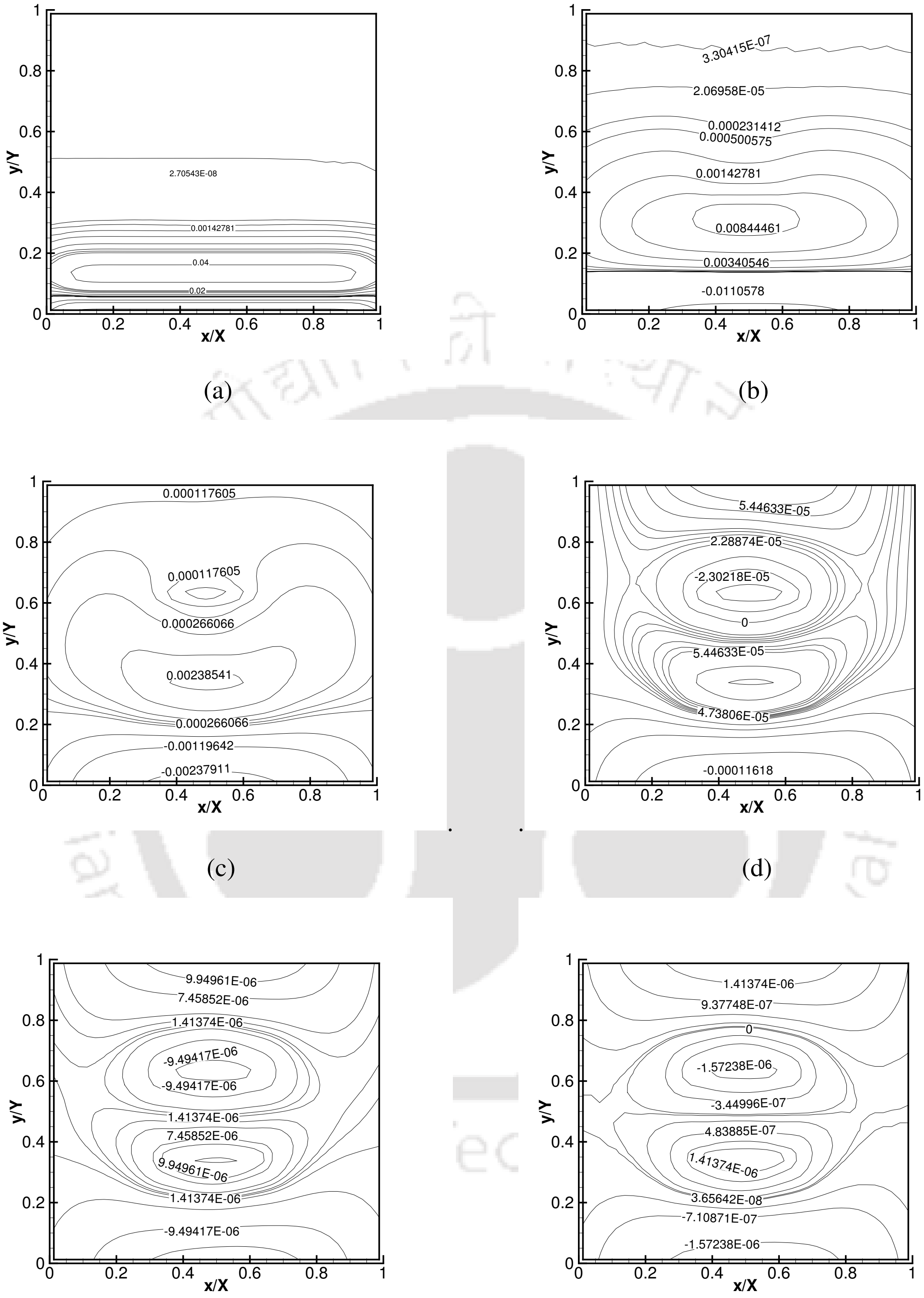

(a) (b)

(c) (d)

(e) (f)

Figure 6.17: Heat flux contours in the medium at time $\dfrac{t^*}{\Delta t^*}$ (a) = 50, (b) = 100, (c) = 200, (d) = 400 (e) = 600 (f) = 800 for β=1.0 and a single-pulse for Case 1.

With an inhomogeneity located in the north-west corner (Fig. 6.1b) for case 2, Figs.6.18a-f show heat flux contours at the previously mentioned time-levels. With $\beta = 1.0$, at $\frac{t^*}{\Delta t^*} = 50$, radiation reaches only half-way in the medium. Thus unlike a centrally located inhomogeneity (Fig. 6.17a), the inhomogeneity located in the north-west corner is not seen to have any effect on the heat flux contours. At $\frac{t^*}{\Delta t^*} = 100$, since radiation has just reached the other boundary and has encountered the inhomogeneity, the heat flux contours are seen to be the most affected the vicinity of the north-west corner.

As time has progressed, it is seen from Fig.6.18c that at $\frac{t^*}{\Delta t^*} = 200$, the negative heat flux extends beyond the central region and the influence of inhomogeneity remains more in the north-west corner. With further advance of time, the domain of negative heat flux shifts towards the south boundary and magnitudes of both positive and negative heat fluxes decrease with time. At $\frac{t^*}{\Delta t^*} = 800$, it is seen from Fig. 6.18f that the signal almost reaches the vanishing stage.

The influence of a localized inhomogeneity present in the south-east corner (case 3, Fig. 6.1c) on heat flux contours has been shown in Figs. 6.19a-f at $\frac{t^*}{\Delta t^*} = 50, 100, 200, 400, 600 \text{ and } 800$, respectively. Since in this case, the radiation has already encountered the inhomogeneity, heat flux contours in the proximity of the inhomogeneity are affected at an early stage. Just like Fig. 6.19a, in Fig. 6.19b, the effect is more prominent in the south-east corner. It is observed from Figs. 6.19c-e that with the advancing of time, the influence of the inhomogeneity decreases, magnitude of the heat flux decreases and its distribution in the medium tends to be more uniform. Like the Cases 1,2(Figs. 6.17f and 6.18f), at $\frac{t^*}{\Delta t^*} = 800$, the signal dies out.

It can be inferred from Figs. 6.17-6.19 that at an early stage $\left(\frac{t^*}{\Delta t^*}=50\right)$, unless radiation reaches the inhomogeneity, no noticeable effect is found. The extinction coefficient β being 1 At $\frac{t^*}{\Delta t^*}=100$, radiation reaches the north boundary, in all three cases, localized inhomogeneity is seen to have influence over heat flux contours. The effect is seen to be the maximum in case 3 in which case radiation is more intense when it encounters the inhomogeneity. When the inhomogeneity is located in the north-west corner, effect is seen to be minimal. In all three cases, signal is tends to vanishing at $\frac{t^*}{\Delta t^*}=800$.

With extinction coefficient $\beta=10.0$ and a 4-pulse train incident normal to the south boundary, for cases 4-6, heat flux contours have been shown in Figs. 10. Unlike results in Figs. 6.17-6.19, here too, heat flux contours have been studied at two time levels, viz., $\frac{t^*}{\Delta t^*}=50 \text{ and } 100$. The results corresponding to Cases 4-6 are for a strongly scattering $(\omega=0.998)$ inhomogeneity and weakly scattering medium $(\omega=0.1)$.

It is seen from Figs. 6.20a, c and e that at an early stage $\frac{t^*}{\Delta t^*}=50$, the heat flux contours are concentrated in the lower half portion and inhomogeneity if present in the south-east corner has more influence. At $\frac{t^*}{\Delta t^*}=100$, it is seen from Figs. 6.20b, d and f that inhomogeneities have more influence near the south boundary. The influence is symmetric about the mid-plane in Figs. 6.20b. In case of Fig. 10e and f when the inhomogeneity is located in the south-east corner, heat flux contours are skewed in the region lodging the inhomogeneity. In all three figures, the region of the negative heat flux is seen concentrated near the south boundary. The inhomogeneity of Case 4 being central and isotropically scattering a central heat zone symmetric about the Z-axis can be observed. Due to the Gaussian temporal nature of the incident profile and high diffusion in the medium, the heat flux concentration though of a less

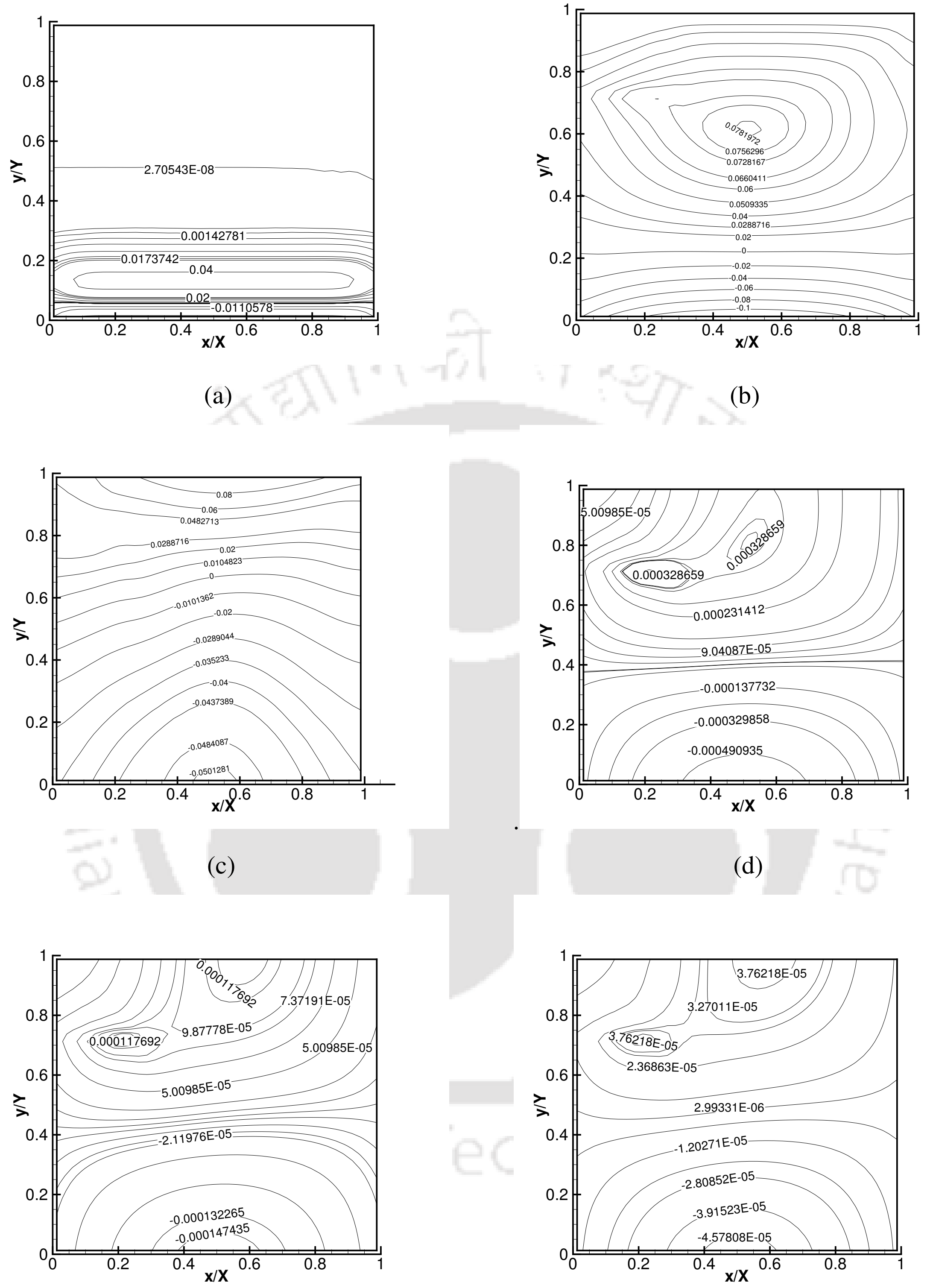

(a) (b)

(c) (d)

(e) (f)

Figure 6.18: Heat flux contours in the medium at time $\frac{t^*}{\Delta t^*}$ (a) = 50, (b) = 100, (c) = 200, (d) = 400 (e) = 600 (f) = 800 for $\beta = 1.0$ and a single-pulse for Case 2.

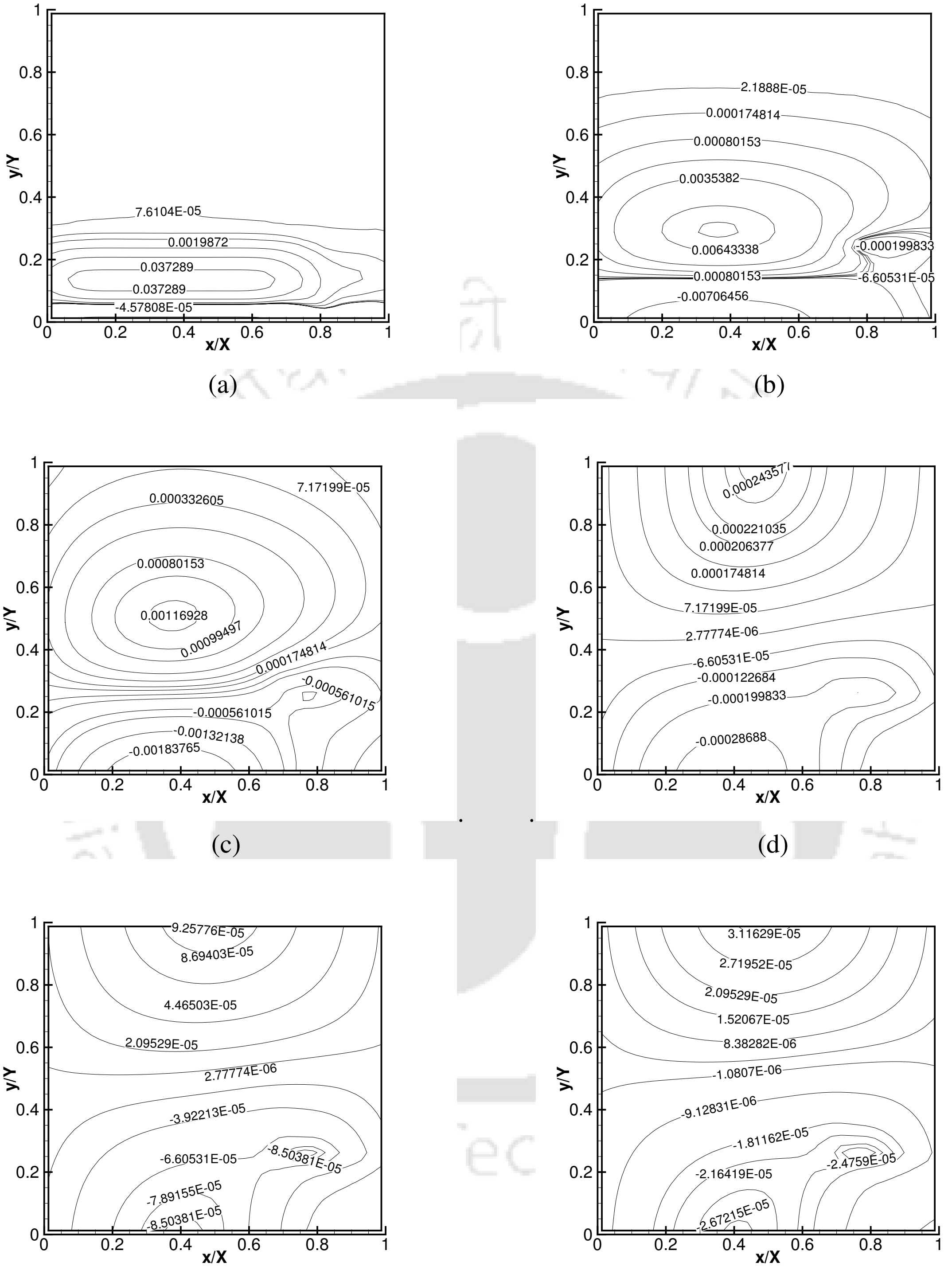

Figure 6.19: Heat flux contours in the medium at time $\frac{t^*}{\Delta t^*}$ (a) = 50, (b) = 100, (c) = 200, (d) = 400 (e) = 600 (f) = 800 for β=10.0 and a single-pulse for Case 3.

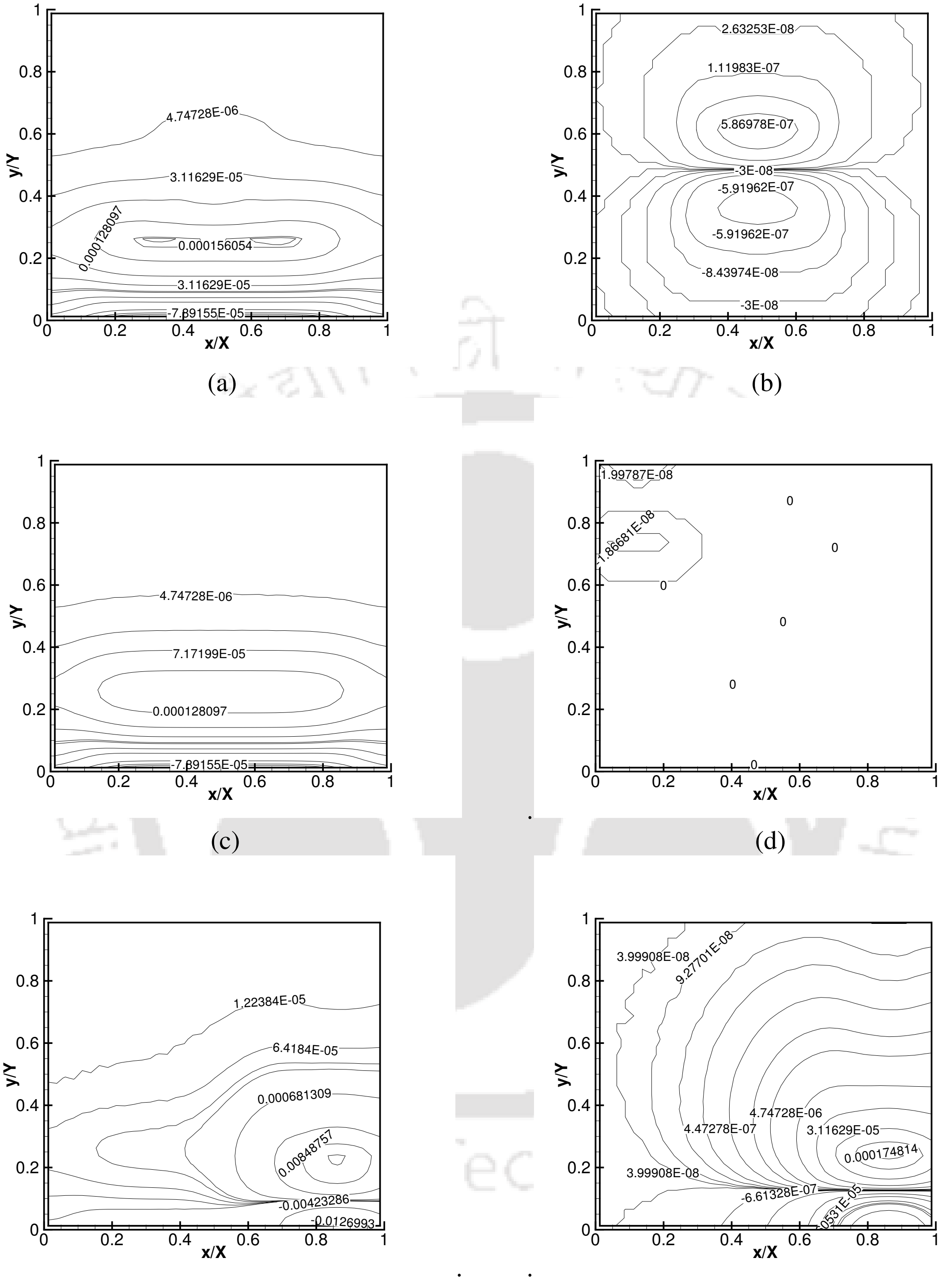

(a) (b)

(c) (d)

(e) (f)

Figure 6.20: Heat flux contours in the medium at time $\frac{t^*}{\Delta t^*}$ (a) = 50, (b) = 100 for Case 4, (d) = 50, (d) = 100 for Case 5, (e) = 50 (f) = 100 for Case 6 with β=10.0

magnitude is found to be staying in the vicinity of the inhomogeneity due to the strong-scattering nature of the inhomogeneity in all the Cases 4-6.

6.5 Summary

Transport of a train of short-pulse radiation through a 2-D rectangular participating medium containing local inhomogeneities differing from the containing medium by their scattering properties, was studied. The analysis was done by considering the south boundary of the medium subjected to a short-pulse radiation. With pulse width of the incident radiation of the order of a nano-second, the problem considered a laser wave consisting of 1 or 4-pulses. Effects of both step as well as Gaussian temporal profile radiation were studied. The transmittance and reflectance signals were studied for the effects of the extinction coefficient and location of inhomogeneities. Heat flux distributions inside the medium were also studied. With a single pulse, results of the present work for homogeneous and inhomogeneous media were compared with those available in the literature. In all the cases, very good comparisons were obtained. Results with 1, 4 pulses were found to have significant effects of the extinction coefficient and the scattering properties of the inhomogeneities.

In chapter 7, effects of circular and elliptical shaped inhomogeneities contained in a 2-D participating medium are studied.

CHAPTER 7

Thermal Signatures of an Inhomogeneous 2-D Participating Medium under the Influence of a Short-Pulse Laser – Effects of Shapes and Locations of Inhomogeneities

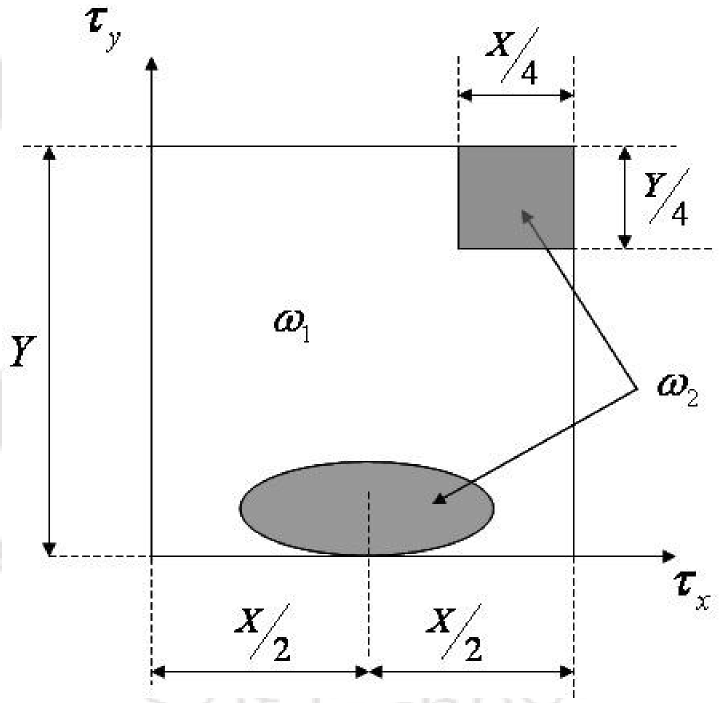

Figure: Co-ordinates of the 2D rectangular participating medium and the location of inhomogeneities

7.1 Introduction

The real life situation is more closely represented by 2-D geometries. As a next step towards approaching a more realistic representation of practical problems, there is a need to consider the possibility of the presence of an inhomogeneity of any shape at any location in the medium. Further, study is also required to analyze the effects of locations and shapes of two inhomogeneities in a medium. The present chapter, therefore, discusses the study of thermal signatures of the inhomogeneities of different shapes placed at various locations in a 2-D rectangular participating medium, one boundary of which is subjected to a short-pulse laser

7.2 Problem

Effects of shapes and locations of inhomogeneities in a 2-D rectangular participating medium on the transport of a short-pulse laser of step temporal profile are investigated. The absorbing and scattering participating medium contains circular, elliptical, and/or square shaped inhomogeneities. The scattering properties of the inhomogeneities are different from the main medium. Transmittance and reflectance signals are analyzed for a strongly as well as weakly participating medium. Spatial distributions of the signals along the boundaries at various times and the temporal evolution of the heat flux distributions inside the medium are also studied. Qualitative idea about the shape and size of the inhomogeneities is predicted through the spatial as well as temporal distributions of signals. The finite volume method discussed in Chapter 5 is used to solve the problem.

Figs. 7.1a-f show the positions of different types of inhomogeneities in the medium. Based on the shapes and locations of inhomogeneities, the different situations are named as Cases 1-6 as shown in Table 7.1. The medium and its inhomogeneity in all the cases are considered to have the same extinction coefficient β.The scattering albedo of the medium and any inhomogeneity are $\omega_1 = 0.998$ and $\omega_2 = 0.1$, respectively. Two values of the extinction coefficient, viz., $\beta = 1.0$ and 10.0 are considered for study.

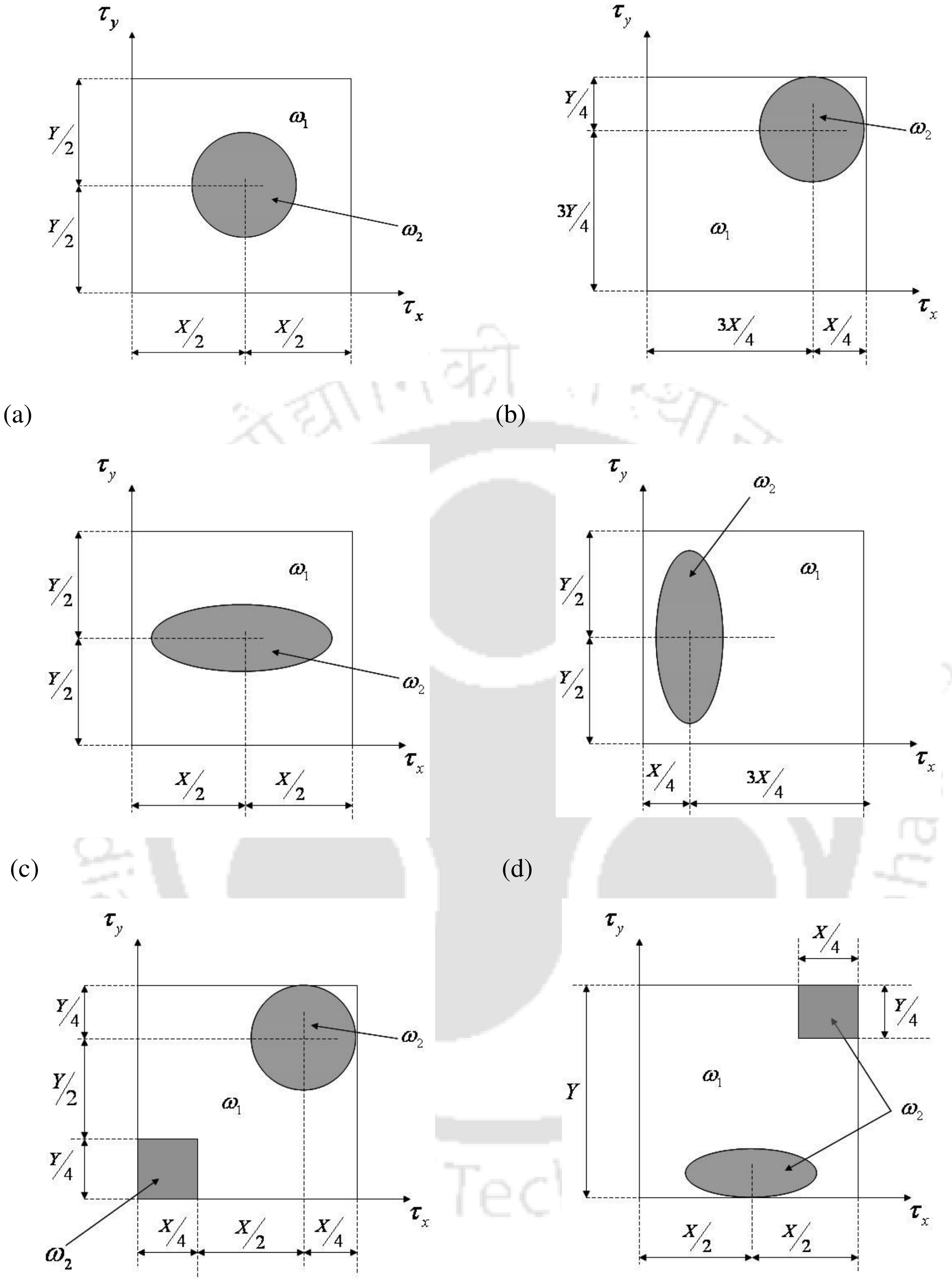

(a) (b)

(c) (d)

(e) (f)

Figure 7.1: Co-ordinates of the 2D rectangular participating medium and the location of inhomogeneities - (a) Case 1(b) Case2 (c) Case 3(d) Case 4 (e) Case 5 (f) Case 6 (figures not to scale).

Case	**Shape of inhomogeneity**	**Position of inhomogeneity in the medium**	**Volume of the inhomogeneity (% of the main medium)**	**Figure**
1	Circular	Centre	25	1a
2	Circular	Top-right corner	25	1b
3	Ellipse(horizontal)	Center	25	1c
4	Ellipse(vertical)	Adjacent to west boundary, symmetric about the horizontal mid-plane	25	1d
5	Circular	Top-right corner	20	1e
	Square	Bottom-left corner	8	
6	Elliptical(horizontal)	Adjacent to south boundary, symmetric about the vertical mid-plane	20	1f
	Square	Top-right corner	8	

Table 7.1: Various inhomogeneous geometries discussed in Chapter 7

7.3 Results and Discussion – Step pulse

For grid independent situation, 50×50 equal size control volumes were used and a maximum of 120 directions covering the 4π solid angle were found enough for the ray-independent solutions. 1000 divisions of the total time t^* domain were found sufficient for marching in the time dimension. The iteration was set to stop at $\left|S^m_{t,\text{old},P} - S^m_{t,\text{new},P}\right| \le 1.0\times10^{-7}$. The computational time on a Xeon 300 dual processor 800 MHz computer ranged from 108 s for $\beta = 1.0$ and 275 s for $\beta = 10.0$

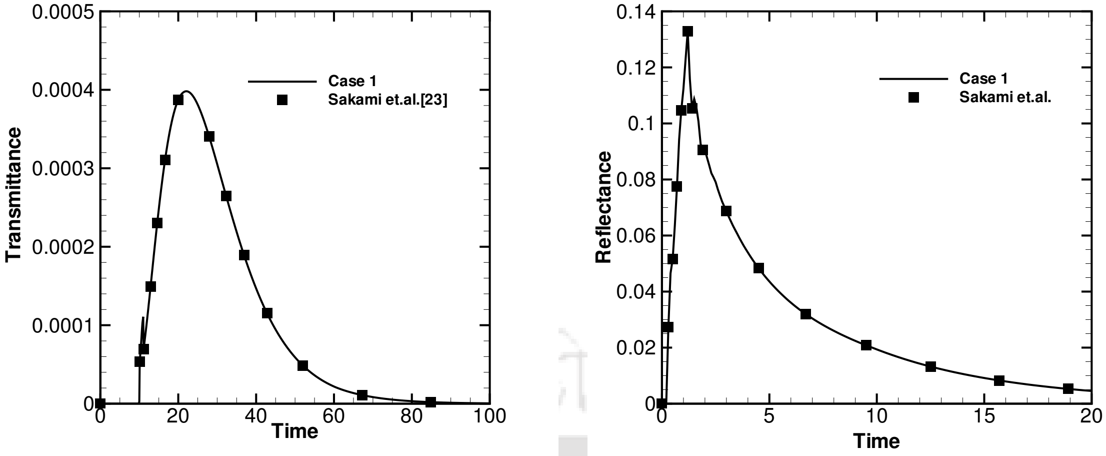

(a) (b)

Figure 7.2: Comparison of (a) transmittance $q_t^*\left(0.5,1.0,t^*\right)$ (b) reflectance $q_r^*\left(0.5,0.0,t^*\right)$ for an inhomogeneous 2D rectangular medium with step-pulse (Case 1 with a square inhomogeneity whose volume is 1/4th the volume that of the medium).

With extinction coefficient $\beta = 10.0$, for a square medium $\left(\frac{X}{Y}=1\right)$ subjected to a single pulse laser, we first validate our results for a simple case with those available in the literature [100]. With a centrally-located square inhomogeneity, Figs. 7.2a and 7.2b show comparison of transmittance and reflectance results of the present work with those of Sakami et al. [100] obtained using the DOM with high order upwind piecewise parabolic interpolation scheme.. It is seen from Figs. 7.2a and 7.2b that the results of the present work are in good agreement with those available in the literature [100].

Results for a square medium $\left(\frac{X}{Y}=1\right)$ containing an inhomogeneity of different shapes at different locations are discussed below. Results for $\beta = 1.0$ and 10.0 are presented for Cases 1-6 considered above. The south boundary of the 2-D medium is subjected to a short-pulse laser of step temporal profile with pulse-width $t_p^* = 1.0$ incident normal to the south boundary.

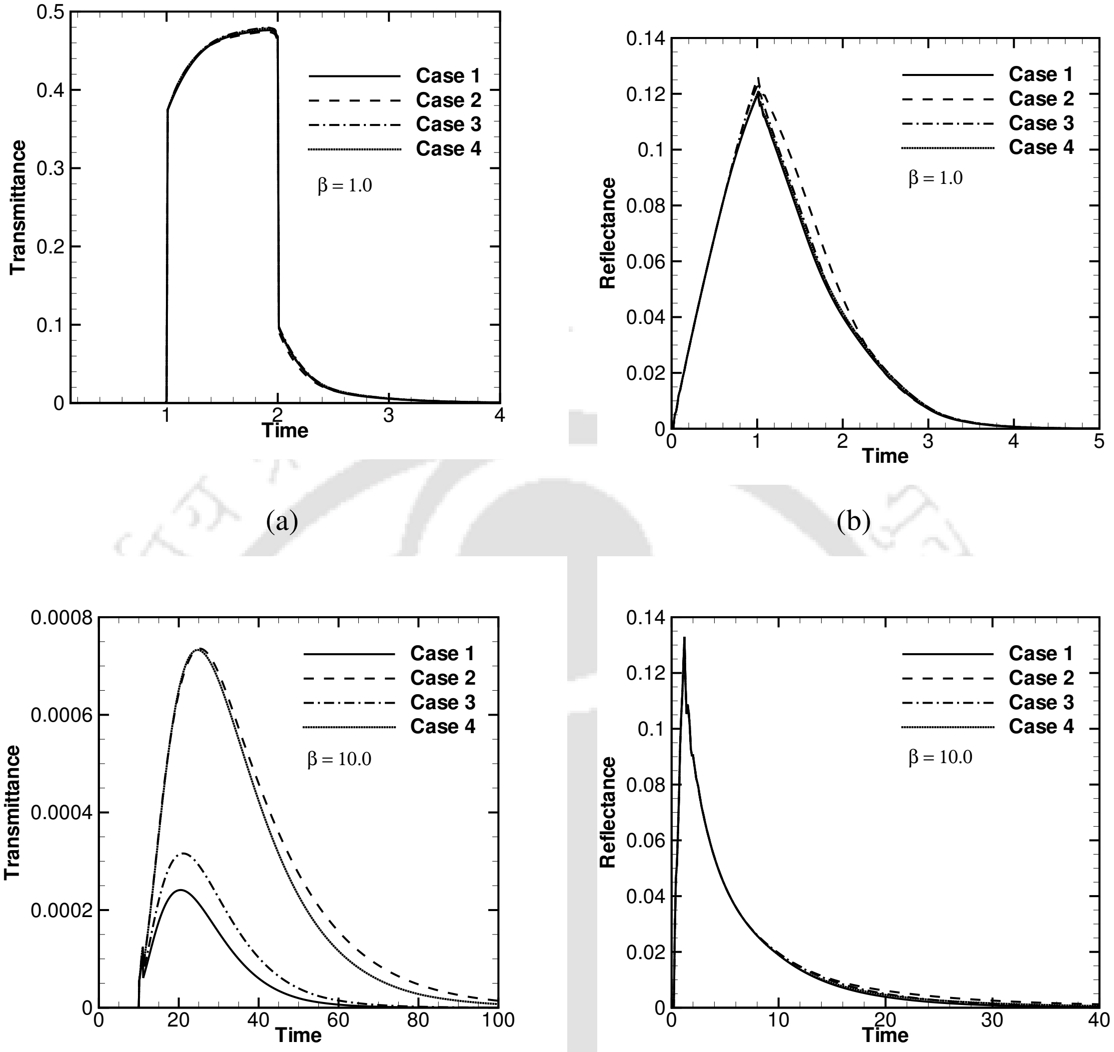

(a) (b)

(c) (d)

Figure 7.3: Transmittance $q_t^*\left(0.5,1.0,t^*\right)$ and Reflectance $q_r^*\left(\frac{x}{X},0.0,t^*\right)$ signals for Cases 1-4 for different values of extinction coefficient.

In all the four cases (Cases 1-4), irrespective of the magnitudes of the extinction coefficient β, the trends of the transmittance $q_t^*\left(0.5,1.0,t^*\right)$ (Fig 7.3a and 7.3c) and reflectance $q_r^*\left(0.5,0.0,t^*\right)$ (Fig 7.3b and 7.3d) signals resemble the trends of the 1-D [25] planar medium, but their temporal spans are much shorter. With $\beta = 1.0$, the peak magnitudes of the signals also approach that of the 1-D case [25] while for $\beta = 10.0$, they are quite different. It is observed from Figs. 7.3a and 7.3c that as the medium becomes more participating, the location of the inhomogeneity has a distinguishable effect on the magnitude of the transmittance $q_t^*\left(0.5,1.0,t^*\right)$ at the centre of the other (north) boundary. However, it is seen from Figs. 7.3b and 7.3d that the location of the inhomogeneity has almost no effect on the reflectance $q_r^*\left(0.5,1.0,t^*\right)$, irrespective of the value of extinction coefficient β.

In Cases 1-4, a major (3/4th by volume) portion of the medium is strongly scattering $(\omega_1 = 0.998)$ and the inhomogeneity which occupies 1/4th of the volume is weakly scattering $(\omega_2 = 0.1)$. With $\beta = 10.0$, for the situation representing Cases 1 (Fig. 7.1a) and 3 (Fig. 7.1c), the centrally located weakly scattering $(\omega_2 = 0.1)$ inhomogeneity is responsible for the low magnitude of transmittance $q_t^*\left(0.5,1.0,t^*\right)$ at the center of the north boundary. Whereas in Cases 2 (Fig. 7.1b) and 4 (Fig. 7.1d), since the weakly-scattering inhomogeniety is offset from the center (Figs. 7.1b and 7.1d), the middle portion of the north boundary receives considerably more energy than that of the Cases 1 and 3. Further due to the presence of the weakly scattering circular inhomogeneity at the top-right corner (Case 2, Fig. 7.1b) of the medium, radiation encounters energy-damping only at a later stage of its propagation

Transmittance $q_t^*\left(0.5,1.0,t^*\right)$ and reflectance $q_r^*\left(0.5,0.0,t^*\right)$ results for Cases 5 and 6 for two different values of the extinction coefficient β are shown in Figs. 7.4a-d. From Fig. 7.4a, it can be observed that for a less participating medium, the location of an inhomogeneity of any shape does not affect the transmittance $q_t^*\left(0.5,1.0,t^*\right)$ signal. With $\beta = 1.0$, since the exponential attenuation of the collimated component of intensity is minimal, a substantial portion of the transmittance signal at the middle of the other boundary is due to the collimated component. Since inhomogeneity also has the same extinction coefficient, the presence (Case 6, Fig. 7.1f) or absence (Case 5, Fig.7.1e) of an elliptical inhomogeneity in the immediate vicinity of the boundary of

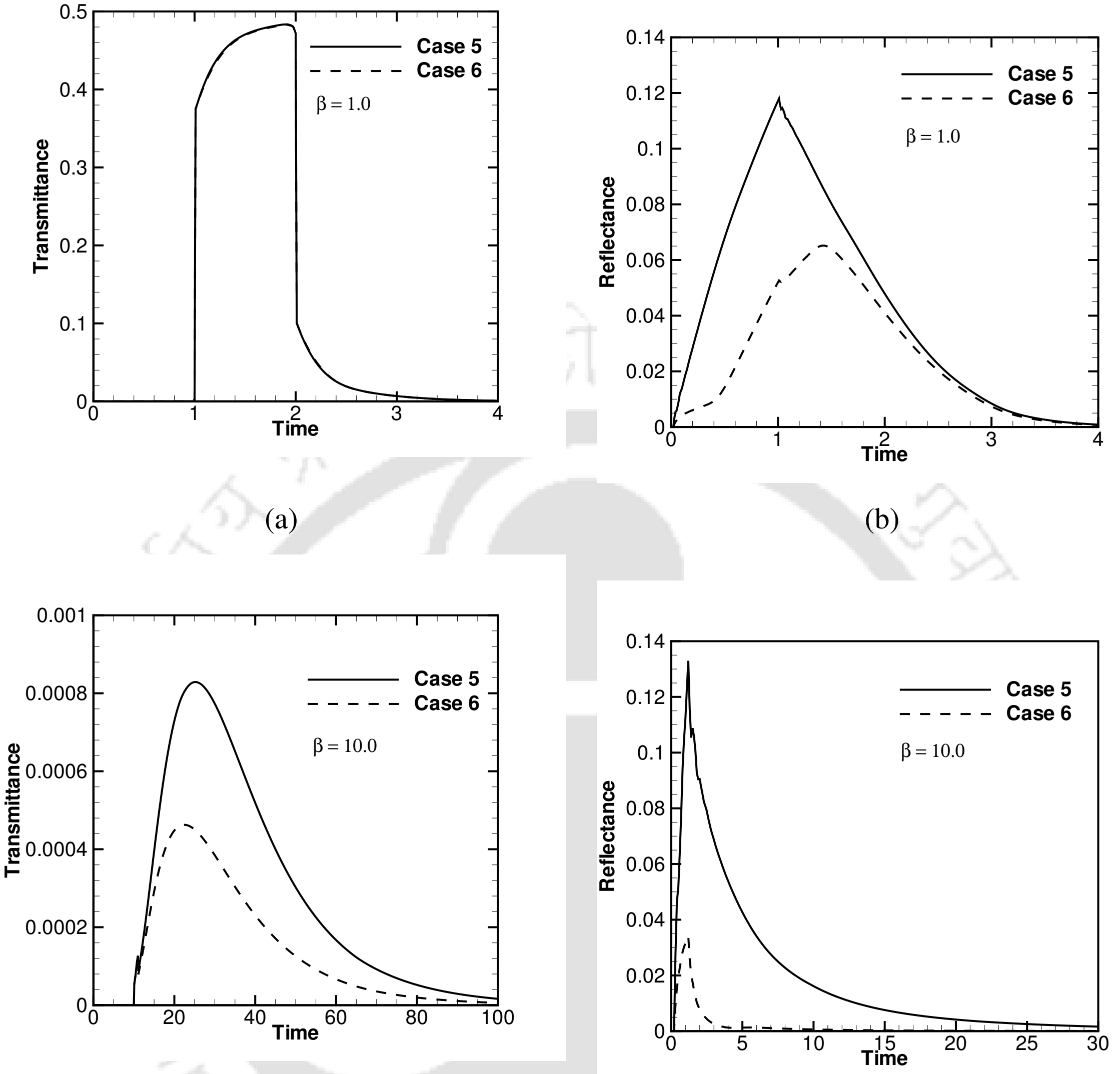

(a) (b)

(c) (d)

Figure 7.4: Transmittance $q_t^*\left(0.5,1.0,t^*\right)$ and Reflectance $q_r^*\left(\frac{x}{X},0.0,t^*\right)$ signals for Cases 5 and 6 for different values of extinction coefficient.

The magnitude of the transmittance $q_t^*\left(0.5,1.0,t^*\right)$ signals (Fig. 7.4c) with $\beta = 10.0$ for Case 5 is almost twice that of Case 6 (Fig. 7.4c). Since in both these cases, the medium and the inhomogeneity are highly participating, the contribution of the collimated component of transmittance signal is almost negligible. However, in Case 6, weak scattering and strong absorption due to the inhomogeneity immediately after the entry of the signal into the medium is responsible for signals of low magnitude at the north boundary.

It is seen from Figs. 7.4b and 7.4d that for both $\beta = 1.0$ and 10.0, the peak magnitude and the temporal stay of the reflectance $q_r^*\left(0.5, 0.0, t^*\right)$ signal in Case 5 (Fig. 7.1e) is much higher than that of Case 6 (Fig. 7.1f). Since the reflectance $q_r^*\left(0.5, 0.0, t^*\right)$ signal is the outcome of the back-scattered diffuse intensities from the medium, the presence of a weakly scattering inhomogeneity in the immediate neighborhood (Case 6, Fig. 7.1f) of the south boundary (the boundary of incidence) has a strong influence on the signal. This is the cause of a considerable difference in magnitudes of the reflectance $q_r^*\left(0.5, 0.0, t^*\right)$ signal between Case 5 (Fig. 7.1e) and Case 6 (Fig. 1f) for $\beta = 1.0$ (Fig. 7.4b) and for $\beta = 10.0$ (Fig. 7.4d).

In Figs. 7.5a-d, for Cases 1 (Fig. 7.1a) and 2 (Fig. 7.1b), distributions of transmittance $q_t^*\left(\frac{x}{X}, 1.0, t^*\right)$ and reflectance $q_r^*\left(\frac{x}{X}, 0.0, t^*\right)$ signals along the boundaries have been plotted for two different values of the extinction coefficient $\beta = 1.0$ and 10.0. For a given β, these distributions are plotted at 6 time levels, viz. $\frac{t^*}{\Delta t^*} = 100,\ 200,\ 300,\ 400,\ 600$ and 800. The two cases at these six time levels have been differentiated by line-types. Solid and dashed lines differentiate cases 1 and 2, respectively The digit n on any curve indicates signal at $n \times 100^{\text{th}}$ time step..

It is seen from Fig. 7.5a that for Case 1 (Fig. 7.1a), the spatial distributions of transmittance $q_t^*\left(\frac{x}{X}, 1.0, t^*\right)$ and reflectance $q_r^*\left(\frac{x}{X}, 0.0, t^*\right)$ signals at all time levels are symmetric about the mid-plane $\left(0.5, y\right)$. For Case 2 (Fig. 7.1b), it is observed that the transmittance $q_t^*\left(\frac{x}{X}, 1.0, t^*\right)$ signal is slightly skewed towards the west boundary. This skew is due to the presence of a circular inhomogeneity near the east boundary

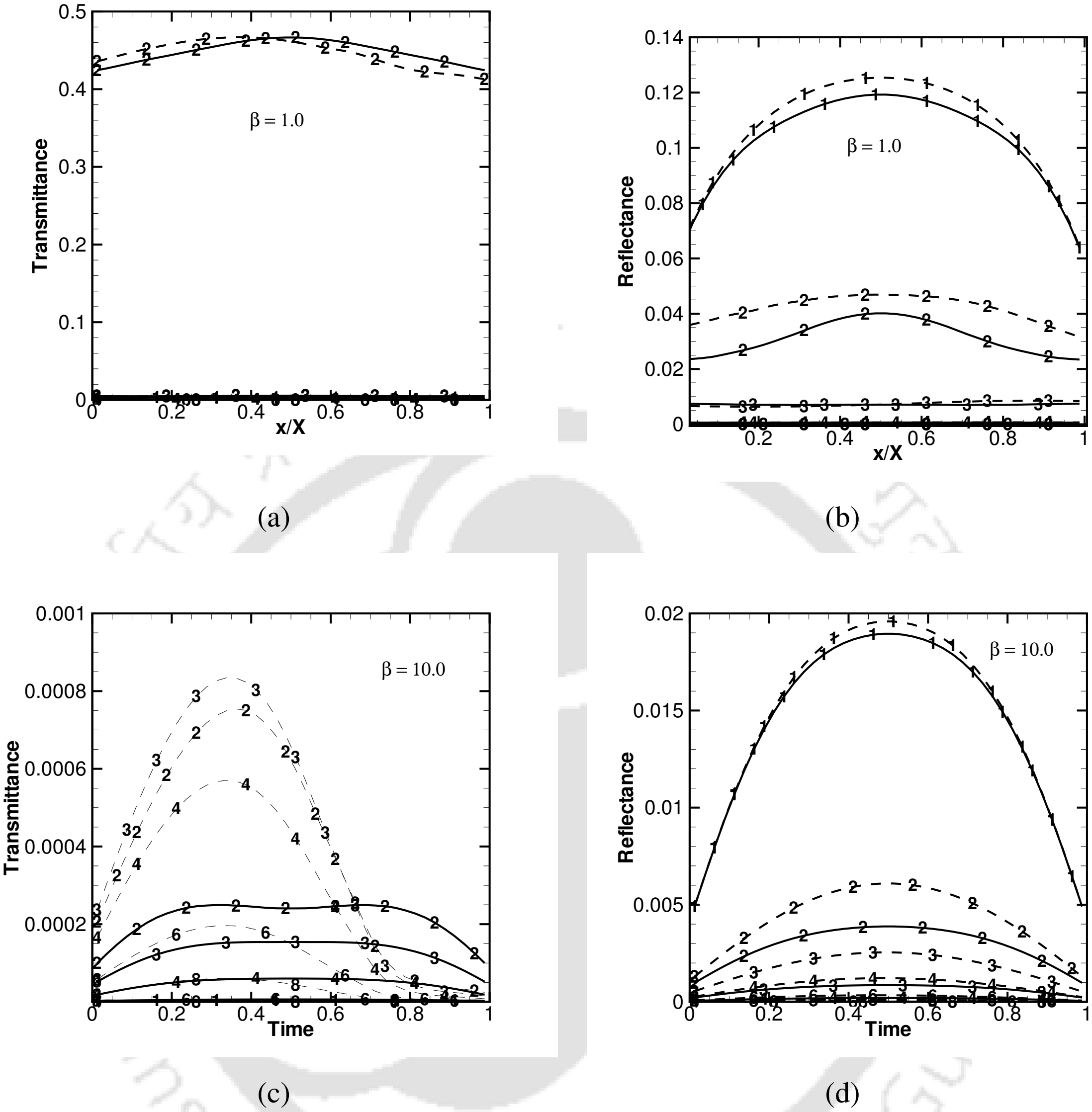

(a) (b)

(c) (d)

Figure 7.5: Time evolution of the distribution of transmittance $q_t^*\left(x/X,1.0,t^*\right)$ and reflectance $q_r^*\left(x/X,0.0,t^*\right)$ signals along the boundaries. The digit n on any curve indicates the distribution of the signal at $n\times100^{\text{th}}$ time step. Solid and dashed lines are results for Cases 1 and 2 respectively.

and the low magnitude of the skew is attributed to a weakly participating medium $(\beta=1.0)$.In Fig. 7.5b, the presence of the central circular inhomogeneity can be observed in the reflectance $q_r^*\left(\frac{x}{X},0.0,t^*\right)$ signals at the 200th time step. The curve is noticed to have a central crest and symmetric troughs of a little curvature, which tend to fall towards both the walls.

As is seen from Fig. 7.5c, for Case 1 (Fig. 7.1a) in case of a highly absorbing medium $(\beta = 10.0)$, the presence of a central inhomogeneity manifests in the form of a trough at the 200th time step. For Case 2 (Fig. 7.1b), from Fig. 7.5c, a sharp skew towards the west boundary is observed and it is due to the presence of a weakly scattering inhomogeneity in the top-right corner of the medium. At all time levels, the reflectance $q_r^*\left(\frac{x}{X}, 0.0, t^*\right)$ signals are found to be symmetric about the vertical mid-plane for both Cases 1 and 2. However, as shown in Figs. 7.5b and 7.5d, the variation in spatial distribution of reflectance $q_r^*\left(\frac{x}{X}, 0.0, t^*\right)$ signals at the initial stages is much higher than in the later stages in both Cases 1 and 2 for the two values of extinction coefficient.

In Figs. 7.6a-d, for Cases 3 (Fig. 7.1c) and 4 (Fig. 7.1d), distributions of transmittance $q_t^*\left(\frac{x}{X}, 1.0, t^*\right)$ and reflectance $q_r^*\left(\frac{x}{X}, 0.0, t^*\right)$ signals along the boundaries have been plotted for two different values of the extinction coefficient $\beta = 1.0$ and 10.0. For a given β, these distributions are plotted at 6 time levels, viz. $\frac{t^*}{\Delta t^*} = 100,\ 200,\ 300,\ 400,\ 600$ and 800. The two cases at these six time levels have been differentiated by line-types in a similar fashion as Figs. 7.5a-d. The digit n on any curve indicates the distribution of the signal at $n \times 100^{\text{th}}$ time step. Solid and dashed lines differentiate Cases 3 and 4, respectively. It is seen from Fig. 7.6a that for Case 3 (Fig. 7.1c), the spatial distributions of transmittance $q_t^*\left(\frac{x}{X}, 1.0, t^*\right)$ and reflectance $q_r^*\left(\frac{x}{X}, 0.0, t^*\right)$ signals at all time levels are symmetric about the mid-plane $(0.5, y)$. This is similar to the trend in Fig. 7.5a. For Case 4 (Fig. 7.1d), it is

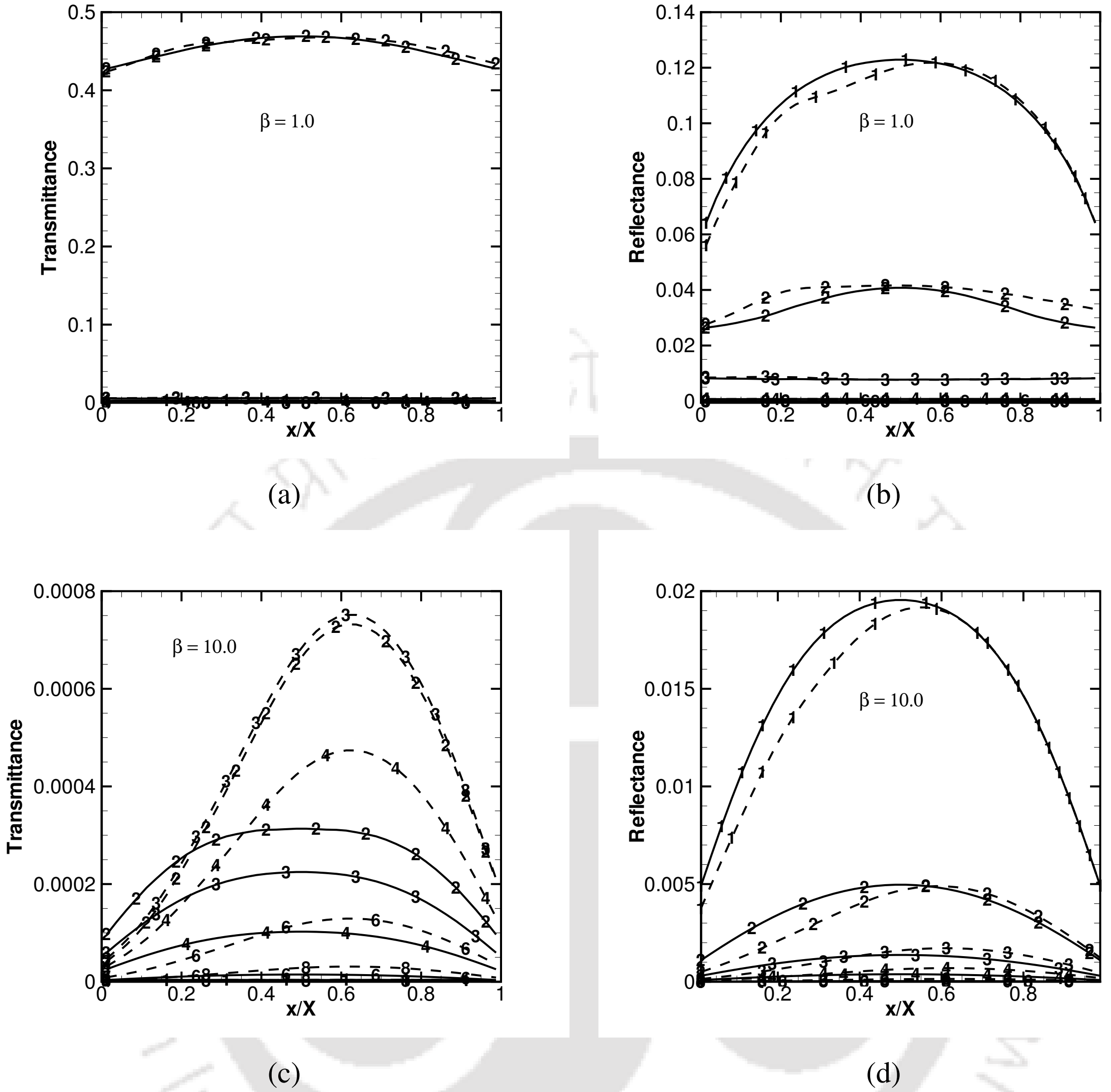

Figure 7.6: Time evolution of the distribution of transmittance $q_t^*\left(x/X, 1.0, t^*\right)$ and reflectance $q_r^*\left(x/X, 0.0, t^*\right)$ signals along the boundaries. The digit n on any curve indicates the distribution of the signal at $n\times100^{\text{th}}$ time step. Solid and dashed lines are results for Cases 3 and 4 respectively.

observed that the transmittance $q_t^*\left(\frac{x}{X}, 1.0, t^*\right)$ signal is slightly skewed towards the east boundary. This skew is due to the presence of a vertical elliptical inhomogeneity near the west boundary and the less magnitude of the skew is attributed to a weakly participating medium $(\beta = 1.0)$. In Fig. 7.6b, the presence of the central horizontal elliptical inhomogeneity can be observed in the reflectance $q_r^*\left(\frac{x}{X},0.0,t^*\right)$ signals at the 200th time step. This is similar to the Case 1 in Fig 7.5b. However, the crest in the curve is observed to have very less curvature corresponding to the flat surface of the horizontal elliptical inhomogeneity in the central region.

As is seen from Fig. 7.6c, for Case 3 (Fig. 7.1c) with a highly absorbing medium $(\beta = 10.0)$, the central inhomogeneity has no significant effect. For Case 4 (Fig. 7.1d), from Fig. 7.6c, a sharp skew towards the east boundary is observed and it is due to the presence of a vertical elliptical weakly scattering inhomogeneity near the west boundary of the medium. From Fig. 7.6b it can be observed that at all time levels, the reflectance $q_r^*\left(\frac{x}{X},0.0,t^*\right)$ signals are symmetric about the vertical mid-plane for both Cases 3 and 4 for $\beta = 1.0$. But since radiation encounters strongly-participating $(\beta = 10.0)$ and weakly-scattering $(\omega = 0.1)$ inhomogeneity very soon after its incidence on the south boundary in Case 4 (Fig.7.1d), an unequal distribution of signals can be observed along the south boundary (Fig. 7.6d).

In Figs. 7.7a-d, for Cases 5 (Fig. 7.1e) and 6 (Fig. 7.1f), distributions of transmittance $q_t^*\left(\frac{x}{X},1.0,t^*\right)$ and reflectance $q_r^*\left(\frac{x}{X},0.0,t^*\right)$ signals along the boundaries have been plotted for two different values of the extinction coefficient $\beta = 1.0$ and 10.0. Similar to Figs 7.5 and 7.6, these figures are plotted at 6 time levels, viz., $\frac{t^*}{\Delta t^*} = 100,\ 200,\ 300,\ 400,\ 600$ and 800. Solid and dashed lines differentiate cases 5 and 6, respectively. The digit n on any curve indicates the distribution of the signal at $n \times 100^{\text{th}}$ time step. It is seen from Fig. 7.7a, that for Case 5 (Fig. 7.1e), the spatial distributions of transmittance $q_t^*\left(\frac{x}{X},1.0,t^*\right)$ signals at all time levels are symmetric about the mid-plane $(0.5, y)$. This is similar to the trend in Figs. 7.5a and 7.6a. For Case 6 (Fig. 7.1d), it is observed that the transmittance $q_t^*\left(\frac{x}{X},1.0,t^*\right)$ signal is

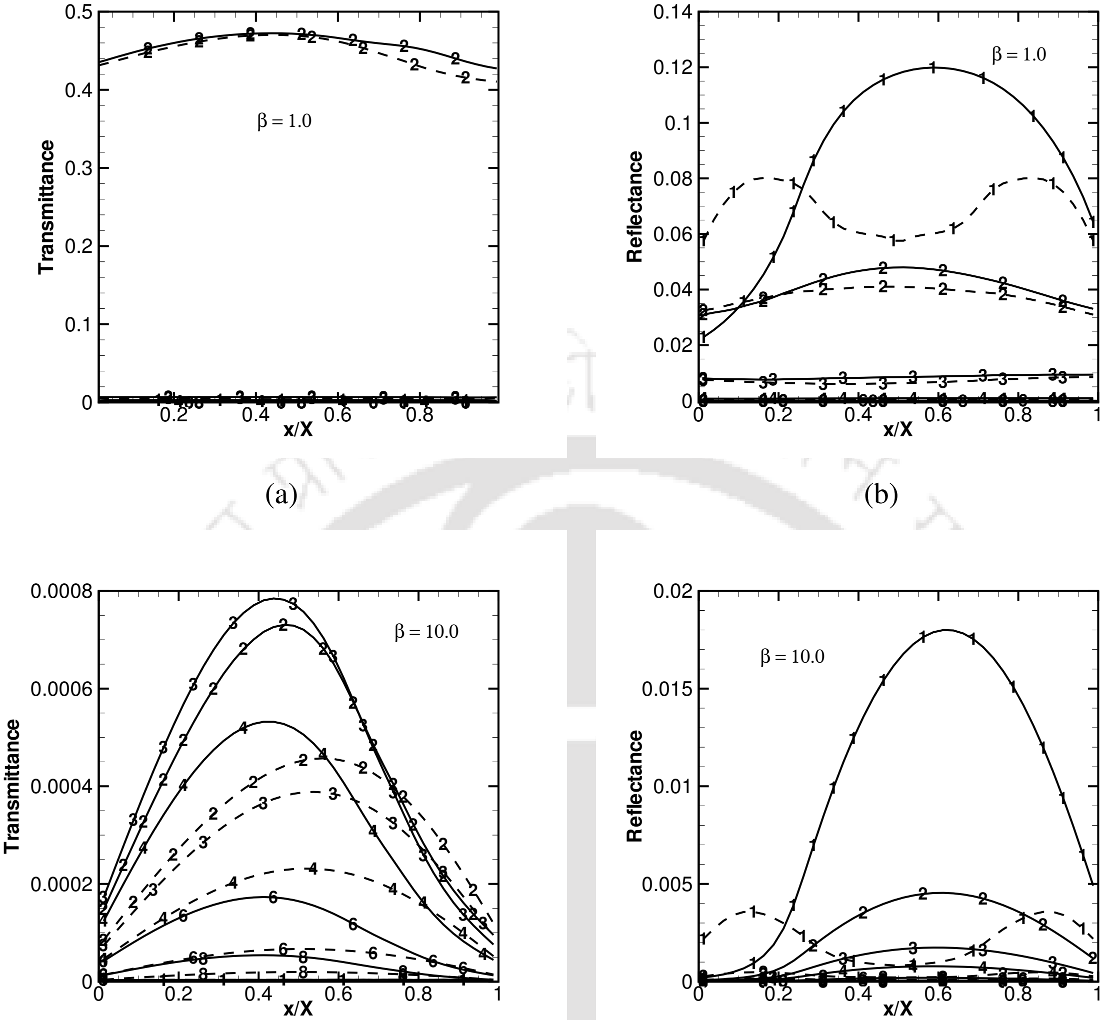

(a) (b)

(c) (d)

Figure 7.7: Time evolution of the distribution of transmittance $q_t^*\left(x/X,1.0,t^*\right)$ and reflectance $q_r^*\left(x/X,0.0,t^*\right)$ signals along the boundaries. The digit n on any curve indicates the distribution of the signal at $n\times100^{\text{th}}$ time step. Solid and dashed lines are results for Cases 5 and 6 respectively.

slightly skewed towards the west boundary. This skew is due to the presence of the circular inhomogeneity near the top-right corner. In Fig. 7.7b, the presence of the elliptical inhomogeneity (Case 6, Fig.7.1f) near the south boundary can be observed in the reflectance $q_r^*\left(\dfrac{x}{X},0.0,t^*\right)$ signals at the 100th time step. The trough and the two crests are well defined in this curve due to the sharp curvature of the horizontal elliptical inhomogeneity encountered by radiation.

It is seen from Fig. 7.7c that for Case 5 (Fig. 7.1e) in case of a highly absorbing medium $(\beta = 10.0)$, the presence of the circular inhomogeneity in the top-right corner of the medium causes a sharp skew of the transmittance $q_t^*\left(\frac{x}{X}, 1.0, t^*\right)$ signals towards the west boundary. Since the elliptical inhomogeneity is located symmetric about the vertical mid-plane and a small inhomogeneity is present at the top-right corner (Fig.7.1f), the skew is less pronounced for Case 6 (Fig.7.7c). In Fig. 7.7d, the reflectance $q_r^*\left(\frac{x}{X}, 0.0, t^*\right)$ signals tend to skew more toward the east boundary due to the presence of a small square inhomogeneity at the bottom-left corner.

Figures 7.8-7.10 provide heat flux $q^*\left(\frac{x}{X}, \frac{y}{Y}, t^*\right)$ contours in the medium for Cases 1 (Fig. 7.1a), 4 (Fig. 7.1d) and 6 (Fig. 7.1f), respectively. For $\beta = 10.0$, in each of these figures, the contours have been plotted at six time levels, viz. $\frac{t^*}{\Delta t^*} = 20, 40, 80, 200, 400$ and 800.

From Figs. 7.8a and 7.8b, it is observed that at $\frac{t^*}{\Delta t^*} = 20$ and 40, negative heat flux which contributes towards the reflectance $q_r^*\left(\frac{x}{X}, 0.0, t^*\right)$ signal appears near the south boundary (the boundary of incidence). At $\frac{t^*}{\Delta t^*} = 200$, it is observed from Fig. 7.8c that a negative heat flux near the south boundary is well established. In Fig. 7.8c, a heat flux front moving through the medium with a convergence in direction towards the centre of the medium is observed. In Fig. 8e, a central region of heat flux concentration symmetric about the geometric centre of the inhomogeneity is observed at $\frac{t^*}{\Delta t^*} = 400$. As the time progresses, it is seen from Figs. 7.8d-f that the magnitudes

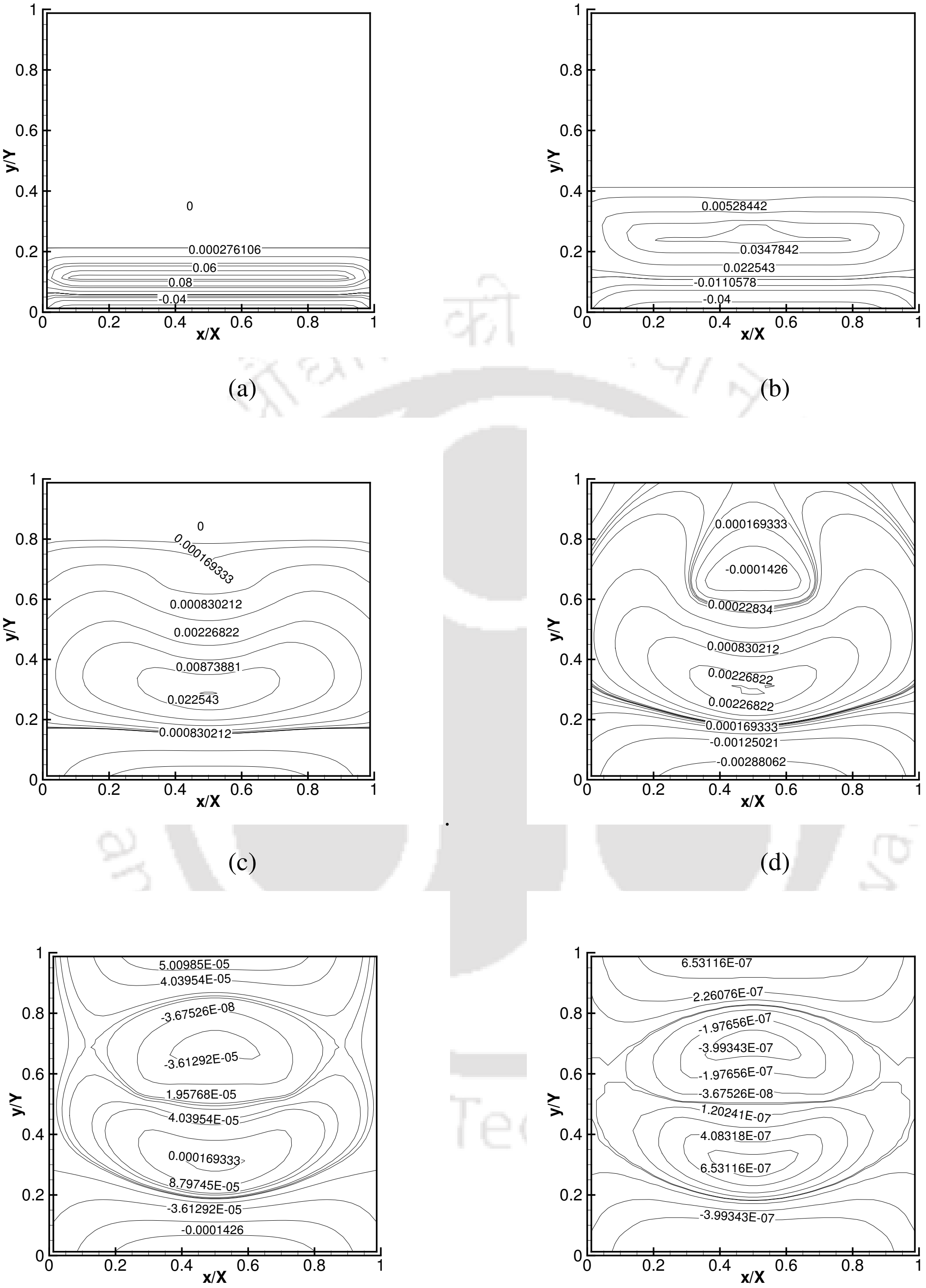

(a) (b)

(c) (d)

(e) (f)

Figure 7.8: Heat flux contours in the medium at time $\frac{t^*}{\Delta t^*}$ (a) = 20, (b) = 40, (c) = 80, (d) = 200 (e) = 400 (f) = 800 for β=10.0 for Case 1.

of the heat flux contours decrease and its distribution gets homogeneous. At $\frac{t^*}{\Delta t^*} = 800$, the signal is almost extinct.

For a vertical-elliptical inhomogeneity symmetric about the horizontal mid-plane and located adjacent to the west boundary (Case 4, Fig. 7.1d), Figs. 7.9a-f show heat flux contours at the six afore-mentioned time-levels. With $\beta = 10.0$, at $\frac{t^*}{\Delta t^*} = 20$ (Fig. 7.9a), radiation has traversed only a little distance in the medium. In Fig. 7.9b, at $\frac{t^*}{\Delta t^*} = 40$, though the radiation has just reached the inhomogeneity, no visible effects on the contours is observed. At $\frac{t^*}{\Delta t^*} = 80$, radiation front has met the inhomogeneity and thus the heat flux contours are observed to be affected by scattering inside the inhomogeneity.

In Figs. 7.9d and 7.9e, the response of the inhomogeneity to the propagation of radiation through it can be observed. A heat flux core representing the shape of the inhomogeneity is observed in the vicinity of the west boundary. A central positive heat flux core is also seen in Fig. 7.9d. This is attributed to radiation transport from the south boundary to the north boundary through the medium. Since the inhomogeneity is isotropically scattering, contours are observed to be symmetric about the minor axis of the ellipse (Fig. 7.9e). With the progress of time, in Fig. 7.9f, at $\frac{t^*}{\Delta t^*} = 800$, the contours tend to have a very low magnitude due to the extinction of the signal.

Figs. 7.10a-f show heat flux contours for a medium containing a horizontal-elliptical inhomogeneity symmetric about the vertical mid-plane located adjacent to the west boundary and a square inhomogeneity at the top-right corner(Case 6, Fig. 7.1f), at the six afore-mentioned time-levels.

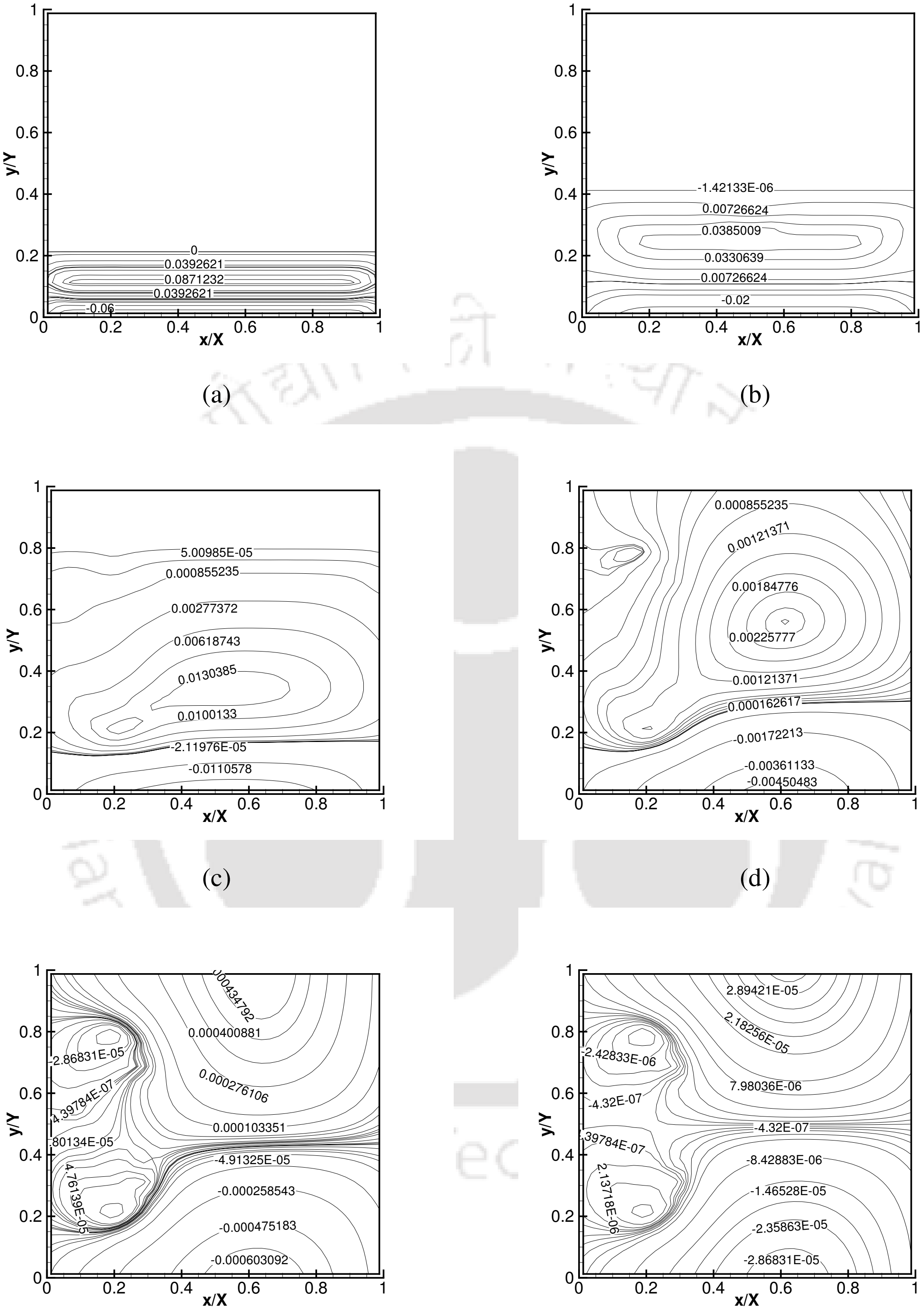

(a) (b)

(c) (d)

(e) (f)

Figure 7.9: Heat flux contours in the medium at time $\frac{t^*}{\Delta t^*}$ (a) = 20, (b) = 40, (c) = 80, (d) = 200 (e) s= 400 (f) = 800 for β=10.0 for Case 4.

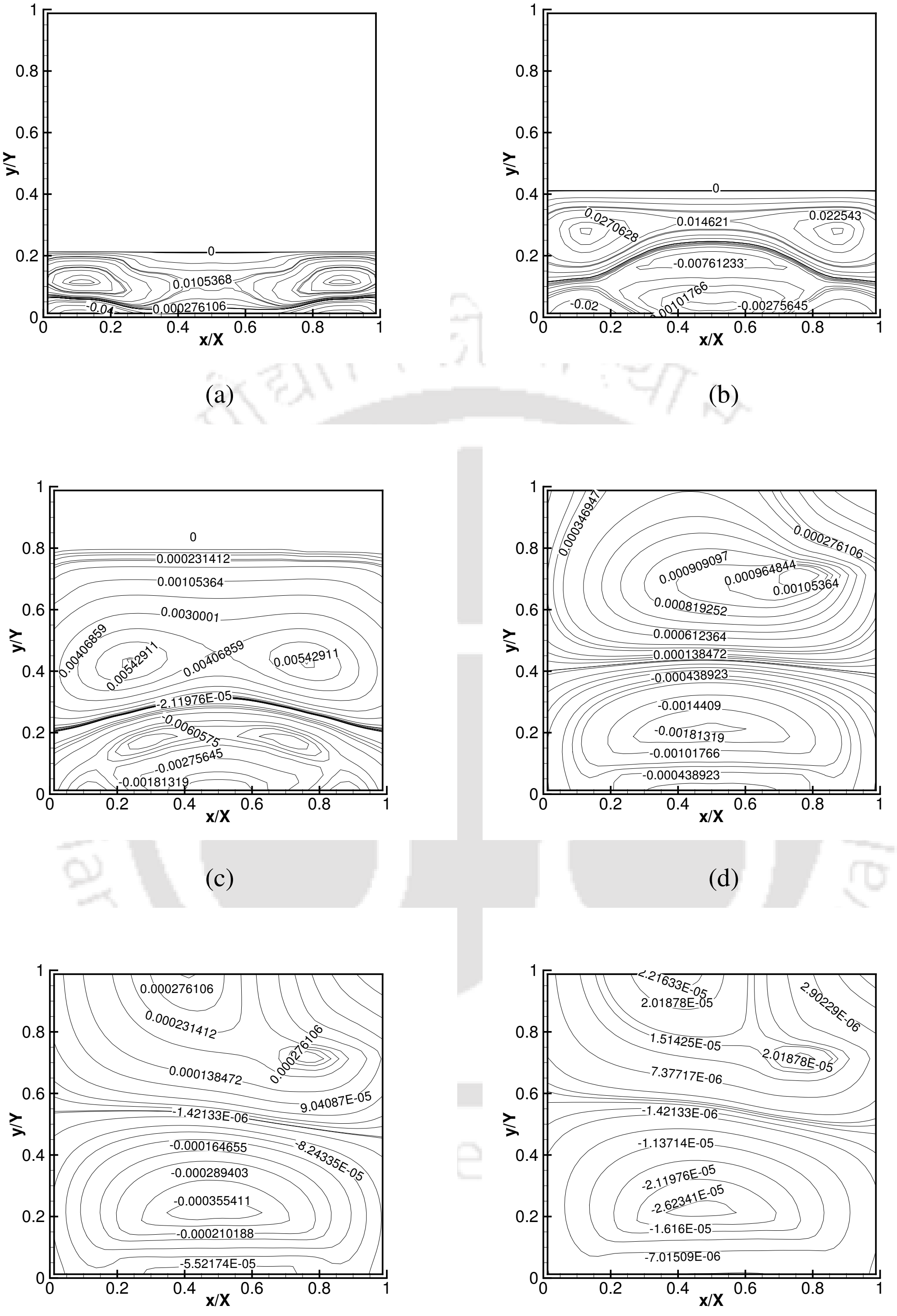

(a) (b)

(c) (d)

(e) (f)

Figure 7.10: Heat flux contours in the medium at time $\frac{t^*}{\Delta t^*}$ (a) = 20, (b) = 40, (c) = 80, (d) = 200 (e) = 400 (f) = 800 for β=10.0 for Case 4.

With $\beta = 10.0$, at $\frac{t^*}{\Delta t^*} = 20$ (Fig. 10a), though the radiation has traversed only a short distance in the medium, since the medium and the inhomogeneity have widely different scattering albedos, heat flux cores of different nature can be observed. In Fig. 7.10b, at $\frac{t^*}{\Delta t^*} = 40$, the scattered radiation is seen to have created a central heat flux core symmetric about the major axis of the inhomogeneity. In Fig. 7.10c, at $\frac{t^*}{\Delta t^*} = 80$, a few heat flux cores along the periphery of the inhomogeneity are observed. The two heat flux fronts emerging from the corners of the medium are also observed. In Figs. 7.10d and 7.10e, the response of the inhomogeneity at the top-right corner of the medium is observed. As time advances, in Fig. 7.10f, at $\frac{t^*}{\Delta t^*} = 800$, the contours tend to have a very low magnitude due to the extinction of the signal.

7.3 Results and Discussion – Gaussian pulse

The results for the same six cases with an incident Gaussian 4-pulse are discussed in this section. In all the four cases (Cases 1-4), irrespective of the magnitudes of the extinction coefficient β, the trends of the transmittance $q_t^*\left(0.5, 1.0, t^*\right)$ (Fig 7.11a and 7.11c) and reflectance $q_r^*\left(0.5, 0.0, t^*\right)$ (Fig 7.11b and 7.11d) signals resemble the trends of the 1-D [97] planar medium, but their temporal spans are much shorter. The pulse pattern of the laser wave is observed for both transmittance $q_t^*\left(0.5, 1.0, t^*\right)$ and reflectance $q_r^*\left(0.5, 0.0, t^*\right)$, with $\beta = 1.0$ .It can also be observed that the peak magnitudes of the signals also approach that of the 1-D case [97] while for $\beta = 10.0$, they are considerably different. By comparing Figs. 7,11a and 7.11c, it can be inferred that for a more participating medium, the location of the inhomogeneity has a noticeable effect on the magnitude of the transmittance $q_t^*\left(0.5, 1.0, t^*\right)$ at the centre of the other (north) boundary. However, it is observed from Figs. 7.11b and 7.11d that

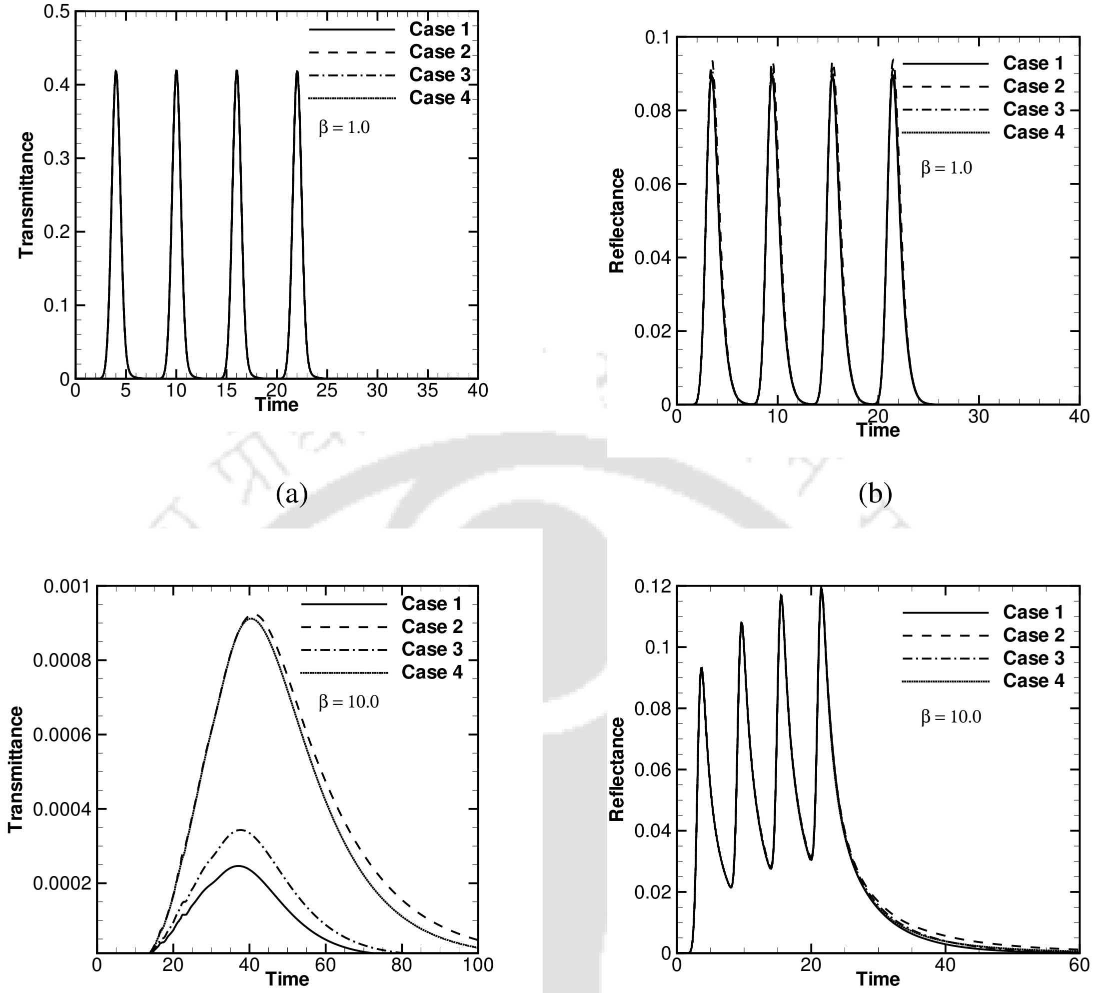

(a) (b)

(c) (d)

Figure 7.11: Transmittance $q_t^*\left(0.5,1.0,t^*\right)$ and Reflectance $q_r^*\left(\frac{x}{X},0.0,t^*\right)$ signals for Cases 1-4 for different values of extinction coefficient.

the location of the inhomogeneity has only a negligible effect on the reflectance $q_r^*\left(0.5,1.0,t^*\right)$, irrespective of the value of extinction coefficient β.

Cases 1-4 represent situations in which a substantial (75%) portion of the medium is strongly scattering $\left(\omega_1 = 0.998\right)$ and the inhomogeneity, which occupies 25% by volume, is weakly scattering $\left(\omega_2 = 0.1\right)$. With $\beta = 10.0$, for the situation representing Cases 1 (Fig. 7.1a) and 3 (Fig. 7.1c), the centrally located weakly scattering

$(\omega_2 = 0.1)$ inhomogeneity causes a low magnitude of transmittance $q_t^*(0.5,1.0,t^*)$ at the center of the north boundary (Fig.7.11c). Whereas in Cases 2 (Fig. 7.1b) and 4 (Fig. 7.1d), since the weakly-scattering inhomogeniety being off-center (Figs. 7.1b and 7.1d), the mid-portion of the north boundary receives considerably more energy than that of the Cases 1 and 3.The presence of the weakly scattering circular inhomogeneity at the top-right corner (Case 2, Fig. 7.1b) of the medium causes energy-damping of radiation occurs only during the later stages of the transport.

Figs. 7.12a-d show the transmittance $q_t^*(0.5,1.0,t^*)$ and reflectance $q_r^*(0.5,0.0,t^*)$ results for Cases 5 and 6 for two different values of the extinction coefficient β. From Fig. 7.12a, it is observed that, for a less participating medium, the position of an inhomogeneity of any shape does not seem to have any effect on the transmittance $q_t^*(0.5,1.0,t^*)$ signal. With $\beta = 1.0$, the exponential decrease of the collimated component of intensity being negligible, a large fraction of the transmittance signal at the middle of the other boundary is due to the collimated component. Since inhomogeneity also has the same extinction coefficient, the regardless of the presence (Case 6, Fig. 7.1f) or absence (Case 5, Fig.7.1e) of an elliptical inhomogeneity in the immediate vicinity of the boundary of incidence the curves of Fig.7.12c do not show any marginal difference in the case of transmittance $q_t^*(0.5,1.0,t^*)$ signals.

The magnitude of the transmittance $q_t^*(0.5,1.0,t^*)$ signals with $\beta = 10.0$ for Case 5 is almost five-fold that of Case 6 (Fig. 7.12c). Since in both these cases, both the medium and the inhomogeneity are highly participating, the role of the collimated component of transmittance signal is insignificant. But in Case 6, weak scattering and strong absorption due to the inhomogeneity immediately after the arrival of the signal into the medium is responsible for signals of low magnitude at the north boundary.

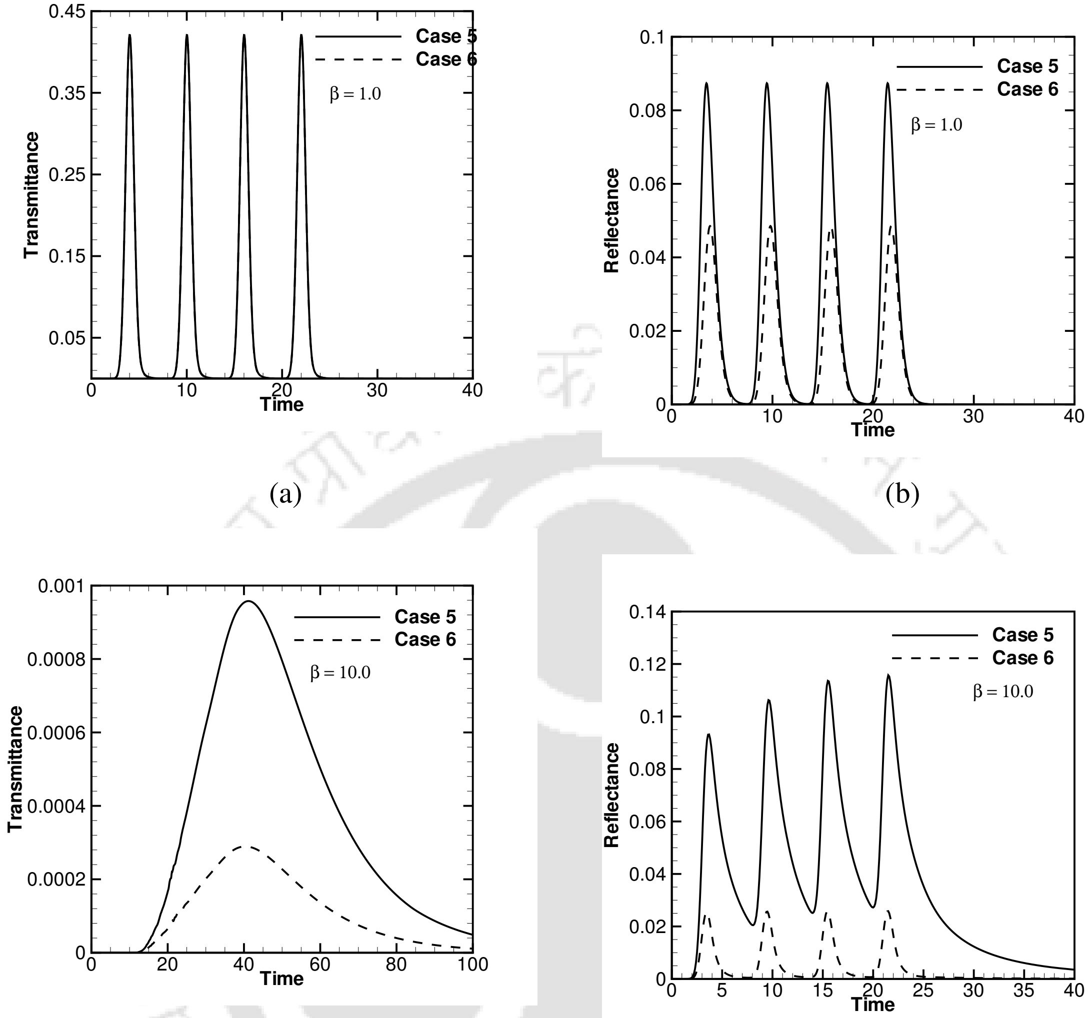

(a) (b)

(c) (d)

Figure 7.12: Transmittance $q_t^*\left(0.5,1.0,t^*\right)$ and Reflectance $q_r^*\left(\frac{x}{X},0.0,t^*\right)$ signals for Cases 5 and 6 for different values of extinction coefficient

It is observed from Figs. 7.12b and 7.12d that for both $\beta = 1.0$ and 10.0, the peak magnitude and the temporal stay of the reflectance $q_r^*\left(0.5,0.0,t^*\right)$ signal in Case 5 (Fig. 7.1e) is much higher than that of Case 6 (Fig. 7.1f). Since the reflectance $q_r^*\left(0.5,0.0,t^*\right)$ signal is the product of the back-scattered diffuse intensities from the medium, the presence of a weakly scattering inhomogeneity in the immediate vicinity (Case 6, Fig. 7.1f) of the south boundary (the boundary of incidence) has a large effect on the signal. This is the cause of a considerable difference in magnitudes of the reflectance $q_r^*\left(0.5, 0.0, t^*\right)$ signal between Case 5 (Fig. 7.1e) and Case 6 (Fig. 7.1f) for $\beta = 1.0$ (Fig. 7.12b) and for $\beta = 10.0$ (Fig. 7.12d).

In Figs. 7.13a-d, for Cases 1 (Fig. 7.1a) and 2 (Fig. 7.1b), distributions of transmittance $q_t^*\left(\frac{x}{X}, 1.0, t^*\right)$ and reflectance $q_r^*\left(\frac{x}{X}, 0.0, t^*\right)$ signals along the boundaries have been plotted for two different values of the extinction coefficient $\beta = 1.0$ and 10.0. For a given β, these distributions are plotted at 6 time levels, viz. $\frac{t^*}{\Delta t^*} = 100, 200, 300, 400, 600$ and 800.. Solid and dashed lines differentiate Cases 1 and 2 respectively. The digit n on any curve indicates signal at $n \times 100^{\text{th}}$ time step.

It is observed from Fig. 7.13a that for Case 1 (Fig. 7.1a), the spatial distributions of transmittance $q_t^*\left(\frac{x}{X}, 1.0, t^*\right)$ and reflectance $q_r^*\left(\frac{x}{X}, 0.0, t^*\right)$ signals at all time levels are symmetric about the mid-plane $\left(0.5, y\right)$. For Case 2 (Fig. 7.1b), it is observed that the distribution of transmittance $q_t^*\left(\frac{x}{X}, 1.0, t^*\right)$ signal is slightly asymmetric about the vertical mid-plane at the 100th time step. This asymmetry is due to the presence of a circular inhomogeneity near the east boundary and the less degree of asymmetry is due to the weakly participating medium $\left(\beta = 1.0\right)$. In Fig. 7.13b, due to the presence of the central circular inhomogeneity a crest is observed in the reflectance $q_r^*\left(\frac{x}{X}, 0.0, t^*\right)$ signals at the 100th time step. The curve is noticed to have a central crest and symmetric troughs of a little curvature, which tend to fall towards both the walls. As is seen from Fig. 7.13c, for Case 1 (Fig. 7.1a) in case of a highly absorbing medium $\left(\beta = 10.0\right)$, the presence of a central inhomogeneity is observed in the form of a trough at the 200th time step. For Case 2 (Fig. 7.1b), from Fig. 7.13c, a sharp

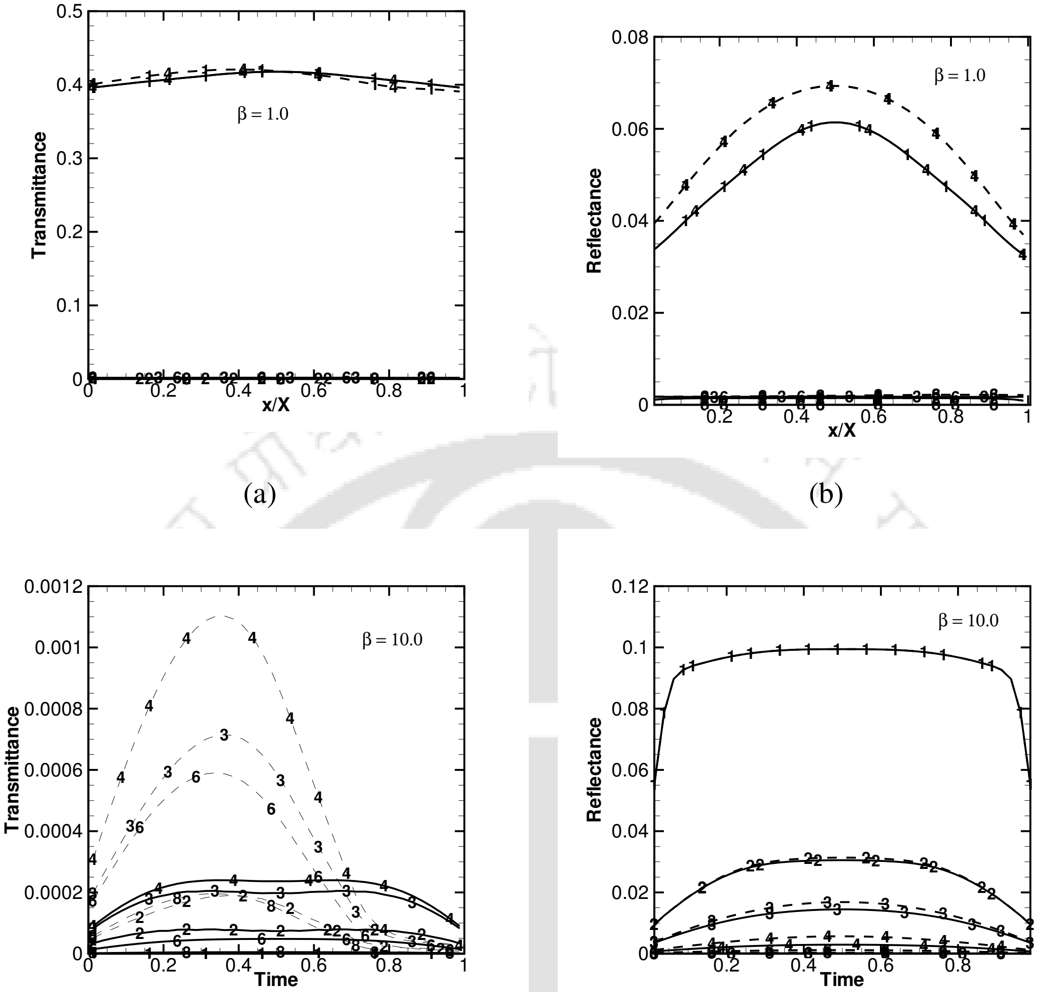

(a) (b)

(c) (d)

Figure 7.13: Time evolution of the distribution of transmittance $q_t^*\left(x/X, 1.0, t^*\right)$ and reflectance $q_r^*\left(x/X, 0.0, t^*\right)$ signals along the boundaries. The digit n on any curve indicates the distribution of the signal at $n\times 100^{\text{th}}$ time step. Solid and dashed lines are results for Cases 1 and 2 respectively.

skew towards the west boundary is observed and it is due to the presence of a weakly scattering inhomogeneity in the top-right corner of the medium. At all time levels, the reflectance $q_r^*\left(\frac{x}{X}, 0.0, t^*\right)$ signals are found to be symmetric about the vertical mid-plane for both Cases 1 and 2. However, as shown in Figs. 7.13b and 7.13d, the variation in spatial distribution of reflectance $q_r^*\left(\frac{x}{X},0.0,t^*\right)$ signals at the early stages is much higher than in the later stages in both Cases 1 and 2 for the two values of extinction coefficient.

In Figs. 7.14a-d, for Cases 3 (Fig. 7.1c) and 4 (Fig. 7.1d), distributions of transmittance $q_t^*\left(\frac{x}{X},1.0,t^*\right)$ and reflectance $q_r^*\left(\frac{x}{X},0.0,t^*\right)$ signals along the boundaries have been plotted for two different values of the extinction coefficient $\beta = 1.0$ and 10.0. For a given β, these distributions are plotted at 6 time levels, viz. $\frac{t^*}{\Delta t^*} = 100,\ 200,\ 300,\ 400,\ 600$ and 800. The temporal profiles at these six time levels have been differentiated by line-types similar to Figs. 7.13a-d. The digit n on any curve indicates the distribution of the signal at $n\times100^{\text{th}}$ time step. Solid and dashed lines differentiate Cases 3 and 4, respectively.

It is seen from Fig. 7.14a that for Case 3 (Fig. 7.1c), the spatial distributions of transmittance $q_t^*\left(\frac{x}{X},1.0,t^*\right)$ and reflectance $q_r^*\left(\frac{x}{X},0.0,t^*\right)$ signals at all time levels are symmetric about the mid-plane $(0.5, y)$. This is comparable to the trend in Fig. 7.13a. In Fig. 7.14b, the presence of the central horizontal elliptical inhomogeneity can be observed in the reflectance $q_r^*\left(\frac{x}{X},0.0,t^*\right)$ signals at the 200th time step. This is similar to the Case 1 in Fig 7.13b. However, the crest in the curve is observed to have very less curvature corresponding to the flat surface of the horizontal elliptical inhomogeneity in the central region. For Case 4 (Fig. 7.1d), it is observed from Fig.7.14b that the reflectance $q_r^*\left(\frac{x}{X},0.0,t^*\right)$ signal is slightly skewed towards the east boundary. This skew is due to the presence of a vertical elliptical inhomogeneity near the west boundary and the less magnitude of the skew is attributed to a weakly participating medium $(\beta = 1.0)$.

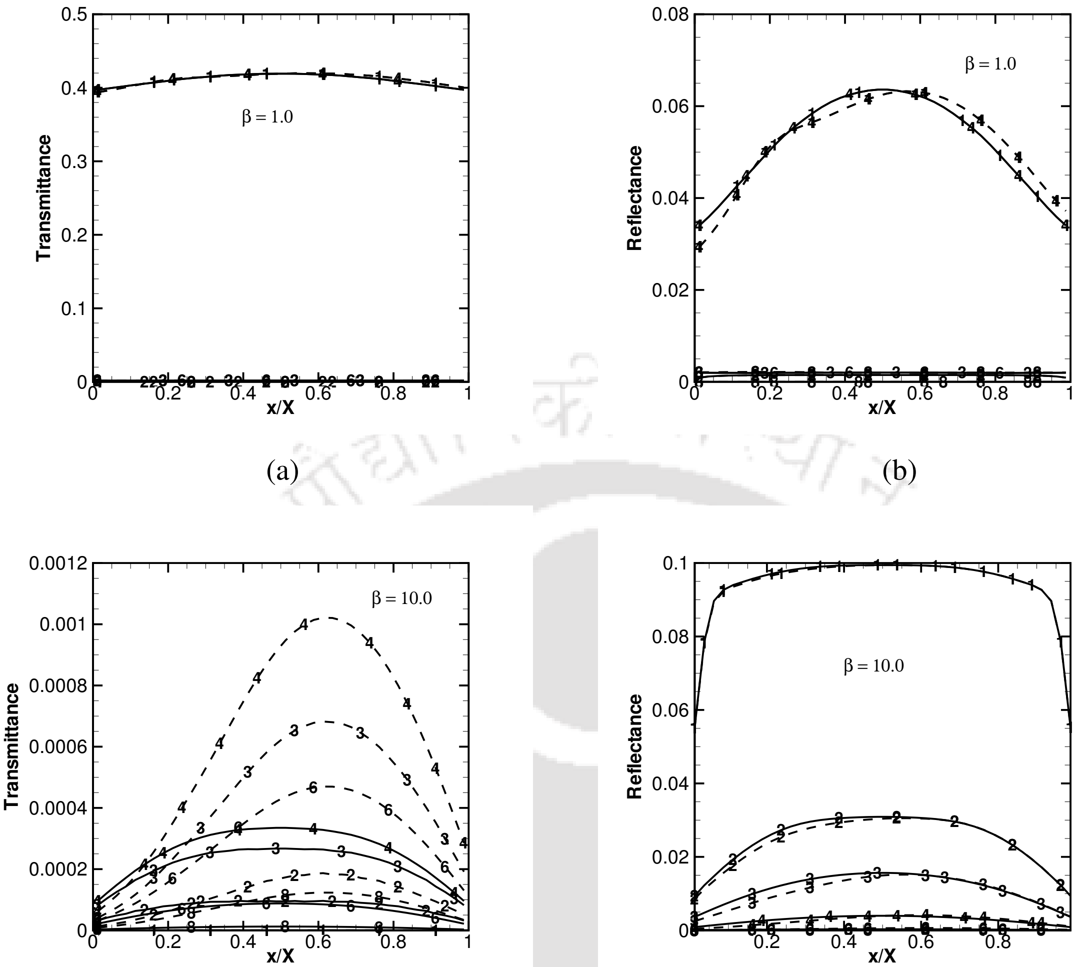

(a) (b)

(c) (d)

Figure 7.14: Time evolution of the distribution of transmittance $q_t^*\left(x/X,1.0,t^*\right)$ and reflectance $q_r^*\left(x/X,0.0,t^*\right)$ signals along the boundaries. The digit n on any curve indicates the distribution of the signal at $n\times100^{\text{th}}$ time step. Solid and dashed lines are results for Cases 3 and 4 respectively.

As is seen from Fig. 7.14c, for Case 3 (Fig. 7.1c) with a highly absorbing medium $(\beta=10.0)$, the central inhomogeneity has no major effect. For Case 4 (Fig. 7.1d), from Fig. 7.14c, a sharp skew towards the east boundary is observed and it is due to the presence of a weakly scattering vertical elliptical inhomogeneity close to the west boundary of the medium. From Fig. 7.14b it can be observed that at all time levels, the reflectance $q_r^*\left(\dfrac{x}{X},0.0,t^*\right)$ signals are symmetric about the vertical mid-plane for both Cases 3 and 4 for $\beta = 1.0$. But since radiation encounters strongly-participating $(\beta = 10.0)$ and weakly-scattering $(\omega = 0.1)$ inhomogeneity very soon after its incidence on the south boundary in Case 4 (Fig.7.1d), an unequal distribution of signals can be observed along the south boundary (Fig. 7.14d) in the later stages of the radiation propagation.

In Figs. 7.15a-d, for Cases 5 (Fig. 7.1e) and 6 (Fig. 7.1f), distributions of transmittance $q_t^*\left(\frac{x}{X}, 1.0, t^*\right)$ and reflectance $q_r^*\left(\frac{x}{X}, 0.0, t^*\right)$ signals along the boundaries have been plotted for two different values of the extinction coefficient $\beta = 1.0$ and 10.0. Similar to Figs 7.13 and 7.14, these figures are plotted at 6 time levels, viz. $\frac{t^*}{\Delta t^*} = 100,\ 200,\ 300,\ 400,\ 600$ and 800. Solid and dashed lines differentiate cases 5 and 6, respectively. The digit n on any curve indicates the distribution of the signal at $n \times 100^{\text{th}}$ time step.

It is seen from Fig. 7.15a, that for Case 5 (Fig. 7.1e), the spatial distributions of transmittance $q_t^*\left(\frac{x}{X}, 1.0, t^*\right)$ signals at all time levels are symmetric about the mid-plane $(0.5, y)$ which is similar to the trend in Figs. 7.13a and 7.14a. For Case 6 (Fig. 7.1d), it is observed that the transmittance $q_t^*\left(\frac{x}{X}, 1.0, t^*\right)$ signal is skewed a little towards the west boundary. This skew is due to the existence of the circular inhomogeneity near the top-right corner. In Fig. 7.15b, the presence of the elliptical inhomogeneity (Case 6, Fig.7.1f) near the south boundary can be observed in the reflectance $q_r^*\left(\frac{x}{X}, 0.0, t^*\right)$ signals at the 100^{th} time step. It is seen from Fig. 7.14c that for Case 5 (Fig. 7.1e) in case of a highly absorbing medium $(\beta = 10.0)$, the presence of the circular inhomogeneity in the top-right corner of the medium causes an unequal distribution of the transmittance $q_t^*\left(\frac{x}{X}, 1.0, t^*\right)$ signals. Since the elliptical

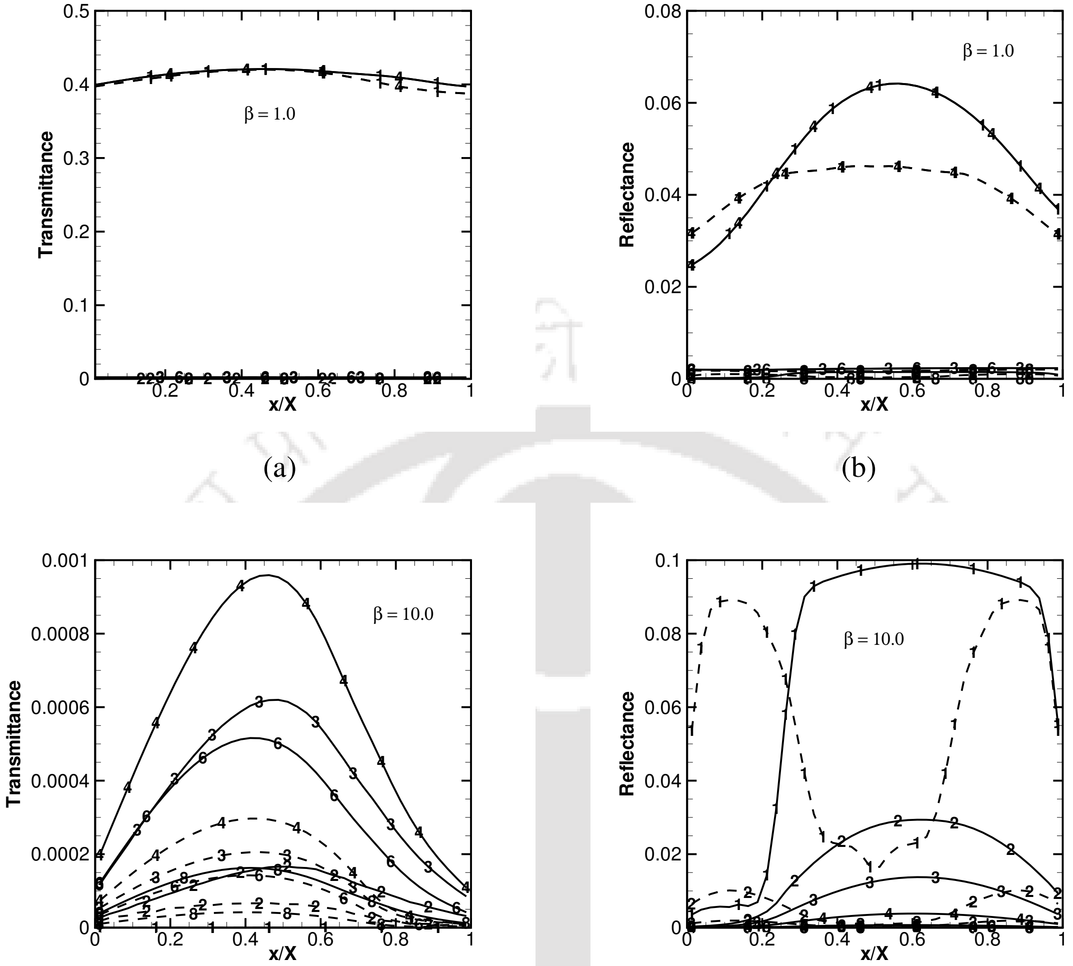

(a) (b)

(c) (d)

Figure 7.15: Time evolution of the distribution of transmittance $q_t^*\left(x/X,1.0,t^*\right)$ and reflectance $q_r^*\left(x/X,0.0,t^*\right)$ signals along the boundaries. The digit n on any curve indicates the distribution of the signal at $n\times100^{\text{th}}$ time step. Solid and dashed lines are results for Cases 5 and 6 respectively.

inhomogeneity is located symmetric about the vertical mid-plane and a small inhomogeneity at the top-right corner (Fig.7.1f), the skew is less pronounced for Case 6 (Fig.7.15c). In Fig. 7.15d, the reflectance $q_r^*\left(\frac{x}{X},0.0,t^*\right)$ signals tend to skew more toward the east boundary due to the small square inhomogeneity at the bottom-left corner. In the same figure, the presence of the horizontal elliptical inhomogeneity adjacent to the south boundary can be observed as a deep trough in the reflectance curve for Case 6(Fig. 7.1f)

Figures 7.15-7.18 provide heat flux $q^*\left(\frac{x}{X},\frac{y}{Y},t^*\right)$ contours in the medium for Cases 1 (Fig. 7.1a), 4 (Fig. 7.1d) and 6 (Fig. 7.1f), respectively. For $\beta = 10.0$, in each of these figures, the contours have been plotted at six time levels, viz. $\frac{t^*}{\Delta t^*} = 20, 40, 80, 200, 400$ and 800.

From Figs. 7.16a and 7.16b, it is observed that at $\frac{t^*}{\Delta t^*} = 20$ and 40, negative heat flux which adds towards the reflectance $q_r^*\left(\frac{x}{X},0.0,t^*\right)$ signal appears near the south boundary (the boundary of incidence). At $\frac{t^*}{\Delta t^*} = 200$, it is observed from Fig. 7.16c that a negative heat flux in the vicinity of the south boundary is well established. In Fig. 7.16d, a heat flux front moving through the medium tending to converge at the centre of the medium is observed. In Fig. 7.16e, a central region of heat flux concentration symmetric about the geometric centre of the inhomogeneity is observed at $\frac{t^*}{\Delta t^*} = 400$. As the time progresses, it is seen from Figs. 7.16d-f that the magnitudes of the heat flux contours diminish and their distribution gets uniform. At $\frac{t^*}{\Delta t^*} = 800$, the signal are observed to be almost vanished.

At the six afore-mentioned time-levels, Figs. 7.17a-f show heat flux contours for a vertical-elliptical inhomogeneity symmetric about the horizontal mid-plane and located bordering the west boundary (Case 4, Fig. 7.1d), With $\beta = 10.0$, at $\frac{t^*}{\Delta t^*} = 20$ (Fig. 7.17a), radiation has propagated only a little distance in the medium. In Fig. 7.17b, at $\frac{t^*}{\Delta t^*} = 40$, though the radiation has just reached the inhomogeneity, no

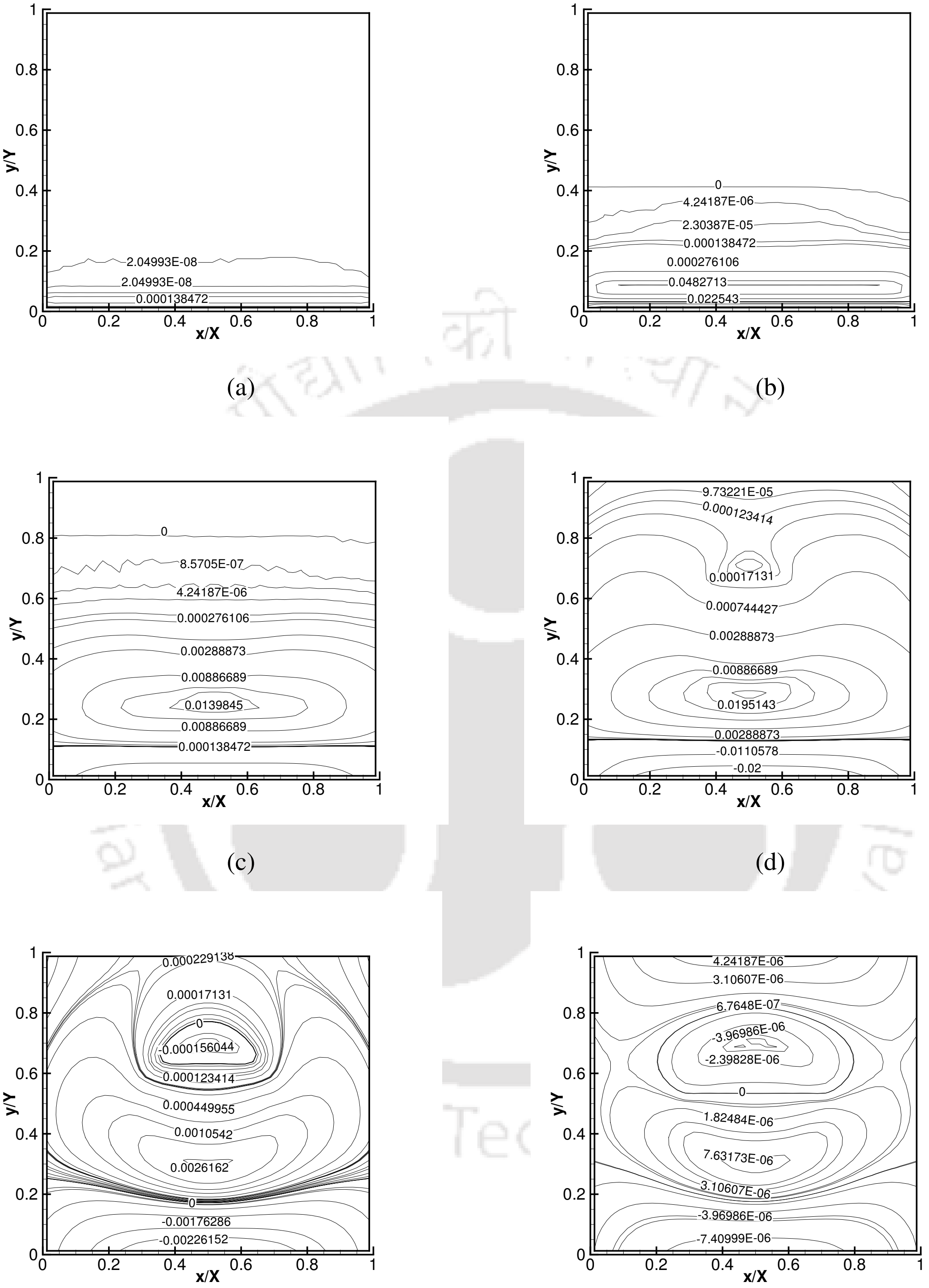

(a) (b)

(c) (d)

(e) (f)

Figure 7.16: Heat flux contours in the medium at time $\frac{t^*}{\Delta t^*}$ (a) = 20, (b) = 40, (c) = 80, (d) = 200 (e) = 400 (f) = 800 for β=10.0 for Case 1.

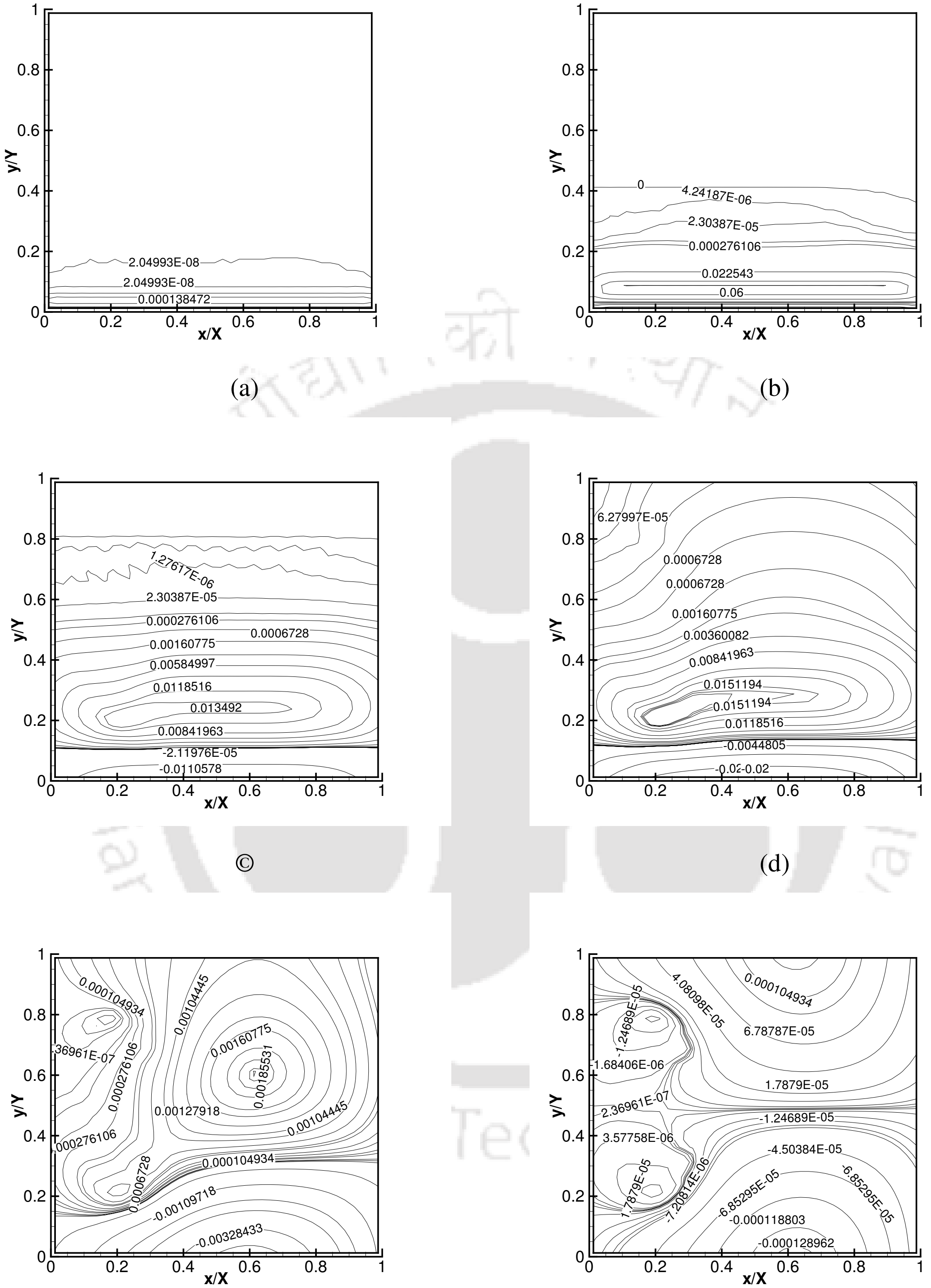

(a) (b)

© (d)

(e) (f)

Figure 7.17: Heat flux contours in the medium at time $\frac{t^*}{\Delta t^*}$ (a) = 20, (b) = 40, (c) = 80, (d) = 200 (e) = 400 (f) = 800 for β=10.0 for Case 4.

visible effects on the contours is observed. At $\frac{t^*}{\Delta t^*} = 80$, the radiation front has met the inhomogeneity and thus the heat flux contours are observed to be affected by scattering inside the inhomogeneity. In Figs. 7.17d and 7.17e, the response of the inhomogeneity to the propagation of radiation through it can be observed. A heat flux core representing the shape of the inhomogeneity is observed in the vicinity of the west boundary. A off-central positive heat flux core is also seen in Fig. 7.17e. This is owing to the radiation transport from the south boundary to the north boundary through the medium. Since the inhomogeneity is isotropically scattering, contours are observed to be symmetric about the minor axis of the ellipse (Fig. 7.17e). With the progress of time, in Fig. 7.17f, at $\frac{t^*}{\Delta t^*} = 800$, the contours tend to have a very low magnitude due to the death of the signal.

Figs. 7.18a-f show heat flux contours for a medium containing a horizontal-elliptical inhomogeneity symmetric about the vertical mid-plane located adjacent to south boundary and a square inhomogeneity at the top-right corner(Case 6, Fig. 7.1f), at the six afore-mentioned time-levels. With $\beta = 10.0$, at $\frac{t^*}{\Delta t^*} = 20$ (Fig. 7.18a), though the radiation has traversed only a short distance in the medium, since the medium and the inhomogeneity are of widely different scattering albedos, heat flux cores of dissimilar natures can be observed. In Fig. 7.18b, at $\frac{t^*}{\Delta t^*} = 40$, the scattered radiation is seen to have created a central heat flux core symmetric about the major axis of the inhomogeneity. In Fig. 7.18c, at $\frac{t^*}{\Delta t^*} = 80$, a few heat flux cores along the periphery of the inhomogeneity are observed. The two heat flux fronts emerging from the corners of the medium are also observed and as expected, these are of equal magnitude. In Figs. 7.18d and 7.18e, the response of the inhomogeneity at the top right corner of the medium is observed. As time advances, in Fig. 7.18f, at $\frac{t^*}{\Delta t^*} = 800$, the contours tend to have a very low magnitude due to the extinction of the signal.

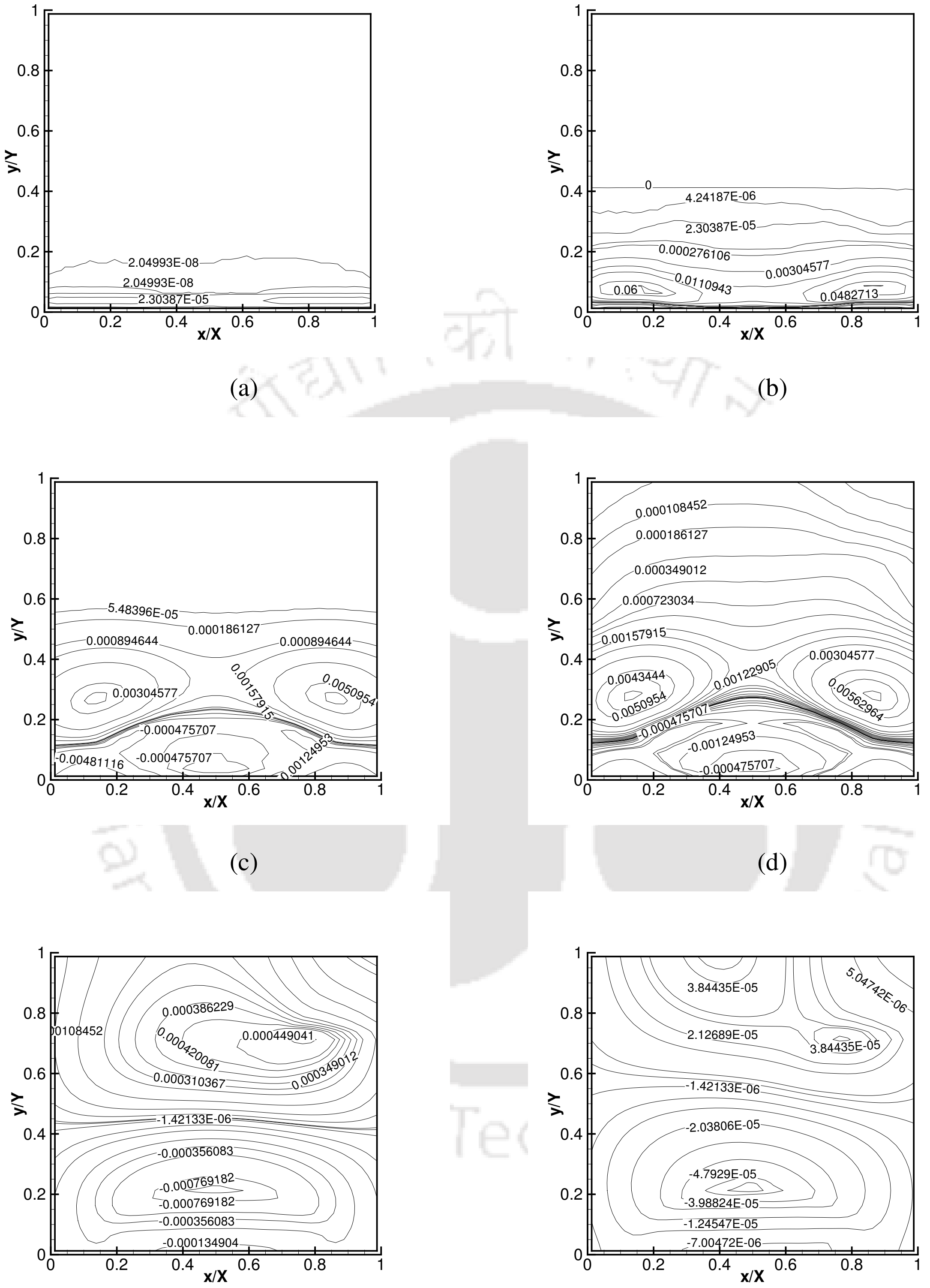

(a) (b)

(c) (d)

(e) (f)

Figure 7.18: Heat flux contours in the medium at time $\frac{t^*}{\Delta t^*}$ (a) = 20, (b) = 40, (c) = 80, (d) = 200 (e) = 400 (f) = 800 for β=10.0 for Case 6.

7.5 Summary

Transport of a short-pulse laser through a 2-D rectangular participating medium containing localized inhomogeneities of different shapes placed at various locations was studied. The inhomogeneities differed from the main medium by their scattering albedos. The laser pulse of unit pulse width of either step or Gaussian temporal profile was considered incident normal to the south boundary. The transmittance and reflectance signals were studied for the effects of the extinction coefficient, shapes and locations of inhomogeneities. Heat flux distributions inside the medium were also studied. The results of the present work for a centrally located square inhomogeneity were compared with those available in the literature and a very good comparison was obtained. The shape and the location of the inhomogeneities were found to have a significant effect on the thermal signatures at the boundaries. The presence of an inhomogeneity of a certain shape and location near a boundary was found to have a more-pronounced effect on the thermal signature at that boundary. The heat flux contours were heavily influenced by the shape and location of the inhomogeneities. With spatial and temporal distributions of heat fluxes inside the medium, information about the shape, size and location of an inhomogeneity were obtained.

In Chapters 2-7, different classes of problems dealing with the transport of short-pulse radiation was considered. Effects of diffuse as well as collimation radiation source having step as well as Gaussian temporal profiles were studied. In all the problems considered so far, the loading on the boundary was uniform. In Chapter 8, cases of a 2-D inhomogeneous media having non-uniform loading are studied.

CHAPTER 8

Effects of the Incidence of Short-Pulse Laser of Gaussian-Temporal and Different Spatial Profiles on a 2-D Rectangular Inhomogeneous Participating Medium

---

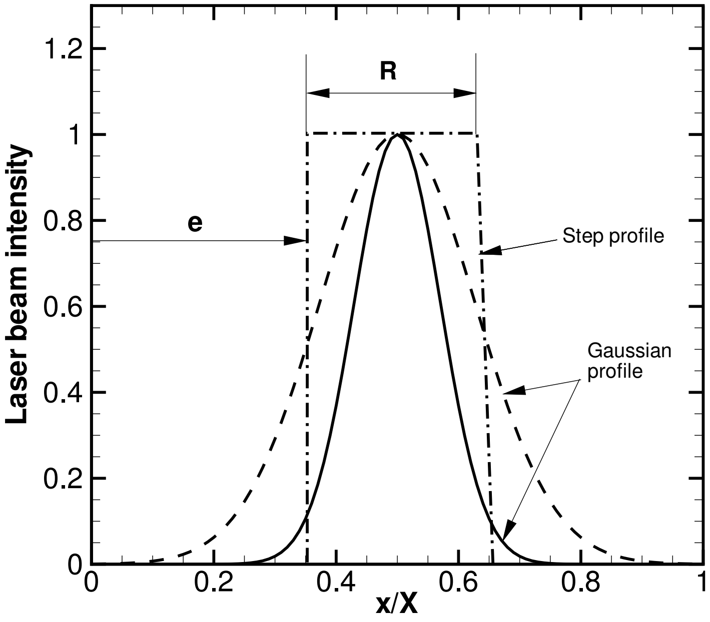

Figure: Various Spatial profiles of the incident laser beam

8.1 Introduction

In the previous chapters, the short-pulse radiation incident on 2-D rectangular participating media was uniformly loaded on the boundary of incidence. But incident laser in many engineering applications has a specific beam radius whose span is less than the dimensions of the boundary of incidence. The occurrence of inclusions of different shapes and locations in particle sizing and turbid media studies are practical instances of this problem. With a short-pulse laser of spatio-temporal Gaussian profile or partial loading with Gaussian temporal profile, the effects of inhomogeneities of different shapes and locations on thermal signatures at the boundaries and the growth of heat flux profiles in the medium have been studied in the chapter.

8.2 Problem

In this problem, effects of a short-pulse laser of Gaussian temporal and different spatial profiles on the signals emanating from a 2-D rectangular participating medium containing localized inhomogeneities are analyzed. Incident short-pulse laser of Gaussian temporal profile has spatial loading on the south boundary either as a Gaussian or as a step function. The absorbing and scattering participating medium consists of a localized circular or elliptical inhomogeneity. The extinction coefficient of the inhomogeneity is the same as the containing medium, while its scattering albedo is different. Transmittance and reflectance signals are analyzed for the effects of the extinction coefficient and the spatial profile of incident short-pulse laser.

Spatial distributions of the signals along the boundaries and the temporal evolution of the heat flux distributions inside the medium are also studied. The problem has been analyzed using the finite volume method. Based on the spatial profiles of the incident laser, and the shapes and locations of inhomogeneities in the main medium, as shown in Table 8.1, the problem is categorized into six cases viz, 11, 12, 21, 22, 31 and 32. As a means of generalization if we consider Case AB, the index A signifies the type of spatial profile and the index B signifies the shape and position of inhomogeneity.

A	**Laser beam spatial profile**	**Figure**
1	Gaussian of beam radius $R = 0.1667$	8.1a
2	Gaussian of beam radius $R = 0.3333$	
3	Step of beam radius $R = 0.3$	
B	**Inhomogeneity**	**Figure**
1	Centrally located, circular, occupying 1/4th volume of the main medium	7.1 a
2	Vertical elliptical, adjacent to the west Boundary, occupying 1/4th volume of the main medium	7.1 d

Table 8.1: Combinations of different cases considered Chapter 8

The medium and its inhomogeneity in all the cases are considered to have the same extinction coefficient β. The scattering albedo of the medium and the inhomogeneity are $\omega_1 = 0.998$ and $\omega_2 = 0.1$ respectively. A study was done for two values of the extinction coefficient $\beta = 1.0$ and 10.0 for all the cases. The two values of β are representative of weak and strong participating medium situations.

8.3 Formulation

The formulation used for a 2-D homogeneous participating medium presented in Chapter 5 can be used for the different spatial profiles of incidence with modifications in the equations for incident pulse as presented below.

The incident short-pulse radiation having Gaussian temporal and Gaussian spatial profile is given by (Figs. 8.1a).

$$\begin{aligned} I_c(\theta,t) = I_{c,\max}(\theta,t)\exp(-\beta s_c)\exp\left[-4\left(\frac{t-\frac{s_c}{c}-t_c}{t_p}\right)^2 \ln 2\right] \\ \times\exp\left[-4\left(\frac{x-0.5X}{R}\right)^2 \ln 2\right] \\ \times\delta(\theta-\theta_c)\,\delta(\phi-\phi_c), \quad 0<t<2t_c \end{aligned} \tag{8.1a}$$

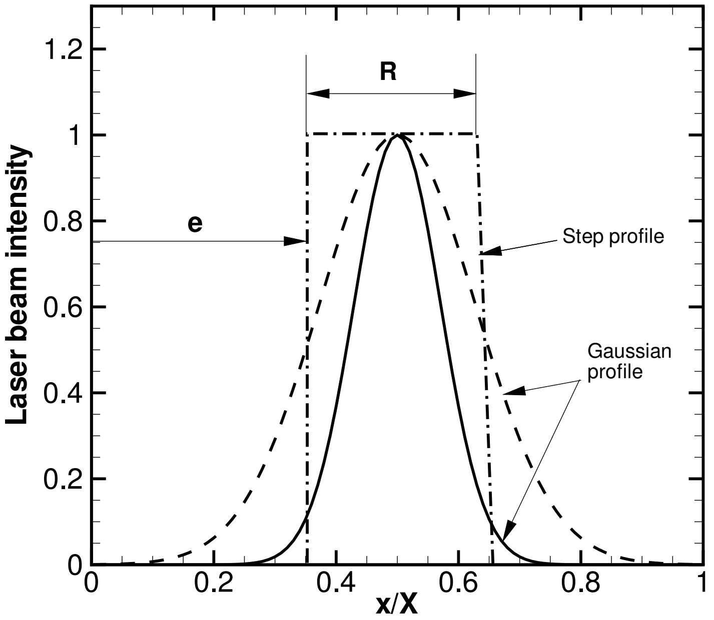

(e)

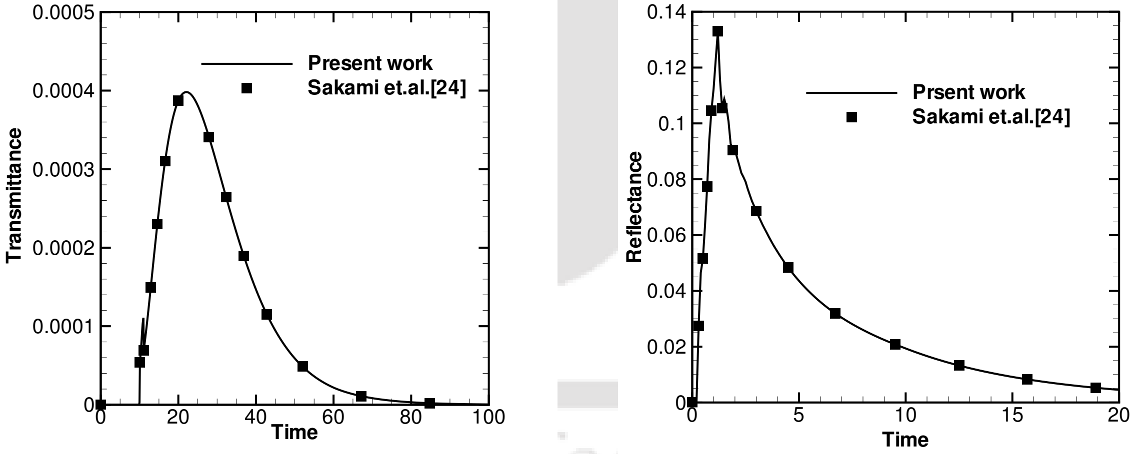

Figure 8.1: (a) Various Spatial profiles of the incident laser beam (b) Comparison of transmittance and reflectance with literature

where in Eq. (8a), $I_{c,\max}$ is the collimated intensity at the south boundary, s_c is the geometric distance in the direction (θ_c, ϕ_c) of the collimated radiation, δ is the Dirac-delta function.

With the incident short-pulse radiation having Gaussian temporal but spatial profile as a step function, the equation is given by (Figs. 8.1a).

$$I_c(\theta,t) = I_{c,\max}(\theta,t)\exp(-\beta s_c)\ \exp\left[-4\left(\frac{t-\frac{s_c}{c}-t_c}{t_p}\right)^2 \ln 2\right] \\ \times\left[H(x-e)-H\left(x-(e+R)\right)\right] \\ \times\delta(\theta-\theta_c)\delta(\phi-\phi_c),\quad 0<t<2t_c \tag{8.1b}$$

where H is the Heaviside function.

If $t^* = \beta ct$ and $t_p^* = \beta ct_p$ are the dimensionless times, Eq. (8.1a) and (8.1b) can be written as

$$I_c\left(\theta,t^*\right) = I_{c,\max}\left(\theta,t^*\right)\exp(-\beta s_c)\ \exp\left[-4\left(\frac{t^*-\beta s_c-t_c^*}{t_p^*}\right)^2 \ln 2\right] \\ \times\exp\left(-4\left(\frac{x-0.5X}{R}\right)^2 \ln 2.0\right) \\ \times\delta(\theta-\theta_c)\delta(\phi-\phi_c),\quad 0<t^*<2t_c^* \tag{8.2a}$$

$$I_c\left(\theta,t^*\right) = I_{c,\max}\left(\theta,t^*\right)\exp(-\beta s_c)\ \exp\left[-4\left(\frac{t^*-\beta s_c-t_c^*}{t_p^*}\right)^2 \ln 2\right] \\ \times\left[H(x-e)-H\left(x-(e+R)\right)\right] \\ \times\delta(\theta-\theta_c)\delta(\phi-\phi_c),\quad 0<t^*<2t_c^* \tag{8.2b}$$

The rest of the formulation is the same that is used elsewhere for the 2-D problems.

8.4 Results and Discussion

50×50 equal size control volumes were found sufficient for grid independency and a maximum of 120 directions covering the 4π solid angle were found enough for the ray-independent solution. 1000 divisions of the total time t^* domain were found sufficient for marching in the time dimension. At every time step, the iteration was set to $\left|S_{t,\text{old},P}^m - S_{t,\text{new},P}^m\right| \le 1.0\times10^{-7}$.

In the following pages, effects of different spatial profiles of the incident laser on a square medium $\left(\frac{X}{Y}=1\right)$ containing an inhomogeneity of circular or elliptical shape at different locations are discussed. Results for $\beta = 1.0$ and 10.0 are presented for the aforementioned six cases. The south boundary of the 2-D medium is subjected to a short-pulse laser incident normal to the boundary.

Regardless of the value of the extinction coefficient β, the trends of the transmittance $q_t^*\left(0.5,1.0,t^*\right)$ (Fig 8.2a and 8.2c) and reflectance $q_r^*\left(0.5,0.0,t^*\right)$ (Fig 8.2b and 8.2d) signals resemble that of the 1-D planar medium [101]. However, their temporal lives are much shorter [30]. With $\beta = 1.0$, the peak magnitudes of the signals also tend toward that of the 1-D case while for $\beta = 10.0$, they are quite different [101]. Case 11 is the combination of a Gaussian spatial profile incident laser of beam radius 0.16667 on a medium containing a central circular inhomogeneity (Fig. 7.1a), while Case 12 is the same laser on a medium containing a vertical elliptical inhomogeneity adjacent to the west boundary (Fig. 7.1d). In both these cases, a major (3/4th by volume) portion of the medium is strongly scattering $(\omega_1 = 0.998)$ and the inhomogeneity which occupies 1/4th by volume is weak scattering $(\omega_2 = 0.1)$. While the medium is less participating $(\beta = 1.0)$, the location of the inhomogeneity is observed to have no effect on the transmittance $q_t^*\left(0.5,1.0,t^*\right)$ (Fig 8.2a) and a little effect on the reflectance $q_r^*\left(0.5,0.0,t^*\right)$ signals (Fig 8.2b) obtained at the middle of the boundaries. When the medium becomes highly participating $(\beta = 10.0)$, the position of the inhomogeneity has pronounced effect on the transmittance $q_t^*\left(0.5,1.0,t^*\right)$ signals as seen from Figs. 8.2c.

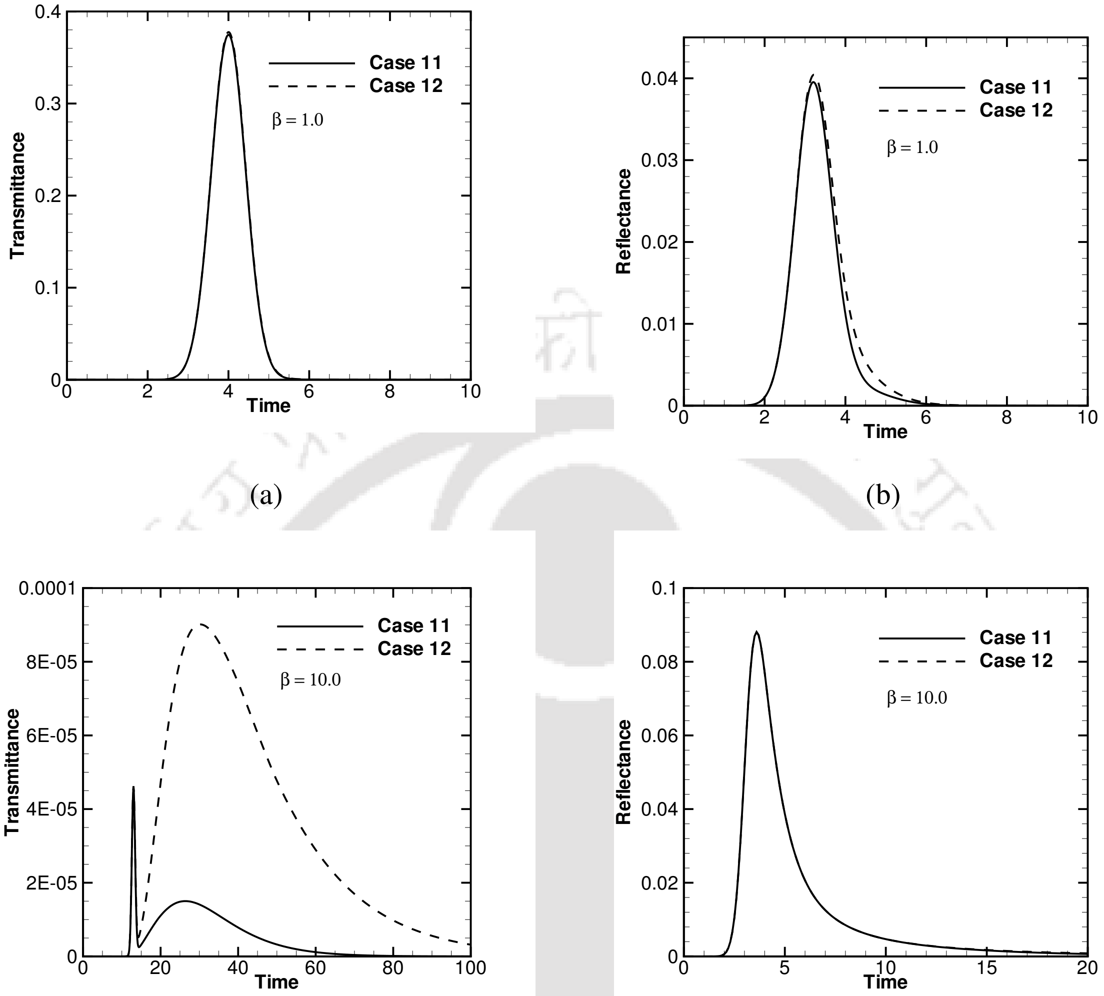

(a) (b)

(c) (d)

Figure 8.2: Transmittance and Reflectance results for Cases 11, 12 for two different values of extinction coefficient.

With $\beta = 10.0$ (Fig.8.2c), for the situation representing Case 11 (Fig. 7.1a), the centrally located weakly scattering $(\omega_2 = 0.1)$ inhomogeneity is accountable for the small magnitude of transmittance $q_t^*\left(0.5, 1.0, t^*\right)$ at the middle of the north boundary. Whereas in Case 12 (Fig. 7.1d), since the weakly scattering inhomogeniety is offset from the center , the middle portion of the north boundary receives more energy than that of the Case 11. Case 21 is the combination of a Gaussian spatial profile incident laser of beam radius 0.3333 on a medium containing a central circular inhomogeneity

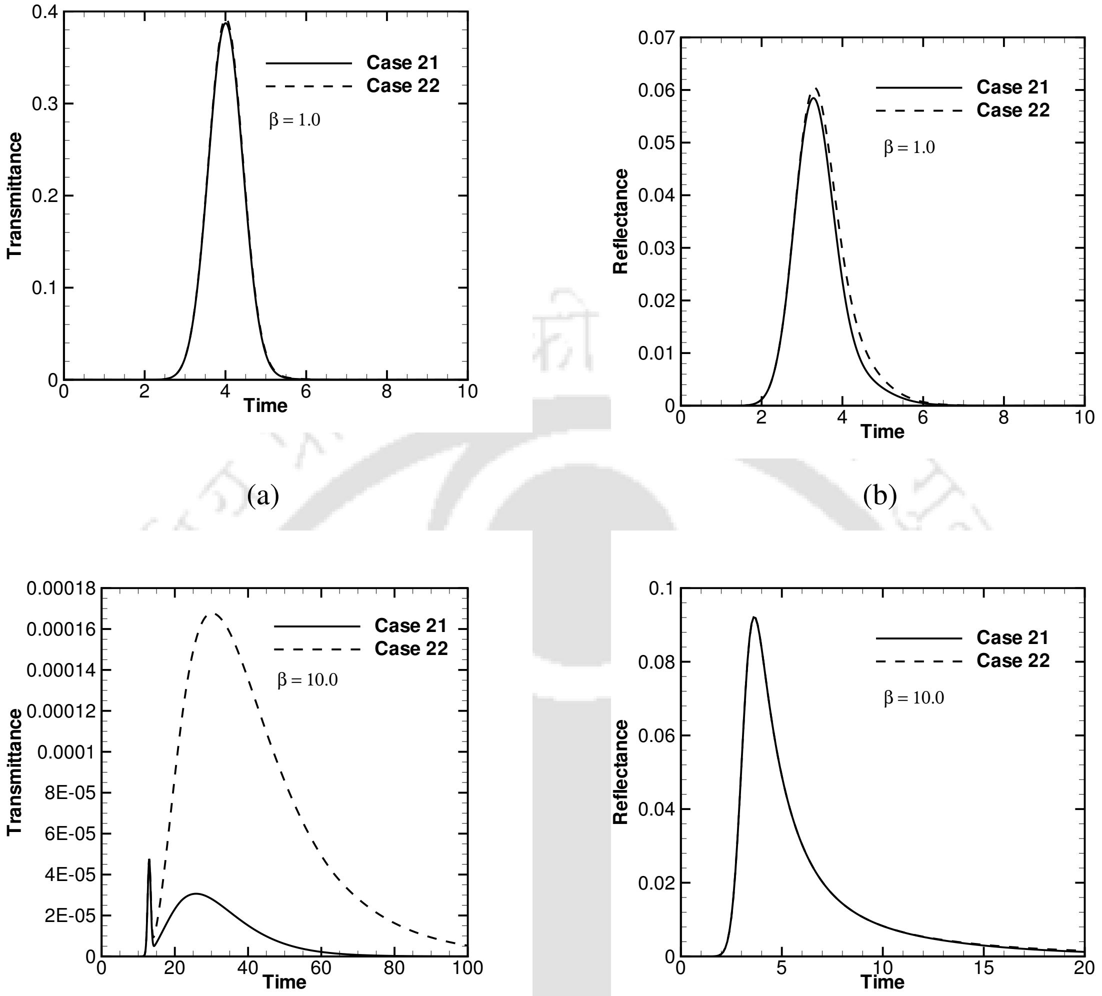

(a) (b)

(c) (d)

Figure 8.3: Transmittance and Reflectance results for Cases 21, 22 for two different values of extinction coefficient.

(Fig. 7.1a), while Case 22 is with the same spatial profile on a medium containing a vertical elliptical inhomogeneity adjacent to the west boundary (Fig. 7.1d). Transmittance $q_t^*\left(0.5,1.0,t^*\right)$ and reflectance $q_r^*\left(0.5,0.0,t^*\right)$ results for Cases 21 and 22 for two different values of the extinction coefficient β are shown in Figs. 8.3a-d. From Fig. 8.3a, it can be observed that for a less participating medium, the location of an inhomogeneity irrespective of its shape does not affect the

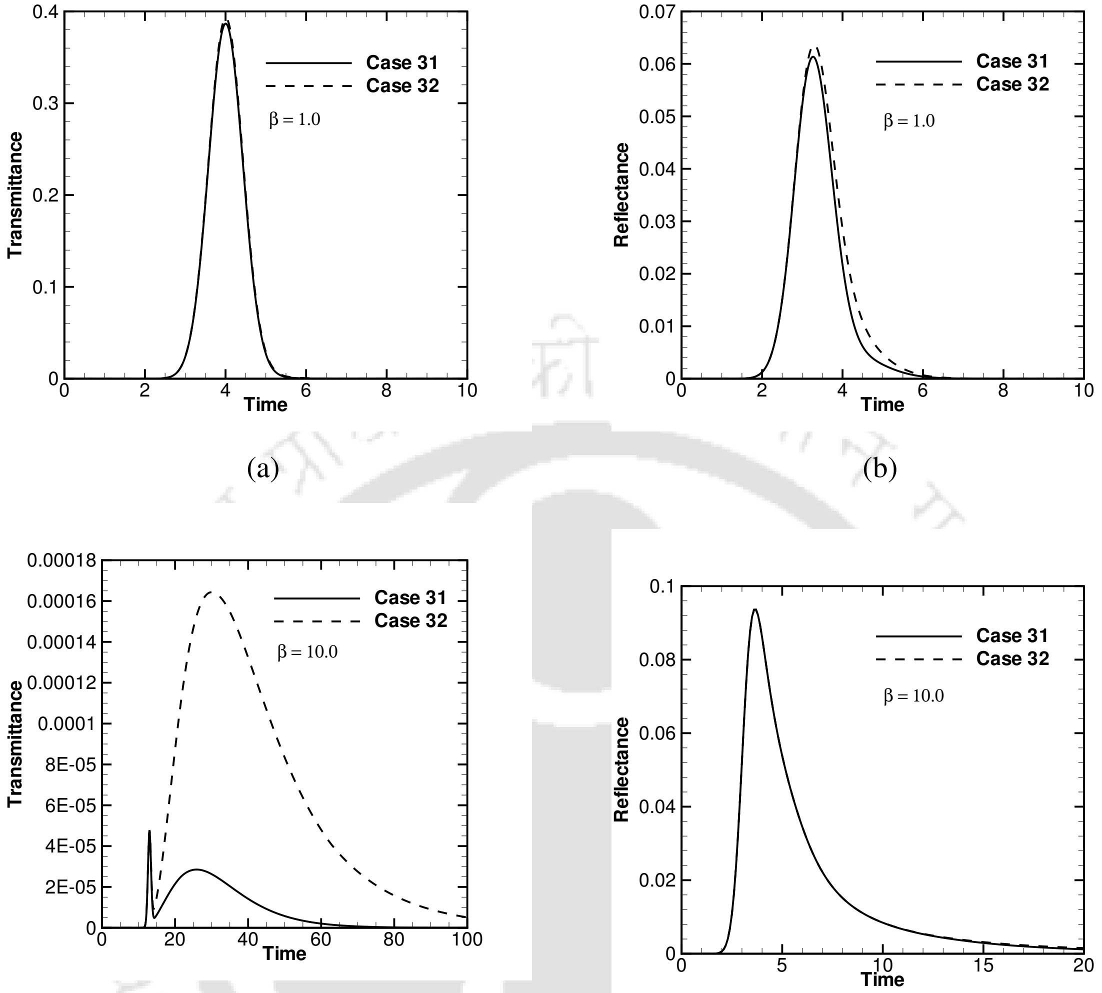

(a) (b)

(c) (d)

Figure 8.4: Transmittance and Reflectance results for Cases 31,32 for two different values of extinction coefficient.

transmittance $q_t^*\left(0.5,1.0,t^*\right)$ signal. With $\beta = 1.0$, since the exponential decay of the collimated component of intensity is minimal, a large fraction of the transmittance $q_t^*\left(0.5,1.0,t^*\right)$ signal at the center of the other boundary is due to the collimated component. But the presence of an inhomogeneity at the centre of the medium causes a great attenuation of energy at the other boundary for Case 21. Whereas in Case 22 (Fig. 7.1a), since the weakly scattering inhomogeniety is offset from the center (Figs. 7.1d), the center of the north boundary receives a good more

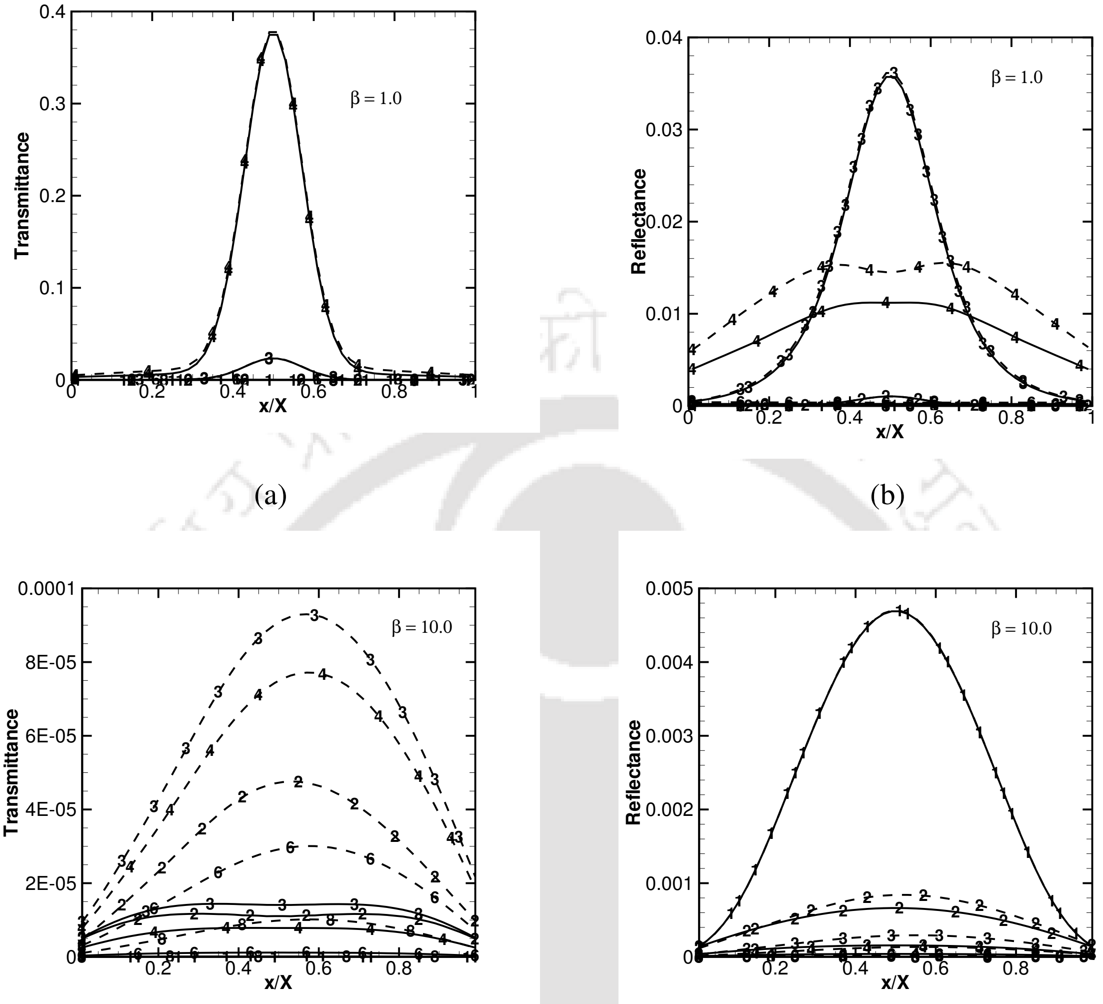

(a) (b)

(c) (d)

Figure 8.5: Spatial distribution of transmittance and reflectance results for Cases 11, 12 for two different values of extinction coefficient.

amount energy than that of the Cases 21. From Figs. 8.3b and 8.3d, it can be observed that the reflectance $q_r^*\left(0.5, 0.0, t^*\right)$ signal in the mid-north boundary is not affected by the inhomogeneities in the medium.

Figs. 8.4a-d have trends almost similar to that of Figs. 8.3a-d. Thus, it can be inferred that a step spatial profile of radius 0.3 is physically equivalent to a Gaussian beam of radius 0.3333 as far as the energy at the central portion of the other boundary is concerned.Solid and dashed lines are results for Cases 11 and 12, respectively. The digit n on any curve indicates the distribution of the signal at $n \times 100^{\text{th}}$ time step.

It is seen from Figs. 8.5a, that for Case 11, the spatial distributions of transmittance $q_t^*\left(\frac{x}{X},1.0,t^*\right)$ and reflectance $q_r^*\left(\frac{x}{X},0.0,t^*\right)$ signals at all time levels are symmetric about the mid-plane $\left(\frac{X}{2},y\right)$. It can also be observed that the distribution of signals resembles the incident Gaussian beam of radius 0.1667. Due to the low value of the extinction coefficient $(\beta=1.0)$, the presence of the inhomogeneity is not observed in the spatial trends. In Fig. 8.5b, the presence of the central circular inhomogeneity can be observed in the reflectance $q_r^*\left(\frac{x}{X},0.0,t^*\right)$ signals at the 400th time step. The energy at the boundary-sides being very less due to the Gaussian spatial profile, the presence of the circular inhomogeneity is visible as a crest of low slope.

For a highly participating medium $(\beta=10.0)$, in Fig. 8.5c, the presence of a central inhomogeneity is evident in the form of a small trough in the trend at the 300th time step. A mild skew towards the east boundary is observed at almost all time levels for Case 12, due to the presence of a weakly scattering inhomogeneity adjacent to the west boundary of the medium. The reflectance $q_r^*\left(\frac{x}{X},0.0,t^*\right)$ signals are observed to be symmetric about the vertical mid-plane for both the Cases 11 and 12. However, as shown in Fig. 8.5b, the variation in spatial distribution of reflectance $q_r^*\left(\frac{x}{X},0.0,t^*\right)$ at the initial stages is much higher than in the later stages for both the cases and for both $\beta=1.0$ and 10.0.

In Figs. 8.6a-d, for Cases 21 and 22, distributions of transmittance $q_t^*\left(\frac{x}{X},1.0,t^*\right)$ and reflectance $q_r^*\left(\frac{x}{X},0.0,t^*\right)$ results along the boundaries have been plotted for two

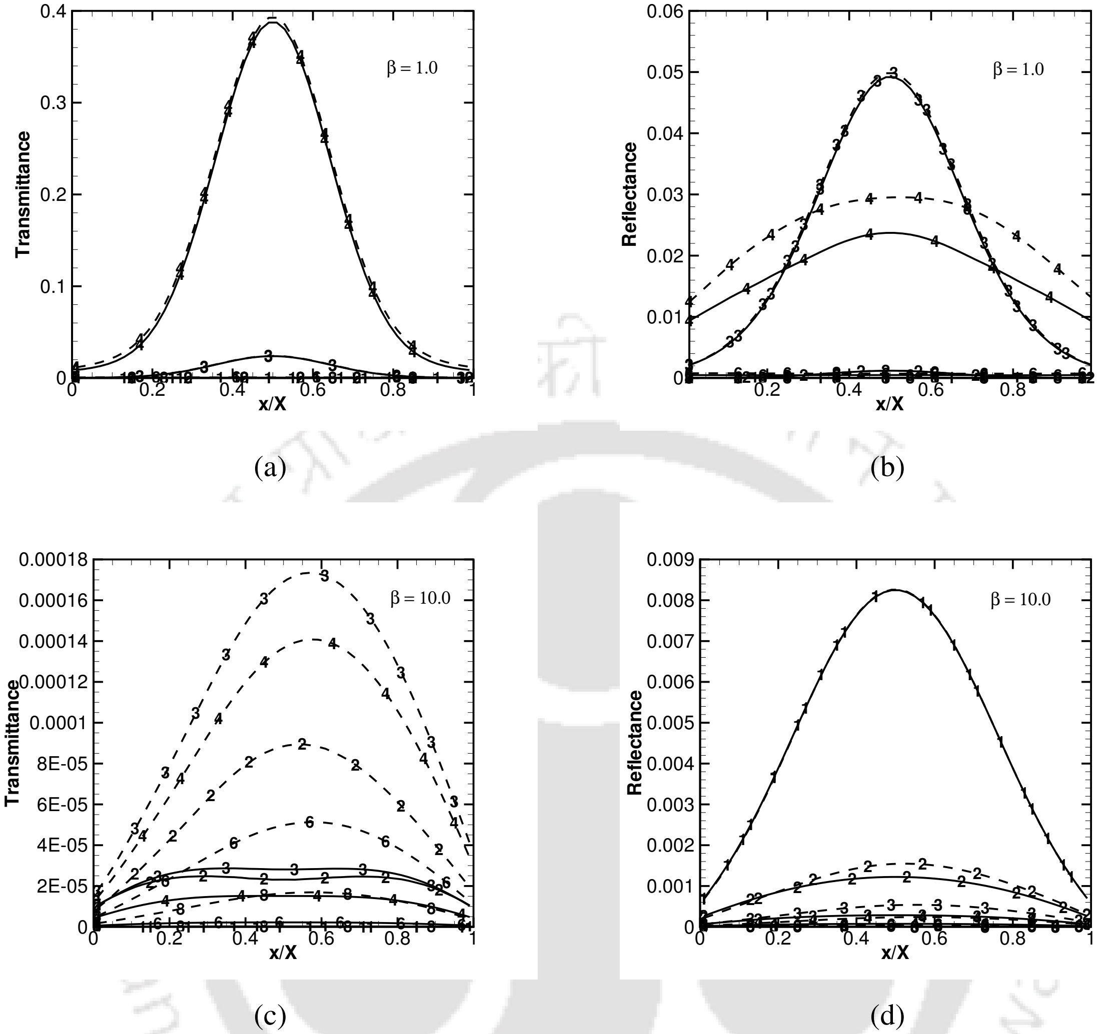

(a) (b)

(c) (d)

Figure 8.6: Spatial distribution of transmittance and reflectance results for Cases 21,22 for two different values of extinction coefficient

different values of the extinction coefficient $\beta = 1.0$ and 10.0. Similar to Figs. 8.5a-d, for a given β, these distributions are plotted at 6 time levels, viz. $\frac{t^*}{\Delta t^*} = 100, 200, 300, 400, 600$ and 800. . Solid and dashed lines are results for Cases 21 and 22, respectively. The digit n on any curve indicates the distribution of the signal at $n \times 100^{\text{th}}$ time step

It is seen from Figs. 8.6a, that for Case 21, the spatial distributions of transmittance $q_t^*\left(\frac{x}{X},1.0,t^*\right)$ and reflectance $q_r^*\left(\frac{x}{X},0.0,t^*\right)$ signals at all time levels are symmetric about the mid-plane $\left(\frac{X}{2},y\right)$. It can also be observed that the distribution of signal resembles the incident Gaussian beam of radius 0.333. Because of the less extinction coefficient, $(\beta=1.0)$ the presence of the inhomogeneity is not observed in the spatial distributions. The energy at the boundary-sides being very less due to the Gaussian spatial profile, the presence of the circular inhomogeneity is visible as a crest of less slope in Fig.8.6b.

For a highly participating medium $(\beta=10.0)$, in Fig. 8.6c, the presence of a central inhomogeneity is evident in the form of a small trough in the trend at the 200th and 300th time steps. A gentle skew towards the east boundary is observed at almost all time levels for Case 22, due to the presence of a weakly scattering inhomogeneity in the top-right corner of the medium. The reflectance $q_r^*\left(\frac{x}{X},0.0,t^*\right)$ signals are observed to be symmetric about the vertical mid-plane for both the Cases 21 and 22. But, as shown in Fig. 8.6b and 8.7d, the variation in spatial distribution of reflectance $q_r^*\left(\frac{x}{X},0.0,t^*\right)$ at the initial stages is much higher than in the later stages in both the cases and for both $\beta=1.0$ and 10.0.

In Figs. 8.7a-d, for Cases 31 and 32, distributions of transmittance $q_t^*\left(\frac{x}{X},1.0,t^*\right)$ and reflectance $q_r^*\left(\frac{x}{X},0.0,t^*\right)$ results along the boundaries have been plotted for two different values of the extinction coefficient $\beta=1.0$ and 10.0. For a given β, these distributions are plotted at 6 time levels, viz. $\frac{t^*}{\Delta t^*}=100, 200, 300, 400, 600$ and 800. Solid and dashed lines are results for Cases 31 and 32, respectively. The digit n on any curve indicates the distribution of the signal at $n\times100^{\text{th}}$ time step.

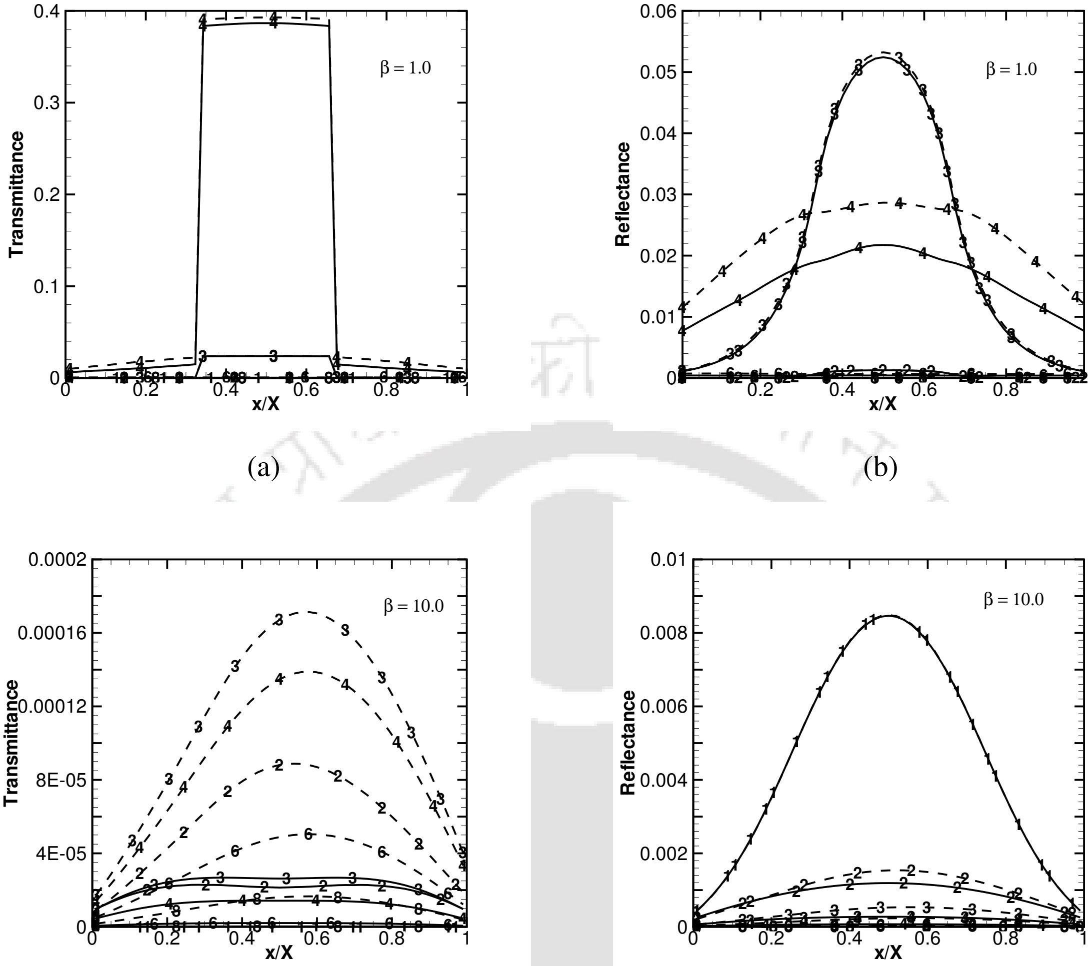

(a) (b)

(c) (d)

Figure 8.7: Spatial distribution of transmittance and reflectance results for Cases 31,32 for two different values of extinction coefficient.

It is seen from Figs. 8.7a, that for Case 31, the spatial distributions of transmittance $q_t^*\left(\frac{x}{X},1.0,t^*\right)$ and reflectance $q_r^*\left(\frac{x}{X},0.0,t^*\right)$ signals at all time levels are symmetric about the mid-plane $\left(\frac{X}{2},y\right)$. It is also observed that the distribution of signal resemble the incident step beam of radius 0.333. Because of the less extinction coefficient, $(\beta = 1.0)$ the presence of the inhomogeneity is not seen in the spatial distributions. The energy at the vicinities of the boundaries being zero due to the step spatial profile, the presence of the circular inhomogeneity is visible as a crest of less slope in Fig.8.7b.

For a highly participating medium $(\beta = 10.0)$, in Fig. 8.7c, the presence of a central inhomogeneity is apparent in the form of a flat portion and a small trough in the trend at the 200th and 300th time steps, respectively. A mild skew towards the east boundary is observed at almost all time levels for Case 32, due to the presence of a weakly scattering vertical elliptical inhomogeneity adjacent to the west boundary of the medium. The reflectance $q_r^*\left(\frac{x}{X}, 0.0, t^*\right)$ signals are observed to be symmetric about the vertical mid-plane for both the Cases 31 and 32.

Figures 8.8 and 8.9 provide heat flux $q^*\left(\frac{x}{X}, \frac{y}{Y}, t^*\right)$ contours in the medium for Cases 11 and 22, respectively. In each of these figures, the contours have been plotted at six time levels, viz. $\frac{t^*}{\Delta t^*} = 20, 40, 80, 200, 400$ and 800 for $\beta = 10.0$.

For a Gaussian beam of radius 0.1667 and centrally located circular inhomogeneity (Case 11), Figs.8.8a-f show heat flux contours at the aforementioned time-levels. From Figs. 8.8a and 8.8b, it is observed, at $\frac{t^*}{\Delta t^*} = 20$ and 40, negative heat flux which contributes towards the reflectance $q_r^*\left(\frac{x}{X}, 0.0, t^*\right)$ signal emerges at the south boundary. At $\frac{t^*}{\Delta t^*} = 200$, it is observed from Fig. 8.8c that a negative heat flux contributing towards reflectance is fully formed. In Fig. 8.8d, a heat flux front moving through the medium with a convergence in direction toward the centre of the medium is observed. In Fig.8.8e, a central core of heat flux concentration symmetric about the geometric centre of the inhomogeneity is observed at $\frac{t^*}{\Delta t^*} = 400$. As the time advances, it is observed from Figs. 8.8d-f, magnitude of heat flux diminishes and its distribution is homogeneous. At $\frac{t^*}{\Delta t^*} = 800$, the signal is almost dead.

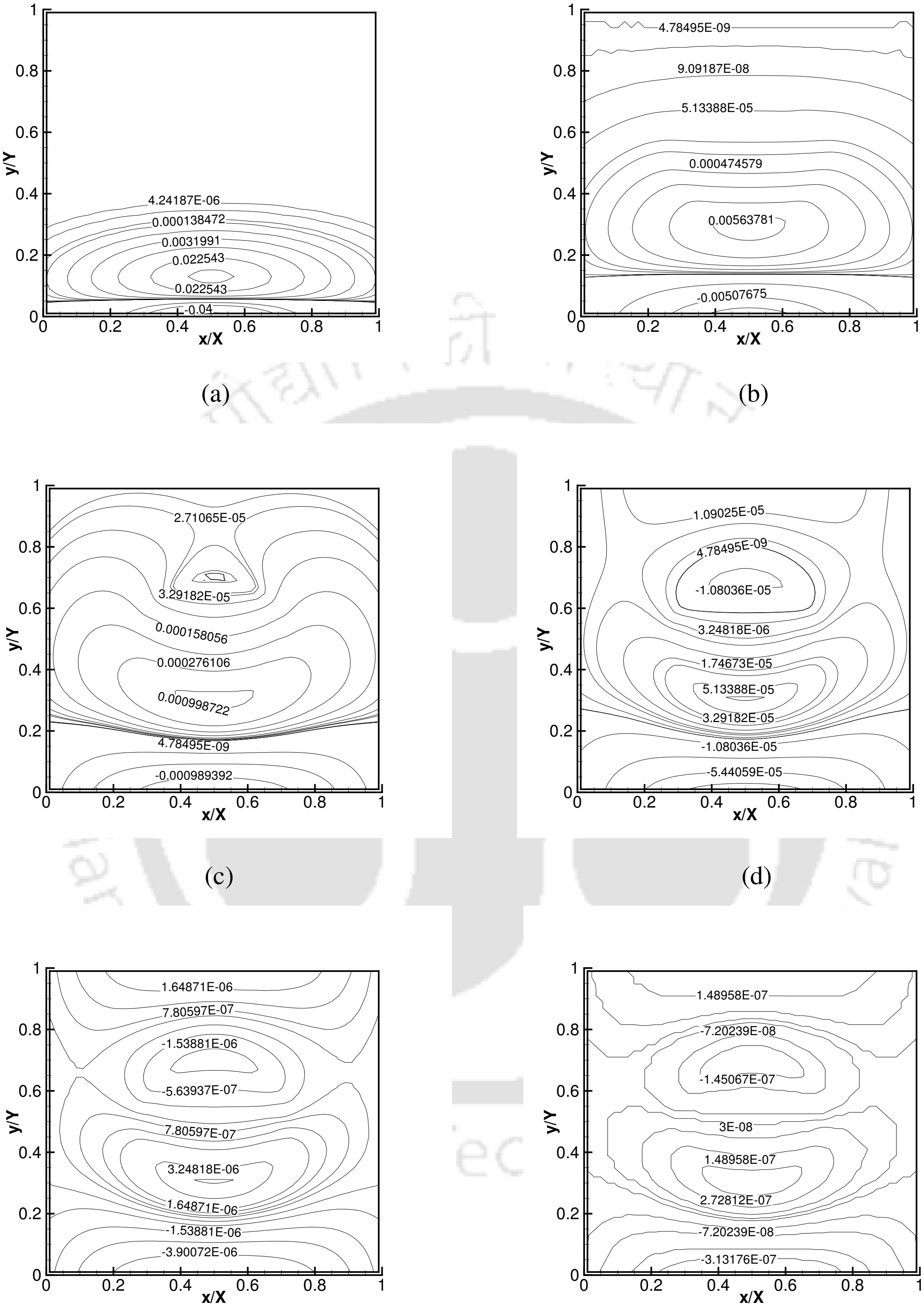

(a) (b)

(c) (d)

(e) (f)

Figure 8.8: Heat flux contours for Case 11 at time levels $\frac{t^*}{\Delta t^*}$ (a) = 20 (b) = 40 (c) = 80 (d) = 200 (e) = 400 (f) = 800.

For a Gaussian beam of radius 0.3333 and an elliptical inhomogeneity symmetric about the horizontal mid-plane and located adjacent to the west boundary corner (Case 22), Figs.8.9a-f show heat flux contours at the six time-levels. With $\beta = 10.0$, at $\frac{t^*}{\Delta t^*} = 20$ (Fig. 8.9a), radiation has traveled only a little distance through the medium. In Fig. 8.9b, at $\frac{t^*}{\Delta t^*} = 40$, though the radiation has just reached the inhomogeneity, no observable effects on the contours is observed. At $\frac{t^*}{\Delta t^*} = 80$, the radiative flux front has met the inhomogeneity, the heat flux contours are seen to be affected by repeated scattering inside the inhomogeneity.

In Figs. 8.9d and 8.9e, the response of the inhomogeneity to the propagation of laser energy through it can be observed. A heat flux nucleus in the neighborhood of the west boundary in the shape of the inhomogeneity can be noticed. Other than the heat flux concentration due to the radiation front-inhomogeneity interaction, a positive heat flux core near the north boundary can be observed in Fig. 8.9d, and it is due to the heat energy transport from the south boundary to the north boundary through the containing medium. Since the inhomogeneity is isotropically scattering, contours are observed to be symmetric about the minor axis of the ellipse. With the progress of time, in Fig. 8.9f, at $\frac{t^*}{\Delta t^*} = 800$, the contours tend to a very low magnitude due to the extinction of the signal.

The program was executed on a Xeon 300 dual processor 800 MHz computer. To study the computational effort, the CPU times were recorded for all the runs. The CPU times for optically thin $(\beta = 1.0)$ to thick $(\beta = 10.0)$ situations ranged from 58 seconds to 350 seconds, respectively.

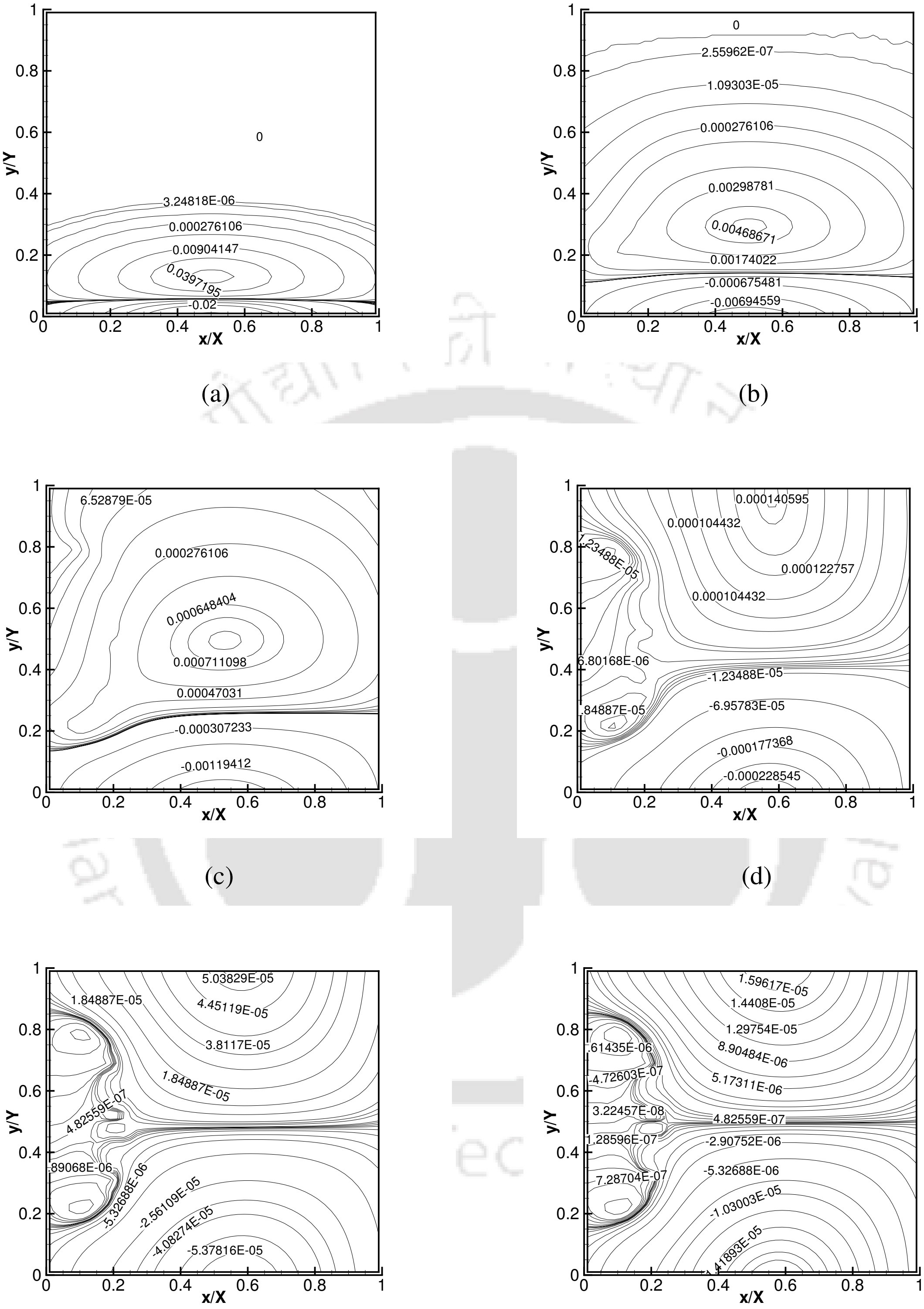

(a)

(b)

(c)

(d)

(e)

(f)

Figure 8.9: Heat flux contours for Case 22 at time levels $\frac{t^*}{\Delta t^*}$ (a) = 20 (b) = 40 (c) = 80 (d) = 200 (e) = 400 (f) = 800.

8.5 Summary

Transport of a short-pulse laser of Gaussian temporal profile of different spatial profiles through a 2-D rectangular participating medium containing circular or elliptical inhomogeneities was studied. The analysis was done considering the south boundary of the medium subjected to a short-pulse laser. The spatial profiles were either Gaussian or step function of the distance along the boundary of incidence. The transmittance and reflectance signals were studied for the effects of the extinction coefficient and location of inhomogeneities. Heat flux distributions inside the medium were also studied. The spatial distribution of the transmittance and reflectance signals at various time levels were found to have a heavy dependence on the spatial profiles of the incident radiation for highly-participating media and a less dependence for less-participating media. A concentration of heat flux in and around the inhomogeneity symmetrical about its geometric center was observed in all the cases. The presence of a weak-scattering inhomogeneity was found to have only a little effect on the spatial distribution of signals in all the cases.

CHAPTER 9

Conclusions and Scope for Future work

9.1 Conclusions

This dissertation dealt with the analysis of transport of a single and/or multiple pulses of radiation through 1-D and 2-D, homogeneous and inhomogeneous participating media. Due to a wide range of optical properties of the participating media considered, this work caters to the radiative solutions of variety problems in science and engineering. Considering the representation of real-time problems, in case of the 2-D medium, localized inhomogeneities of square, circular and elliptical shapes placed at different locations in the medium were studied. Studies were made with both diffuse and collimated (laser) short-pulse radiation of either step or Gaussian temporal profile in all the cases. For a step-pulse, the half period of the multiple pulses was the same as the pulse-width, while it was three times that of the pulse-width in the case of a Gaussian pulse. Since in many engineering applications, the dimension of the incident laser is much lesser compared with the dimensions of the medium, the impact of the various dimensions of the laser are studied. Thus the loading on the boundary was either spatially uniform or Gaussian or a step function of distance. In all the cases, analyses were done using the FVM.

In all cases, the media were considered cold and absorbing-scattering. At the time-scale of the travel of light, radiation is the only mode of heat transfer that can be thought of. So the effects of conduction and convection were not considered. The time dimension was normalized by the optical thickness of the participating medium as $t^* = \beta ct = \beta s$. Thus in a medium of constant extinction coefficient β, the non-dimensional time t^* spent to travel a geometric distance of z and an optical thickness of $\tau = \beta z$ is the optical thickness itself. All media were considered to be of unit refractive index. The boundaries of all problems considered were cold and diffuse-gray.

The fundamentals of radiative transfer in comparison with the other modes of heat transfer were presented in Chapter 1. It emphasized the need to study in detail, the energy transfer of short-pulse radiation through participating media and the practical significance of such studies. It discussed the availability of literature in this area and the founding of the thesis work. In Chapter 2, a FVM formulation to solve the TRTE for the incidence of a single step-profile short-pulse laser on a 3-D Cartesian enclosure was presented.

Chapter 3 presented an analysis of the transport of diffuse and/or collimated, step and/or Gaussian temporal profile, single and/or multiple, short-pulse radiation through a 1-D planar participating medium. A 1-D formulation necessary to solve multi-pulse (pulse train/wave) short-pulse incidence with all the above variations was presented. The basic results were compared with the results available in the literature and text in order to validate the advanced problems. The fact that the value of transmittance tends to the steady state value, due to the incidence of a pulse of very large pulse width was discussed. This occurs in both the cases of diffuse ($t_p^* = 25.0$) and collimated short-pulse incidence. The time variation in the incident pulse was found to be manifesting in the heat flux at the boundaries viz., transmittance and reflectance but with a widening effect depending on the extinction coefficient and scattering albedo. A train of pulses was found to provide useful information about the nature of the signals and its temporal spans.

Chapter 4 dealt with the case of a 1-D inhomogeneous planar participating medium consisting of 2-3 layers having different optical properties subjected to a collimated pulse train of 1-4 pulses and a step and/or Gaussian temporal profile The total optical thickness of the medium was found to be the most contributing factor for the peak magnitudes of the transmittance signals The scattering albedo of the layer adjacent to the boundary of incidence was the most contributing factor of the peak reflectance. For a given total optical depth of the medium, irrespective of the scattering albedo of the various layers, the magnitudes of the peaks of the transmittance signals were found to be of the same order. The case of a medium with continuous variation of scattering albedo was of hypothetical nature and was studied to contrast with the layered inhomogeneous medium. The time span of transmittance $q_t^*\left(Z,t^*\right)$ signals in case C02 was found to be more than that of C01, due to the fact that the mean scattering coefficient of the former was greater than that of the latter. Following which the case C01 was inferred to be a medium consisting of a large number of layers with increasing scattering albedos from the north to the south boundaries. Though the trends in the two cases were different, the saddle points in the transmittance $q_t^*\left(Z,t^*\right)$ signal were found to occur at the same time for both the cases C01 and C02. In case of C02, the layers of the medium lying in the nearby vicinity of the north boundary were moderately scattering, while, in the case C01, they were very weakly scattering. Since the peak magnitude of the reflectance signals depends primarily upon the properties of the medium adjacent to the boundary of incidence, the reflectance $q_r^*\left(0,t^*\right)$ signals were found to be one order higher in the case C02.

In Chapter 5, the results for the transport of a train of diffuse or a collimated short-pulse train through a 2-D homogeneous participating medium was presented. For a very high aspect-ratio of $\frac{X}{Y}=100$, transmittance at the middle of the north boundary, was found to be the same as that of the 1-D problem. In the case of an incident diffuse radiation an aspect ratio of 10 was found to be enough for the formulation to reach the 1-D results. This reiterates the fact that in a less-participating medium, the collimated component of the traveling radiation is more pronounced irrespective of the geometry. With a low value of the extinction coefficient i.e., $\beta=1.0$ the demarcations due to time variation were found to be distinctly visible for both the collimated and diffuse pulses. Since the medium tends to be more attenuating with the increase in extinction coefficient, the spatial distribution of transmittance becomes highly dependent on the extinction coefficient. In the case of reflectance, a contrary effect was observed.

Chapter 6 dealt with the transport of a pulse train of a step or a Gaussian profile through a square participating medium consisting of a square local inhomogeneity differing from the main medium by its scattering albedo. The comparison with the results from literature was found to be excellent. From the results, it can be inferred that an inhomogeneity near a particular boundary produces more effect on the spatial distribution of a temporal signal at that boundary. A centrally located inhomogeneity distributed the temporal signals symmetrically about the mid-plane. When the medium was less attenuating $(\beta = 1.0)$, the presence of the inhomogeneity had almost no effect on the transmittance $q_t^*\left(0.5, 1.0, t^*\right)$ (Fig 6.3a) and reflectance $q_r^*\left(0.5, 0.0, t^*\right)$ signals at the middle of the boundaries. But when the medium became more and more attenuating $(\beta = 5.0, 10.0)$, the location of the inhomogeneity was found to have more effect on the transmittance $q_t^*\left(0.5, 1.0, t^*\right)$ signals. For Case 3, due to the presence of a weak-scattering inhomogeneity near the east boundary, the curve corresponding to Case 3 (Fig. 6.1c) in Fig. 6.5b was found to be skewed heavily towards the west boundary. When an inhomogeneity was located in the south-east corner, heat flux contours were observed to be skewed in the region containing the inhomogeneity.

The effects of circular and elliptical shape inhomogeneities in a 2-D square medium were studied in Chapter 7. Three different possible positions of a localized inhomogeneity were considered. Inhomogeneities differed from the main medium by their scattering properties as in the case of Chapter 6. Study was made with collimated radiation. Both step and Gaussian profiles were considered. In comparison to the square-shaped inhomogeneity considered in Chapter 6, in this case, due to the curvature in the shape of the inhomogeneity, abrupt spatial distributions in the signals were observed to be absent.

For the problem considered in Chapter 8, the south boundary of a 2-D medium was subjected to a Gaussian loading and the temporal profile of the pulse radiation was also considered to be a Gaussian. Study was made for both homogenous and inhomogeneous media. The spatial profiles of the loading of the short-pulse laser were found to have a great influence on the spatial distribution of the transmittance and reflectance signals at various time levels in the case of highly-participating media. A concentration of heat flux in and around the inhomogeneity symmetrical about its geometric center was observed in all the cases. The presence of a weak-scattering inhomogeneity was found to have only a little effect on the spatial distribution of signals in all the cases.

The results presented in this thesis will serve as benchmark results for studies of many practical problems. The oceanographic lidar basically being an instrument that detects reflected signals from a vertical stratum of atmosphere, the results presented in Chapter 4 can be used considering the atmosphere to be a 1-D planar participating medium. The evolution of heat flux fronts in a 2D Cartesian enclosure containing inhomogeneities is a good model for the laser surgery of tissues. Various types of cases considered in Chapters 5-8 provide a wealth of information regarding effects of medium composition and behavior on transmittance and reflectance signals. These results will be useful in medium characterization as well as biomedical applications.

9.2 Scope for Future work

All the above problems discussed in this thesis dealt with an exhaustive combination of a variety of 1-D/2-D optically participating media of homogeneous/inhomogeneous nature subjected to single/ multiple short-pulse collimated/diffuse radiation of step/Gaussian temporal profile. The inhomogeneities considered were of different shapes at different locations. The spatially varying loadings of radiation were also considered.

The work presented in the thesis is a valuable addition to the know-how about the resulting signals due to the transport of a short-pulse radiation through a participating medium. Many new observations were found which will help in further advancement to this field of research. Some of the problems that can be taken as future work are the following:

- A 3-D Cartesian enclosure subjected to laser waves of high power and very short duration is a common application in industrial machining. Quantitative information pertaining to the above application has not yet been included in the literature. Simulation studies of laser transport through such a 3-D participating medium will be of immense help in dealing with real-time problems.

- The pulse-width and period of laser considered in many of these problems is a non-dimensional time t_p^* of magnitude unity. The effects of still lesser non-dimensional time t_p^* pulse widths in the range $\left[O\left(10^{-3}\right),O\left(10^{-6}\right)\right]$ is necessary to move closer to real-time problems which involve pico-, femto-second time scales.

- Analysis software packages used widely for commercial CFD applications like FLUENT lack a module for dealing with the TRTE, though the significance of solving the same has been felt in the industry and academy for long. The FVM procedure used for solving all the problems in this thesis can be optimized for computational efficiency using spatial resolution techniques and can be implemented in commercial software packages.

- Considering the improbability of the other modes of heat transfer viz. conduction and convection, the problems were focused on calculating the transients in the radiative heat flux inside the domains and at the boundaries. In case of an incidence of a radiation for a very large duration, say for a few seconds, the medium gets heated and radiation will not be the singular mode of heat transfer. The effect of non-Fourier conduction and the heat wave propagation through the material has to be studied in this situation. Then, convection also is a possibility in case of fluids. Since this has many practical applications of utmost importance, the work can be taken ahead in that direction.

- The pulse radiation problems in this thesis dealt with rectangular Cartesian coordinates. All of these situations can be applied to cylindrical and spherical coordinate systems as well. In such cases, though the formulation and computation will get complicated, the endeavor will enrich the literature and provide immense information for the industries which see these situations often. For example in laser corneal surgery, the precision of the instruments and the expertise and experience of the surgeons have been the only guidelines in performing the procedure. The actual data of the energy flux and the duration of energy stay in the eyeball are still to be simulated to benchmark the situation. A simulation study on the laser incidence on spherical systems might prove helpful in such a case.

- Stochastic methods like the MCM and the reverse MCM and unconventional methods like the REM which are computationally highly-demanding were adapted before to solve laser transport through an inhomogeneous system. In the present work, for the first time, a whole spectrum of pulse radiation problems was solved by the FVM. The implementation of the FVM to more intricate and complex problems for pulse radiation applications can be explored.

- A correlative study relating the radiation pulse parameters and the material properties can be done. The resulting empirical general solution can be followed as a thumb rule in specific applications.

- In the present work, all media were considered to be of unit refractive index and their boundaries were assumed to be black and diffuse. The work can be extended to spectrally reflective and emitting boundaries, media of refractive indices non-unity and graded media. The normalization of the time dimension will have to be done in a different manner in the case of graded media.

References

---

1. M. F. Modest, *Radiative Heat Transfer*. 2nd Edition, Academic Press, New York, 2003.
2. R Siegel and JR Howell, *Thermal Radiative Heat Transfer*. Hemisphere, Washington DC, 1992
3. J.P. Longlin and C.L. Tien, *Micro scale radiation phenomena.* In: Tien CL, Majumdar A, Gerner FM, editors, Micro scale energy transfer, Taylor and Francis, Washington D.C., 119-147, 1997.
4. V. Tuchin, *Tissue Optics*. SPIE Press, Bellingham, WA,2000.
5. John F Ready, *Industrial Applications of Lasers*, New York City: Academic Press, 1997.
6. *LIA Handbook of Laser Materials Processing*, ed. John F Ready (Orlando, FL: Laser Institute of America, Magnolia Publishing, 2001.
7. N. Rykalin, A. Uglov and A. Kokora, *Laser Machining and Welding*. - Pergamon Press, Inc., 1979.
8. G. Chryssolouris, *Laser Machining: Theory and Practice*. Springer Verlag, New York, NY, 1st ed., 1991.
9. Chandrasekhar S, *Radiative transfer*, Oxford: Oxford University Press, 1950.
10. S.Kumar and K. Mitra, Microscale aspects of thermal radiation transport and laser applications, *Advances in Heat Transfer* 33,187-295,1999.

11. Y. Yamada, *Light-tissue interaction and optical imaging in biomedicine*, Annual Review of Heat Transfer 6, 1-59, 1995.

12. K. Mitra and J. H. Churnside, Transient radiative heat transfer equation applied to oceanographic lidar, *Applied Optics*, 38, 889-895,1999.

13. S.C. Chen, C.P. Grigoropoulos, H.K. Park, P. Kersterns and A.C. Tam, Photothermal displacement measurement of transient melting and surface deformation during pulsed laser heating, *Applied Physics Letters*, 73, No.15,2093-2095, 1998.

14. M.Sadoqi, P.Riseboro, and S.Kumar, *Analytical models for pulsed laser flourescence imaging in tissues*, Physics in Medicine and Biology, 46, 2725-2743, 2001.

15. H.Y. Quan and Z.X. Guo, Fast 3-D optical imaging with transient fluorescence signals, *Optics Express* 12, 449-457, 2004.

16. G. Pal, S. Basu, K. Mitra and S. Kumar, Bioheat transfer in layered skin model subjected to short pulse laser irradiation, *Lasers in Surgery and Medicine*, 13, 12-37, Suppl. 17 , Mar 2005.

17. J.Kim and Z.X.Guo, Ultrafast radiation in heat transfer in tissue welding and soldering, *Numerial Heat Transfer. Part A- Applications* 46, 23-40, 2005.

18. M.Sadoqi, S.Kumar, and Y.Yamada, Photochemical and photothermal model for pulsed laser ablation, *Journal of Thermophysics Heat Transfer*, 16, No.2, 193-199, 2002.

19. L. S. Bass and M.R. Treat, Laser tissue welding: A comprehensive review of current and future applications, *Lasers in Surgery and Medicine*, 17, 315–349, 1995.

20. F.H. Loesel, F.P. Fisher, H. Suhan and J.F. Bille, Non-thermal ablation of neutral tissue with femtosecond laser pulses, *Applied. Physics. B*, 66, 121-128, 1998.

21. M. Sakami, K. Mitra and T. Vo-Dinh, Analysis of short-pulse laser photon transport through tissues for optical tomography, *Optics Letters*, 27, 336-338, 2002.

22. S.K. Wan and Z. Guo, Correlative studies in optical reflectance measurements of cerebral blood oxygenation, Journal of Quantitative Spectroscopy and Radiative Transfer, 98, 189-201, 2006.

23. V.V. Kancharla and S.C. Chen, Fabrication of biodegradable polymeric micro-devices using laser micromachining, *Biomedical Microdevices*, 4, 105-109, 2002.

24. B.J. Garrison, and R. Srinivasan, Laser ablation of organic polymers: microscopic models for photochemical and thermal processes, *Journal of Applied Physics*, 57, No.8, 2909-2914,1985.

25. S. George and K. Mitra, Analysis of ablation characteristics of absorbing dielectrics caused by short laser pulses, *Journal of Thermophysics and Heat Transfer* 15, 190-196, 2001.

26. R.L. Fork, J.Y. Brito, C.H. Cruz, P.C. Becker and C.V. Shank, Compression of optical pulses to six femtoseconds by using cubic phase compression, *Optics Letters*, 12, 483-485, 1982.

27. M.Q. Brewster and Y. Yamada, Optical properties of thick, turbid media from picosecond time-resolved light scattering measurements, *International Journal of Heat Mass Transfer* 38, 2569-2581, 1995.

28. R.Elaloufi, R.Carminati and J.J.Greffet, Diffusive- to-ballistic transition in dynamic light transmission through thin scattering slabs: a radiative transfer

approach, *Journal of the Optical Soceity of America., A-Optics Image Science and Vision* 21, 1430-1437, 2004.

29. R.Elaloufi, R.Carminati and J.J.Greffet, Time-dependent transport through scattering media: from radiative transfer to diffusion, *Journal of Optics A-Pure and Optics* 4, 103-108, 2002.

30. S. Kumar, K. Mitra and Y. Yamada. Hyperbolic damped-wave models for transient light-pulse propagation in scattering media, *Applied Optics*, 35,188-196, 1999.

31. K.Mitra and S.Kumar, Development and comparison of models for light-pulse transport in scattering absorbing media, *Applied Optics.*35, 3372-3378, 1996.

32. D.W. Balsara, An analysis of the hyperbolic nature of the equations of radiation hydrodynamics. *Journal of Quantitative Spectroscopy and Radiative Transfer* 6,135-153, 119832.

33. J.R. Singer, F.A. Grunbaum, P.Kohn and J.P. Zubelli, Image reconstruction of the interior of bodies that diffuse radiation, *Science* 248, 990-993,1990

34. B.Chance and A. Katzir, Time-resolved spectroscopy and imaging of tissue. *Proceedings of SPIE* 1431, 1-332, 1991.

35. F.Liu, K.M.Yoo and R.R. Alfano, Ultrafast laser pulse transmission and imaging through biological tissue, *Applied Optics,* 32, 554-558, 1993.

36. S.Proskurin, Y.Yamada and Y.Takahashi, Absorption coefficient measurements of strongly scattering media using time-resolved transmittance of a short-pulse in a near-infrared wavelength range, *Optics Review 2*, pp 292-297, 1995.

37. O.Minet, G.Muller and J.Beuthan, *Selected Papers on Optical Tomography, Fundamentals and Applications*, SPIE Press, Bellingham, WA,1998.

38. A.Gandjbakche, V.Chernomordik, J.C.Hebden and R.Nossal, Time-dependent contrast functions for quantitative imaging in time-resolved transillumination experiments, *Applied Optics,* 37, 1973-1981,1998

39. J.C.Hebden, S.R. Arridge and D.T. Delpy, Optical imaging in medicine: I. Experimentation techniques, *Physics in Medical Biology* 42, 825-840, 1997

40. S.K. Gayen and R.R. Alfano, Sensing lesions in tissues with light. *Optics Express* 4, 475-480, 1999.

41. H.Jiang, K.D. Paulsen, U.L. Osterberg, B.W. Pogue and M.S. Patterson, Simultaneous reconstruction of optical absorption and scattering maps in turbid media from near-infrare frequency-domain data, *Optics letters*, 20, 2128-2130.

42. E.Gratton, W.M. Mantulin, M.J. vande Ven, J.B. Fishkin, M.B. Marris and B.Chance, A novel approach to laser principles, *Bioimaging* 1, 40-46, 1993.

43. K.W. Berndt and J.R. Lakowicz, Detection and localization of absorbers in scattering media using frequency domain principles, *Proceedings of SPIE* 1431, 149-160, 1991.

44. M.A.O'Leary, D.A. Boas, B.Chance and A.G. Yodh, Experimental images of heterogeneous turbid media by frequency domain diffusing photon tomography, *Optics Letters*.20, 426-428, 1995.

45. Y.Yamada, Light-tissue interaction and optical imaging in biomedicine, *Annual Review of Fluid Mechanics and Heat Transfer,* 6, 1-59, 1995.

46. R.Berg, S.Andersson-Engels, O.Jarlman and S.Svanberg, Time-gated viewing studies on tissue-like phantoms, *Applied Optics* 35, 3432-3440, 1996.

47. M.S. Patterson, B.Chance and B.C.Wilson, Time-resolved reflectance and transmittance for the non-invasive measurement of tissue optical properties, *Applied Optics*, 28, 2331-2336, 1989.

48. A.H. Heelscher, S.L. Jacques, L.Wang and F.K. Tittel, Influence of boundary conditions on the accuracy of diffusion theory in time-resolved reflectance spectroscopy of biological tissues, *Physics in Medicine and Biology* l, 40, 1957-1975, 1995.

49. B.Chen, K.Stamnes and J.J. Stamnes, Validity of the diffusion approximation in bio-optical imaging, *Applied Optics*, 40, 6356-6366, 2001.

50. A.Ishimaru, Diffusion of light in turbid media, *Applied Optics* 28, 2210-2215, 1989.

51. S.L.Jacques, Time-resolved propagation of ultrashort laser pulses within turbid tissues, *Applied Optics* 28, 2223-2229.

52. A.Yodh and B.Chance, Spectroscopy and imaging with diffuse light, *Physics Today* 48, 34-40, 1995.

53. R.D. Skocypec and R.O. Buckius, Photon path length distributions for an isotropically scattering planar medium, *Journal of Quantitative Spectroscopy and Radiative Transfer* 28, 425-439, 1982.

54. A.Vedavarz, S.Kumar and M.K. Moallemi, Significance of non-Fourier heat waves, *Journal of Heat Transfer* 116, 221-224, 1993.

55. M. Rioux, R. Tremblay, and P.A. Belanger, Linear, annular, and radial focusing with axicons and applications to laser machining (ET). *Applied Optics* 17, 1532- 1536, 1978.

56. F. W. Dabby and U.-C. Paek, High-intensity laser-induced vaporization and explosion of solid material, *I.E.E.E. Journal of Quantum Electronics.*, QE-8, 106, 111-117, 1972.

57. R.E. Wagner, Laser Drilling Mechanics, *Journal of Applied Physics*, 45, 4631-4637, 1974.

58. 3. D. Schu¨ocker and W. Abel, Material removal mechanism of laser cutting, In *Proceedings of the SPIE*, 1983.

59. D. Petring, P. Abels, and E. Beyer, Werkstoffbearbeitung mit Laserstrahlung. *Feinwerktechnik and Messtechnik*, 96, 364-372, 1988.

60. M. F. Modest and H. Abakians, Heat conduction in a moving semi-infinite solid subjected to pulsed laser irradiation, *Journal of Heat Transfer*, 108, 597-601, 1986.

61. M. F. Modest and H. Abakians, Evaporative cutting of a semi-infinite body with a moving CW laser, *Journal of Heat Transfer*, 108, 602-607, 1986.

62. H. Abakians and M. F. Modest, Evaporative cutting of a semi-transparent body with a moving CW laser, *Journal of Heat Transfer*, 110, 924-930, 1988.

63. S. Roy and M. F. Modest, Three-dimensional conduction effects during evaporative scribing with a CW laser, *Journal of. Thermophysics and Heat Transfer*, 4, 199-203, 1990.

64. S. Roy and M. F. Modest, Evaporative cutting with a moving cw laser-part i: effects of three-dimensional conduction and variable properties, *International Journal of Heat and Mass Transfer*, 36, 3515- 3528, 1993.

65. S. Y. Bang and M. F. Modest, Multiple reflection effects on evaporative cutting with a moving CW laser, *Journal of Heat Transfer*, 113, 663-669 1991.

66. S. Y. Bang, S. Roy, and M. F. Modest, CW laser machining of hard ceramics - part II: effects of multiple reflections, *International Journal of Heat and Mass Transfer*, 36, 3529-3540, 1993.

67. S. Y. Bang and M. F. Modest, Evaporative scribing with a moving CW laser - effects of multiple reflections and beam polarization, In *Proceedings of ICALEO '91, Laser Materials Processing*, 74, 288-304, 1992.

68. P Rairoux, H Schillinger and S Niedermeier M, Remote sensing of the atmosphere using ultrashort laser pulses, *Applied Physics B*: *Lasers and Optics*, 573-580, 2000.

69. Killinger and D K Mooradian, *Optical and laser remote sensing*. A Berlin, Springer-Verlag (Springer Series in Optical Sciences. Volume 39), 1983, 394.

70. F. Liu, K.M. Yoo and R.R. Alfano, Ultra-fast laser pulse transmission and imaging through biological tissues, Applied Optics., 32, 554-558, 1993.

71. Y. Yamada. *Light-tissue interaction and optical imaging in bio-medicine*, vol. 6, 1-59, Beggel House, New York, 1995.

72. R.E. Walker and J.W. Mclean, Lidar equation for turbid media with pulse stretching, *Applied Optics*, 38, 2384-2397, 1999.

73. K. Mitra and J.H. Churnside, Transient radiative transfer equation applied to oceanographic lidar, *Applied Optics*, 38, 889-895, 1999.

74. S. Kumar and K. Mitra, Microscale aspects of thermal radiation transport and laser applications, *Advanced Heat Transfer*, 33, 187-294, 1999.

75. L. Jiang and H.L. Tsai, Repeatable nanostructures in dielectrics by femtosecond laser pulse trains. *Applied Physics Letter.,* 87, 2000(doi:10.1063/1.2093935).

76. K.J. Grant, J.A. Piper, D.J. Ramsay and K.L. Williams, Pulse lasers in particle detection and sizing, *Applied Optics*, 33, 416-417, 1993.

77. A.D. Kim, J.N. Kutz and D. J.Muraki, Pulse-train uniformity in optical fiber lasrs passively mode-locked by nonlinear polarization rotation, *IEEE Journal of Quantum Electronics*, 36, 465-471, 2000.

78. C.M. Ngabireng, P.T. Dinda, K. Nakkeeran and P.K.A. Wai, Radiating and non-radiating trains of light pulses in dispersion-managed optical fiber systems, *Optics Communications*, 250, 24-35, 2005.

79. Z. Guo and S. Kumar, Radiation element method for hyperbolic radiative transfer in plane – parallel inhomogeneous media, *Numerical Heat Transfer B*, 39, 371-387, 2001.

80. J.C. Chai, One-dimensional transient radiative heat transfer modeling using a finite volume method, *Numerical Heat Transfer B*, 44, 187-208, 2003.

81. J.C. Chai, P.F. Hsu and Y.C. Lam, Three-dimensional transient radiative transfer modeling using the finite volume method, *Journal of Quantitative Spectroscopy and Radiative Transfer*, 86, 299-313, 2004.

82. K. Mitra, M.S. Lai and S. Kumar, Transient radiation transport in participating media within a rectangular enclosure, *Journal of Thermophysics and Heat Transfer*, 11, 409-414, 1997.

83. A Vedavarz, K Mitra and S Kumar, Hyperbolic temperature profiles for laser surface interactions, *Journal of Applied Physics*, 76, 5014 (1994), (doi:10.1063/1.357213)

84. Z.M. Tan and P.F. Hsu, An integral formulation of transient radiative transfer, *Journal of Heat Transfer*, 123, 466-475, 2001.

85. Z.M. Tan and P.F. Hsu, Transient radiative transfer in three-dimensional homogeneous and non homogeneous participating media, *Journal of Quantitative and Spectroscopy and Radiative Transfer*, 73, 181-194, 2002.

86. C.Y. Wu and S.H. Wu, Integral equation formulation for transient radiative transfer in an anisotropically scattering medium, *International Journal of Heat and Mass Transfer*, 122, 818-822, 2000.

87. R. Muthukumaran and S.C. Mishra, Interaction of a short-pulse laser of a Gaussian temporal profile with an inhomogeneous medium, *Numerical Heat Transfer, Part A,* 53, 625-640, 2008.

88. R. Muthukumaran and S.C. Mishra, Transient response of a planar participating medium subjected to a train of short-pulse radiation, *International Journal of Heat and Mass Transfer* (DOI: 10.1016/j.ijheatmasstransfer.2007.08.035) 2008.

89. R. Muthukumaran and S.C. Mishra, Transport of a train of short-pulse radiation of step temporal profile through a 2-D participating medium, *International Journal of Heat and Mass Transfer*, (doi:10.1016/j.ijheatmasstransfer.2007.08.032) 2008.

90. R. Muthukumaran and S.C. Mishra, Thermal signatures of a localized inhomogeneity in a 2-D participating medium subjected to an ultra-fast step-pulse laser wave, *Journal of Quantitative Spectroscopy and Radiative Transfer*, 109, 705-726, 2008.

91. R. Muthukumaran and S.C. Mishra, Analysis of a short-pulse laser irradiation on a planar inhomogeneous participating medium using the finite volume method, *International Congress on Computational Mechanics and Simulation (ICCMS- 06)*, 8-10 December 2006, IIT Guwahati.

92. R. Muthukumaran and S. C. Mishra, Short-pulse laser wave propagation through a 2-D rectangular participating medium containing an inhomogeneity

of different shapes and at different locations, *19th National & 8th ISHMT-ASME Heat and Mass Transfer Conference*, Hyderabad 3-5 January 2008.

93. R. Muthukumaran and S. C. Mishra, Analysis of the interaction of a diffuse short-pulse wave of radiation with a radiatively-participating homogeneous slab. *19th National & 8th ISHMT-ASME Heat and Mass Transfer Conference*, Hyderabad 3-5 January 2008.

94. R. Muthukumaran and S. C. Mishra, Finite volume method solutions for short-pulse laser incidence in an inhomogeneous planar participating medium. *19th National & 8th ISHMT-ASME Heat and Mass Transfer Conference*, Hyderabad 3-5 January 2008.

95. C.Y. Wu and N.R. Ou, Differential approximation for transient radiative transfer through a participating medium exposed to collimated radiation. *Journal of Quantitative Spectroscopy and Radiative Transfer*, 73, 111-120, 2002.

96. P. Rath, S.C. Mishra, P. Mahanta U.K. Saha and K. Mitra, Discrete transfer method applied to transient radiative problems in participating medium, *Numerical Heat Transfer A*, 44, 183-197, 2003.

97. S.C. Mishra, P. Chug, P. Kumar and K. Mitra, Development and comparison of the DTM, the DOM and the FVM formulations for the short-pulse laser transport through a participating medium, *International Journal of Heat and Mass Transfer*, 49, 1820-1832, 2006.

98. Z. Guo, J. Aber, B.A. Garetz and S. Kumar, Monte Carlo simulation and experiments of pulsed radiative transfer, *Journal of Quantitative Spectroscopy and Radiative Transfer*, 73, 159-168, 2002.

99. Z. Guo and S. Kumar, Discrete-ordinates solution of short-pulsed laser transport in two-dimensional turbid media, *Applied Optics*, 40, 3156-3163, 2001.

100. M Sakami, K. Mitra and P.F. Hsu, Analysis of light-pulse transport through two-dimensional scattering and absorbing media, *Journal of Quantitative Spectroscopy and Radiative Transfer*, 73, 169-179, 2002.

101. T. Okutucu and Y. Yener. Radiative transfer in participating media with collimated short-pulse Gaussian irradiation, *Journal of Physics D: Applied Physics*, 39, 1976-1983, 2006.

102. T. Okutucu Y. Yener and A.A. Busnaina, Transient radiative transfer in participating media with pulse-laser irradiation - an approximate Galerkin solution, *Journal of Quantitative Spectroscopy and Radiative Transfer*, 103, 118-130, 2007.

103. S.C. Mishra and H.K. Roy, Solving transient conduction-radiation problems using the lattice Boltzmann method and the finite volume method. Journal of Computational Physics, 233, 89-107, 2007.

104. D.J. Sarma, S.C. Mishra and P. Mahanta, Analysis of collimated radiation using the discrete transfer method, *Journal of Quantitative Spectroscopy and Radiative Transfer*, 96, 123-135, 2005.

105. H.K. Park, D.Kim, C.P. Grigoropoulos and A.C. Tan, Pressure generation and measuermnt in the rapid vaporisation of water on pulsed laser heat source, *Journal of Applied Physics*, 80, 4072-4083, 1996.

106. X Lu and P Hsu, Reverse Monte Carlo simulations of light pulse propagation in nonhomogeneous media, *Journal of Quantitative Spectroscopy and Radiative Transfer*, 93, 349–367, 2005.

107. M.J.C. Gemert and J.J. Wetch. Clinical use of laser-tissue interaction, *JEEE Engineering Medicine and Biology Magazine*, 100-113, 1989.

108. D.P.Poppas, G.B. Rucker and D.S. Scerr, Laser tissue welding- poised for the new millenium, *Surgical Technology International*, 9, 33-41, 2000.

109. H.G. Pettit and R.Sauerbrey, Pulsed ultraviolet laser ablation, *Applied Physics A*, 56, 51-63, 1993.

110. S.A. Prahl. M.J.C. Van Gemert and A.J.Welch, Determining the optical properties of turbid media by using the adding-doubling method, *Applied Optics*, 32, 559-568, 1998.

111. S.T. Flock, M.S. Patterson, B.C. Wilson and D.R. Wyman, Monte Carlo modelling of light propagation in highly scattering tissues-i: prediction and comparison of diffusion theory, *IEEE Transactions in Biomedical Engineering*, 36, 1162-1168, 1989.

112. H.Schweiger, A.Oliva, M.Costa and C.D.P. Segerra, A Monte Carlo Method for the simulation of transient radiation heat transfer: application to compound honeycomb transparent insulation. *Numerical Heat Transfer B*, 35, 113-136, 2001.

113. M.Sakami, K.Mitra and P.F. Hsu. Transient radiative transfer in anisotropically scattering media using monotonicity-preserving schemes, *2000 Int.Mechanical Engineering Congress and Exposition*, November 5-10 2000, Orlando, FL, USA.

114. A.L.McKenzie. Physics of thermal processes in laser-tissue interaction, *Physics in Medicine and Biology*, 35, 9, 1175-1209, 1999.

115. T. Hassan, K.R. Naqvi. S.A. El-Wakil and E.M. Abulwafa. Transient radiative heat transfer through thin films using Laguerre-Galerkin method. *Journal of Physics D: Applied Physics,* 36, 3014-3026, 2003;

116. A. Trivedi, S. Basu and K. Mitra. Temporal analysis of reflected optical signals for short pulse laser interaction wih nonhomogeneous tissue phantoms, *Journal of Quantitative Spectroscopy and Radiative Transfer*,93, 325-36, 1996.

117. JC Chai, HOS Lee, SV Patankar. Ray effect and false scattering in the discrete ordinates method. *Numerical Heat Transfer, Part B: Fundamentals*, 24, 373-389, 1993.

118. K.Kim and Z.Guo, Discrete ordinates method for transient radiation transfer in cylindrical enclosures, *Proceedings of 2003 ASME Summer Conference*, July 21-23, Las Vegas, Nevada, USA.

119. K.Kim and Z.Guo, Thermal relaxation times in biological tissues subjected to pulsed laser irradiation, *9th AIAA/ASME Joint Thermophysics and Heat Transfer Conference*, 5-8 June 2006, SF, California.

120. S.K. Wan, Z. Guo and S.Kumar, Rapid diagnosis of inhomogeneity in turbid media, *Proceedings of IMECE'03, 2003 ASME International Mechanical Engineering Congress Washington D.C.*, November 15-21, 2003.

121. P.F. Hsu, Z.M. Tan, S.H. Wu and C.Y.Wu, Radiative heat transfer in finite cylindrical homogeneous and nonhomogeneous scatteirng media exposed to collimated radiation, *Numerical Heat Transfer, Part A* 35, 655-679, 1999.

122. K. M. Katika and L. Pilon. *Modified Method of Characteristics for Transient Radiative Transfer*. University of California Postprints Year 2006 Paper 1646.

123. Z.Guo, S.Kumar and S. Maruyama, Transient radiation element method for three-dimensional scattering, absorbing and emitting method, *2001 International Mechanical Engineering Congress and Exposition,*November 11-16, 2001, New York.